

Structural and magnetic investigations of two spreading systems around the Rodriguez Triple Junction with respect to hydrothermal activities

Von der Naturwissenschaftlichen Fakultät
der Gottfried Wilhelm Leibniz Universität Hannover

zur Erlangung des Grades

Doktorin der Naturwissenschaften

Dr. rer. nat.

genehmigte Dissertation

von

Master of Science Carolin Bartsch

geboren am 05.04.1987 in Rathenow

2014

Referentin: Prof. Dr. Andrea Hampel

Korreferent: PD Dr. Udo Barckhausen

Tag der Promotion: 14.07.2014

Abstract

Hydrothermal vent fields along mid-ocean ridges can appear in many varieties and because they are very metal-rich the fields can be of great importance for the industries in the future. It is important to identify areas of hydrothermal activities along mid-ocean ridges from datasets which are acquired at the sea surface to save valuable research time. In the work presented here it was possible to prepare a list with main features of hydrothermal vent sites from bathymetric and magnetic datasets from the sea surface along two mid-ocean ridges in the western Indian Ocean. The features are separated into magmatic and tectonic activities.

The area of interest is located between 21°S and 28°S and includes the southern Central Indian Ridge (CIR), the Rodriguez Triple Junction (RTJ), and the northern Southeast Indian Ridge (SEIR). With a full spreading rate of 4.7 cm/a the Central Indian Ridge represents a slow spreading mid-ocean ridge system and is mainly characterized by several offsets of the ridge axis, an overlapping spreading center, a Knorr rise, and an oceanic core complex. To the south the intermediate spreading Southeast Indian Ridge with a full spreading rate of 5.7 cm/a follows. This ridge is defined by several offsets of the ridge axis, three oceanic core complexes, and a large number of seamounts. Analysis of three known hydrothermal vent fields Sonne, Edmond, and Kairei of the Central Indian Ridge shows a dominance of features caused by tectonic activities such as ridge axis offsets, pull-apart basins, oceanic core complexes, and fault zones cross-cutting at some places. Magmatic processes pronounced in terms of neovolcanic ridges and seamounts seem to play a secondary role as heat source. During a detailed magnetic survey a decrease in the magnetic susceptibility of the basalts was observed right above the hydrothermal vent field Edmond. This altered rock body caused by hydrothermal processes is 3D forward modeled with IGMAS+ to get an impression of its dimensions. Characteristic for the hydrothermal vent fields is a great distance to the ridge axis between 5 and 7 kilometers. Furthermore, an increase in the elevation of the hydrothermal vent fields with increasing distance to the spreading axis was observed. The two active hydrothermal vent fields Edmond and Kairei are located at the segment ends of the ridges and on the steeper northeastern ridge shoulders.

Keywords: mid-ocean ridges, hydrothermal vent fields, spreading rates

Zusammenfassung

Hydrothermalfelder, die an mittelozeanischen Rücken in vielfältiger Form und Gestalt auftreten, sind auf Grund ihres hohen Metallgehaltes von zukünftig wichtiger Bedeutung für die Industrie. Um wertvolle Forschungszeit zu sparen ist es wichtig, anhand von Daten, die mit Geräten von der Meeresoberfläche gewonnen werden, Gebiete entlang mittelozeanischer Rücken einzugrenzen, die hydrothermale Aktivitäten aufweisen. In der vorliegenden Arbeit ist es gelungen, anhand bathymetrischer und magnetischer Datensätze Eigenschaften, unterteilt in magmatische und tektonische Aktivitäten aufzulisten, die für hydrothermale Aktivitäten entlang zweier mittelozeanischer Rücken im westlichen Indischen Ozean sprechen. Das Forschungsgebiet liegt zwischen 21°S und 28°S und umfasst den südlichen Zentralindischen Rücken, die Rodriguez Triple Junction und den nördlichen Südostindischen Rücken. Der Zentralindische Rücken stellt mit einer vollen Spreizungsrate von 4,7 cm/a ein langsam spreizendes System dar und ist hauptsächlich gekennzeichnet durch mehrere Versätze der Rückenachse, einem sich überlappenden Spreizungszentrum, einer Knorr Aufdomung und einem ozeanischen Mantelgesteins Komplex. Richtung Süden schließt sich der intermediär spreizende Südostindische Rücken mit einer vollen Spreizungsrate von 5,7 cm/a an, der ebenfalls durch etliche Versätze der Rückenachse, drei ozeanische Mantelgesteins Komplexe und zahlreiche Seamounts charakterisiert ist.

Analysen dreier bekannter Hydrothermalfelder Sonne, Edmond und Kairei des Zentralindischen Rückens zeigen eine Dominanz von tektonisch bedingten Merkmalen wie Versätzen der Rückenachse, pull-apart Becken und Störungszonen, die sich teilweise kreuzen. Magmatische Prozesse, die in Form von neovulkanischen Rücken und Seamounts zum Ausdruck kommen, spielen eine sekundär wichtige Rolle als Wärmequelle. Während einer magnetischen Detailvermessung konnte eine Abnahme der magnetischen Suszeptibilität der Basalte direkt über dem Edmond Hydrothermalfeld aufgezeichnet werden. Dieser durch hydrothermale Prozesse alterierte Gesteinsbereich wird mit IGMAS+ 3D vorwärts modelliert, um eine Vorstellung zu dessen Dimensionen zu bekommen. Charakteristisch für die Hydrothermalfelder sind eine große Entfernung zur Rückenachse von 5 km – 7 km, sowie ein Anstieg in der Heraushebung der Felder in Bezug auf das Spreizungszentrum mit ansteigender Entfernung zu diesem. Die zwei aktiven Hydrothermalfelder Edmond und Kairei befinden sich jeweils an den Segmentenden der Rücken und an deren steileren nordöstlichen Rückenschultern.

Schlagwörter: mittelozeanische Rücken, Hydrothermalfelder, Spreizungsraten

Content

1) Introduction.....	8
2) The Indian Ocean: an overview	13
2.1) Evolution of the Indian Ocean	14
2.2) The western Indian Ocean and ridge systems	18
3) Methods.....	22
3.1) Bathymetry	22
3.1.1) Multibeam echo sounder EM120 & EM122	24
3.1.2) Data processing.....	26
3.2) Magnetism	27
3.2.1) Measurement principle	29
3.2.2) Data processing.....	32
3.3) Modeling of the magnetic data.....	34
4) Results.....	37
4.1) A slow spreading ridge system.....	37
4.1.1) Structural description.....	37
4.1.2) Magnetic observations	59
4.2) An intermediate spreading ridge system	68
4.2.1) Structural description.....	68
4.2.2) Magnetic observations	93
4.3) Hydrothermal vent field Sonne	100
4.4) Hydrothermal vent field Edmond.....	103
4.5) Hydrothermal vent field Kairei	106
5) Discussion	109
5.1) Review of the two active spreading systems.....	109
5.2) Review of the HTFs along the CIR	113
5.3) Slow spreading Central Indian Ridge system	116
5.4) Intermediate spreading SEIR system	133
5.5) Slow vs. Intermediate	144
5.6) Magnetic modeling of Edmond.....	148
5.7) Characteristic areas of other HTFs.....	154
6) Conclusions.....	164

7) References.....	166
8) Acknowledgments.....	176
9) Curriculum Vitae	177
10) Appendix A & B	180

List of Abbreviations

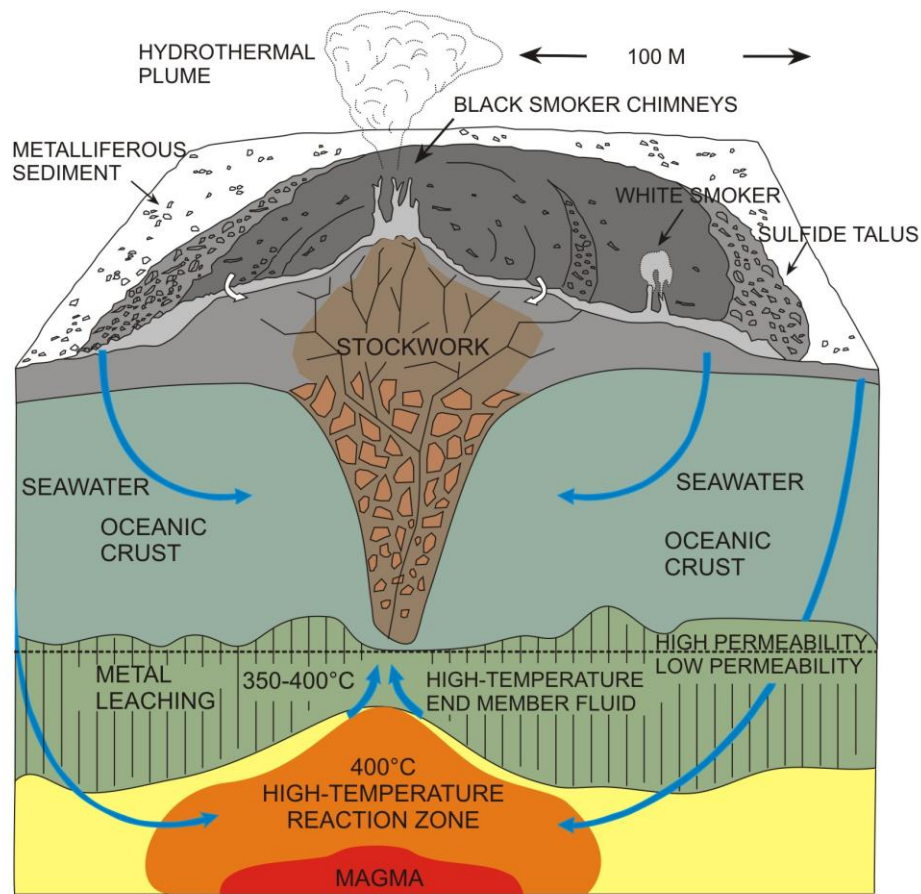
CAMH	Central Anomaly Magnetic High
CIR	Central Indian Ridge
GEODAS	GEophysical Data System
Gemino	Geothermal Metallogensis Indian Ocean
GMT	Generic Mapping Tool
HTF	hydrothermal vent field
IGMAS+	Interactive Geophysical Modelling Assistant
INDEX	Indian Ocean Exploration For Seafloor Massive Sulfides
NTD	non-transform discontinuity
OCC	oceanic core complex
OSC	overlapping spreading center
ROV	remotely operated vehicle
RTJ	Rodriguez Triple Junction
SEIR	Southeast Indian Ridge
SWIR	Southwest Indian Ridge
TAG	Trans Atlantic Geotraverse
TF	transform fault

1) Introduction

Mid-ocean ridges are the interfaces of the Earth where new seafloor originates. They have a length of approximately 65.000 km (SEARLE, 2013) and are offset and segmented by transform faults and smaller discontinuities. Four ridge types can be distinguished depending on their full spreading rates: the ultra-slow-, slow-, intermediate-, and fast-spreading ridges. Mid-oceanic ridges are complex systems defined by their magmatic and tectonic processes and they can have totally different morphological appearances. Along mid-ocean ridges hydrothermal activities in the form of hydrothermal vent sites can be observed, evolving due to the interaction of magmatic and tectonic processes. In the future these hydrothermal vent fields may be of great economic importance with respect to metal resources.

Slow and intermediate spreading mid-ocean ridges display a large diversity of hydrothermal systems. This includes vent systems along neovolcanic axes, large axial volcanoes at transform faults, and offsets associated with low angle detachment faults (TIVEY & DYMENT, 2010). Hydrothermal systems can evolve because cold seawater migrates through the oceanic crust along fault zones in the recharge zone (SEARLE, 2013). In the reaction zone (SEARLE, 2013) the cold seawater reaches the high-temperature reaction zone of a magma chamber and on its way up to the seafloor interacts with the surrounding rock material in the discharge zone (SEARLE, 2013) (**Figure 1**). On its way up to the seafloor the now called fluid leaches out the metals of the rocks which it passes through. Along fault zones the fluid reaches the seafloor and reacts with the cold seawater. This results in a precipitation of metal-rich sulfides because chemical and physical conditions change due to the mixture of cold ($\sim 2^{\circ}\text{C}$), oxygen-rich seawater with the high temperature metal-rich hydrothermal fluid (HERZIG & HANNINGTON, 1995). HERZIG & HANNINGTON (1995) postulate that polymetallic massive sulfides can only develop when so called black smokers are active during a long time span. They published some studies which show that hydrothermal vent fields consist of a sulfide mound and a stockwork zone (**Figure 1**). The mound grows because of continued hydrothermal fluid circulation and old collapsed chimneys which become part of the mound. Particles can be transported by currents and accumulate at great distances from the hydrothermal vent. A typical black smoker can produce ~ 250 t of massive sulfides per year (HERZIG & HANNINGTON, 1995).

Depending on the fluid temperatures, high- and low-temperature hydrothermal vent fields can

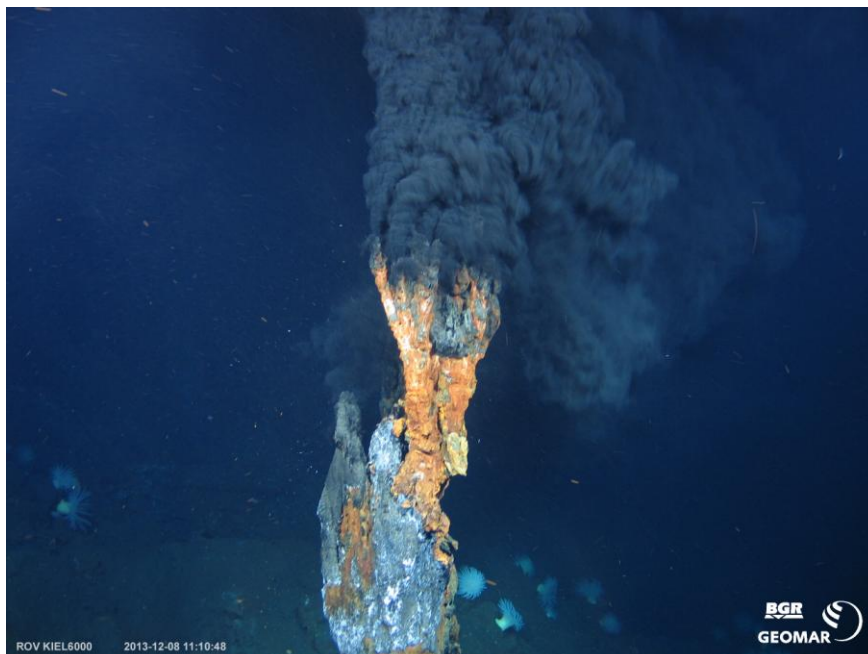


be distinguished and depending on the type of the surrounding rocks, basalt- and ultramafic-hosted hydrothermal vent fields can be observed (TIVEY & DYMENT, 2010).

Figure 1: Cross section of a hydrothermal vent field (HERZIG et al., 2000, modified)

Until now not much is known about the detailed bathymetry and magnetic structure of the mid-ocean ridge systems of the western Indian Ocean. The southern Central Indian Ridge (CIR) between 21°S and 25°40'S was investigated during several research cruises since 1983 (SO28-Gemino1, 1983; SO43-Gemino2, 1986; SO52-Gemino3, 1987/88; SO92-Hydrotrunc, 1993/94; M33-Hydrock, 1995). The first massive sulfides were found and recovered in the Indian Ocean in December 1993 from the Sonne hydrothermal vent site (HALBACH et al., 1998). Questions and targets of the research project INDEX from the BGR Hannover are the following three: The first one is the understanding of how hydrothermal vent sites were built in interaction with structural features. The second one is to find and define prospective areas for marine polymetallic massive sulfide deposits, and the third one is to applicate areas for an exploration license at the International Seabed Authority (ISA). For a future mining, inactive hydrothermal vent fields are of great importance because active ones with fluid temperatures of approximately +418°C (SCHWARZ-SCHAMPERA & Shipboard Scientific Party, 2014) would destroy any exploration equipment. To find them, as a first step active hydrothermal vent fields have to be identified which further away from the ridge axis may become inactive.

Many hydrothermal vent fields have been found by plume detection with methane anomalies (e.g. GAMO et al., 1996). The goal of this work is to find hydrothermally active areas out of bathymetric and magnetic datasets acquired at the sea surface to save important research and ship time. Out of these two datasets which features are characteristic for hydrothermal vent fields? Is it possible to limit areas at two mid-ocean ridge systems which have the potential for hydrothermal activities? To answer these questions structural and magnetic analyses of three known hydrothermal vent fields were done and the defined characteristics transferred to other areas along the ridge systems. With respect to structural conditions, normal faults and detachment faults as well as non-transform discontinuities seem to play a role in defining slow spreading ridge systems with hydrothermal vent field occurrence. To prepare an exploration license application for polymetallic sulfides, three research cruises were carried out in an area of importance between 21°S/28°S and 68°E/74°E. During the first one INDEX2011, 500 kilometers of the southern Central Indian Ridge were mapped with bathymetric, magnetic, and gravimetric measurements. In 2012 (INDEX2012) the same measurements have taken place along 500 kilometers of the northern Southeast Indian Ridge (SEIR). Additionally, the two hydrothermal vent fields Edmond (first discovered in 2001, VAN DOVER et al, 2001; GALLANT & VON DAMM, 2006) and Kairei (discovered and sampled in 2000, HASHIMOTO et al., 2001; GALLANT & VON DAMM, 2006) were mapped in detail.



During the third cruise INDEX2013 possible license clusters were mapped in detail and hydrothermal vent fields were investigated (**Figure 2**) and sampled with a remotely operated vehicle (ROV).

Figure 2: Active chimney of the hydrothermal vent field Edmond at the Central Indian Ridge observed with a remotely operated vehicle (ROV) during the research cruise INDEX2013 (SCHWARZ-SCHAMPERA & Shipboard Scientific Party, 2014).

After a short introduction about the evolution of the Indian Ocean and its three active spreading ridge systems, a structural and magnetic description of two ridge systems CIR and SEIR follows. The known hydrothermal vent fields will first be marked in this description and afterwards be described in more detail. Prominent structures of every ridge system will be discussed and the mapped ridge system as a whole will be interpreted in terms of its structural evolution, magmatically and/or tectonically active areas, and spreading rate behavior/evolution. A list of characteristic structural and magnetic features associated with hydrothermal vent fields and an outlook for further potential areas sum up the work.

For the structural description of the two spreading systems some definitions must be made. In the following the bathymetric minimum of the rift valley is defined as the active spreading center and plate boundary. The width of the rift valley was measured from the youngest (first) normal fault west and east of the rift valley. Especially for the intermediate spreading SEIR words such as “elevated” and “depressed” ridge shoulders are used. This definition was done by TUCHOLKE & LIN (1994) and means that the ridge shoulders on one flank are stronger uplifted (elevated) than the corresponding ones (depressed). Offset structures of the ridge axis which are no transform faults will be named “discontinuity” following a definition by BRIAIS (1995). In contrast to transform faults (first order discontinuities) these second order discontinuities are associated with a wide deformation zone, showing complex morphology and tectonics as well as a short life span (GRINDLAY et al., 1991; Van WIJK & BLACKMAN, 2005).

The following three hydrothermal vent sites have been investigated in the past by several authors. HALBACH et al. (1998) analyzed the deposits of the inactive Sonne hydrothermal vent site and recognized that they are typical for MOR massive sulfides, but in a stage of decomposition and beginning to be covered with sediments. The chimney structures had been built by several hydrothermal events and now they are removed through mass transports and decomposition (HALBACH et al., 1998). The authors published that the mineralization zone of Sonne has dimensions of approximately 1500 m by 400 m.

For the Edmond HTF, GALLANT & VON DAMM (2006) calculated the dimensions of the area of extinct sulfide structures and talus with ~100 m by 60 m. With decreasing temperatures the Fe/Mn ratio also decreases which is likely a result of the loss of Fe from the fluids into sulfide and oxide phases (GALLANT & VON DAMM, 2006). Fe concentrations in fluids at the Edmond

field measured by GALLANT & VON DAMM (2006) are unusually high compared to a global data set. The very high temperatures of the fluids led to conclude that there must be a heat source that is relatively close to the surface which means that some of the basalts that underlie this site may have been emplaced relatively recently (GALLANT & VON DAMM, 2006). The same authors investigated the Kairei hydrothermal vent field with the help of elemental systematics and found out that it is hosted on altered crust. The fluids they collected are most similar to fluids collected from black smokers at the TAG (TransAtlanticGeotraverse) field and led to suggest that the substrate at both locations is extensively altered.

2) The Indian Ocean: an overview

The Indian Ocean, located between Asia, Australia, Antarctica, and Africa, is characterized by several ridge and fault systems which divide the ocean into various basins (**Figure 3**), such as the Madagascar Basin, the Crozet Basin, the Central Indian Basin, and the Wharton Basin. In the east the Indian Ocean is defined by the Ninetyeast Ridge and the Broken Ridge. Active spreading systems such as the Central-, Southeast-, and Southwest Indian Ridge (CIR, SEIR and SWIR) which meet at the Rodriguez Triple Junction (RTJ) characterize the western Indian Ocean. The three active spreading ridge systems represent the boundaries between the African and Indian plate (CIR), the Indian and Antarctic plate (SEIR), and the African and Antarctic plate (SWIR). The relief of the seafloor is defined by transform faults and their traces which could be regarded as witnesses of the long-lasting drift process of the Indian plate.

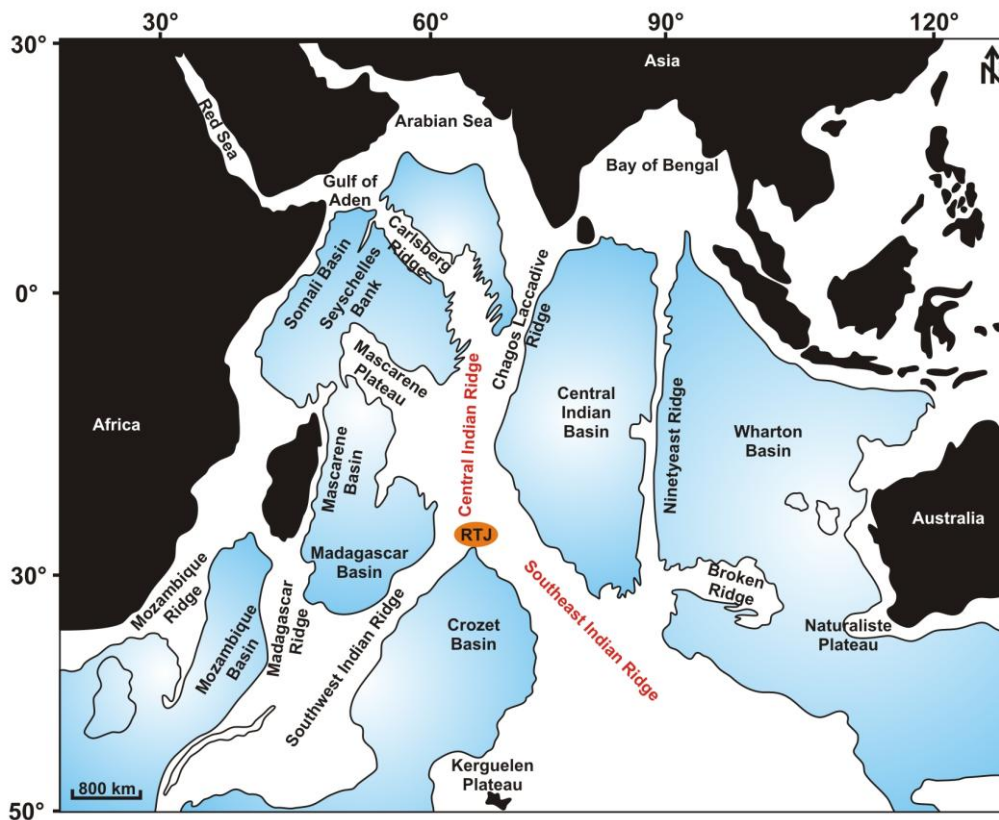


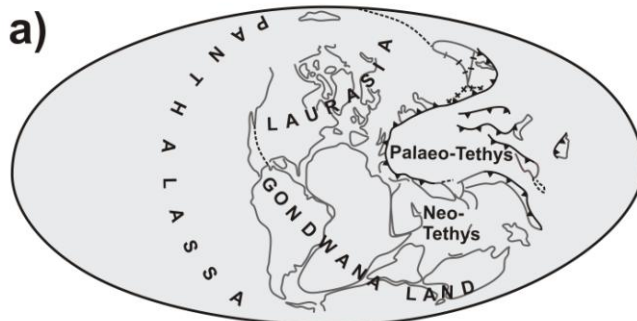
Figure 3: The Indian Ocean with its main bathymetric features surrounded by the 4000 m contour lines. The highlighted Rodriguez Triple Junction (RTJ) and active spreading ridge systems Central Indian Ridge (CIR) and Southeast Indian Ridge (SEIR) are the subjects of the work presented here (after HOCUTT, 1987, modified).

2.1) Evolution of the Indian Ocean

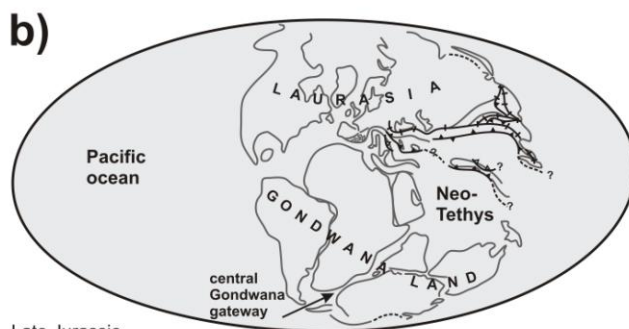
The evolution of the Indian Ocean as it is known today is the result of seafloor spreading between the African, Antarctic, and Indian plates. The following text is based on research results of HEINE et al. (2004) unless otherwise indicated. The Indian Ocean is closely linked to the break-up of the supercontinent Pangaea during the upper Jurassic (~150 Ma) and the opening of the Tethys. The break-up of Pangaea was quite complicated and is still not fully understood. FRISCH & MESCHEDE (2007) postulate that multiple subduction zones existed along the boundaries of Pangaea and its surrounding ocean Panthalassa. According to these authors, these subduction zones caused a suction effect resulting in Pangaea getting under extension. Furthermore, the in some places very old lithosphere of the supercontinent acted as a thermal shield towards the deeper mantle causing a heat accumulation under the lithosphere of Pangaea. This heat accumulation resulted in an uplift of the supercontinent's lithosphere in huge bulges and caused the supercontinent to break-up along weak zones. As a consequence, trench systems developed. These rift valleys continued to develop due to the tensile stress of Pangaea, leading to the break-up of the supercontinent into Laurasia in the north and Gondwana in the south (HOCUTT, 1987). The Tethys is considered to be a remaining part of Panthalassa and was an E-W oriented Proto-Mediterranean Sea (FRISCH & MESCHEDE, 2007). Therefore, the Indian Ocean is a successor of the Tethys, more specifically the Neotethys (**Figure 4a & b**).

Around 165 m.y. ago spreading caused Gondwana to be divided into an eastern part, including Antarctica, Australia, India, and Madagascar, and a western part consisting of South America and Africa (**Figure 4c**). With progressing extension and the final separation of Africa/South America and Antarctica, a “central Gondwana gateway” opened, representing a marine connection between the southeastern Pacific and the central Tethys (**Figure 4b**). Approximately 20 m.y. later seafloor spreading in the Enderby basin lead to a renewed opening of a second “eastern Gondwana gateway” (**Figure 4c**). This gateway between Antarctica, Great India, and Australia had a marine connection to the eastern Tethys, whereby Madagascar and Great India became isolated. At late Jurassic times (160-140 Ma) the Mesotethys was a triangular shaped ocean with a passive, southern boundary and an active, northeastwards trending northern subducting boundary (**Figure 5a & b, MT**).

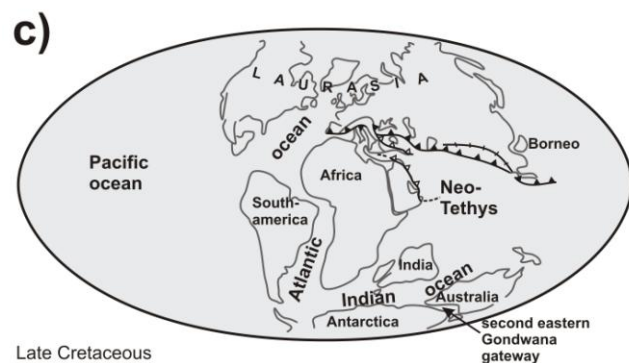
The active, mesotethic spreading ridge (**Figure 5a**, MTR), which opened the Mesotethys, migrated to the northern half of the Mesotethys. The direction of subduction was changing from a northeastern to a more northern direction due to rifting and active seafloor spreading around the northern part of Gondwana. Around 150 Ma the convergence rates increased from 0.9 cm/a to 1.4 cm/a. The reason for this increase was the opening of the Argo abyssal plain and the spreading around the northern boundary of Gondwana. 140 m.y. ago the spreading



Early Triassic, CK = Cimmeric Continent



Late Jurassic



Late Cretaceous

Figure 4: Development of the continents with a special look at the Tethys region and the Indian Ocean from the Early Triassic to the Late Cretaceous (after SENGÖR et al., 1988, modified)

ridge of the Mesotethys was subducted along the southeastern part of the Proto-Sunda deep sea trench. **Figure 5b** points out that the subducting crust was younger than 20 m.y. Between 140 and 135 Ma the subduction rate suddenly decreased to 0.3 cm/a due to the subduction of the spreading ridge of the Mesotethys and another change in the spreading direction from N to NNW occurred. This change developed because of a newly emerging spreading system which separated India and Australia in the Lower Cretaceous. After the reorganization, the subducting rates increased again to 0.8-0.9 cm/a. The Proto-Indian Ocean (**Figure 5d**, PIO) developed around 132 m.y. ago due to a rifting between India-Australia and India-Antarctica. Around 130 Ma the Mesotethys spreading ridge was almost fully subducted. Around 100 - 95 Ma last small relicts of the Mesotethys were subducted along the northwestern area of the Proto-Sunda deep sea trench. At around 99 Ma India started to move northwards with

evidence for this motion being provided by magnetic anomalies in the southern and central Indian Ocean (**Figure 5e-i**). During the Late Cretaceous to Paleocene (80-60 Ma) the oldest seafloor of the Neotethys was subducted northwards under the southern boundary of Eurasia. 65 to 55 m.y. ago northwest Great India collided with southern Eurasia. This event triggered great tectonic plate movements, which can be achieved only by a huge oceanic plate pushing India to the north and at the same time a spreading ridge in the proto-southern Indian Ocean which pushes India from the South. From Paleocene to Eocene (60-40 Ma) another compression along the Tethys-Eurasia boundary took place as a result of the subduction of progressively younger seafloor from the Neotethys and the active spreading ridge of the Wharton basin (see **Figure 5f-g**). During the Eocene (53 Ma) Australia separated from Antarctica and became part of the Indian Plate (**Figure 5f**, HOCUTT, 1987).

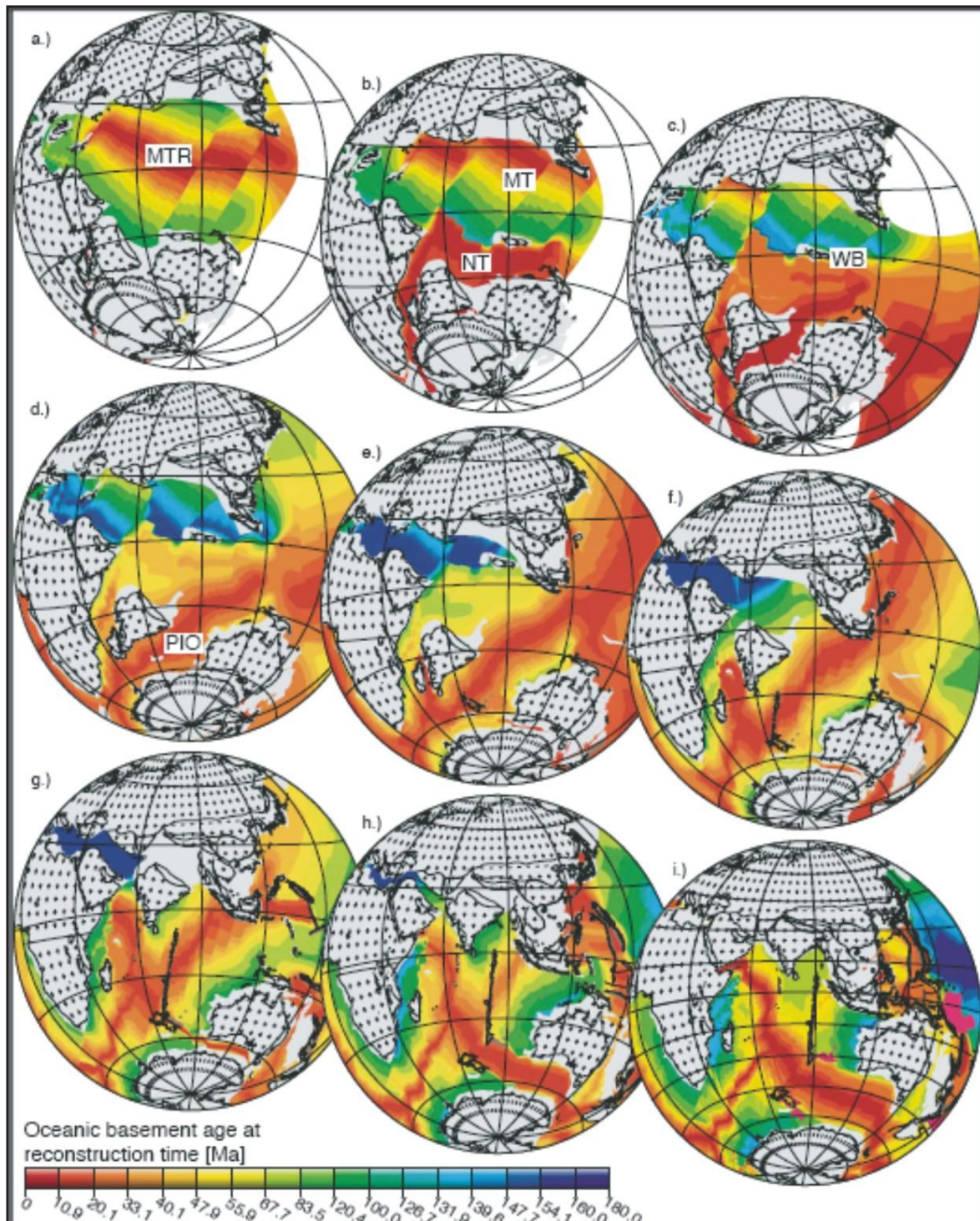


Figure 5: Palaeo-ages for the time between 160 Ma and today in steps of 20 Ma a=160 Ma, b=140 Ma, c=120 Ma, d=100 Ma, e=80 Ma, f=60 Ma, g=40 Ma, h=20 Ma, i= today, MTR=Mesotethys spreading ridge, MT=Mesotethys, NT=Cenotethys (Neotethys), WB=West Burma Block PIO=Proto Indian Ocean (after HEINE et al., 2004)

2.2) The western Indian Ocean and ridge systems

The western Indian Ocean developed during five major episodes of seafloor spreading (PATRIAT & SEGOUFIN, 1988). These are:

- 1) Late Cretaceous – Early Paleocene (Anomaly 29 - Anomaly 27)
- 2) Middle Paleocene – Early Eocene (Anomaly 27 - Anomaly 22)
- 3) Middle Eocene – Late Eocene (Anomaly 22 – Anomaly 18)
- 4) Late Eocene – Early Miocene (Anomaly 18 – Anomaly 8)
- 5) Early Miocene – Recent (Anomaly 8 – Anomaly 5)

If not labeled in a different way, the following explanations to these five different time intervals are based on PATRIAT & SEGOUFIN (1988).

KAMESH RAJU & RAMPRASAD (1989) suggest that shortly before 80 Ma the existing ridge axis of the CIR north of Madagascar jumped to the south resulting in a change of the spreading direction and the start of the separation of Madagascar from India. Furthermore, they assume that during this time a Ridge-Ridge-Ridge type triple junction, the Rodriguez Triple Junction, developed in the southeastern part of the Madagascar Ridge which connected the new CIR spreading center with the already active SWIR and SEIR.

Magnetic anomaly studies of PATRIAT & SEGOUFIN (1988) indicate that the plate boundary of the Africa-India plate was continuously extending during Anomaly 29 (~64.7 Ma) to 27 (~61.2 Ma) (**Figure 6**). It developed at the eastern side of the Mascarene plateau into the Madagascar basin at the expense of the SEIR. That led to a reorganization of the Africa-India-Antarctic triple junction (equal to RTJ with CIR, SEIR and SWIR) and the development of the CIR. At this time the spreading rates were highest with ~20 cm/a in the Indian Ocean (PATRIAT & SEGOUFIN, 1988). Analyses of PATRIAT & SEGOUFIN (1988) have shown that the traces of the Rodriguez Triple Junction in the African and Antarctic plates cross each other. This indicates that the SWIR got a complex tectonic modification at this time, eventually resulting in ridge jumps. Since the Late Cretaceous spreading along the western side of the SEIR seems to have been continuous with fast to medium spreading rates (ROYER & SCHLICH, 1988).

Seafloor spreading rates between Anomaly 27 (~61.2 Ma) and Anomaly 22 (~49.7 Ma) were very high with 15 cm/a along the CIR and SEIR (**Figure 7** and **Figure 8**). The evolution of

the Central Indian triple junction caused an extension of the SWIR. Until Anomaly 24 (~52.6 Ma) the SWIR spread in a NNW-SSE direction, after that time the spreading direction rotated into its recent N-S orientation. After Anomaly 23 (~50.9 Ma) (**Figure 8**) the spreading rates of the CIR decreased and a small ridge jump took place at the CIR to maintain the R-R mode at the Rodriguez Triple Junction.

Between Anomaly 22 (49.7 Ma) and 21 (~47.9 Ma) a strong decrease in the spreading rates along the CIR and SEIR can be observed. In addition, a change in the spreading direction along the CIR towards NE occurred. From Anomaly 20 (~43.7 Ma) to 18 (~39.5 Ma) the most notable changes in plate movement took place along the CIR and SEIR with spreading direction changing approximately 20°. Typical features for the reorganization of the SEIR are: a combination of ridge segments at Anomaly 21 (~47.9 Ma), a ridge jump at Anomaly 20 (~43.7 Ma), and oblique variations at Anomaly 18 (~39.5 Ma). Changes in the evolution of the triple junction at that time suggest that a R-T (ridge-transform) or R-T-T (ridge-transform-transform) mode dominated. At Anomaly 18 (~39.5 Ma) a change in the seafloor spreading direction from a fast northern spreading to a slower northeastern spreading took place. This change in spreading direction and velocity is attributed to the collision of India with Eurasia and resulted in the beginning of spreading at the CIR (NORTON & SCLATER, 1979).

In a time span between Anomaly 18 (~39.5 Ma) and Anomaly 8 (~25.9 Ma) the plate boundaries evolved to their recent appearance. Between Anomaly 18 (~39.5 Ma) and Anomaly 13 (~33.5 Ma) the spreading rates along the CIR decreased and some ridge jumps to the east in spreading direction have taken place. To a lesser extent this scenario occurred also along the SEIR. NORTON & SCLATER (1979) discovered that the triple junction was relocated by 7° to the west (with respect to Africa) during Anomaly 16 (~35.5 Ma) and also the SWIR migrated 3-4° northwards towards Africa. However, the Rodriguez Triple Junction moved faster in eastern direction as the SWIR spread (**Figure 9**).

Most parts of the Central Indian Basin and the Crozet Basin which separates India from Antarctica today evolved along the SEIR between Anomaly 8 (~25.9 Ma) and Anomaly 5, ~9.9 Ma (ROYER & SCHLICH, 1988). In comparison to earlier times the spreading rates along the CIR, SEIR and SWIR were very slow.

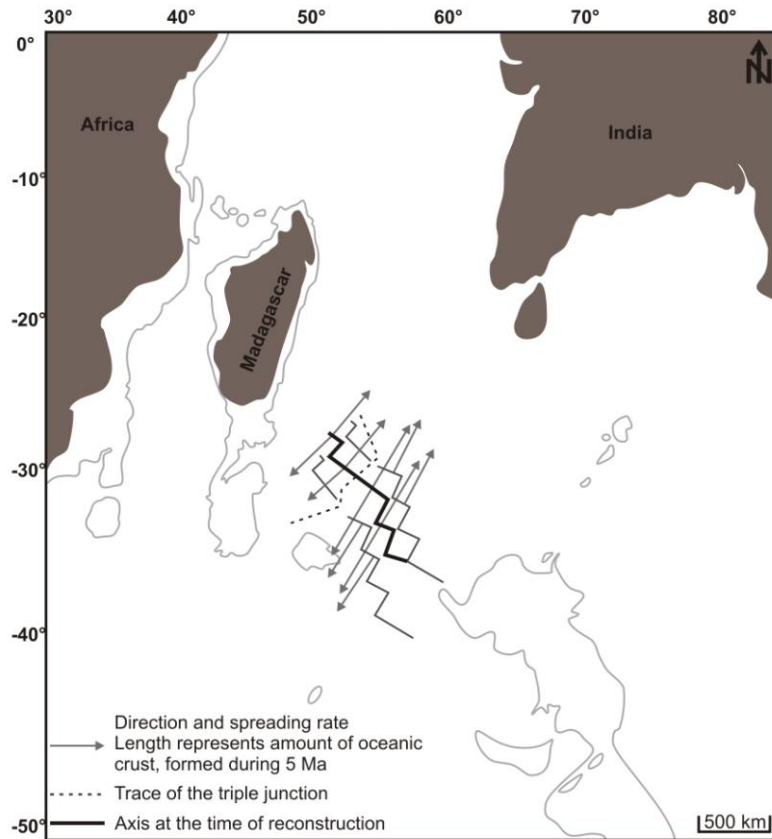


Figure 6: Reconstruction of the Central Indian Ocean in terms of Africa, Anomaly 28 (63 Ma) (after PATRIAT & SEGOUFIN, 1988, modified)

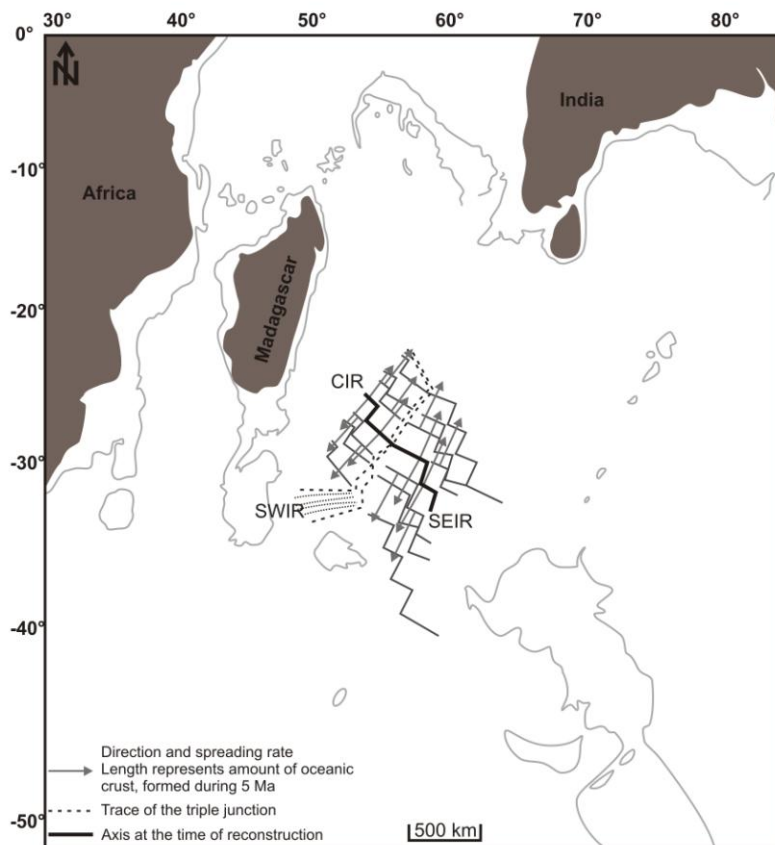


Figure 7: Reconstruction of the Central Indian Ocean in terms of Africa, Anomaly 26 (57.9 Ma) (after PATRIAT & SEGOUFIN, 1988, modified)

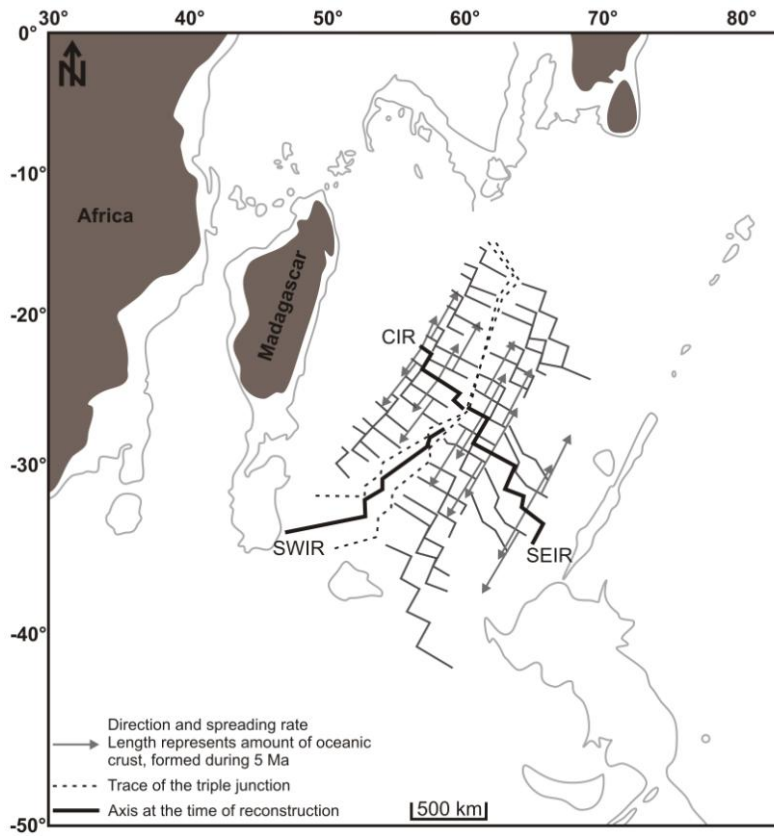


Figure 8: Reconstruction of the Central Indian Ocean in terms of Africa, Anomaly 22 (49.7 Ma) (after PATRIAT & SEGOUFIN, 1988, modified).

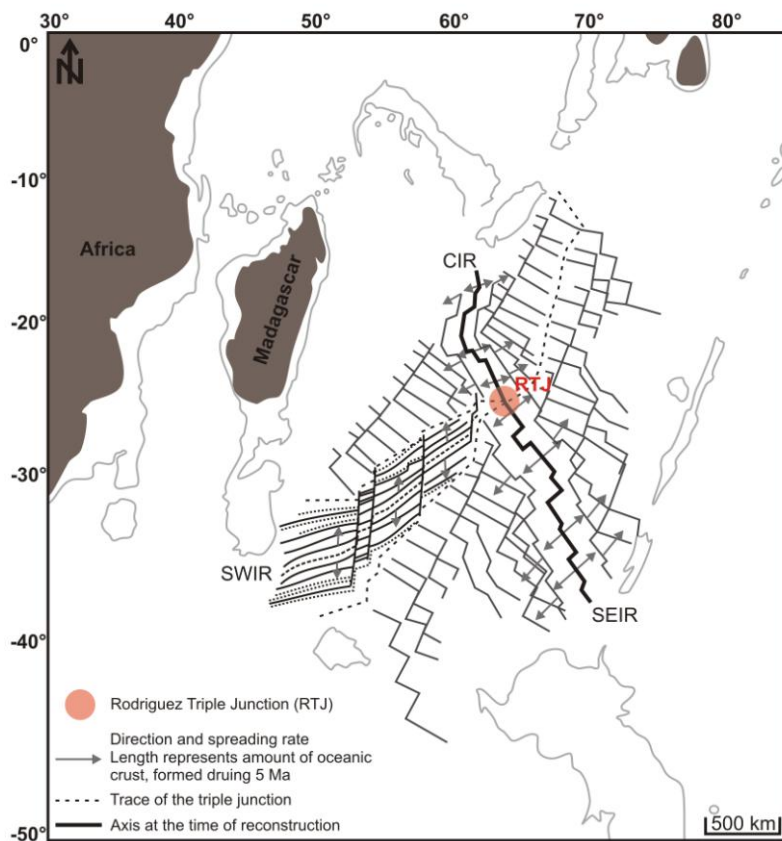


Figure 9: Reconstruction of the Central Indian Ocean in terms of Africa, Anomaly 13 (33.5 Ma) (after PATRIAT & SEGOUFIN, 1988, modified).

3) Methods

3.1) Bathymetry

To map the seafloor several possibilities exist. For a large spatial overview satellite measurements can be used with satellites like the American SEASAT (1978) and the European ERS-1 (1992) and ERS-2 (1994) (GIERLOFF-EMDEN, 1999). The missions are based on the fact that the sea surface reacts to gravity anomalies, which means the sea level correlates with irregular mass distribution at the seafloor due to the gravitational force (GIERLOFF-EMDEN, 1999). For example, seamounts result in a bulge of the sea surface of several meters but due to the attenuation effect of the water column this bulge at the sea surface has not the real size of the seamount (SANDWELL & SMITH, 1997). GIERLOFF-EMDEN (1999) showed that a very important factor for the measurement is the density distribution of the masses beneath the seafloor, meaning the specific weight of the rock bodies. The authors published the case of a salt diapir beneath a smooth seafloor which is expressed in a depression structure within the satellite measurements. Here, the density variation between the salt diapir and the surrounding rocks falsifies the resulting bathymetric estimations. That means gravity anomalies which are important for the measurements are not only caused by morphological shapes but also by their density (GIERLOFF-EMDEN, 1999). Deformations of the sea surface caused by local changes in the gravitational field must be large enough to be measured by a radar altimeter of a satellite orbiting the Earth (GIERLOFF-EMDEN, 1999). The measurement principle is based on radar waves sent from a satellite which will be reflected from the sea surface back to the satellite. Subsequently, the travel time is measured. A global tracking network with orbit calculations from a gravity model is used to measure the height of the satellite at a reference ellipsoid (SANDWELL & SMITH, 1997). A correlation exists between the bathymetry of the seafloor and the gravity within a 15-200 km wavelength band (SMITH & SANDWELL, 1997). So this limited frequency spectrum is needed to be measured from the radar altimeter. SMITH & SANDWELL (1997) argued that the estimation of bathymetry from gravity anomalies must be limited to the short wavelength band due to a “gravity-to-topography transfer function” explained in detail in the study work of the authors. According to these two authors, the bathymetry/gravity ratio varies from one region to the other. Due to the great distance between the satellite and the object being measured and assumptions which must be made (position of the satellite, distance to a reference surface, reflection properties,

absorption, scattering, and different wavelengths) this measurement principle has a limited accuracy and a resolution of only 15 km (SMITH & SANDWELL, 1994). However, the advantage of the satellite data is that they cover the whole planet with only small gaps in the high polar regions.

To obtain more detailed maps of the seafloor topography, the method of surveying bathymetry with a multibeam echo sounder is used. High resolution images with great accuracy can only be achieved with these bathymetric measurements being either conducted from a ship or an instrument near the seafloor. The measurement principle of the multibeam echo sounder is the localization of sound. An acoustic signal is sent from the vessel's transducer to the seafloor where it is being reflected. The vessel registers the reflected signal and measures the travel time. The total travel time of the wave (t) and the known mean sound velocity (c) are then used to calculate the water depth (h) using the equation of JONES (1999):

$$h = \frac{1}{2} ct$$

The average velocity of an acoustic signal which travels vertically through the water column is approximately 1500 m/s (JONES, 1999). However, changes in several parameters such as pressure, water temperature, or salinity can influence the velocities (JONES, 1999). An increase of temperature by 1°C or in salinity by 1‰ for example causes an increase in the velocities by 3 m/s or 1.3 m/s, respectively. Therefore it is essential that these parameters are determined in the form of sound velocity profiles on a regular basis.

3.1.1) Multibeam echo sounder EM120 & EM122

The functional principle of the multibeam swath sonar SIMRAD EM120 can be found in the manufacturer's manuals of Kongsberg Simrad EM120 (KONGSBERG, 2006). This system is installed on the research vessel SONNE and was used to map the southern Central Indian Ridge. It is designed for full ocean depth and works with a sonar frequency of 12 kHz. 191 beams are generated per ping as narrow as 2°. For shallow water depth the coverage sector can be set up to 150° and in water depths greater than 5000 m the swath width is up to 25 km. These parameters can be adjusted to the actual water depth in the research area. Furthermore, the movements of the vessel such as roll, pitch, and yaw can automatically be compensated by the system up to a certain level. The soundings are placed on a line perpendicular to the survey track to guarantee a uniform sampling of the bottom and a 100% coverage (**Figure 10**). The transducers are linear arrays mounted in a Mills cross configuration amidships (**Figure 11**). Each transmitter unit which consists of 48 modules with 18 elements can be steered according to the roll, pitch and yaw movement of the vessel. The receiver transducer has 16 modules with 8 hydrophone arrays each. The latter one can be selected individually. The operation of the system during a cruise is controlled by a pc-workstation with real-time displays. For the bathymetric surveys a speed of around 8 kn over ground is ideal.

The EM122, successor system to the EM120, is a multibeam system installed on the research vessel FUGRO GAUSS and was used to obtain a map of the northern Southeast Indian Ridge. It is a high performance multibeam echo sounder with unsurpassed high resolution, coverage, and precision. For more detailed information the reader is referred to the user manual of Kongsberg EM122 (2006). The transducers are the same as the ones of the EM120, but they contain a newer software package and electronic devices. 288 beams are generated at the same time per ping and the ping rate is twice as high as in the case of the EM120. This guarantees a resolution four times higher than before. The system also works with a sonar frequency of 12 kHz and a coverage sector of up to 150°. The recoverable swath width is on the order of 30 km at a water depth of 5000 m. The high density signal processing keeps the size of the acoustic footprint even for the outermost beams in the swath as small as possible. The transmit fan is divided into several small sectors which can be selected individually, depending on the roll, pitch, and yaw movements of the vessel. With this mechanism the soundings are placed on a "best fit" line perpendicular to the vessels track, thus ensuring a 100% coverage. Like the EM120 the transducers are linear arrays mounted in a Mills cross

configuration (**Figure 11**). The transmitter unit consists of up to 96 modules, each with 18 elements arranged in a row of 6 elements. The receive unit contains up to 16 modules. The data are controlled at a pc-working station with the SIS (seafloor information system) software, involving survey strategy, 2-D and 3-D display, seafloor image, water column, and other individually selectable information.

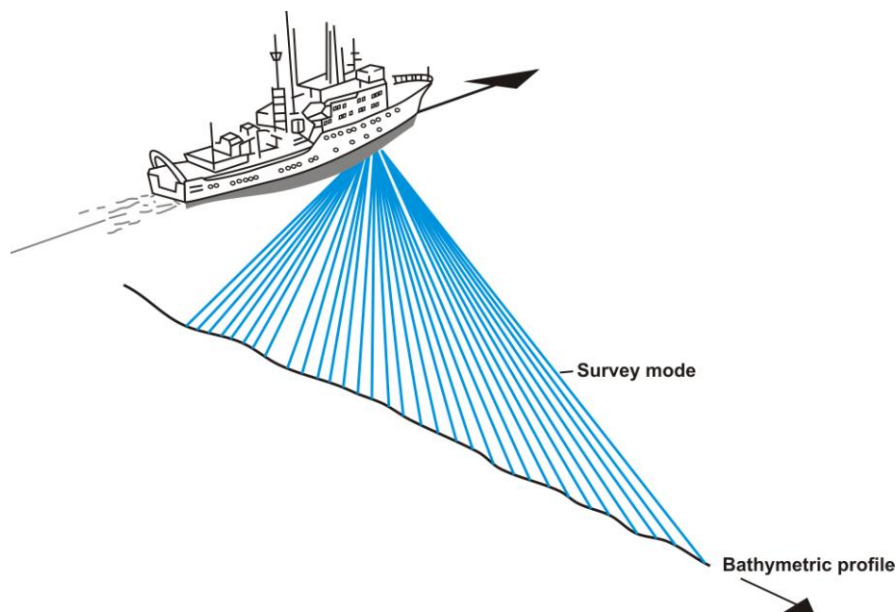


Figure 10: The multibeam echo sounder system with the transducer beam pattern. Blue lines show the survey mode perpendicular to the vessel track. (after JONES, 1999, modified)

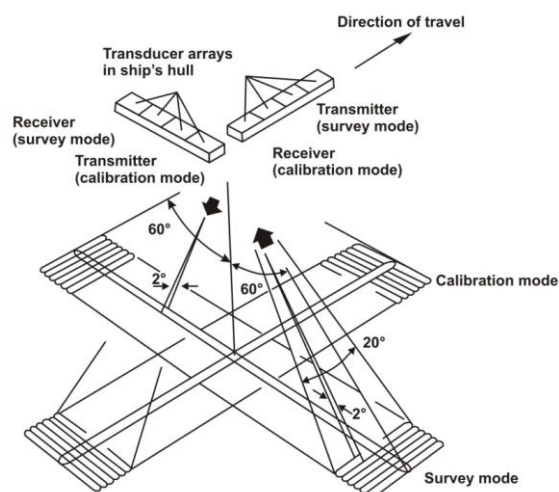


Figure 11: The Mills cross of the multibeam echo sounder system. The figure shows the ray paths for surveying sounding velocities (perpendicular to the vessel) and for calibration sounding velocities. (after JONES, 1999, modified)

3.1.2) Data processing

As described before, bathymetric measurements work with the localization of sound. Several parameters such as the water depth, vessel velocity and the roll and pitch behavior of the vessel depending on weather conditions influence the data quality. Therefore it is necessary to edit the resulting data and delete beams which display a wrong, senseless water depth. For the data processing of the CIR map the open source software MB-system (version-5.2, CARESS & CHAYES, 1996) was used, whereas data of the SEIR were processed with the commercial Fledermaus software (QPS-hydrographic and marine software solutions). One benefit of editing with Fledermaus is the 3-D view of the dataset. The user can display the lines in 3-D and gets a complete overview of the bathymetric data which allows the user to easily identify and delete erroneous beams. After editing, bathymetric maps were created with the software Fledermaus and GMT (Generic Mapping Tools, Version 4.5.7., WESSEL & SMITH, 1995).

The bathymetric profiles with simultaneous magnetic data acquisition were measured with a line spacing of approximately 5 km and a mapping velocity of 8 kn. In the following, the bathymetric maps have been generated with the software GMT where the color ranges from red-yellow to green-blue. Detailed maps from special areas of interest and cross profiles were prepared with the software Fledermaus and show 3-D views. Also slope maps can be created with Fledermaus making it easier to identify seamounts or directions of the slope dip.

3.2) Magnetics

In the late 1950s investigations of the seafloor in the Pacific Ocean with marine magnetic measurements revealed long stripes of alternating positive and negative magnetic anomalies (LOWRIE, 2007). This pattern runs parallel to the mid-ocean ridges (**Figure 12**) and originates because of changing polarities of the Earth's magnetic field in geological times when lithospheric plates drift apart and new oceanic crust is formed (JOCHUM et al., 1997). This mechanism was first described correctly by VINE & MATTHEWS (1963) which was a critical breakthrough for the concept of plate tectonics. Spreading rate velocities along the mid ocean ridge influence the stripe pattern of the magnetic anomalies in a way that high spreading velocities are causing wider stripes because a lot of material can accumulate in a short time interval (LOWRIE, 2007).

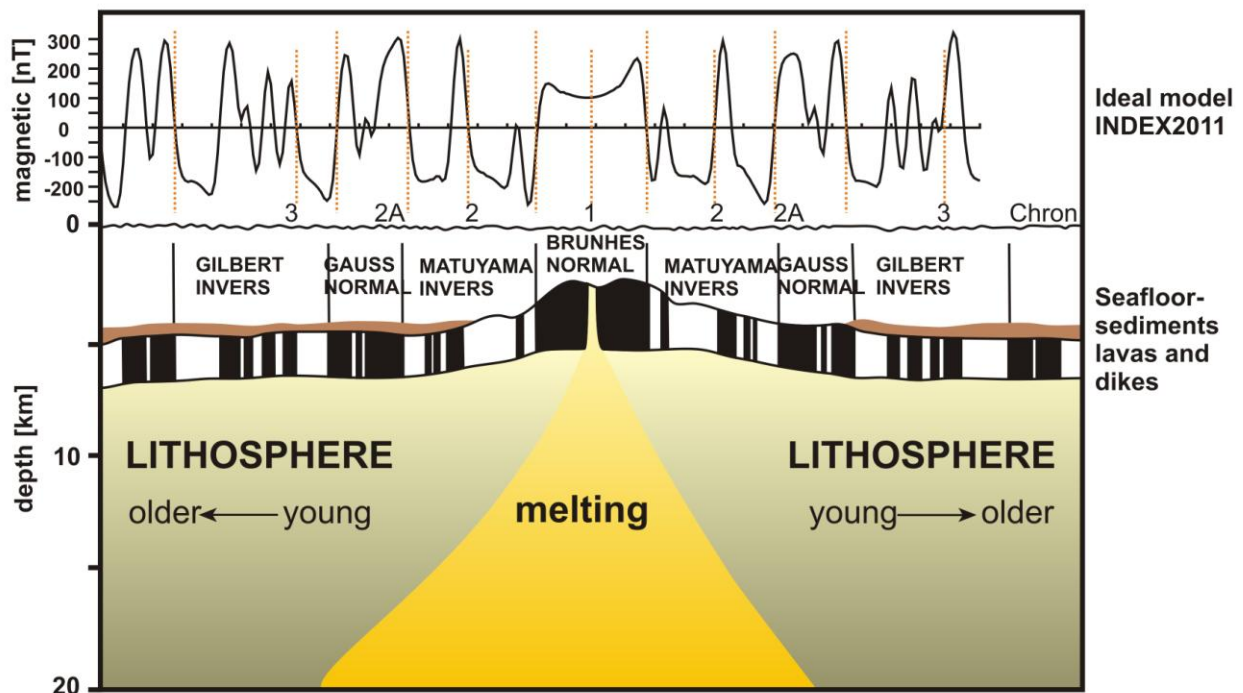


Figure 12: Profile of the seafloor across a mid-ocean ridge with its typical stripe pattern and corresponding magnetic anomalies/times. On top is a ideal magnetic profile from INDEX2011 perpendicular to the Central Indian Ridge. With increasing distance from the mid-ocean ridge the lithosphere gets older (after JOCHUM et al., 1997, modified).

LOWRIE (2007) describes the process called thermoremanent magnetization as follows. Before the melt rises to the surface, grains of ferromagnetic minerals in igneous rocks are generally above their Curie temperature, which lies for magnetite at 578°C and for hematite at 675°C. There is no molecular field and the atomic magnetic moments can behave in a chaotic way.

The material has a paramagnetic magnetization as shown on the right side in **Figure 13**. During solidification of the rock it cools and the temperature decreases below the Curie temperature (**Figure 13**, top), a spontaneous magnetization takes place. With cooling progressing this magnetization increases. The magnetic moments of the grains are blocked in the direction of the magnetic field at that time (**Figure 13**, left side), the rock becomes ferromagnetic. The newly formed rock retains the prevalent Earth magnetic field and is thermoremanently magnetized. MEYER (1999) assumes that there are different mechanisms for the formation and conservation of this permanent induced magnetic field depending on the rock material. LOWRIE (2007) explains that titanomagnetite series (iron oxide minerals) are responsible for the magnetic properties of oceanic basalts. They point out that magnetite (one end member of the series), a ferromagnetic mineral, has the strongest magnetic susceptibility of all naturally occurring minerals and furthermore a strong spontaneous magnetization.

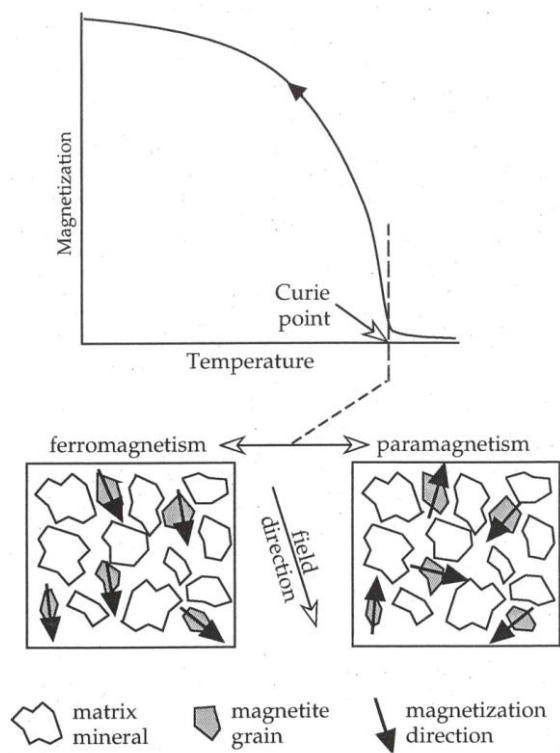


Figure 13: Schematic sketch of the magnetization behavior of magnetic grains from paramagnetic to ferromagnetic with changing temperature above Curie point. During the paramagnetic phase the grains behave in a chaotic way. With cooling under the Curie temperature the magnetizations of the magnetite grains become blocked and align parallel to the prevalent field direction (after LOWRIE, 2007).

3.2.1) Measurement principle

Marine measurements of the magnetic field were carried out with three BGR magnetometers towed astern of a research vessel. The measuring system consists of two Overhauser magnetometer sensors and one MagsonTM fluxgate sensor. As shown in **Figure 14** the array is towed 700 m astern of the vessel with a distance of 75 m between the individual sensors. The front and rear sensors are of Overhauser type, a proton-precession magnetometer enhanced with the Overhauser effect, which in gradiometer mode measures the total magnetic field in two different positions at the same time. This represents a scalar measurement. Based on the calculated difference of these two measurements it is possible to delete time variable parts of the Earth's magnetic field and only the spatial changes remain (BARCKHAUSEN & BARGELOH, 2012). As a result of the following integration of the measured gradient the inner part of the Earth's magnetic field along a profile can be shown. Between these two sensors the MagsonTM fluxgate sensor is mounted which measures the magnetic field vector in its three components (vector measurement). The total distance of 700 m between the sensors and the vessel guarantees a decrease of the ship's magnetic field to less than 1 nT and therefore minimizes the disturbing factor of the vessel. Furthermore, the measurement with three sensors has the advantage that data are still reliably obtained even in the case that one sensor experiences a malfunction.

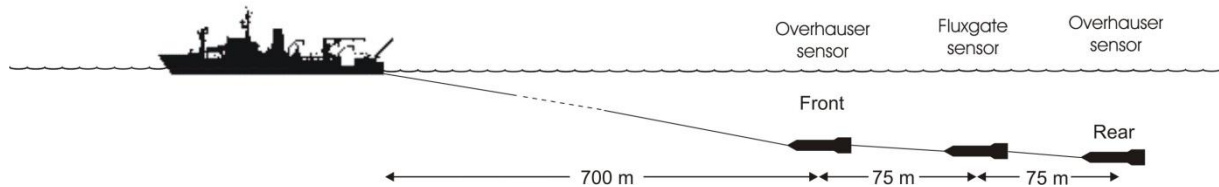


Figure 14: Schematic principle of the measurement array for the magnetic data (after BARCKHAUSEN & BARGELOH, 2012)

In the following the detailed measurement principles of these sensors will be explained based on BARCKHAUSEN & BARGELOH (2012), starting with the Overhauser magnetometer sensor. Here, the measurement is based on the stimulation of the proton sense (polarization) through radio waves. This is a difference to the standard proton magnetometers where a strong DC magnetic field is used for polarization. The wave length of the radio waves injects the spin of the electrons into an organic, proton rich fluid within the sensor. Electrons then transfer their

spin to the protons of the fluid through a mechanical process, called Overhauser effect (**Figure 15** left side). The actual measurement of the prevalent magnetic field takes place with the relaxation frequency, which means the attenuation of the spin from the protons (**Figure 15** right side). The precession frequency (occasionally called Larmor frequency) is a measuring unit for the intensity of the prevalent magnetic field because a linear proportionality exists between the precession frequency and the field strength (HEINRICH, 1968). Within the sensor the generated signal is digitized and afterwards transmitted to the vessel through the tow cable which also provides the power supply.

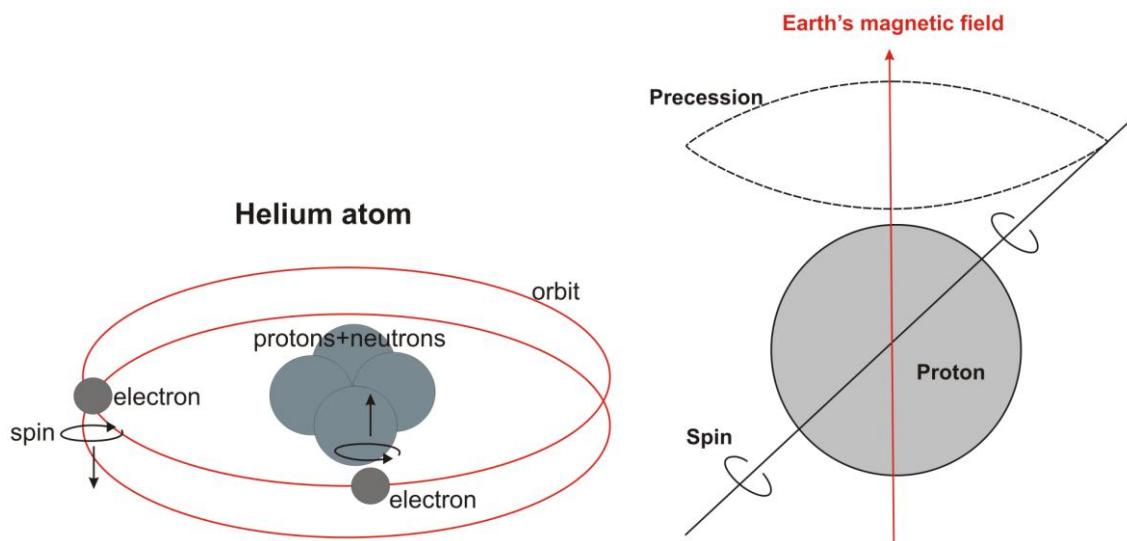


Figure 15: Schematic sketch of electrons transferring their spin to the protons on the left side and a schematic sketch of the principle precession frequency on the right side (after BASAVAIAH, 2011, modified).

The MagsonTM Fluxgate magnetometer consists of three orthogonally oriented fluxgate sensors and a set of inclinometers. The assembly is mounted on a platform into a glass fiber tube. The principal of vector compensation of three ring-core sensors based on three independent Helmholtz-coils is used. A precise zero level of the field inside the ring-core compensating the external magnetic field (in this case the Earth's magnetic field) will be achieved through an internal feedback circuit, which is based on digitally controlled direct currents fed into the Helmholtz-coils. Because of this function it is possible to use the amplitude of the current as a signal and to measure the vector components of the magnetic field. Measurements conducted in the marine environment suffer from sensor motions caused by the sea waves. To measure the movement of the Magson Fluxgate sensor a special

platform is mounted inside on which two tilt sensors are attached. The first tilt sensor measures the pitch and roll angle through a conducting liquid in a half filled glass vial. The liquid covers five electrodes and from the level of that covering the inclination angle can be derived. Values from $\pm 25^\circ$ to $\pm 40^\circ$ can be reached depending on the settings of the system. The second tilt sensor represents a dual axis accelerometer, measuring the pitch and roll angle in a span of $\pm 50^\circ$ (roll) to $\pm 20^\circ$ (pitch). This second sensor is generally more accurate, but also very temperature sensitive. In addition to the static acceleration both sensors also measure the dynamic acceleration, which results from the continuously moving fish. Within the water movements of the Fluxgate sensor such as rotating cannot be avoided, therefore it is very important to measure the motion angle with high accuracy. This then allows rotating the field coordinates from the coordinate system of the sensor into the geomagnetic coordinate system. By that kind of rotation about the Euler angle, the vertical and horizontal vector components are obtained. It would also be desirable to separate the horizontal component into a north and east component. This would require precise knowledge of the true north direction with respect to the sensor orientation. In theory this could be achieved with a gyro mounted to the instrument platform inside the sensor. Practically gyros have a high power consumption and suffer from drift problems which makes their use in vector magnetometer very problematic. An alternative way of estimating a true north direction is a method introduced by ENGELS et al. (2008) called “numerical yaw”. This method is used at BGR for the calculation of full three component vector data from measurements carried out with the towed Magson fluxgate sensor.

3.2.2) Data processing

The raw data measured with the towed magnetometer sensors must be checked for quality and whether external parameters such as the course of the vessel, the velocity, time, field differences, magnetic storms, or daily variations could have affected the magnetic data providing erroneous results. First the sensor positions are corrected based on GPS data from the vessel and an interpolation of existing small gaps is carried out. Time deviations in the dataset on the order of a few seconds, which may occasionally occur, are interpolated as well. As a third step outliers have to be eliminated using a median filter. The expected value of the Earth's magnetic main field at any place is taken to be that of the International Geomagnetic Reference Field, IGRF2010 (MAUS, 2010). Because the magnetic anomaly is defined as the difference between the observed and the expected values (LOWRIE, 2007), it is necessary to subtract the IGRF from the data. That process is called normal field reduction and results in the field anomalies of the oceanic crust. In this case it is assumed that either external field variations are neglectable or absent because the magnetic field was reconstructed from gradient measurements.

LOWRIE (2007) points out that on the one hand deep-seated magnetic sources produce broad, long-wavelength magnetic anomalies and on the other hand shallow sources create narrow, short-wavelength anomalies. The crustal anomalies observed during the investigations presented here can be counted to the latter ones. Therefore it is important to filter the wavelength related to the anomalies originating from crustal sources (ENGELS et al., 2008). The process of band pass filtering is described in detail by ENGELS et al. (2008). They postulate that the relevant wavelength range can either be derived from spectral analysis or from the reversal time scales and spreading rate estimations out of the survey area data itself. The method was applied by FRANKE et al. (2008) to data from the South China Sea. The authors used a lowpass filter (LP) for the removal of wavelengths shorter than 2-4 km for short profiles crossing the spreading ridge axis. For long profiles like transit profiles they used a highpass filter (HP) which removed wavelengths longer than 250 km. This also removes much of the external daily variations which at typical survey speeds have a wavelength of 400-500 km.

Another correction which can be made is the crossover error correction between the profiles. In case of the profiles from west to east along the Central Indian Ridge and the Southeast

Indian Ridge no crossover points exist between the profiles, thus no correction with this method is possible. For two detailed mapping datasets with profiles running from north to south and west to east the crossover correction was carried out. The crossover errors of single sensor magnetic data sets are due to first, offsets between the profiles of different surveys and second, external variations like differences in passing the same location at different local times (HEYDE et al., 2014). ENGELS developed a code for the crossover error correction which detects the position of the errors and automatically levels all profiles with the help of a least square algorithm (EHRHARDT & Shipboard Scientific Party, 2011). The reduction of the average error is on the order of 70% (HEYDE et al., 2014).

During the course of a day the intensity of the geomagnetic field at the Earth's surface can change due to the Earth's rotation beneath different layers of the ionosphere (LOWRIE, 2007). Such daily variations in mid-latitudes have a range of 10 to 100 nT (MEYER, 1999). The working area in the Indian Ocean (CIR and SEIR between 21°S and 28°13'S) is characterized by a long distance from the magnetic dip equator (inclination 0°). At this longitude the magnetic dip equator lies 8° north of the geographic equator, hence it is unlikely that the equatorial electrojet has influenced the measurements (BARCKHAUSEN & BARGELOH, 2012).

The desired accuracy of the data can be adjusted depending on the goal of the measurements, for example, whether seafloor spreading anomalies as time markers need to be identified, or a zone of decreased magnetic values due to hydrothermal processes is of primary interest. Sources of error could be measurement errors of the sensors or failures, errors in the position coordinates, and interruptions of the measurements in order to perform sampling of rocks. The error in the measured data and the subsequent evaluation of these data is estimated to be 10 nT for the survey profiles. In the case of the detailed surveys over hydrothermal sites, the error after all corrections is on the order of 2 nT.

With the final filtered and processed data, representing the crustal anomalies, further modeling steps can be done.

3.3) Modeling of the magnetic data

With the program SFLAS (1989), developed at the BGR Hannover, it is possible to calculate forward models to make assessments regarding the magnetic anomalies of the oceanic lithosphere over a specified time interval (ROESER, 1986). For the calculation of seafloor spreading anomalies the magnetic reversal time scale of CANDE & KENT (1995) was used. After some definitions of the magnetization parameters like inclination/declination of the recent field, strike direction of the spreading ridge, direction of the profiles, the spreading rates, and the time interval, the program calculates the stripe pattern and the assumed trend of the magnetic anomalies. The spreading rates over time were adapted iteratively until the model provides a good fit with the measured data curve. In doing so the flanks of Anomaly 1 and, where present, the Jaramillo event were picked as age marks. In addition some transit profiles or older profiles from the GEODAS database (NOAA, 2009) which extend further from the ridge axis and also cover older anomalies could be used to increase the accuracy. With the help of these resulting models it was possible to locate the center of Anomaly 1 on each profile. An asymmetric or symmetric behavior of the spreading ridge areas results from the calculated models which sometimes reveal that one side of the ridge axis spreads faster than the other. At the end, as many measured curves as possible should fit into the model boundaries (**Figure 16**). While carrying out the modeling it is important not to lose the geological sense of the values, because there is never a 100% match of the modeled and measured curves. Afterwards the full spreading rate was calculated for each profile as follows, whereby for every profile the distance of the Anomaly 1 boundaries was measured and converted into spreading rates per year:

$$780000 \text{ a/km} = \text{spreading rate.}$$

A difference in the measurement of 1 km in the distance of the Anomaly 1 boundaries produces a 1.3 mm/a difference in the spreading rate. It is estimated here that the actual error in measuring the distance of the Anomaly 1 boundaries is below 1 km for each individual profile. Since the spreading rates determined for ridge segments represent an average over ~10 or more profiles, the resulting uncertainty in the calculated spreading rates can be assumed to be not higher than 0.5 mm/a. All in all 57 profiles along the slow spreading CIR and 64 profiles along the intermediate spreading SEIR were analyzed in this way. The profiles

have all been projected to 60°E (CIR) and to 50°E (SEIR) and thus perpendicular to the spreading axe and run from SW to NE.

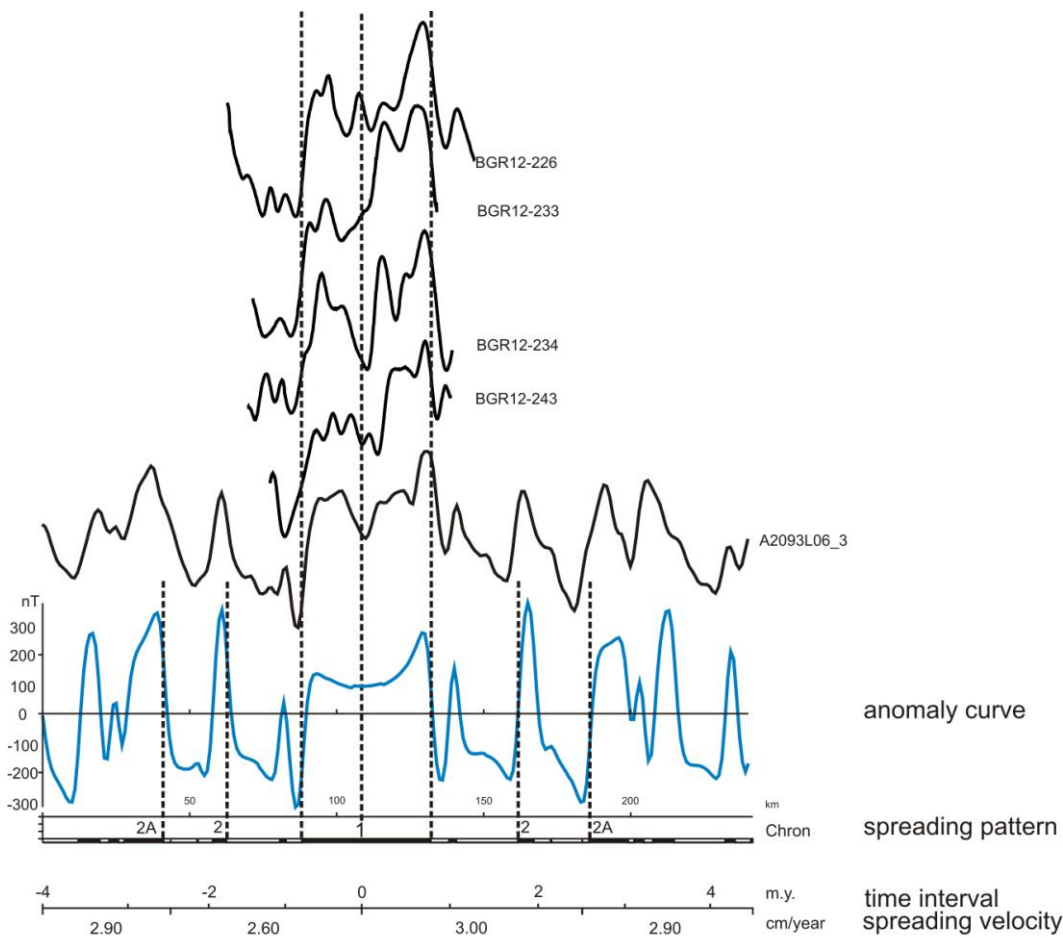


Figure 16: SFLAS model for the spreading rates and time interval of Section 3 from the SEIR. A longer profile A2093L06_3 from the GEODAS database was used as a reference and to increase the precision of the modeling with further anomaly time marks.

During detailed magnetic surveys over one hydrothermal vent field a decrease of the magnetic values was recorded. To model this zone of lower magnetic values another software was used, the Interactive Geophysical Modelling Assistant (IGMAS+). This involves a 3D forward modeling software of the University of Kiel which is based on the principle of triangulation of subsurface structures and uses potential field data (SCHMIDT & GÖTZE, 2012). The program uses Universal Transverse Mercator (UTM) coordinates and the reference ellipsoid WGS84. Bathymetric and magnetic data must be prepared in a spreadsheet with the following order: x,y coordinates, water depth, and in case of magnetics the nT values. For the modeling outlined in **Chapter 5.6** the main profile direction was W-E. The bathymetric dataset is required to be larger than the magnetic one to also allow modeling of the boundaries of the

magnetic dataset without creating misleading edge effects. With 21 sections and a minimal vertical distance of 5m the bathymetry represents the basis of the project. For the stations magnetic data are imported. For different layers the magnetic susceptibility can be defined individually and is necessary for the calculation of the models anomalies (calcMAGtotr. ~ total Field induced remanent). Some magnetic model parameters for the survey area are the total magnetic field of 49441 nT, an inclination of 60°, and a declination of 24°. From the large magnetic overview it is known that the modeled body lies within Anomaly 1 and therefore embedded in rocks which are magnetized parallel to the recent field. For the process of modeling the oceanic crust was separated into two layers (**Figure 17**). In general there are three layers, however, the first layer consists of sediments and therefore can be neglected in this case as the CIR is a young ridge system with almost no sediments being accumulated. Oceanic layer two represents the volcanic crust which can be subdivided into layer 2A with pillow basalts and a thickness of 0.5 km and layer 2B the Diabase dikes and 1.5 km thickness (KENT et al., 1978; LOWRIE, 2007). The third layer is the plutonic crust consisting of gabbros and ultramafic rocks and a thickness of 5 km (KENT et al., 1978; LOWRIE, 2007). Layer 2, especially 2A, exhibits the highest magnetic values (LOWRIE, 2007) and so the magnetic susceptibility values used in IGMAS+ are relatively high. The aim of the modeling process is to get an idea of the dimensions of the hydrothermally altered zone (**Figure 17**) and therefore the absolute magnetic susceptibility values used in the model are not in the focus of the study.

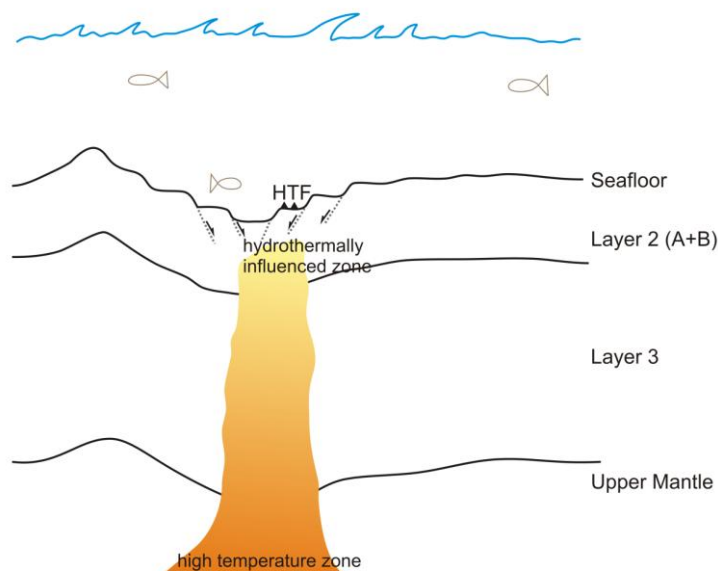


Figure 17: Cross section of the oceanic lithosphere with layer division and location of a possible hydrothermally influenced zone. HTF stands for hydrothermal field.

It is only necessary to keep the contrast of the higher magnetized layer 2 and the all other model bodies high. The geometry of the hydrothermally altered rock body must be modified till the measured and the calculated magnetic lines fit on top of each other. Crossing lines in the model cannot be processed by IGMAS+ because of the triangulation principle.

4) Results

4.1) A slow spreading ridge system

4.1.1) Structural description

The slow spreading ridge system of the southern Central Indian Ridge (CIR) was mapped during the first INDEX research cruise in 2011 and has a length of 500 km between 21°S and 25°40'S (**Figure 18**). It strikes NNW-SSE and is characterized by a continuous well defined rift valley which strikes ~145° SE. Several discontinuities and one transform fault (Gemino transform fault) offset the ridge in a right-lateral sense (**Figure 18**). The southern Central Indian Ridge was divided into five working areas from north to south: EXFX, JX, Meso (after the research vessels Meteor and Sonne, HALBACH, 1997), Edmond and Kairei which will be described in more detail in the following. Afterwards the structures are analyzed and interpreted in **Chapter 5.3**.

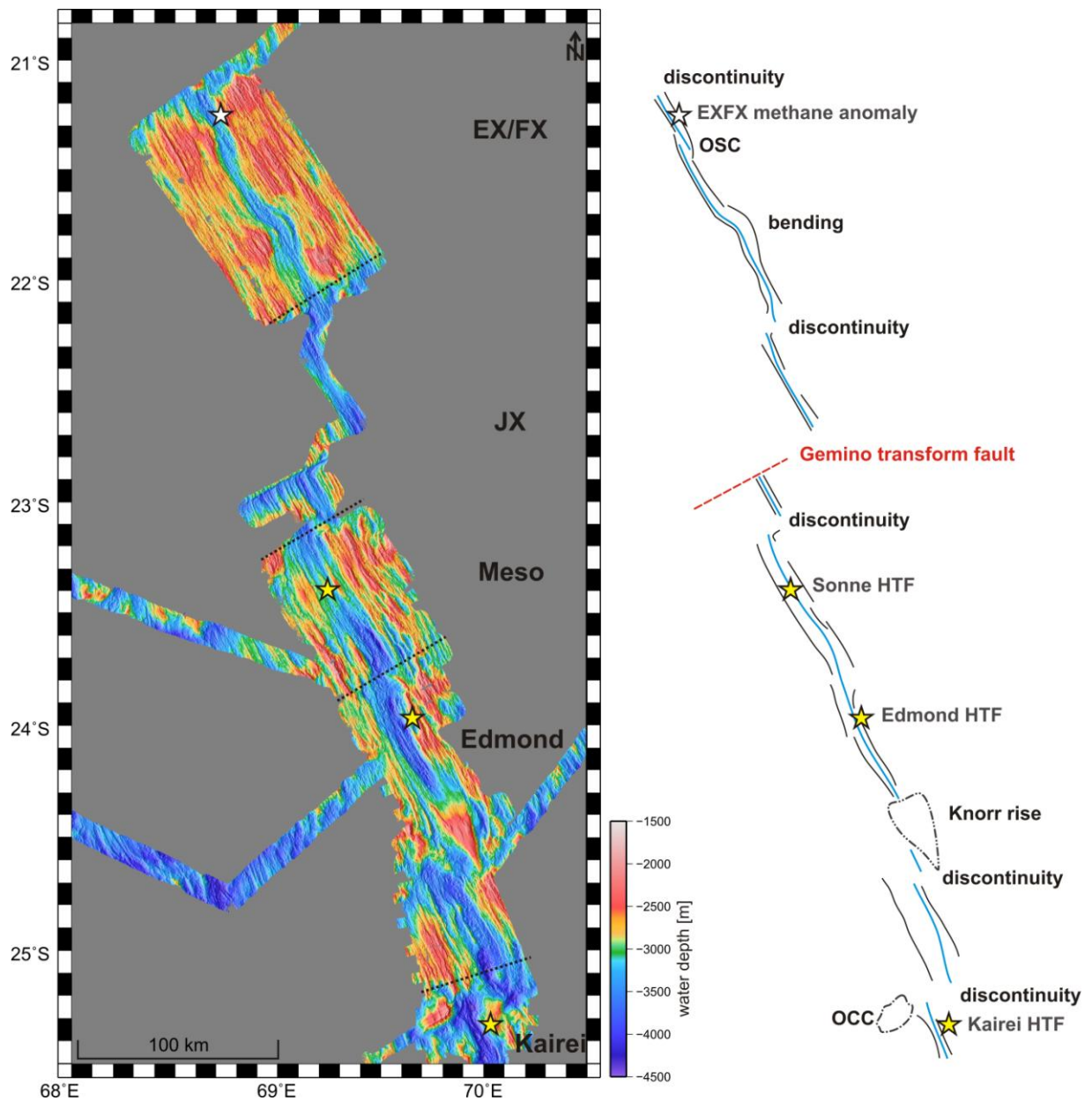


Figure 18: Bathymetric map of the southern Central Indian Ridge. The dotted lines separate the five working areas (left side). Sketch of the main structural features along the CIR (right side). The blue line marks the ridge axis and the black lines are the rift valley boundaries. The known hydrothermal vent sites are marked with yellow stars. The white star labels a methane anomaly at EXFX.

EXFX, the first working area, is located between 21°S and 22°S with a length of ~130 km (**Figure 19**). Two structures of this ridge area stand out: in the northern part an overlapping spreading center (OSC) and more to the south a structure which can be described as bending of the rift valley and the youngest rift shoulders (**Figure 19**). The rift valley strikes ~145° SE, is asymmetric and well expressed along the whole working area by pronounced major faults on the western flank. It can be outlined with the 3250 m contour lines shown in **Figure 20** where the OSC and the bending structure can clearly be seen. It has an average width of ~6-9 km where 9 km occur in the area of the bending. The average depth of the rift valley is ~3450 m with two shallower areas in the middle and south of EXFX. The rift shoulders show an average water depth of 2200 m and the shallowest point is reached in the south of EX/FX on the eastern flank at ~2000 m (**Figure 19**). In general the eastern side shows more large-scale uplift than the western flanks. This behavior can be seen in **Figure 20** with the 2500 m contour lines and in the profiles across the ridge axis from west to east shown in **Chapter 5.3**. Typical for an overlapping spreading center such as in the north of EXFX is an offset of the active spreading center (**Figure 19**). Here the spreading center shows an offset to the western side, but without any change in the strike direction. Both the old and the new rift valley have a width of 2000 m in the area of the overlapping, which is 9.5 km long. North of that area the rift valley gets wider with ~9 km-9.5 km. The average water depth in both areas is ~3400 m. One obvious feature is in the northern part of the old spreading system a complex of three seamounts arranged like a string of pearls along a fault (**Figure 21**, **Figure 22a & b**). The two spreading centers are separated by an elongated bathymetric high in the middle with a difference in height to the valley floor of ~200 m. With a view on the bathymetric map the southern part of EXFX is dominated by a structure that can be described as some kind of bending (**Figure 19**). The rift valley and bordering rift shoulders bend to the east. The whole structure has a length of ~25 km and the rift valley gets wider up to ~9 km. Two strongly curved neovolcanic ridges rise ~500 m to 600 m over the surrounding seafloor (**Figure 21** and **Figure 22a**). In the middle of that bending on the eastern side some kind of caldera is located with a seamount in it (**Figure 23**). Probably the caldera is a relatively old feature and the round shaped seamount the expression of youngest magmatic activity. A small basin structure in the rift valley on the western flank has a rhombus shape, typical for a pull-apart basin. At ~3700 m water depth this basin is significantly deeper than the surrounding valley floor (**Figure 22c** and **Figure 23**). In the area of the bending, the western rift shoulders show a bathymetric high whereas the rift shoulders on the eastern flank could be defined as a

bathymetric low (**Figure 20**, 2500 m contour line). With a look at the distribution of the seamounts in **Figure 22b** it is obvious that they are rarely located at the older rift shoulders on the eastern flank. Regardless where they occur, the majority shows no signs of shear, instead they are evolved in the neighborhood of such shear planes (**Figure 22a**). Inside of the rift valley several seamounts occur, most of them in the northern part. Two sheared volcanic fabrics influenced by faults are located on the western ridge shoulder (**Figure 22b**). All in all the seamounts show a round shape with characteristics of initial erosion. On the older rift shoulders on the eastern side one seamount has a large caldera structure (**Figure 22b**, green circle). More or less, the seamounts seem to be oriented along the major faults and vary distinctly in diameter from 400 m to 1000 m whereby the smallest diameters can be found within the rift valley. The maximum height over the seafloor is ~200 m. The major faults dip towards the rift valley (**Figure 22c**, grey=east and yellow=west) and strike approximately 145° SE, in the same direction as the rift valley. A few faults in the north and south which dip to the south (**Figure 22c**, black lines) show different strike angles of $10^\circ/20^\circ$ NE up to 90° E. In the vicinity of the bending structure there are some faults which run towards each other. To sum up, characteristic structures for the working area EXFX are the overlapping spreading center, the bending of the rift valley and rift shoulders, stronger uplifted eastern rift shoulders, and one pull apart basin inside the bending structure.

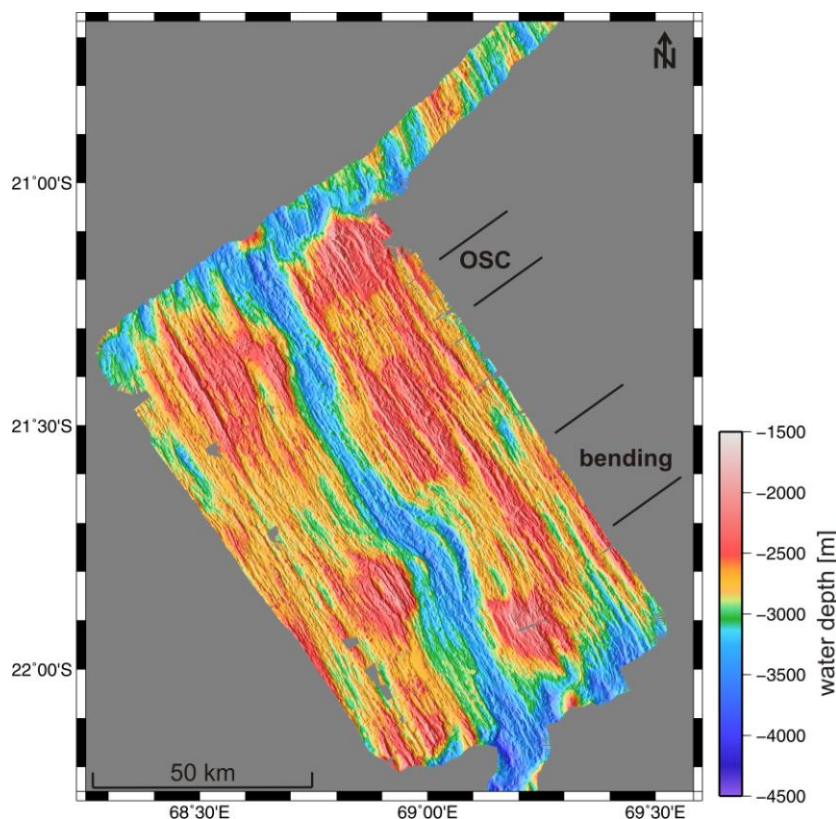


Figure 19: Bathymetric map of the working area EXFX with two prominent structural features, an overlapping spreading center (OSC) in the north and a bending structure in the south.

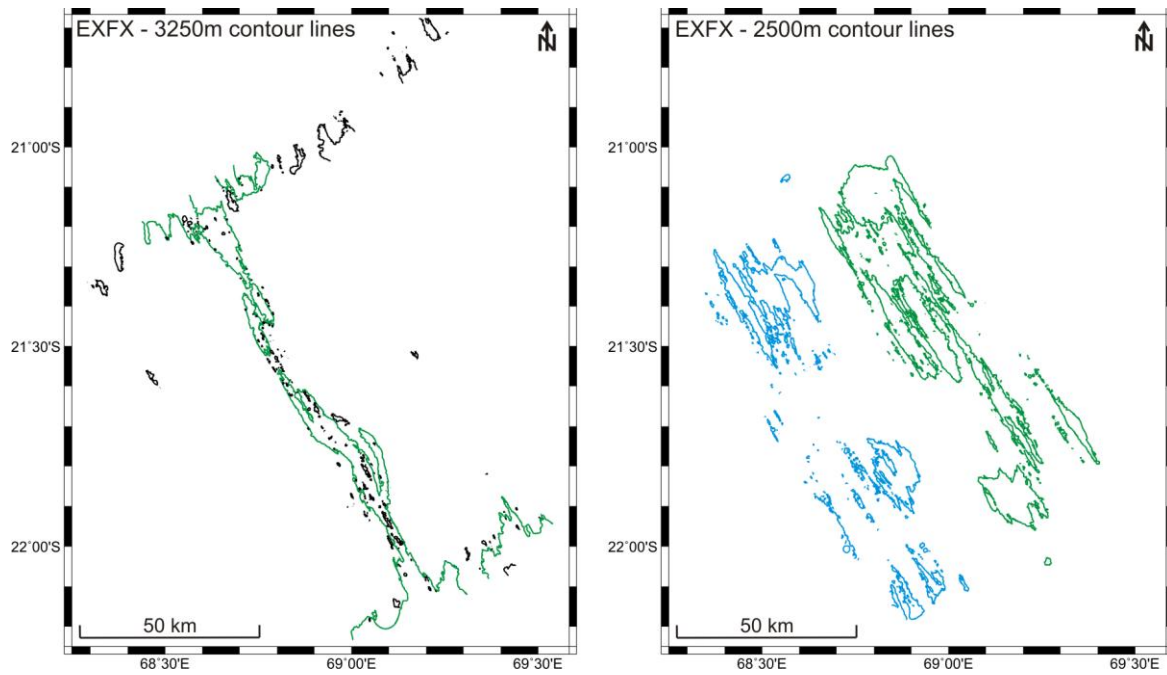


Figure 20: Map of the contour lines from EXFX. On the left side the 3250 m lines which mark the rift valley. On the right side the 2500 m contour lines characterizing the stronger uplifted eastern side (green lines) and the western (blue lines) ridge shoulders.

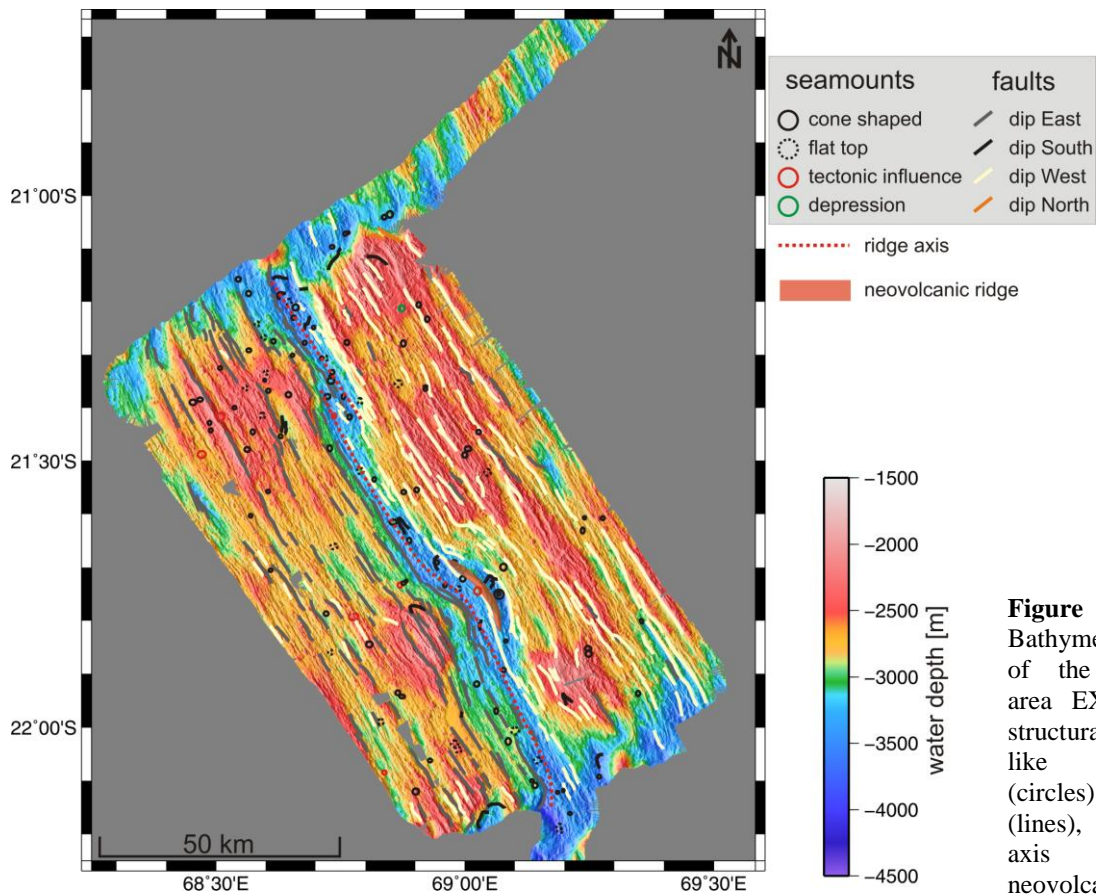
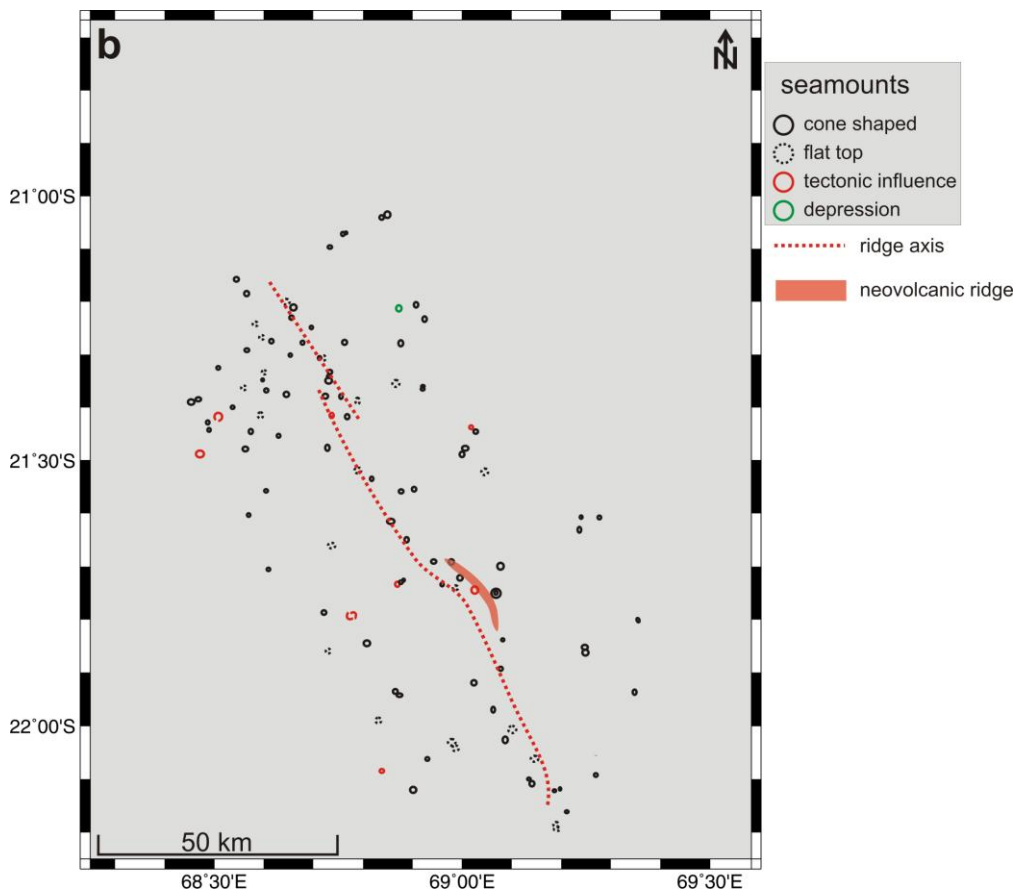
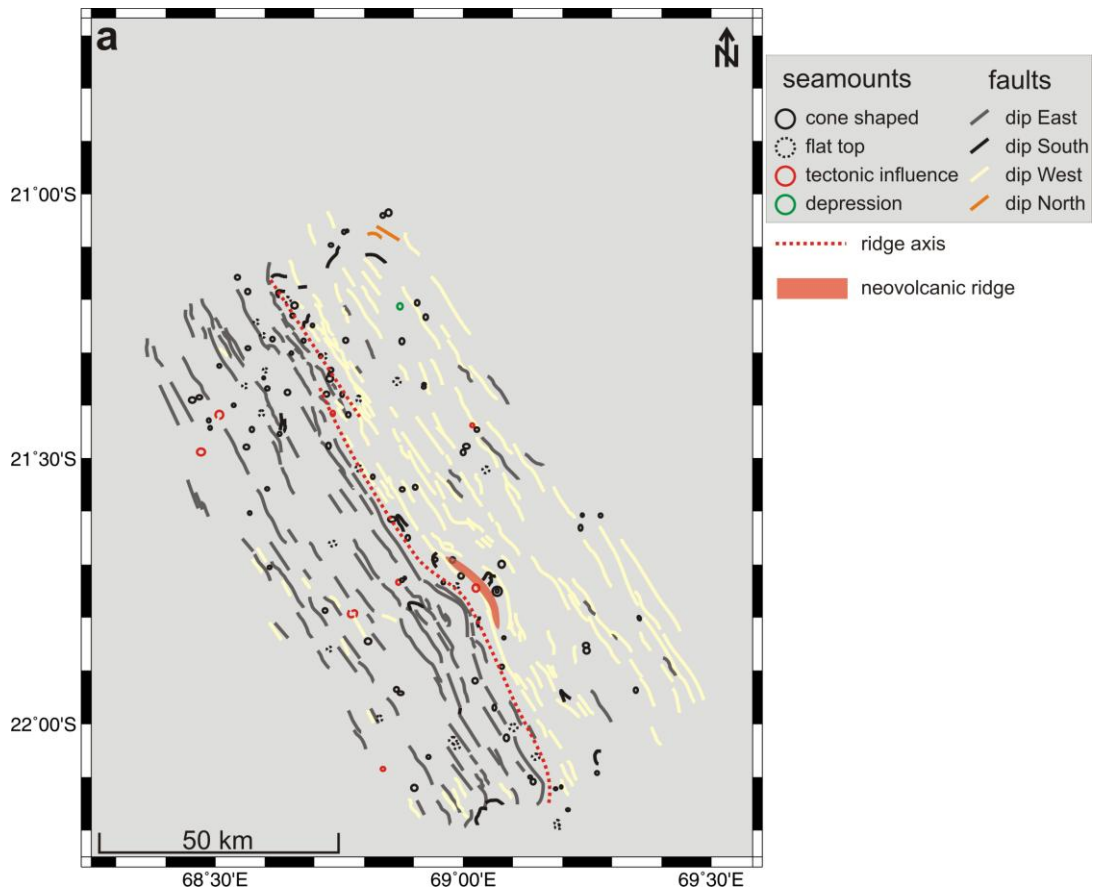


Figure 21: Bathymetric map of the working area EXFX with structural features like seamounts (circles) and faults (lines), the ridge axis and a neovolcanic ridge.



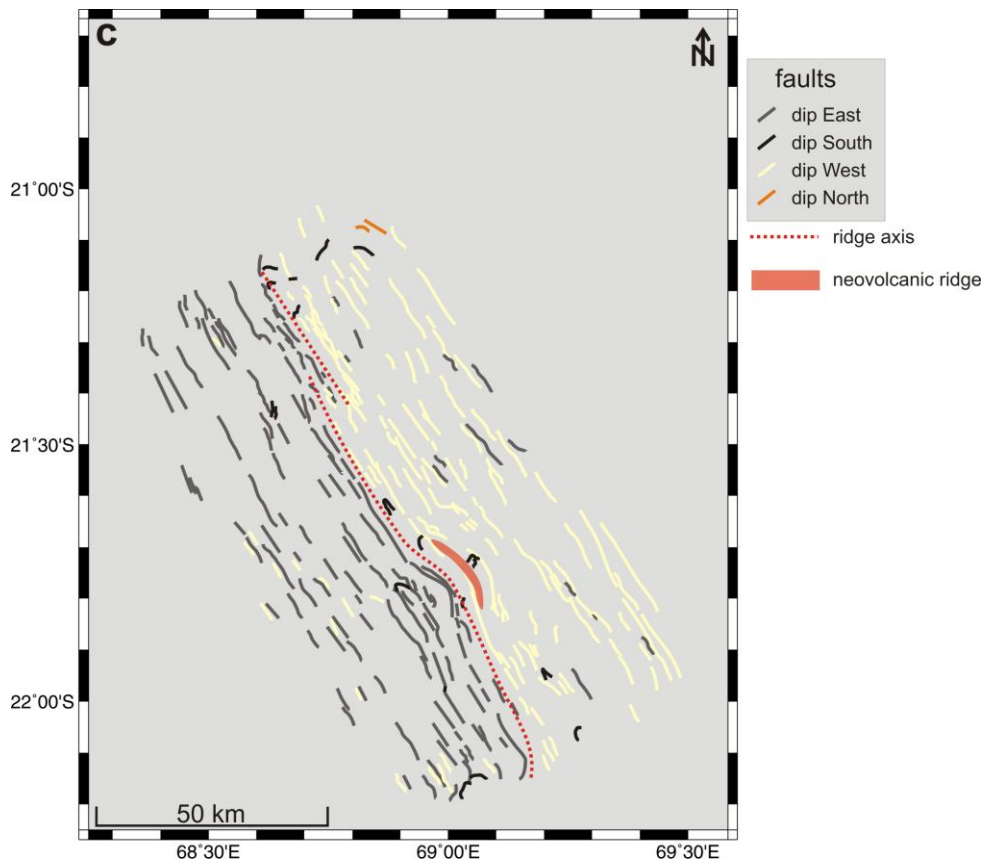


Figure 22: Structural maps of the working area EXFX: **a)** labeled with circles for the seamounts and with lines for the faults; **b)** labeled with circles for the seamounts divided into those who are cone shaped, have a flat top or are tectonically influenced and with green circles for depression structures; **c)** labeled with lines for the faults dipping in different directions.

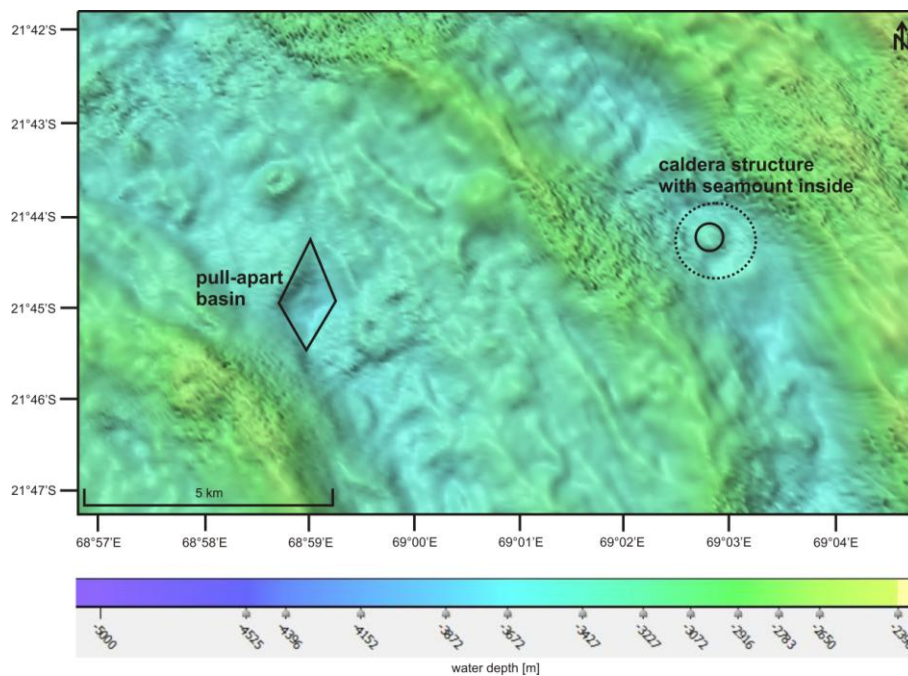


Figure 23: Detailed bathymetric map of the bending structure with outlined special features such as a pull-apart basin and a caldera structure with a seamount inside.

Adjacent to EXFX is the second working area JX from 22°S to 23°04'S (**Figure 24**). The northern part of JX was only mapped by a 65 km long transit profile. Here the rift valley has a width of ~4.5 km and is well expressed by the first normal faults on both valley sides (**Figure 25**). The water depth at the segment ends is around 3900 m and gets shallower at 3300 m in the middle of that transit area. The few major faults strike parallel to the rift valley. At 22°50'S the only real transform fault of the entire INDEX2011 survey area, the Gemino transform fault offsets the CIR (**Figure 25**). It was mapped over 46 km and offsets the rift valley by ~35 km in a left-lateral sense, however, the plate boundaries are offset in a right-lateral sense (**Figure 26**). The Gemino transform fault strikes ~60° north-east and has a v-shaped valley. One seamount is located directly in the eastern part of the transform fault (**Figure 27a & b**). It has a diameter of ~1500 m and a height of ~400 m above the seafloor. It seems that the seamount has the original rounded shape. To the north the transform fault shows a very sharp boundary. In a cross section of the transform fault from north to south there is a relief difference of up to 800 m. South of the Gemino transform fault very prominent major faults and older ridges strike parallel to the rift valley (**Figure 27c**). In the area of the transform fault these faults and ridges were bended to the north-east, which is the movement direction along the transform fault (**Figure 25** and **Figure 27c**). The rift valley has a width of ~8 km and shows a neovolcanic ridge in the middle at ~3200 m water depth. To the south some seamounts occur in the vicinity of the rift valley and mainly on the western ridge flank (**Figure 27a & b**). The average water depth of the rift valley is ~3800 m. The rift shoulders on the western side experienced a stronger uplift at ~2100 m water depth than the rift shoulders on the eastern side as far as they were mapped. The ridge parallel faults (**Figure 27c**, yellow and grey lines) which dip towards the ridge axis also strike ~145°SE. At the Gemino transform fault there are some faults dipping to the north (orange lines **Figure 27c**) and strike ~50°NE. Prominent features for the working area JX are the Gemino transform fault and in the southern part strongly pronounced ridge parallel normal faults.

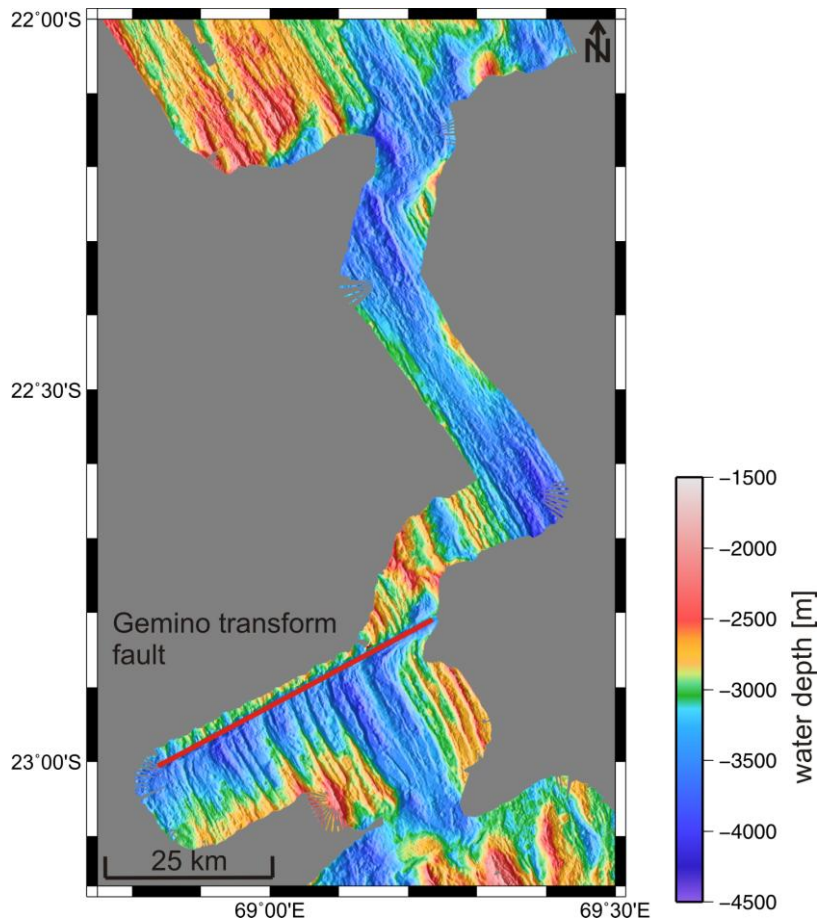


Figure 24: Bathymetric map of the working area JX.

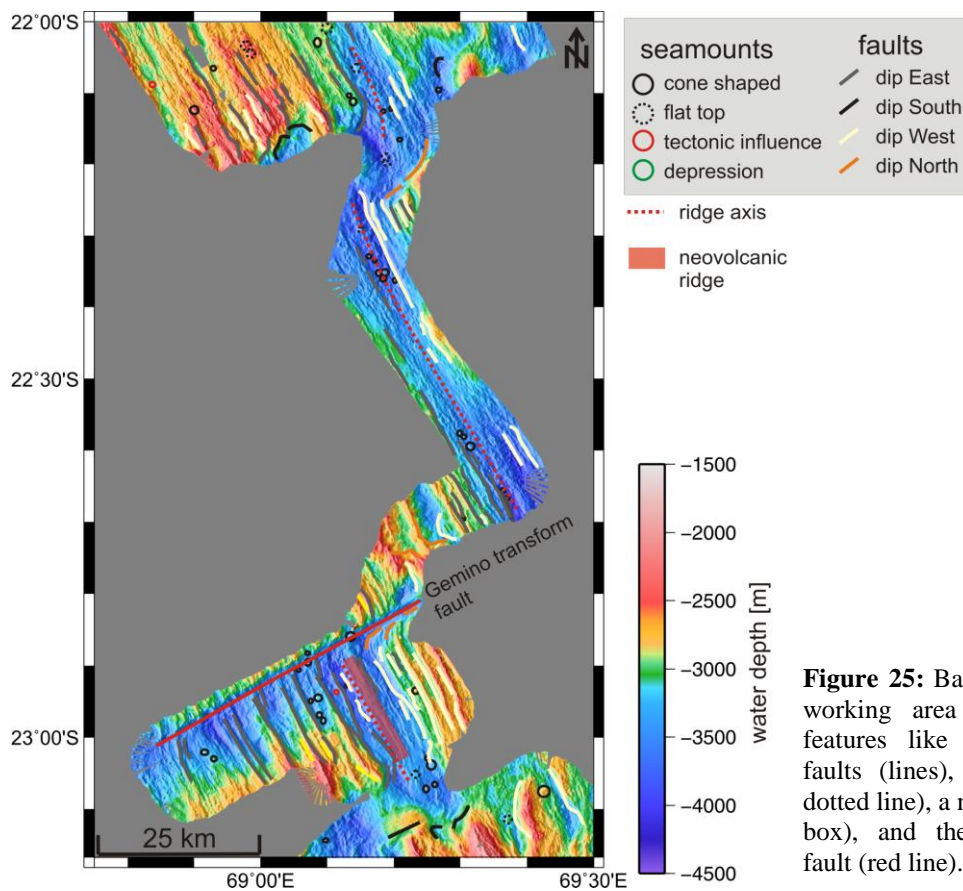


Figure 25: Bathymetric map of the working area JX with structural features like seamounts (circles), faults (lines), the ridge axis (red dotted line), a neovolcanic ridge (red box), and the Gemino transform fault (red line).

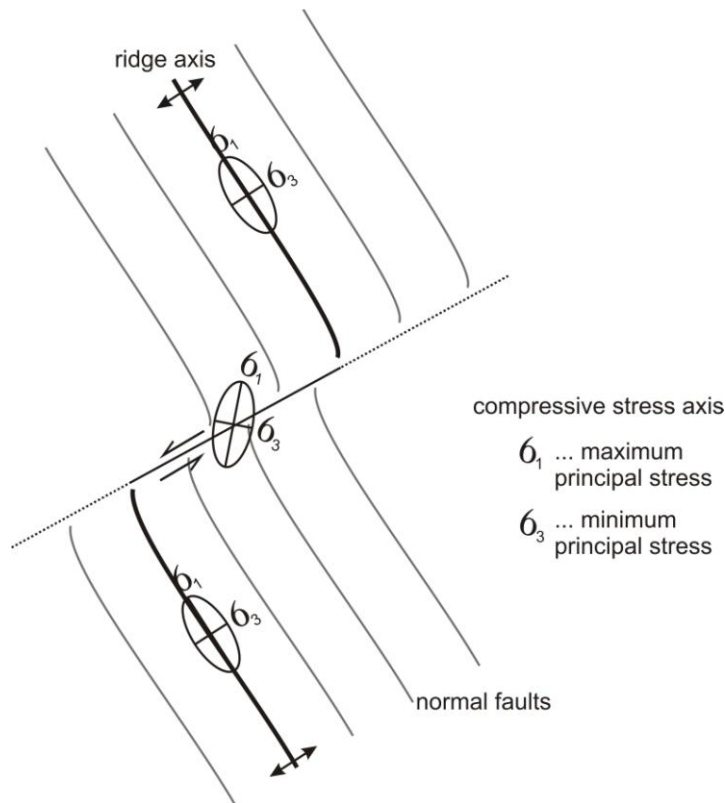
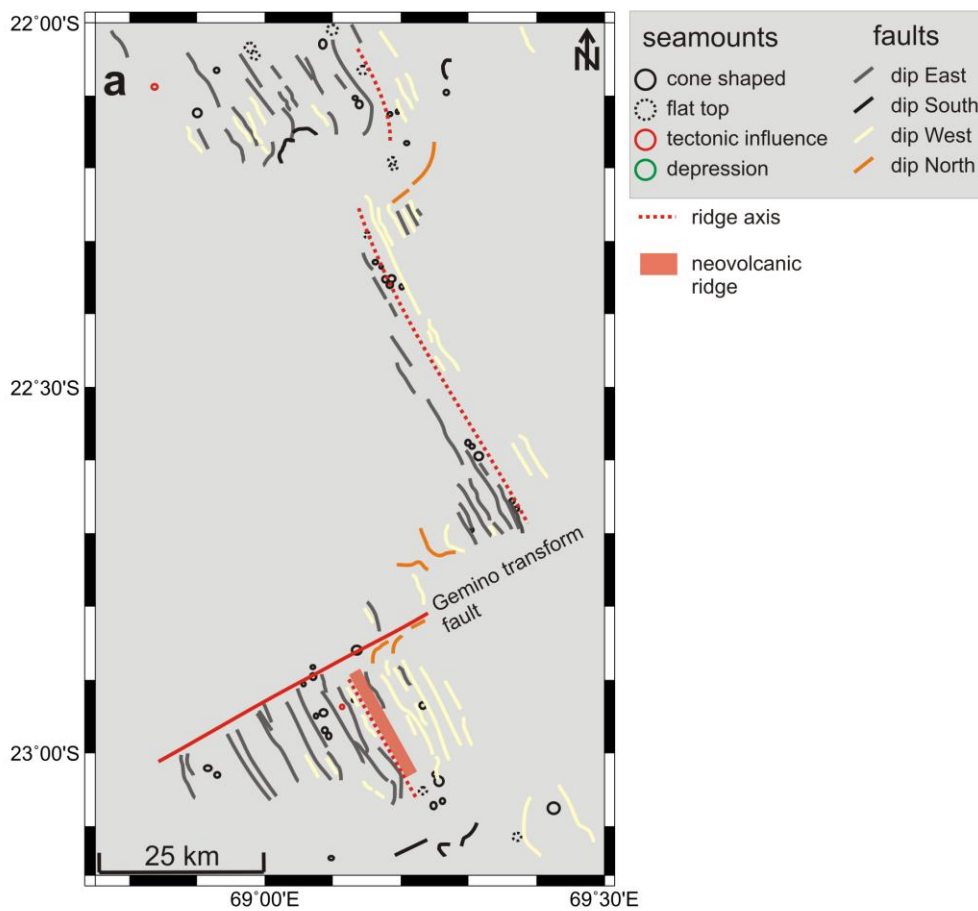


Figure 26: Schematic sketch of the Gemino TF marked with stress ellipse. At the transform fault the ridge axis is offset left-laterally and the plate boundaries show right-lateral sense of movement (after SEARLE, 2013, modified).



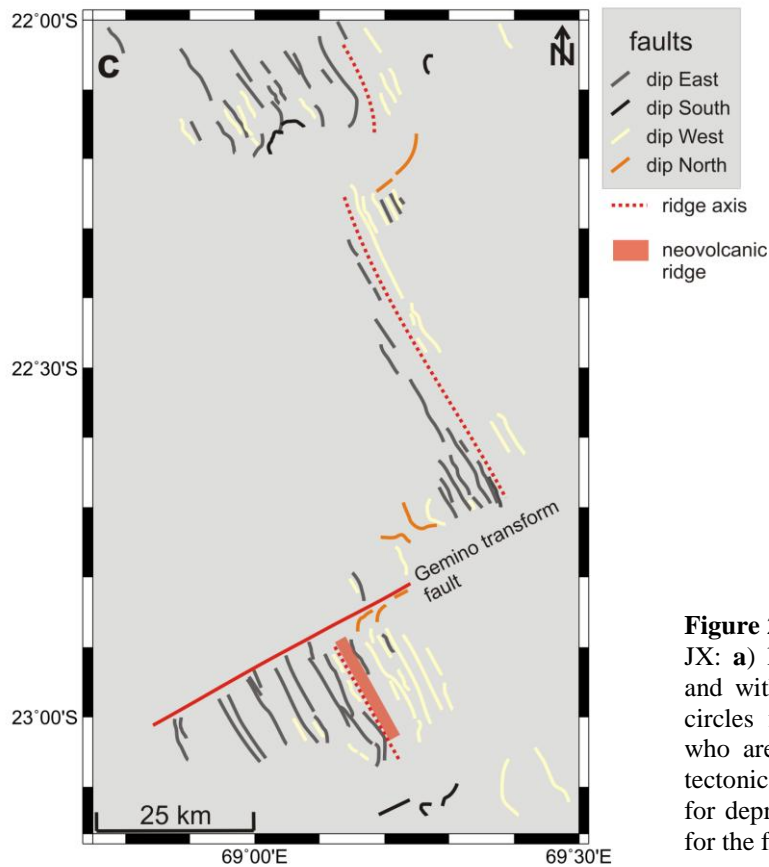
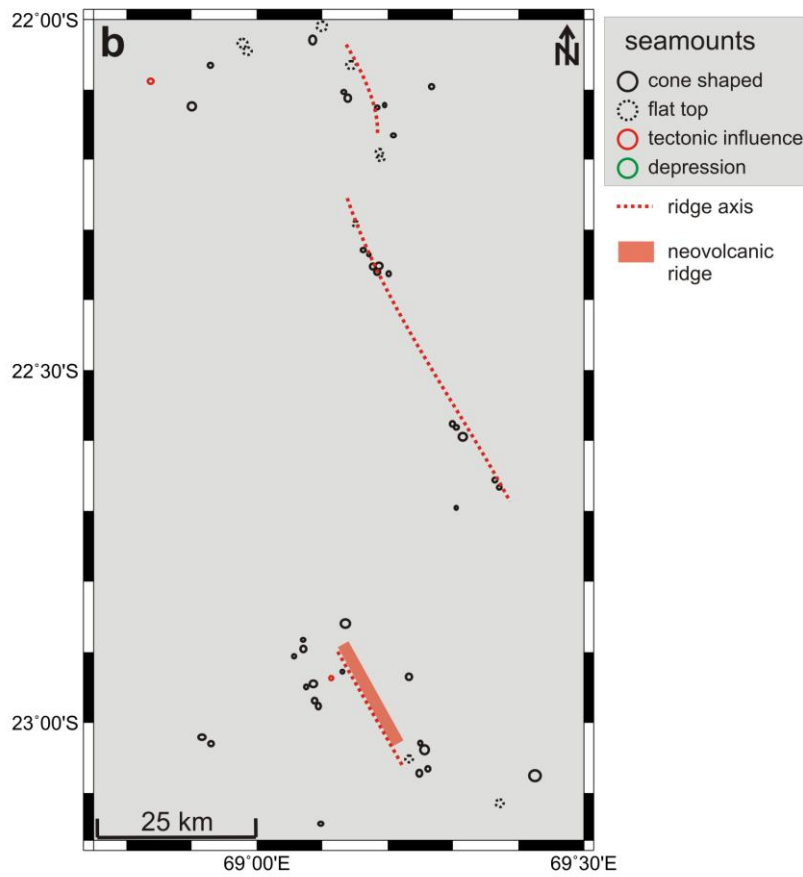


Figure 27: Structural maps of the working area JX: **a)** labeled with circles for the seamounts and with lines for the faults; **b)** labeled with circles for the seamounts divided into those who are cone shaped, have a flat top or are tectonically influenced and with green circles for depression structures; **c)** labeled with lines for the faults dipping in different directions.

Between 23°05'S and 23°33'S the third working area named Meso extends over 8.4 km (**Figure 28**). The rift valley is well expressed and asymmetric with steeper eastern ridge flanks. It is wider at ~9 km at the section ends and narrower in the middle part at ~1600 m where neovolcanic ridges develop (**Figure 29**). In the northern part the average water depth of the rift valley lies around 3700 m and gets deeper to the south at ~4100 m. All in all the ends of the Meso region are deeper than the middle part where the neovolcanic ridges occur. This hourglass morphology (narrow middle part, wider and deeper ends) can be found on several sections along the slow spreading ridge (**Figure 18**). The seamount distribution is concentrated in the rift valley and on the western rift shoulders (**Figure 30a & b**). Most of them show no signs of shear and they concentrate in the north and south of the working area. Together with the large neovolcanic ridges in the middle of the Meso area (location of the Sonne hydrothermal vent site) the seamounts hint at an active heat source beneath. The neovolcanic ridge including the Sonne hydrothermal vent site (**Figure 28**, star) represents an along axis updoming in an elongated shape with some normal faults (**Figure 29** and **Figure 30a & c**). In north-south direction it has a length of 28 km, is situated in ~2700 m water depth and rises ~400 m above the seafloor. The other updoming structure east of the rift valley is clearly thicker and more homogeneous in its structure (**Figure 29**) with a smaller number of significant faults on the top. It has a length of ~21 km, rises 500 m to 600 m above the seafloor and lies in a water depth of ~2500 m. In general, the uplift of the rift shoulders is more pronounced in the east. Away from the rift valley there are areas with basin structures. The main faults run parallel to the rift valley and dip to the east or west. Summarizing features for the working area Meso are the two prominent neovolcanic ridges and, like in EXFX,

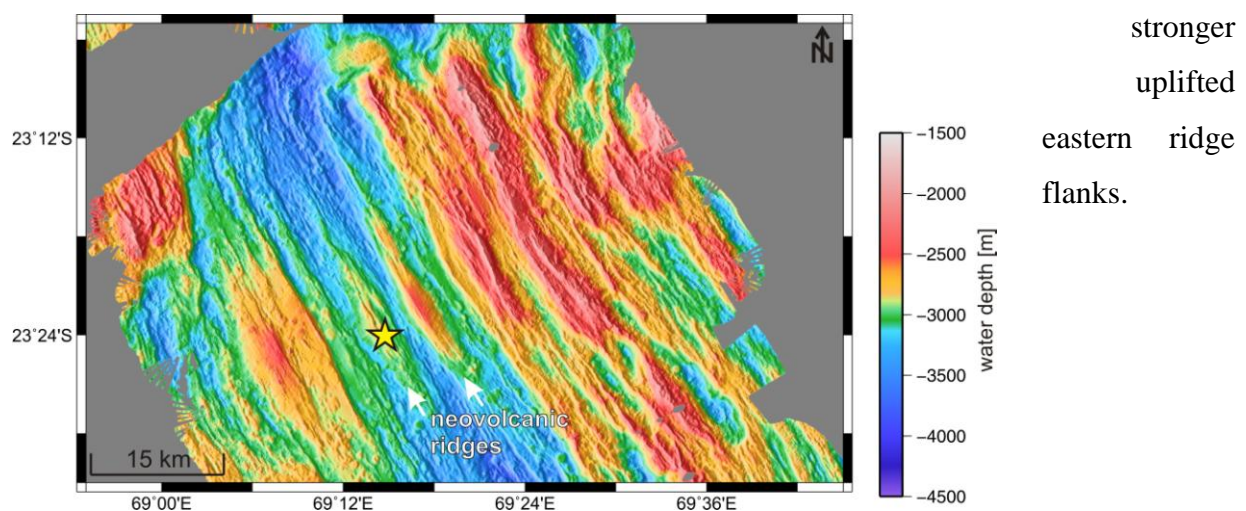


Figure 28: Bathymetric map of the working area Meso with two prominent neovolcanic ridges. The inactive hydrothermal vent field Sonne is marked by the yellow star.

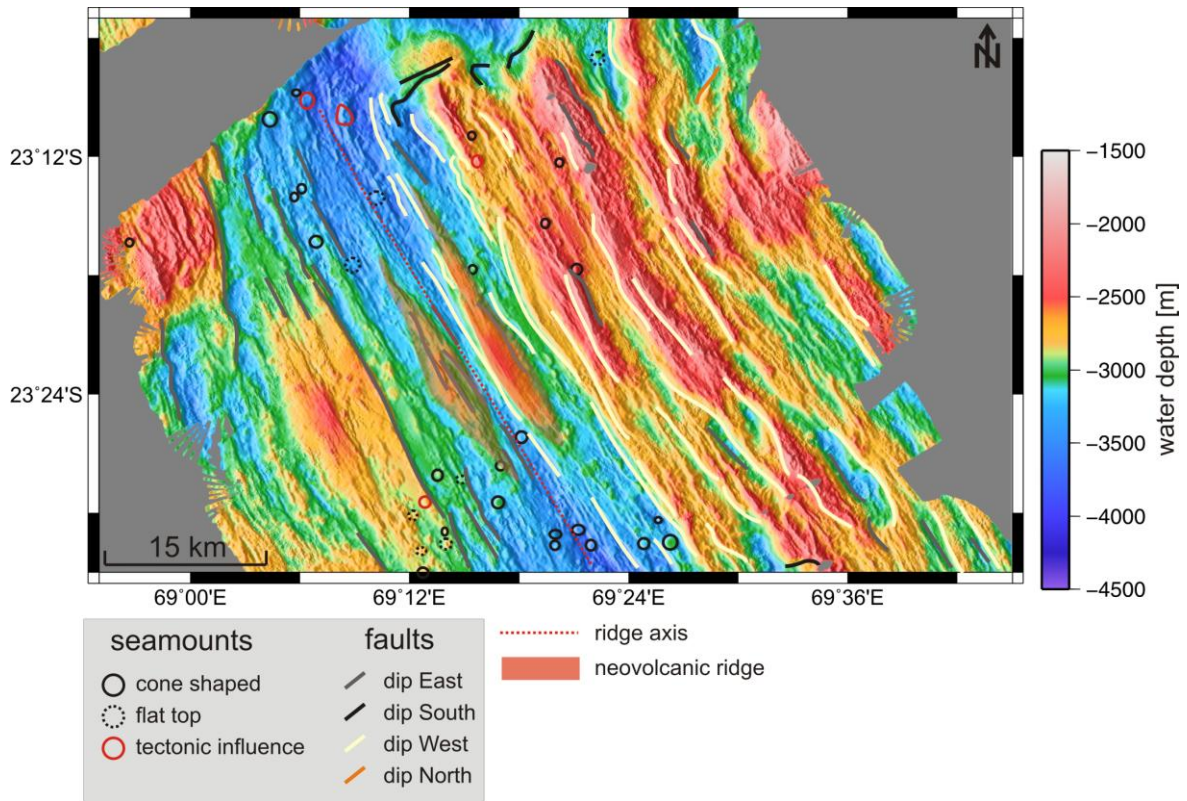
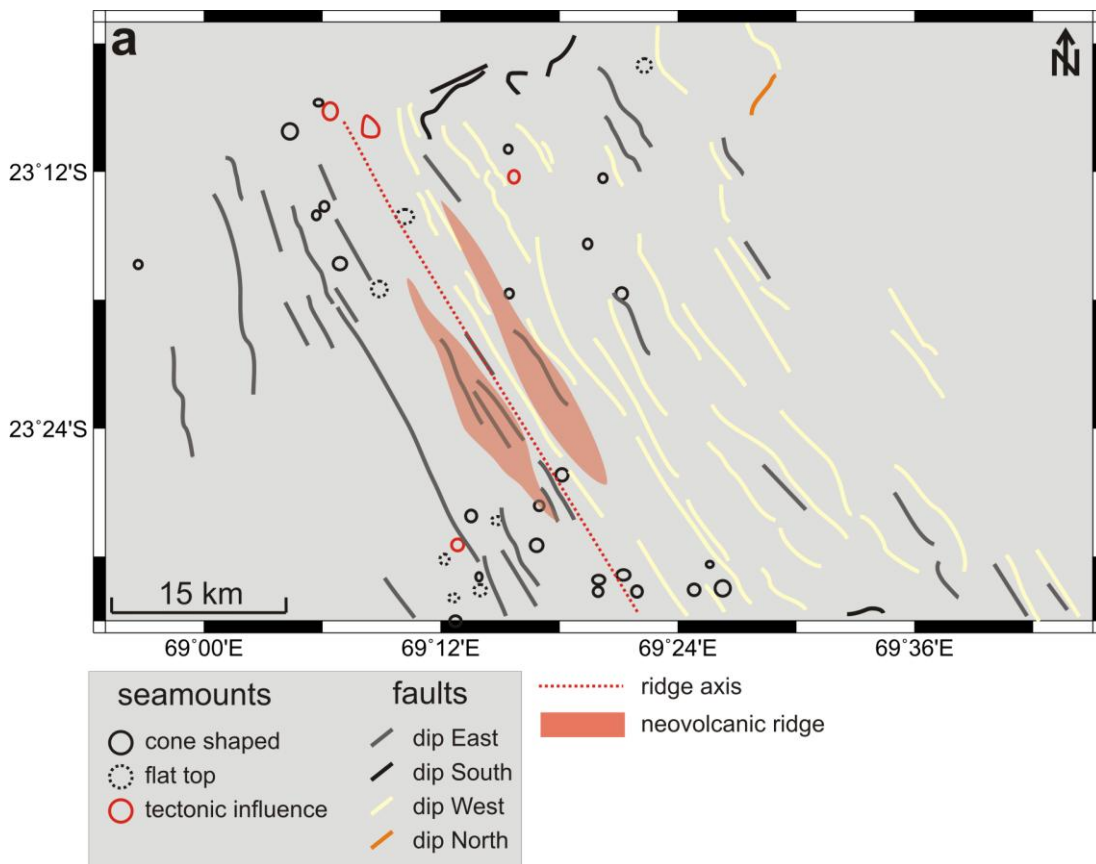


Figure 29: Bathymetric map of the working area Meso with structural features like seamounts (circles), faults (lines), the ridge axis (red dotted line), and two neovolcanic ridges (red areas).



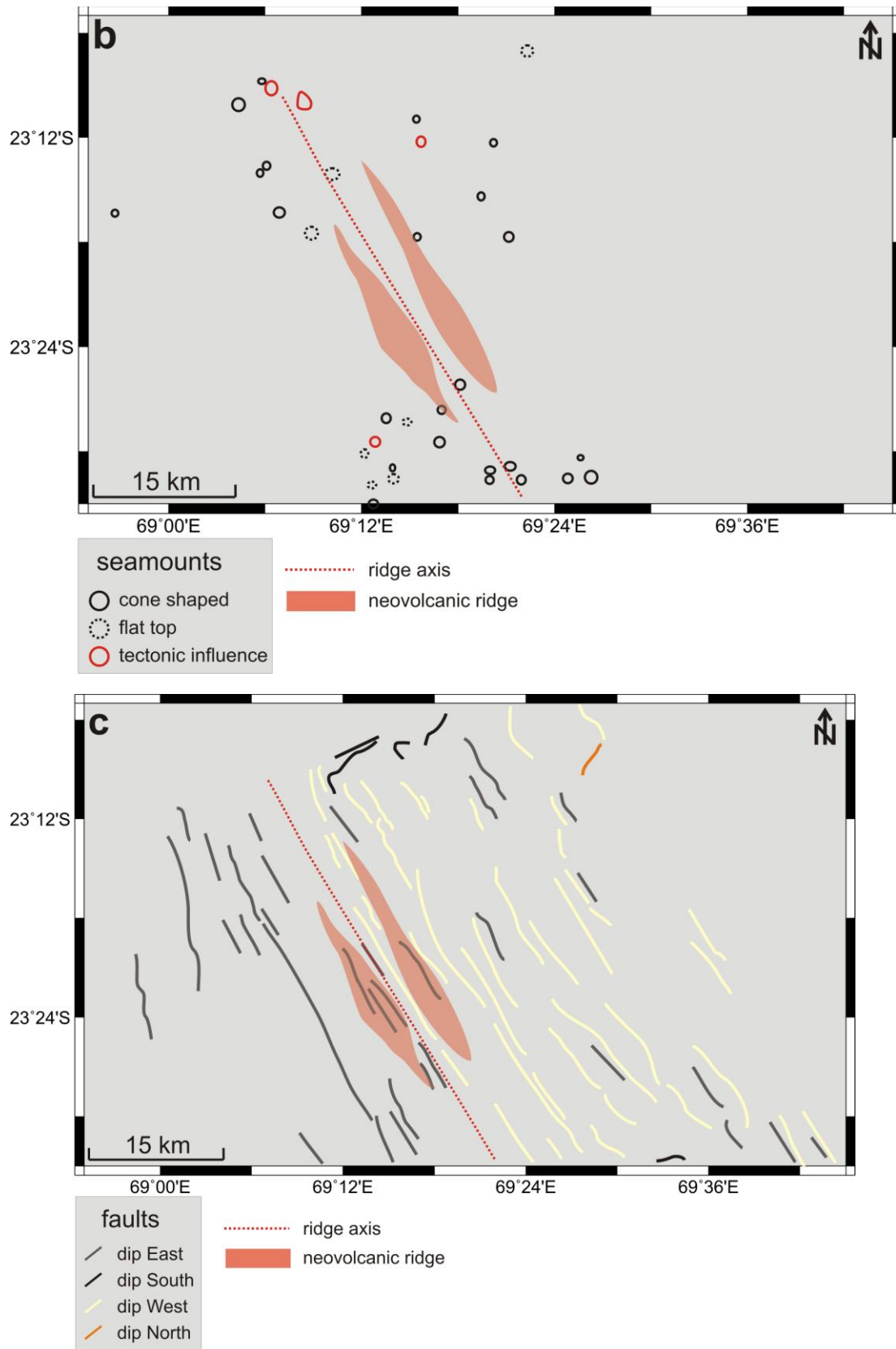


Figure 30: Structural maps of the working area Meso: **a)** labeled with circles for the seamounts and with lines for the faults; **b)** labeled with circles for the seamounts divided into those who are cone shaped, have a flat top or are tectonically influenced; **c)** labeled with lines for the faults dipping in different directions.

The fourth working area Edmond is located between 23°33'S and 25°09'S and has a length of ~170 km (**Figure 31**). Here, the rift valley is well expressed in the north and also in the south where neovolcanic ridges give it an asymmetrical character. It has an average width of 6.5 km -7 km in the northern part and 13 km in the southern area, but here it is difficult to define the boundaries. The average water depth is around 3700 m. A most prominent feature is the Knorr rise in the middle of that working area. It is a very young structure which interrupts the spreading center. The Knorr rise offset the spreading center by about 12 km and changes its course more to the western flank. Very distinct is the triangle-shaped outline of the rise with the peak in the south and shallower parts to the north (**Figure 32**). The whole seamount rises ~1200 m above the seafloor to a water depth of ~2200 m. Its surface structure is flat and smooth with valley features running parallel to the rift valley. In **Figure 33** the 2500 m contour line marks out that the rift shoulders north of the Knorr rise show a higher uplift east of the rift valley with water depths of around 2100 m whereas the western rift shoulders remain at ~2800 m. Here the major faults strike parallel to the rift valley. Despite this, there are also fault structures intersecting with other ones and cross cutting each other directly in the vicinity of the Edmond hydrothermal vent field (**Figure 32** and **Figure 34a**). They are shown and discussed in more detail in **Chapter 4.4**. At the northern boundary of the working area Edmond a structure from a rift shoulder is located which bends towards northwest into the rift valley (**Figure 31**). Beneath that structure a further basin is found with characteristics of a pull-apart basin (**Figure 35**). North of the Knorr rise there exist remarkably few seamounts in the rift valley and again more of them on the western rift shoulders (**Figure 34b**). No seamounts are observed around the hydrothermal vent site. The well defined rift valley south of the Knorr rise shows the highest number of seamounts along the slow spreading ridge (**Figure 34b**). They are all of different size and shape. The smaller seamounts show the typical seamount structure, round and cone shaped. The bigger fabrics have almost all a flat, eroded top. They are located in the rift valley and in addition a few on the western ridge flank (**Figure 34b**). Some of them show influences of faults. Further prominent features are two developing neovolcanic ridges, both ~28 km long and with a water depth at the shallowest part of ~2700 m (**Figure 34a**). The northern part of those ridges is defined by a north-east bending and a greater width at that place (**Figure 34a**). The eastern flank is the steepest at both ridges. Major faults also run parallel to the rift valley as in the areas described before. In addition there are faults which directly taper off (**Figure 34a & c**). In a large area on the western side the rift shoulders show a greater uplift, nevertheless the

shallowest point with ~2000 m water depth is on the eastern side. A look at the bathymetric map makes clear that the area south of the Knorr rise is characterized by an hourglass morphology. At the section ends water depths of 3800m - 4200 m are reached, while the middle part with all the seamounts and neovolcanic ridges is shallower. At the southern section end in a water depth of ~4000 m lies a structure which has the shape of a pull-apart basin, but in the middle there is a cone like a seamount (**Figure 35**). To sum up for the working area Edmond five features are characteristic: first the evolving discontinuity in the northern area, second the two pull-apart basins, third the Knorr rise, fourth the neovolcanic ridge in the southern area, and fifth the highest number of seamounts in the south.

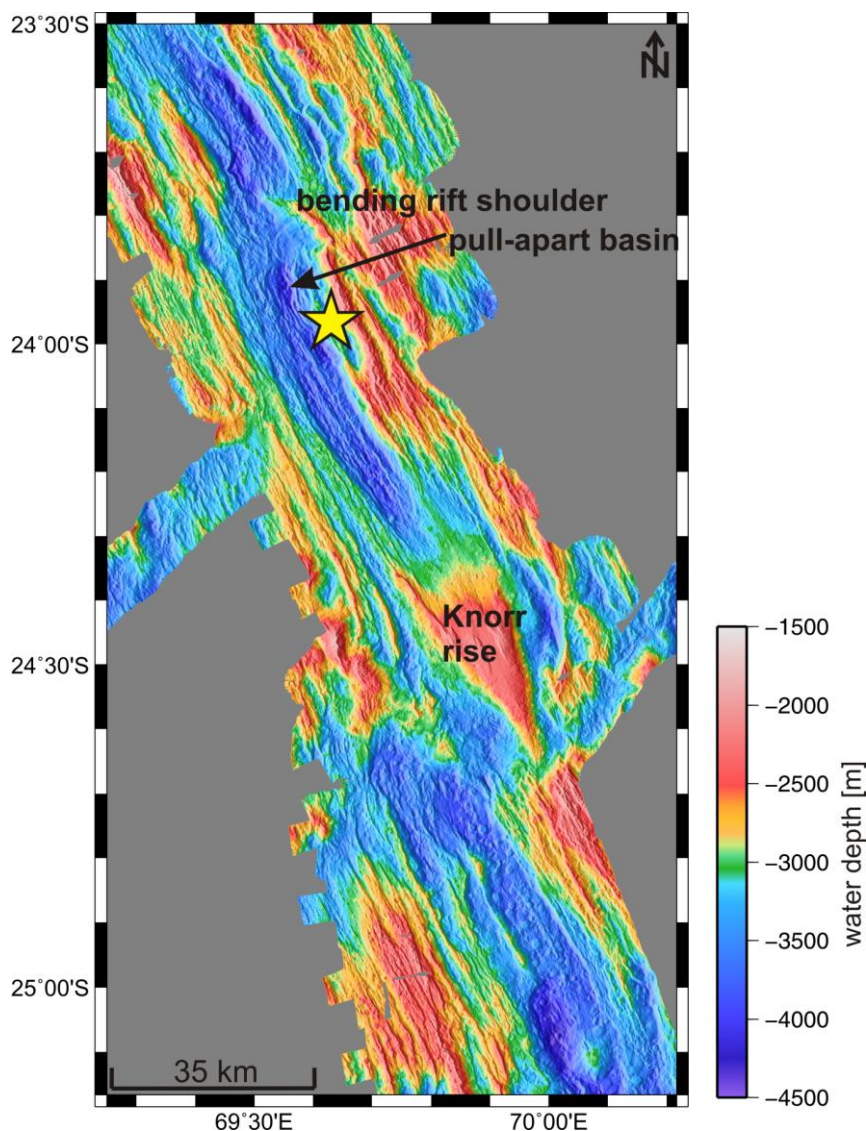


Figure 31: Bathymetric map of the working area Edmond with two pull-apart basins, the Knorr rise, and a prominent bending of the northeastern ridge shoulder in the northern part. The active hydrothermal vent field EDMOND is marked by the yellow star.

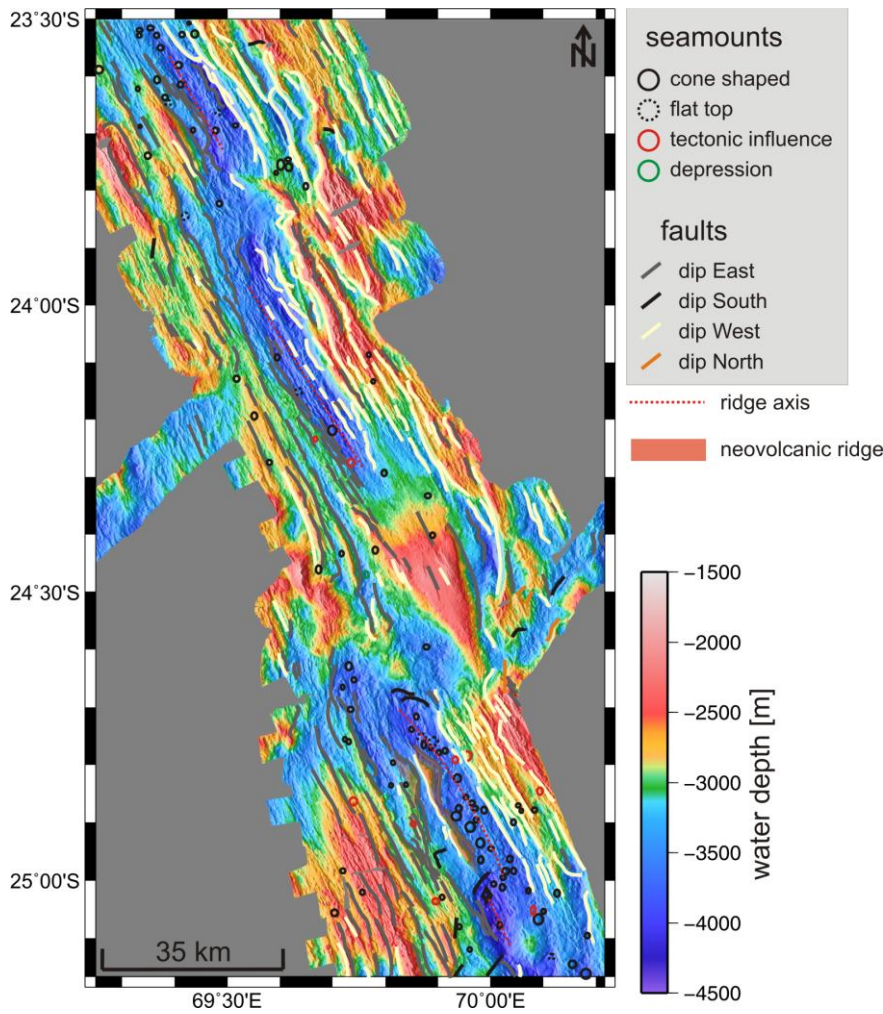


Figure 32: Bathymetric map of the working area Edmond with structural features like seamounts (circles) and faults (lines).

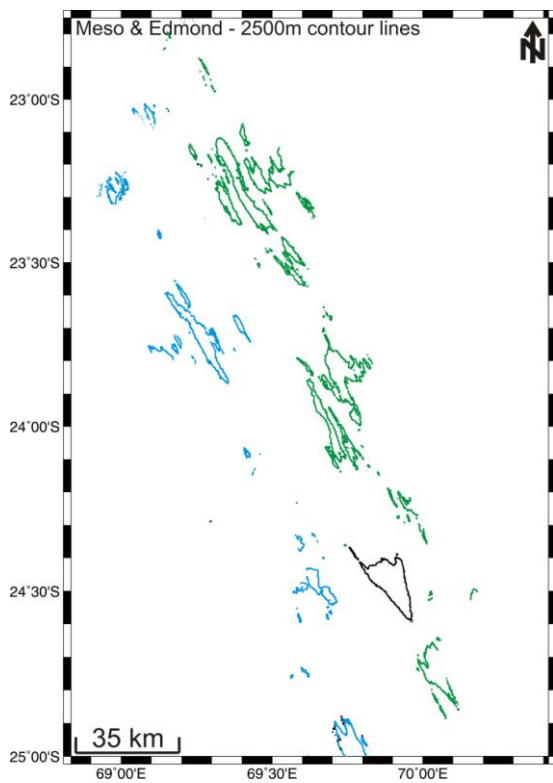
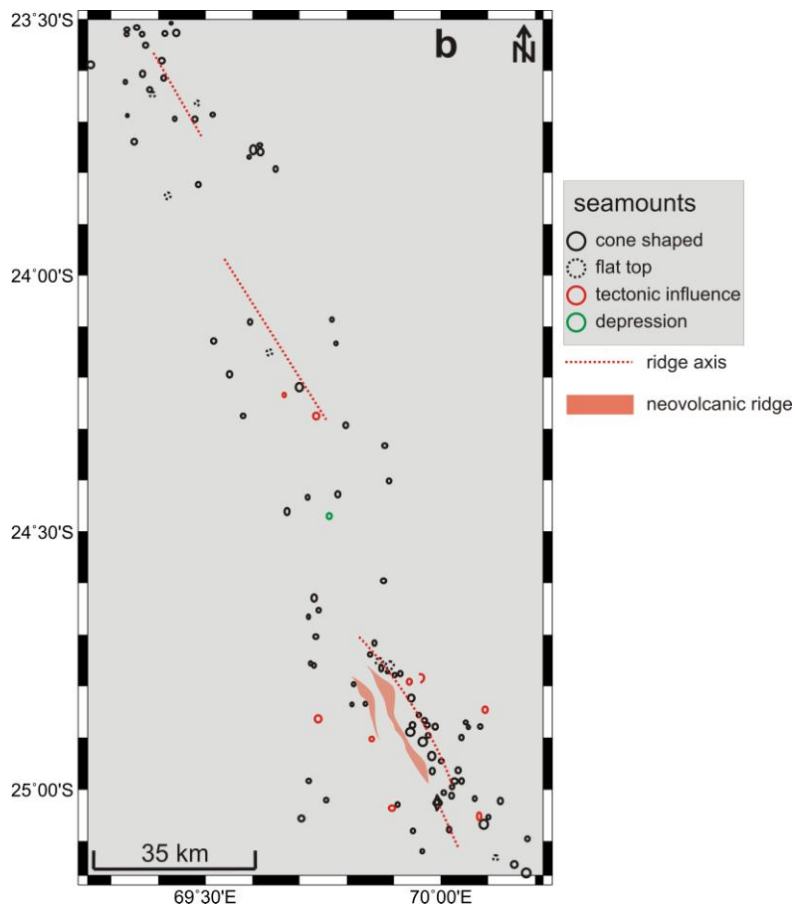
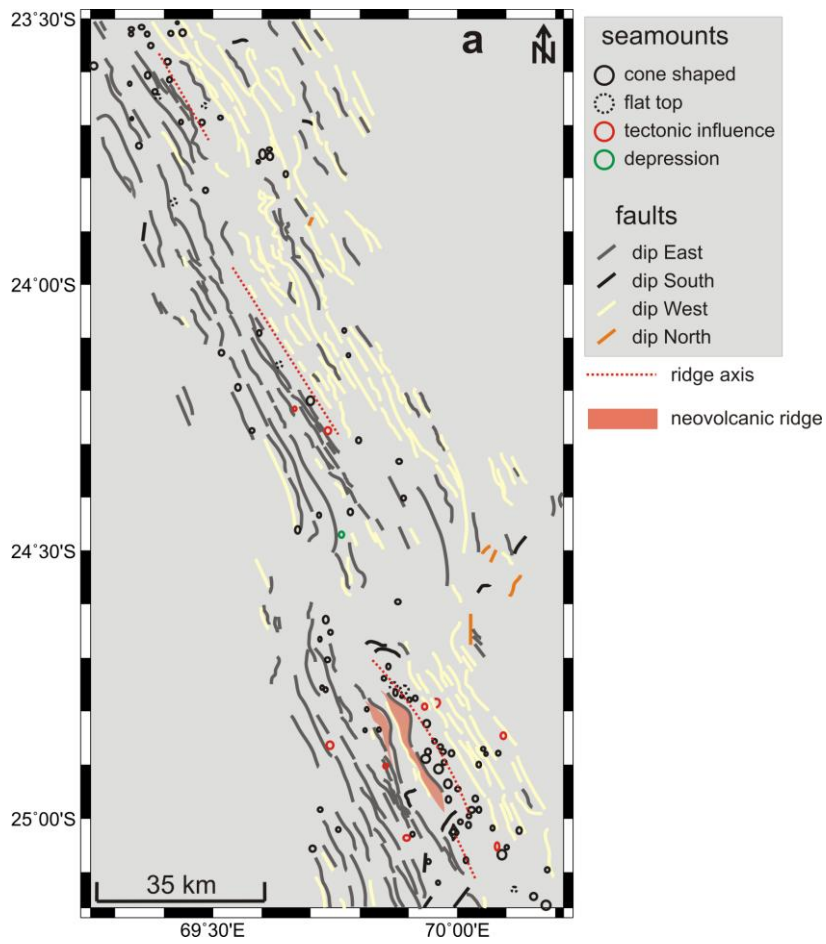


Figure 33: 2500 m contour lines of the areas Meso and Edmond. Blue lines represent the western ridge flank and the green lines the stronger uplifted eastern one. Black lines out marks the Knorr rise.



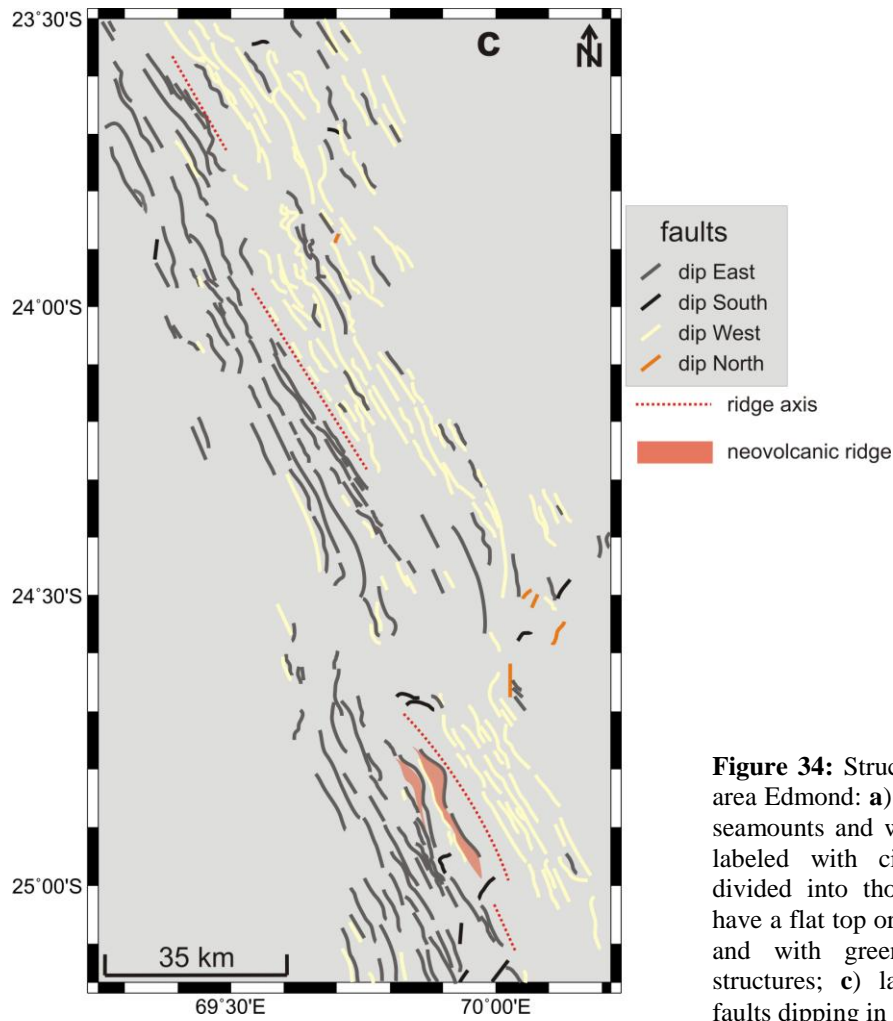


Figure 34: Structural maps of the working area Edmond: **a)** labeled with circles for the seamounts and with lines for the faults; **b)** labeled with circles for the seamounts divided into those who are cone shaped, have a flat top or are tectonically influenced and with green circles for depression structures; **c)** labeled with lines for the faults dipping in different directions.

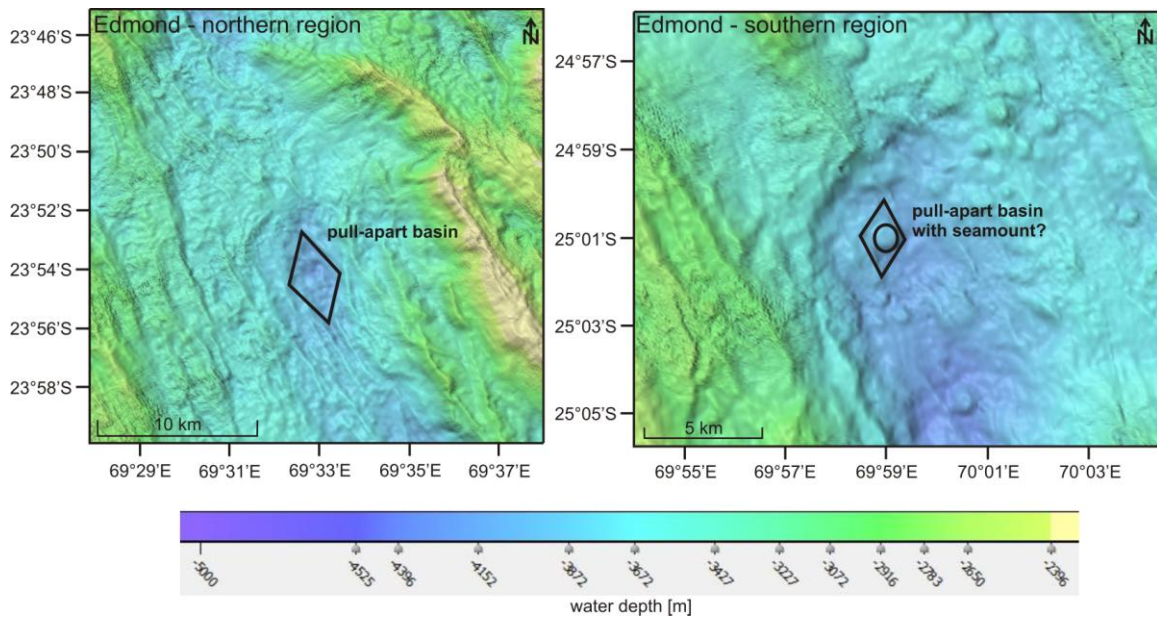


Figure 35: Detailed bathymetric map of two pull-apart basins located in the working area Edmond.

Kairei is the last working area limited by the coordinates 25°09'S to 25°30'S and has a length of 43 km (**Figure 36**). The rift valley is well expressed and more or less symmetric with a width between 5 and 6 km. The average water depth is ~4200 m. In the east the rift shoulders show the highest uplift with ~2200 m water depth (**Figure 36**). The northern part of the Kairei area is characterized by a ~16 km offset of the spreading center in a right-lateral sense. At this discontinuity a large seamount has evolved in the east (**Figure 37**). It has a diameter of ~7.4 km and rises 900 m above the seafloor. In the vicinity of that large seamount a few other small cones are observed (**Figure 38b**). Once again there is a lack of seamounts around the Kairei hydrothermal vent field. The major faults are running parallel to the rift valley but there are also some which are oriented around 40° (**Figure 37** and **Figure 38a & c**). Besides the large seamount there is another outstanding feature in the western part of the discontinuity, an oceanic core complex (OCC) (**Figure 37**). This complex is defined by lineations running perpendicular to the rift valley. North and east of the OCC faults are observed which strike 40°NE. The OCC has a length of 22 km and a width of 13 km. Its top has a relatively smooth surface but faults running across the OCC divide the complex into three sections. In the south several slope scarps and slides are evolved. The southern end of the working area Kairei is limited by the Rodriguez Triple Junction. As a summary the oceanic core complex as well as the stronger uplifted eastern ridge shoulders are typical features for the working area Kairei.

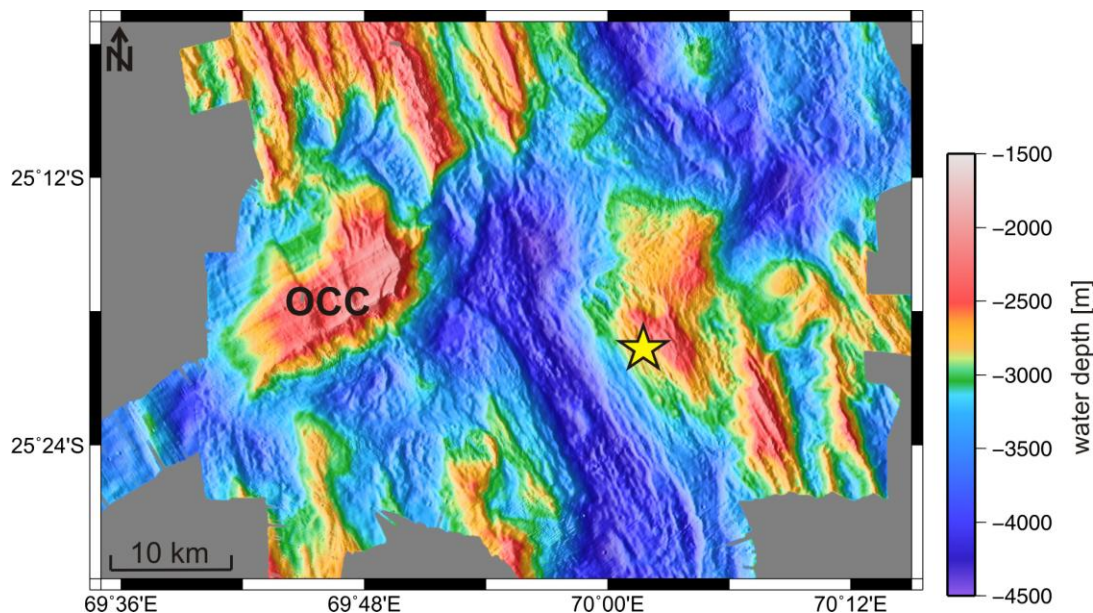


Figure 36: Bathymetric map of the working area Kairei with the prominent oceanic core complex (OCC) and the location (yellow star) of the Kairei hydrothermal vent field.

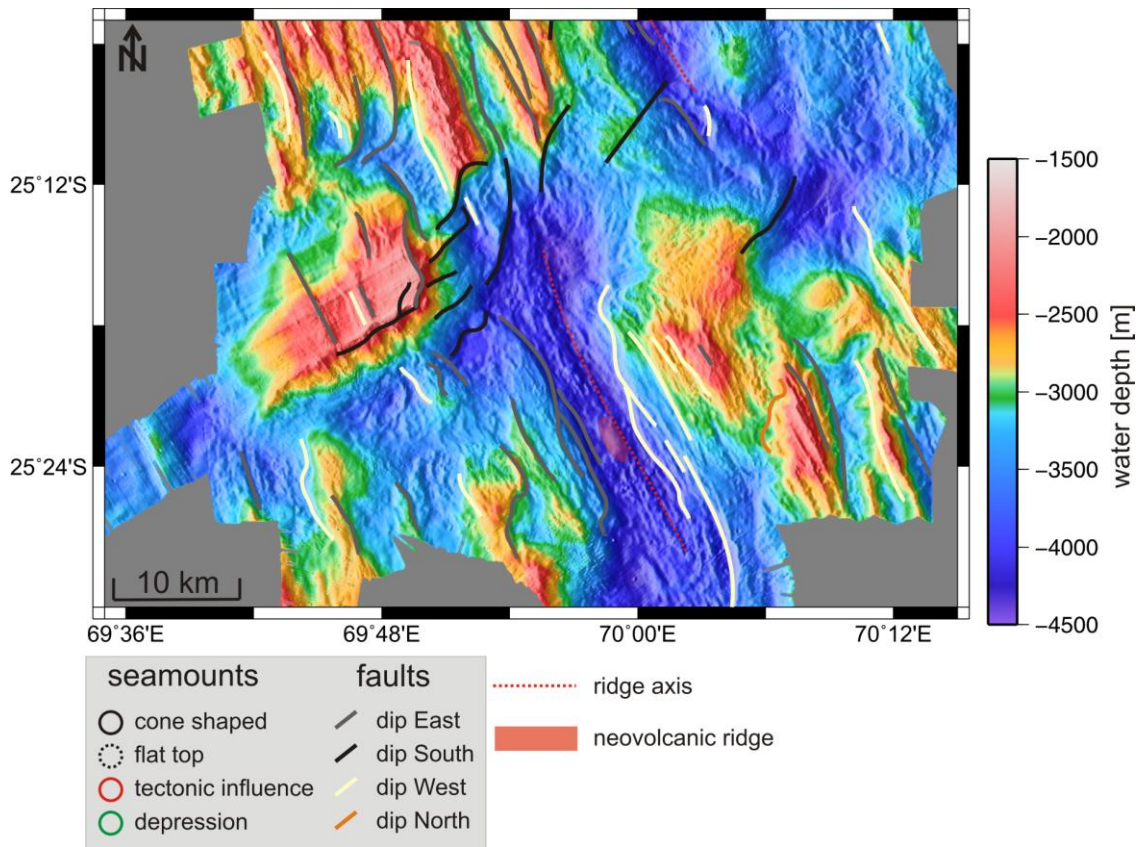
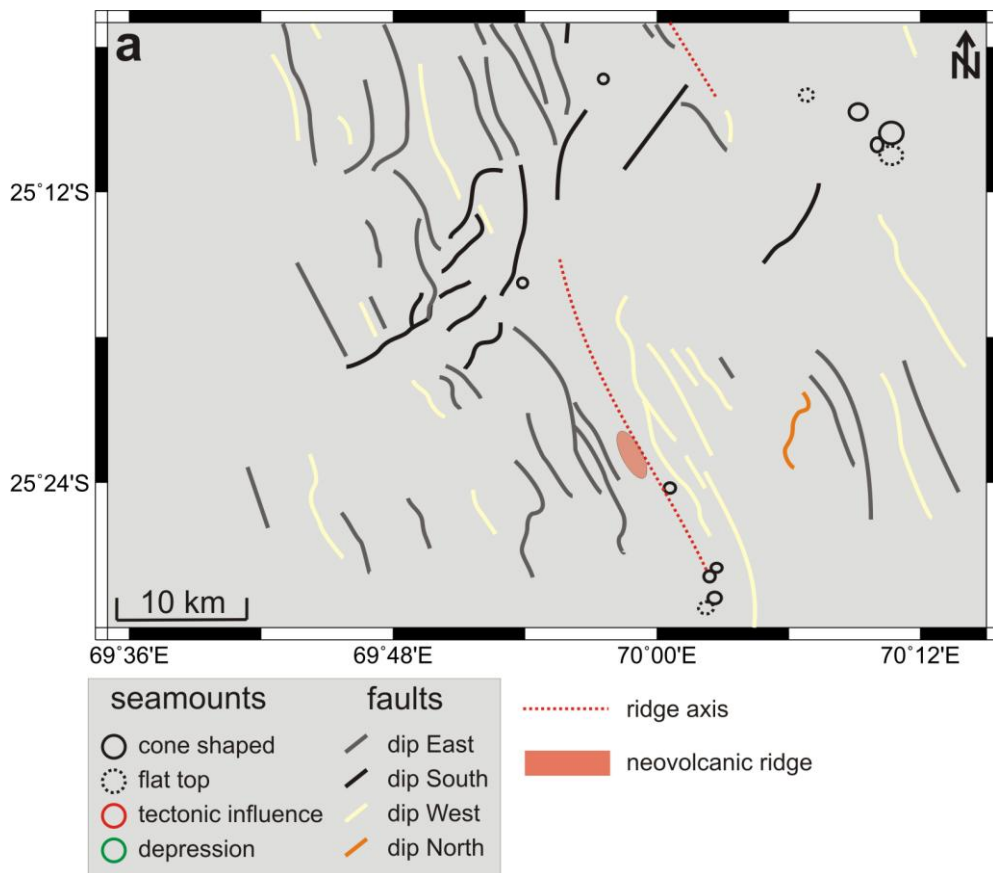


Figure 37: Bathymetric map of the working area Kairei with structural features like seamounts (circles) and faults (lines).



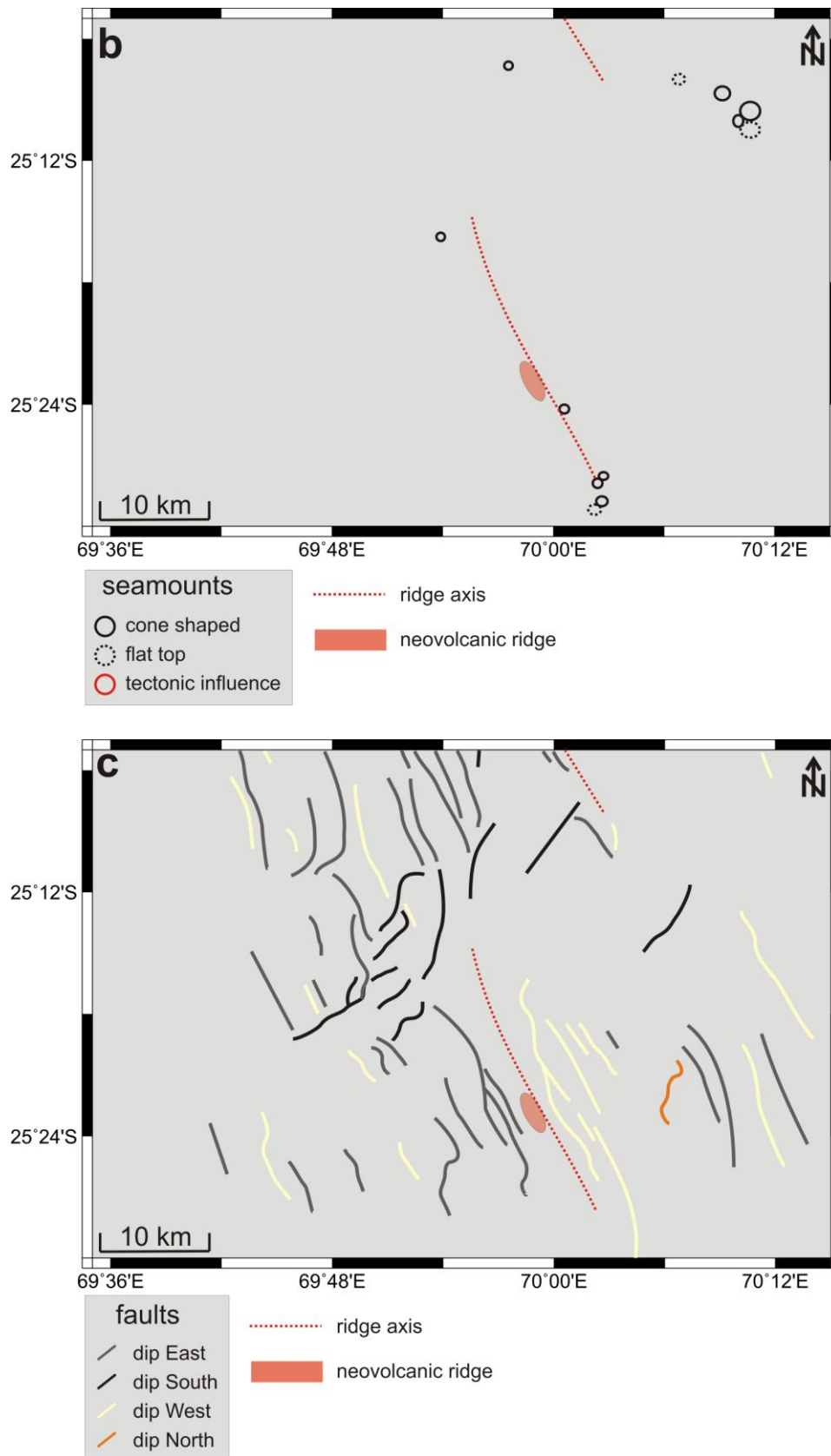


Figure 38: Structural maps of the working area Kairei: **a)** labeled with circles for the seamounts and with lines for the faults; **b)** labeled with circles for the seamounts divided into those who are cone shaped, have a flat top or are tectonically influenced and with green circles for depression structures; **c)** labeled with lines for the faults dipping in different directions.

4.1.2) Magnetic observations

A total of 57 magnetic profiles was measured along the southern part of the CIR which is a slow spreading ridge with 4.7 cm/a full spreading rate on average. For the analysis, some of these profiles have to be left out because they were measured along discontinuities or they are too short. The trend of the profiles from north to south can be seen in **Figure 39**. As described

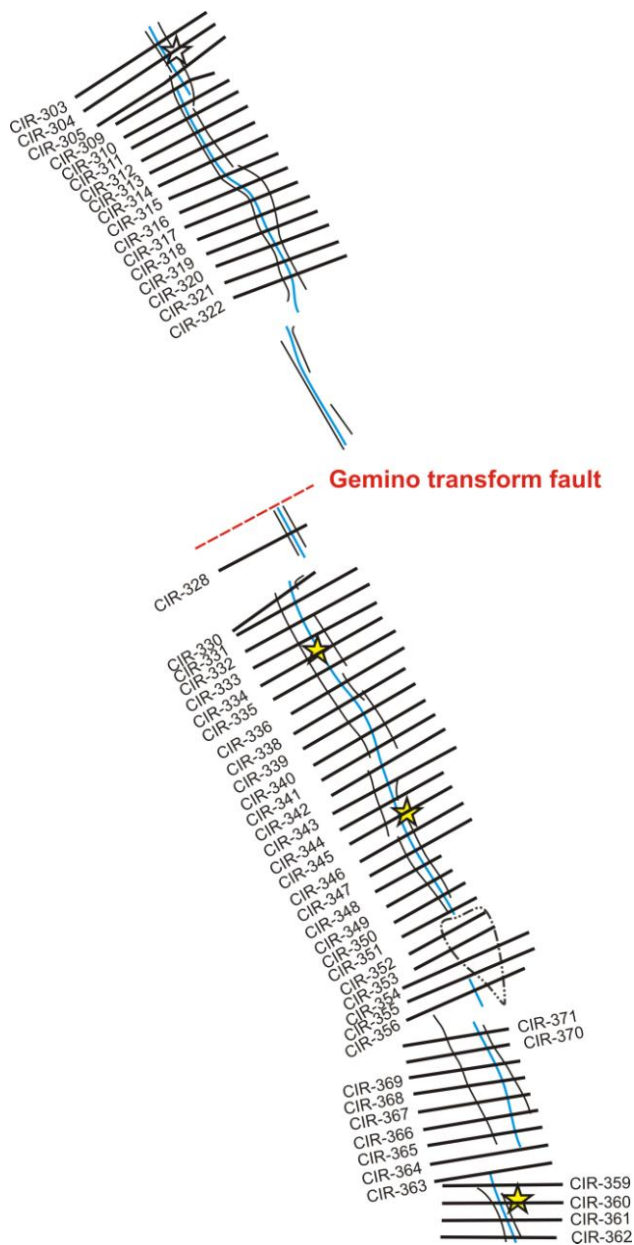


Figure 39: Schematic sketch of the profiles running from north to south at the Central Indian Ridge. The yellow stars mark the active and inactive hydrothermal vent fields. The white star marks the methane anomaly at EXFX.

in **Chapter 3.2.1** the magnetic profiles were acquired at the sea surface which limits the resolution with respect to small source areas at the seafloor.

The first 17 profiles (303-322) in the northern working area are characterized by bathymetric minima which lie to the west of the center of magnetic Anomaly 1 (**Figure 40**). Where the center of magnetic Anomaly 1 is close to the bathymetric minimum, in many cases the magnetic center is located on a bathymetric high which could be a neovolcanic ridge (**Figure 41**). The profiles strike $\sim N60^{\circ}E$ perpendicular to the ridge axis. On all profiles the complete Anomaly 1 (0-0.78 Ma) could be mapped and the average full spreading rate for that area is approximately 4.7 cm/a. Only a few profiles are long enough to cover the Jaramillo event on one side. Half of the profiles range around ± 500 nT with the exception of profile 312 which shows a peak at 700 nT (**Figure 42**). The profiles 303 to 312 in the northern part of EXFX have

symmetric spreading velocities of 2.30 cm/a to the eastern and western side. That behavior changes to the south (**Figure 40**) where the spreading rates are getting asymmetric with 2.30 cm/a to the west and 2.50 cm/a to the east (profiles 313-322). The locations with asymmetric spreading show an increase in the distance between the center of magnetic Anomaly 1 and the bathymetric minima. According to hydrothermal plume signals described by PLÜGER (1988) the profiles 304 and 305 should include a hydrothermal vent site corresponding to the overlapping spreading center structure in EXFX.

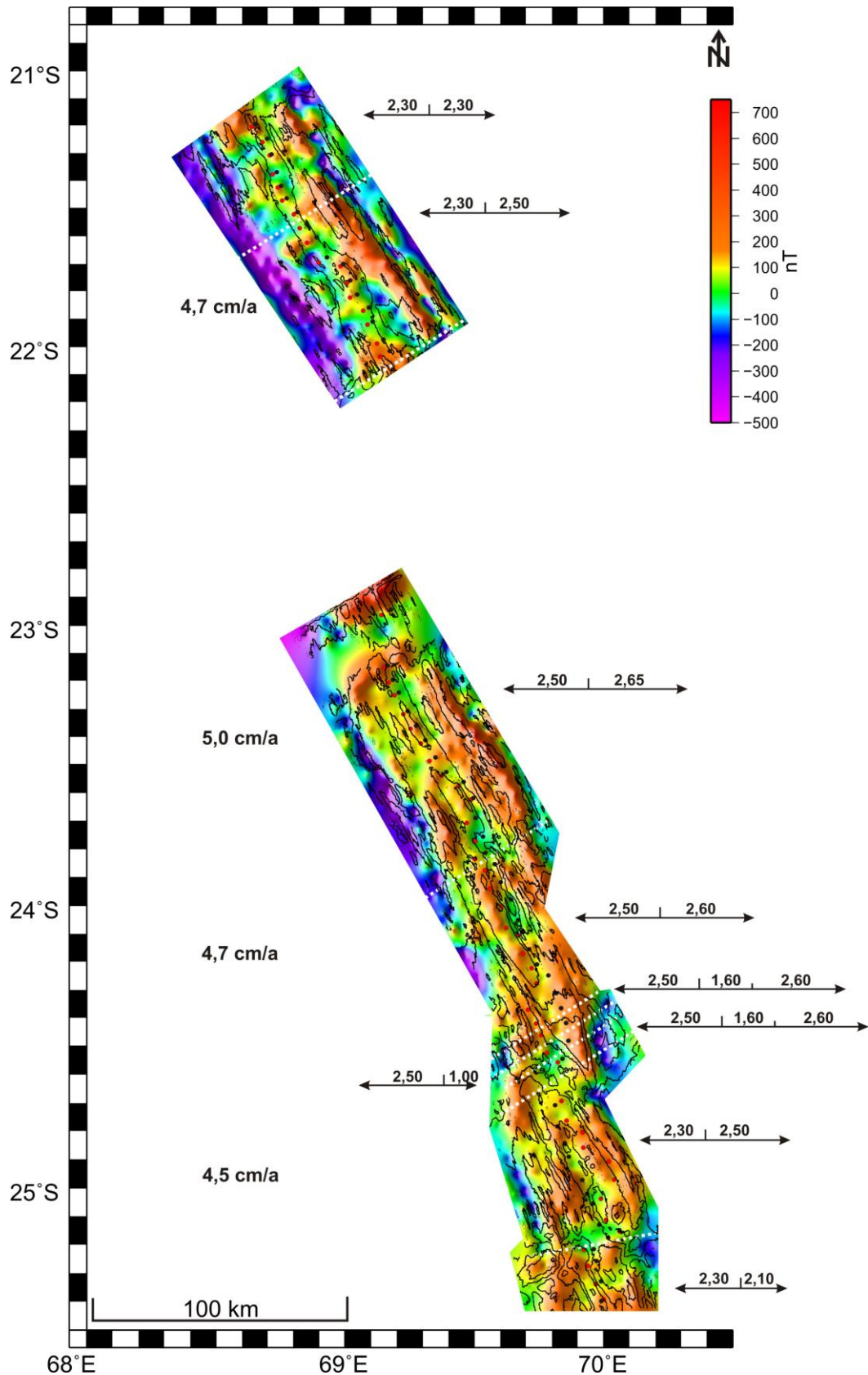


Figure 40: Magnetic map of the southern CIR with calculated full spreading rates on the left side and the asymmetric spreading behavior shown on the right side. The black circles mark the center of magnetic Anomaly 1 and the red circles the ridge axis. The white dotted lines limit the areas where the spreading behavior of the ridge flanks changes. The map is superimposed with the bathymetric contour lines every 500 m.

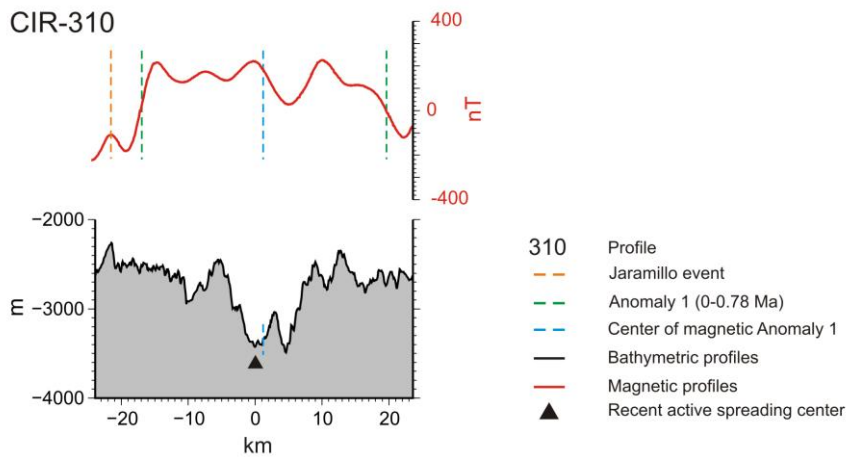


Figure 41: Magnetic (top) and bathymetric (bottom) profile 310 of the Central Indian Ridge with both Anomaly 1 boundaries (green) and one flank of the Jaramillo event (orange). The center of magnetic Anomaly 1 is labeled with a blue line and the recent active spreading center, defined as bathymetric minimum, is labeled with a black triangle.

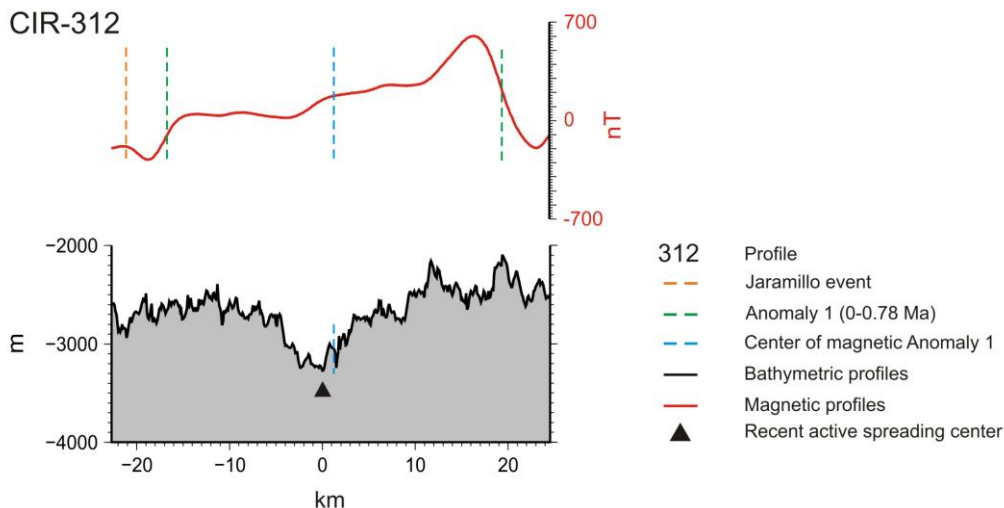


Figure 42: Magnetic (top) and bathymetric (bottom) profile 312 of the Central Indian Ridge with both Anomaly 1 boundaries (green) and one flank of the Jaramillo event (orange). The center of magnetic Anomaly 1 is labeled with a blue line and the recent active spreading center, defined as bathymetric minimum, is labeled with a black triangle.

After the short transit profile which is not included here the next 14 profiles (328-343) were measured with a strike direction of N60°E again. Almost all profiles show the flanks of Anomaly 1 (0-0.78 Ma). With a full spreading rate of 5.0 cm/a this part of the working area is the fastest along the slow spreading ridge. More than half of the profiles reveal the center of magnetic Anomaly 1 at the location of a bathymetric peak. For the whole area an asymmetric spreading is obvious with 2.50 cm/a to the western side and 2.65 cm/a to the eastern side (**Figure 40**). The distance between the center of magnetic Anomaly 1 and the bathymetric

minima increases southwards. The profiles 333 and 335 are located at two neovolcanic ridges where one of them hosts the inactive hydrothermal vent site Sonne crossed by profile 334.

The following 13 profiles 344 to 356 show a slight asymmetric spreading whereby the eastern ridge flank has higher spreading rates with 2.60 cm/a than the western flank with 2.50 cm/a (**Figure 40**). The full spreading rate for the area is approximately 4.7 cm/a. In the northern and central part, the spreading axis migrates in the eastern direction, but to the south this behavior changes and the spreading axis moves to the western side. The tectonic and magmatic activity and the influence on the spreading behavior can clearly be seen in the southern region with the Knorr rise. The profiles 354 and 356, located just north and south of the Knorr rise, are characterized by an obvious asymmetric spreading pattern. To the west the ridge shows high full spreading rates of 2.50 cm/a and to the east the ridge spreads with 1.60 cm/a between 0 and 0.8 m.y. and increases to 2.60 cm/a between 0.8 and 2 m.y. (**Figure 40**). That the Knorr rise acts as a spreading stop becomes clear with profile 355 running through the central part of the seamount. Here the ridge spreads with 2.50 cm/a to the west while to the east the spreading decreases significantly and has the lowest value of 1.0 cm/a. The center of magnetic Anomaly 1 does not correlate with a bathymetric peak as in many profiles as before. The profiles 352 and 353 show the highest distance between the active spreading center and the center of magnetic Anomaly 1 (**Figure 43**). An explanation for that mismatch could be very recent, tectonically driven changes of the spreading geometry which cannot be seen in the magnetic anomalies yet. In detail, the changes occurred during the last 100 000 years and the newly formed spreading center evolves because of high crustal extension even before volcanism can take place (BARCKHAUSEN & BARGELOH, 2012).

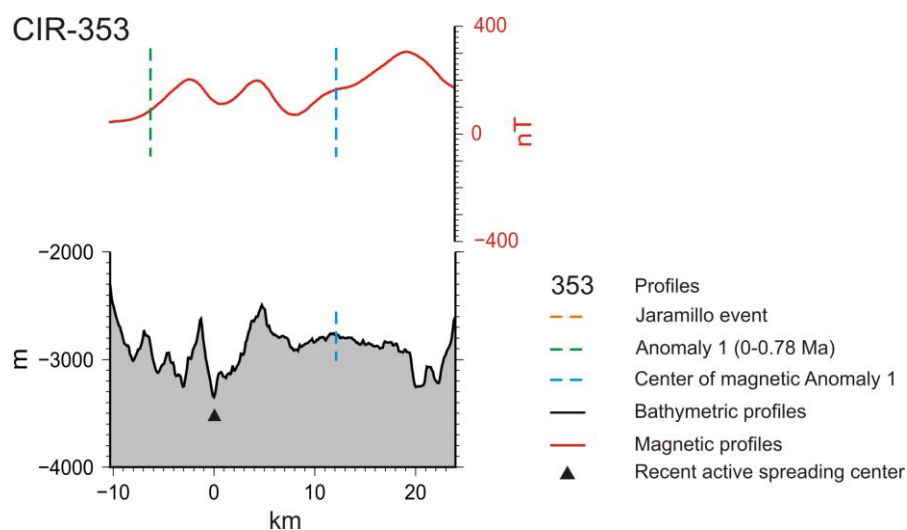


Figure 43: Magnetic (top) and bathymetric (bottom) profile 353 of the Central Indian Ridge with one flank of Anomaly 1. The approximate center of magnetic Anomaly 1 is labeled with a blue line and the recent active spreading center is labeled with a black triangle.

The profiles 371-362 show an average full spreading rate of 4.5 cm/a. The ridge spreads asymmetrically and changes the flanks of faster spreading. That means in detail that in the northern area (profiles 371-363) the eastern ridge side spreads faster with 2.50 cm/a than the western side with 2.30 cm/a (**Figure 40**). That behavior changes to the south (profiles 359-205) where the western flank spreads faster with 2.30 cm/a than the eastern side with 2.10 cm/a. The profiles 371-363 are characterized by the greatest distance between the center of magnetic Anomaly 1 and the spreading center and a ridge jump which could be identified by the change of the location of the spreading axis south of the center of magnetic Anomaly 1. The last two profiles measured during INDEX2011 (361-362) are replaced by the first two profiles of INDEX2012 (204-205), because these show a better data quality.

To sum up, the trend of the full spreading rates along the slow spreading ridge is shown in **Figure 44**. A large variation in full spreading rates between 3.72 cm/a and 5.58 cm/a exists from 21°S towards the RTJ. South of Edmond there is a general decrease in the full spreading rates from 5.0 cm/a to 3.72 cm/a before they sharply increase at the Kairei vent field. The influence which structural edifices like the Knorr rise have on the spreading rate can clearly be seen. With a look at the trend there is a decrease in spreading rate of the single profiles south of the Knorr rise. Also, the hydrothermal vent site locations are labeled and with exception of EXFX which is just a methane anomaly, the vent sites are characterized by high full spreading rates between 4.87 cm/a and 5.6 cm/a.

With a detailed look at the nT values within Anomaly 1 there are sometimes obvious spikes (relatively high magnetic values) which are located above the spreading center as can be seen in **Figure 45** or other young, recent structures. In the following this feature will be called Central Anomaly Magnetic High (CAMH) as defined by POULIQUEN et al. (2001). In case of the profile crossing the SONNE hydrothermal vent site this CAMH is located directly at the larger eastern neovolcanic ridge as shown in **Figure 46**. In **Figure 47** the CAMH is closely linked to the western flank of the Knorr rise (profile CIR-354), another neovolcanic ridge (profile CIR-369) and a huge seamount within the rift valley (profile CIR-364). In all cases the width of this CAMH is approximately 3 km.

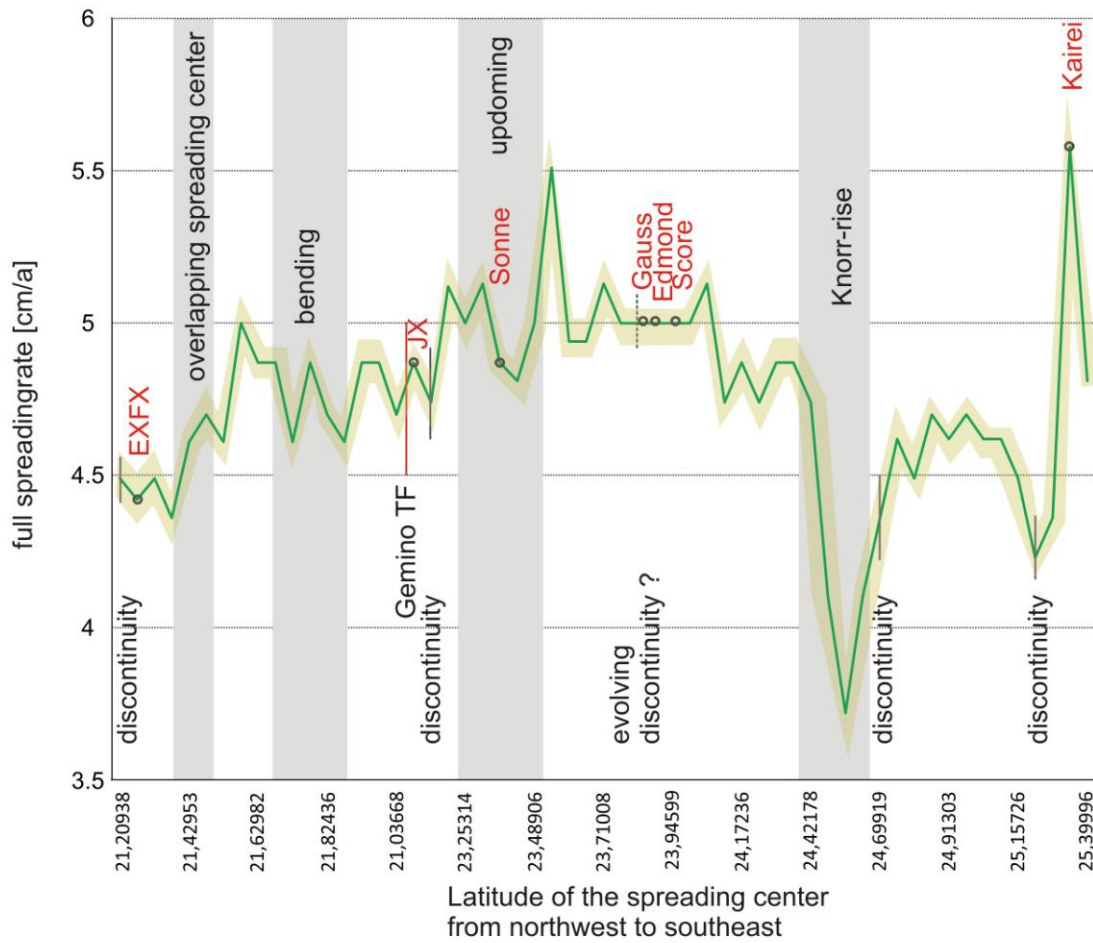


Figure 44: Full spreading rate versus latitude of the slow spreading ridge system (CIR) from 21°S to the RTJ. The effect of the structural edifices to the spreading rate (Knorr rise, discontinuities) is obvious. The transparent area marks the error estimation according to **Chapter 3.3**.

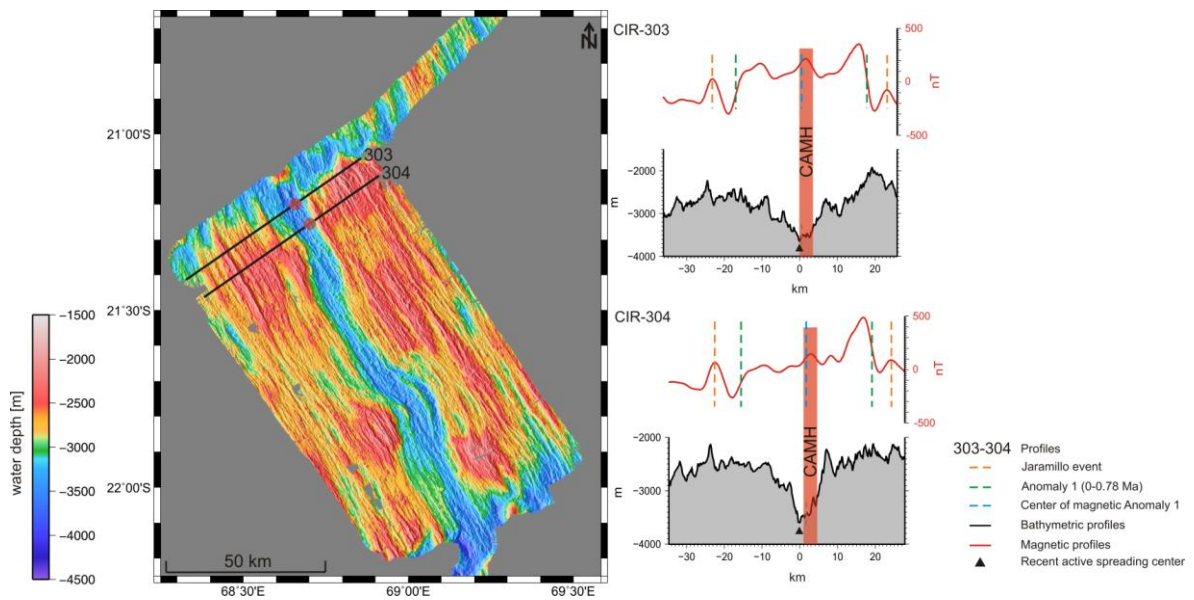


Figure 45: Bathymetric map of the working area EXFX and two cross profiles containing bathymetry (grey) and magnetic (orange) data. The transparent red zone (circle and box) marks the central anomaly magnetic high (CAMH).

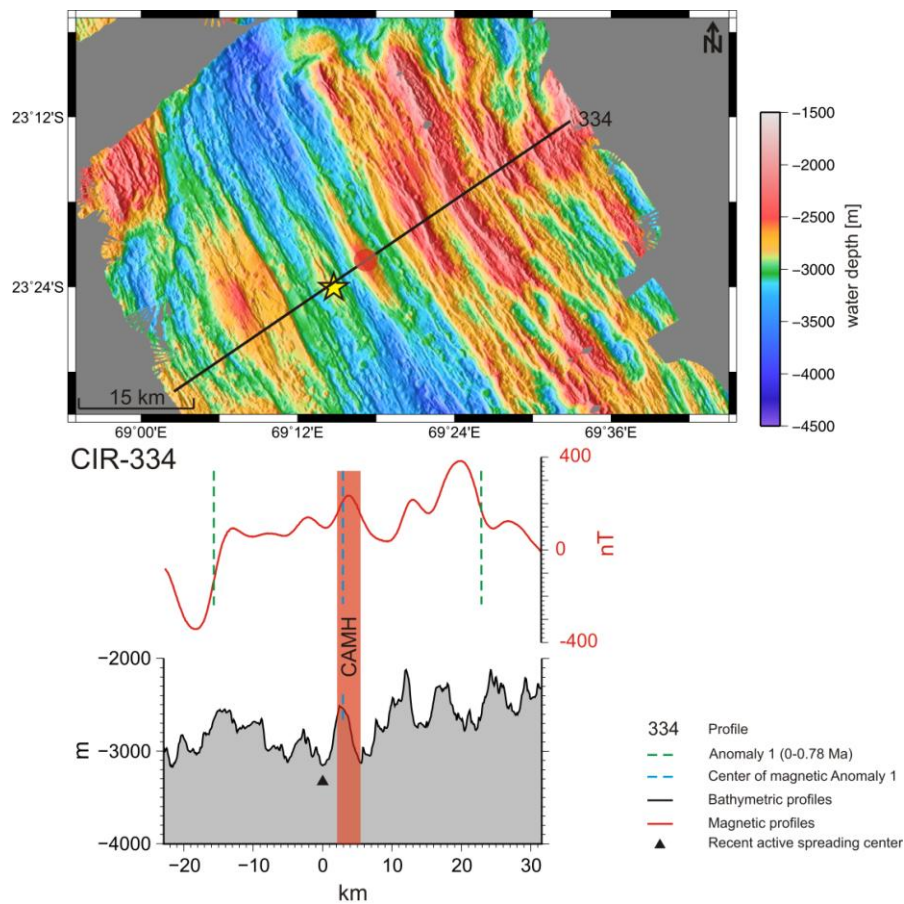


Figure 46: Bathymetric map of the working area Meso and one cross profile with magnetic (orange) and bathymetric (grey) data. The star marks the hydrothermal vent site Sonne. The transparent red zone shows the central anomaly magnetic high (CAMH).

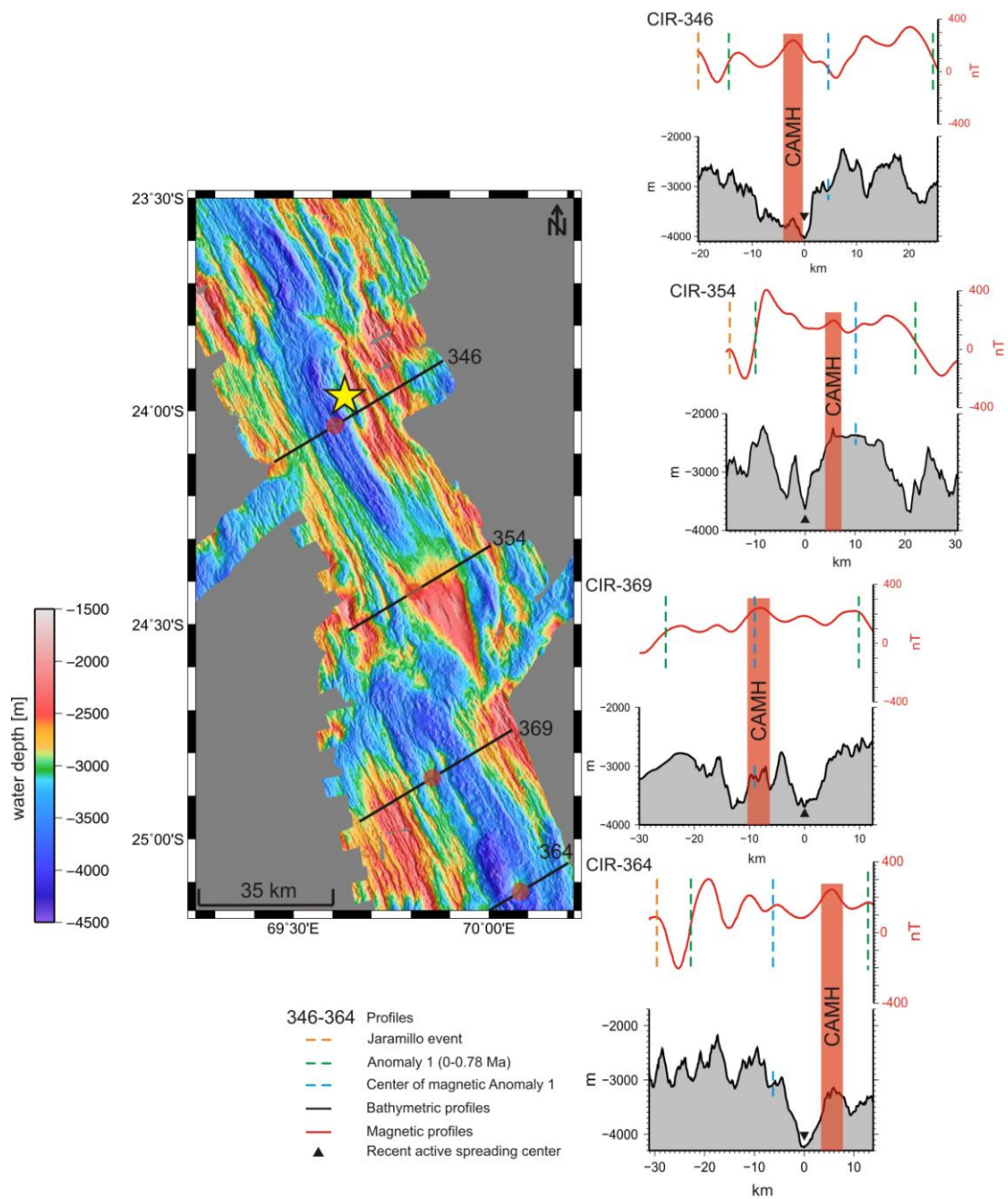


Figure 47: Bathymetric map of the working area Edmond and four cross profiles with magnetic (orange) and bathymetric (grey) data. The star marks the hydrothermal vent site Edmond. The transparent red zone shows the central anomaly magnetic high (CAMH).

4.2) An intermediate spreading ridge system

4.2.1) Structural description

In 2012 the northern part of the intermediate spreading Southeast Indian Ridge was mapped during the second research cruise at a length of ~500 km between 25°30'S and 28°S (**Figure 48**). To the north it is bounded by the Rodriguez Triple Junction. The ridge strikes NW-SE and is characterized by a continuous well expressed rift valley, which strikes ~135° SE. Five discontinuities offset the ridge in a left-lateral sense. The SEIR was divided into 6 working areas, which are numbered consecutively (section 1-6). Sections 2 and 5 are defined as accommodation zones characterized by a rift valley which is not well expressed and rift shoulders not running parallel to the rift valley (**Figure 48**). Compared to the CIR more seamounts can be found in the rift valley and on the rift shoulders over the whole intermediate spreading ridge.

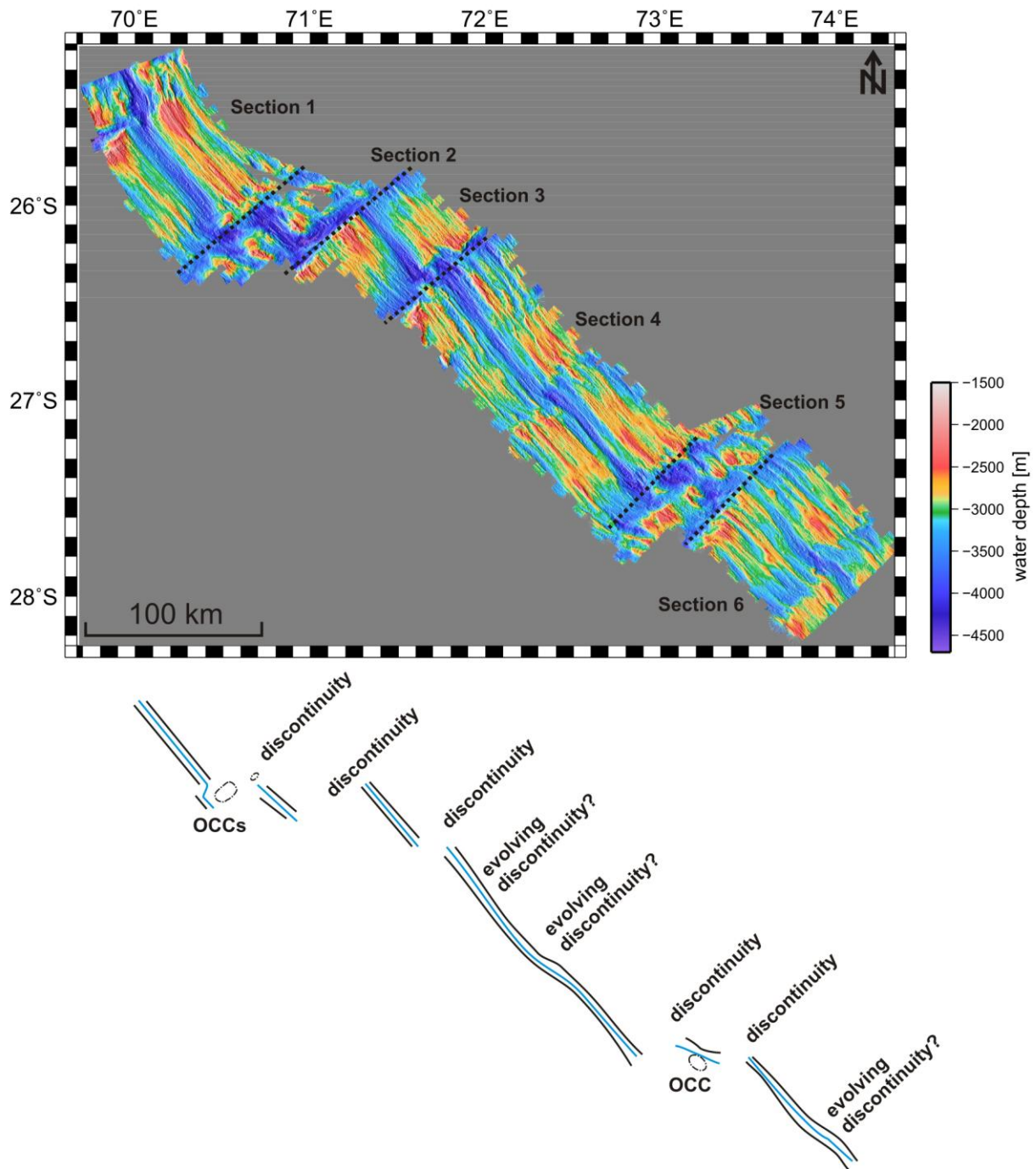


Figure 48: Bathymetric map of the northern Southeast Indian Ridge. The dotted lines separate the six working areas (top). Sketch of the main structural features along the SEIR (bottom). The blue lines mark the ridge axis and the black lines are the rift valley boundaries.

The Rodriguez Triple Junction (RTJ) is defined by the three ridge systems Southwest Indian Ridge (SWIR), Central Indian Ridge (CIR), and Southeast Indian Ridge (SEIR) as shown in **Figure 49**. The CIR and SEIR in that area show ridge parallel major faults. The SWIR instead is characterized by a series of step faults on the northern ridge flank. The east and west flanks of the SEIR are more uplifted in the direct vicinity of the RTJ. Between the CIR and the SEIR an offset is obvious which is characterized by an evolving small ridge structure inside the rift valley.

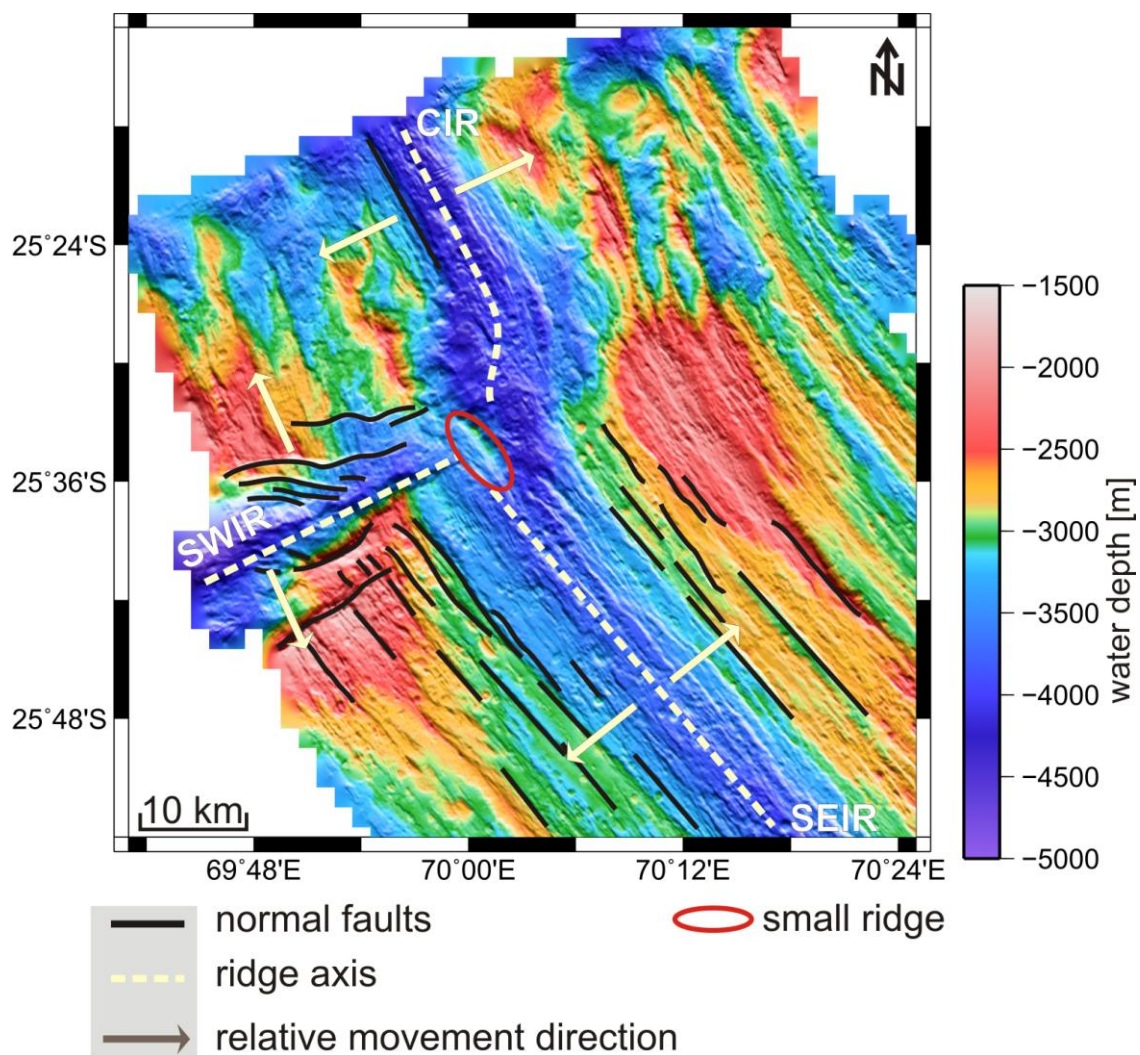
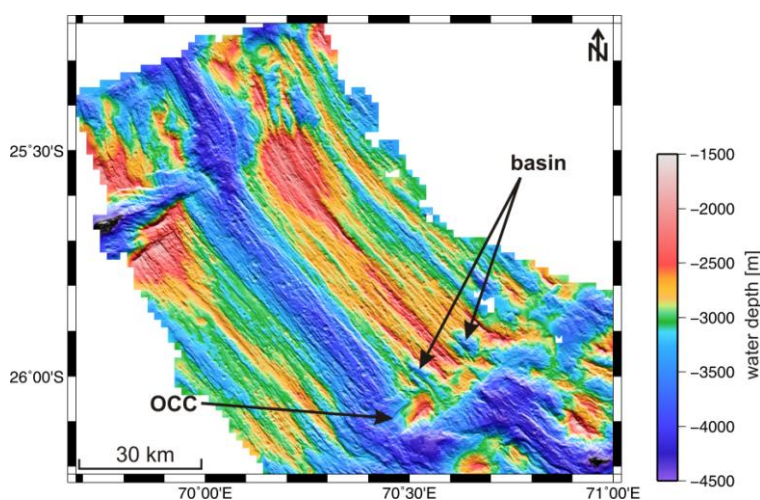


Figure 49: Bathymetric map of the Rodriguez Triple Junction with major tectonic elements. The arrows show the relative movement directions and the red oval marks a small evolving ridge inside the RTJ. A small offset between the CIR and the SEIR became obvious.

Section 1 extends from 25°30'S to 26°08'S with a length of 85 km (**Figure 50**). The rift valley is very well defined with an average water depth of 3800 m and a width of 4 km to 6 km. There is a trend from north to south where the rift valley is getting deeper. In **Figure 51** (left side) the 3750 m contour lines show the typical hourglass shaped morphology of this section where the water depth is shallowest in the middle and increases to the ends. Several faults are running parallel to the rift valley and dip towards it. The rift shoulders east of the rift valley show altogether a higher uplift. This can be seen in **Figure 51** on the right side with the 2750 m contour lines. The shallowest point is reached on the western rift shoulder with ~1700 m water depth. Many seamounts can be found in the rift valley as well as on the rift shoulders. Some are characterized by fault structures which cause the seamounts to be offset in one direction (**Figure 52**, **Figure 53**, and **Figure 54b**). The majority of the seamounts is defined by a flat top and not the typical cone shape. Other seamounts show caldera structures which are more or less well expressed. Like in the case of the slow spreading ridge system, the majority of the seamounts is located on the western ridge flank, however, a lot more are tectonically influenced (**Figure 54a & b**). Furthermore many seamounts occur inside the rift valley. To the south there is another oceanic core complex like the one at the CIR (**Figure 50**). Typical characteristics can be seen like the lineations (mullions) striking perpendicular to the rift valley. In the northwestern part of the OCC the line of movement is well distinct. The development of the OCC forces the rift valley to find another course, so in its northern part the ridge axis is offset by ~7 km. The adjacent older rift shoulders show a slight bending where they come together with the OCC. In the same area north-east of the OCC two basin structures are observed (**Figure 50**). To sum up, typical features for Section 1 are the stronger



uplifted eastern flanks, several sheared seamounts, OCCs, two basins, and extremely ridge parallel faults (**Figure 54c**).

Figure 50: Bathymetric map of Section 1 with prominent structural features like two basins and an OCC.

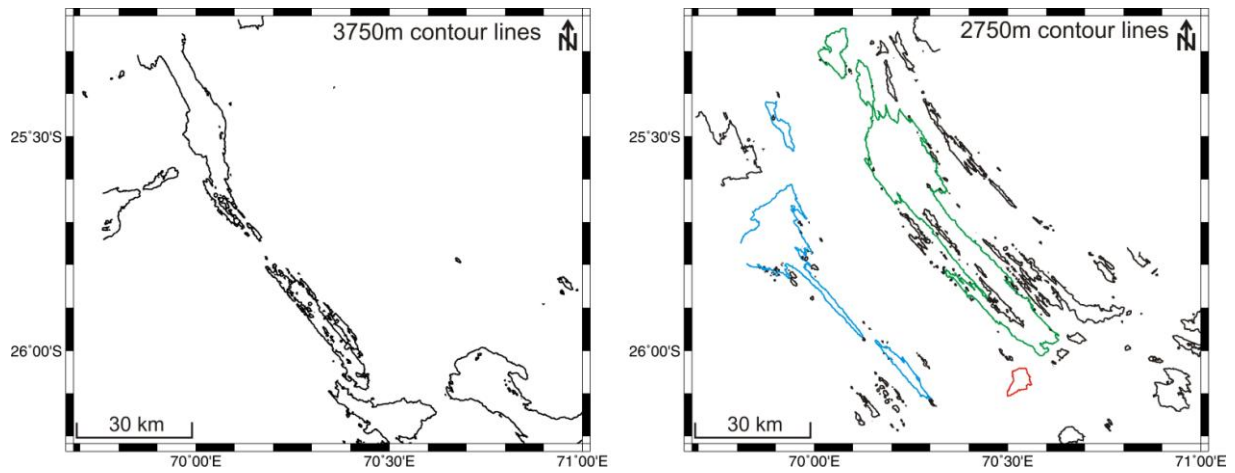


Figure 51: Map of the contour lines of Section 1. On the left side the 3750 m lines which mark the rift valley. On the right side the 2750 m contour lines characterizing the stronger uplifted eastern side (green lines) and the corresponding western flank (blue lines).

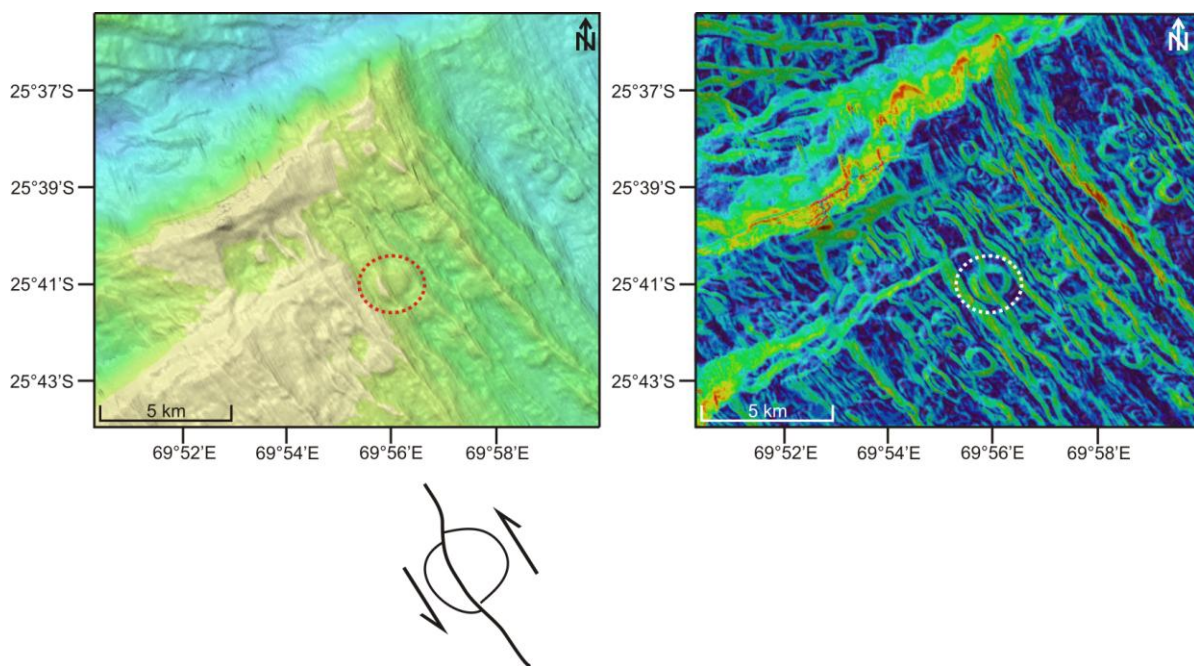


Figure 52: Detailed bathymetric (left side) and slope inclination (right side) map of a sheared seamount in the vicinity of the RTJ.

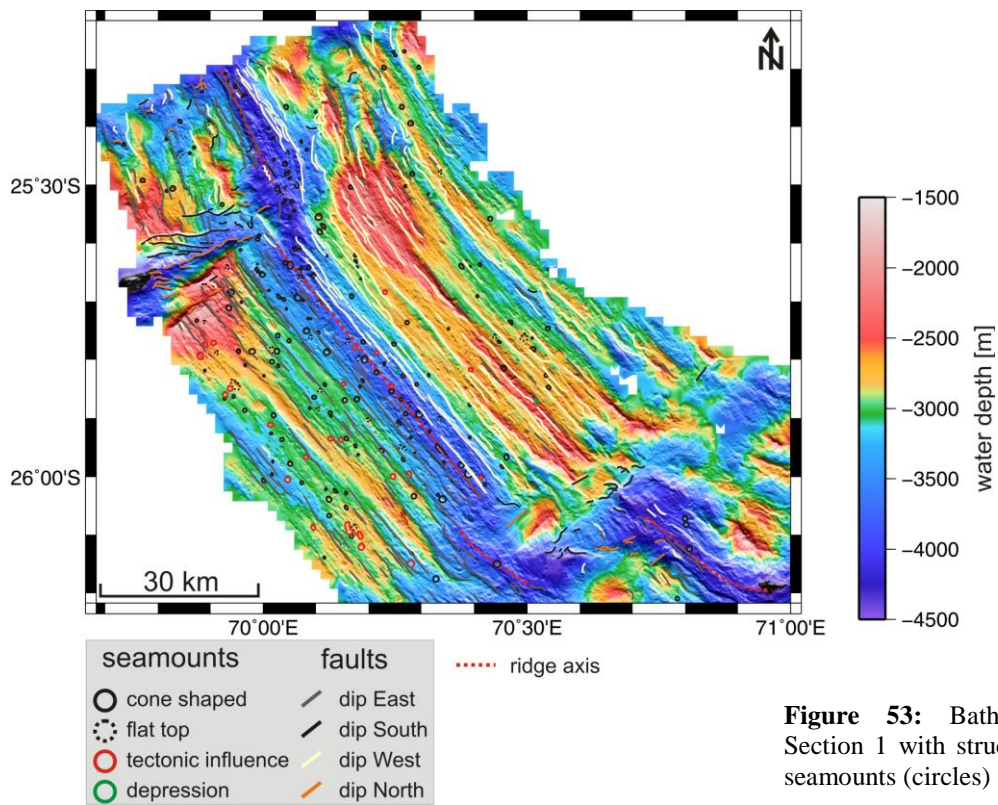
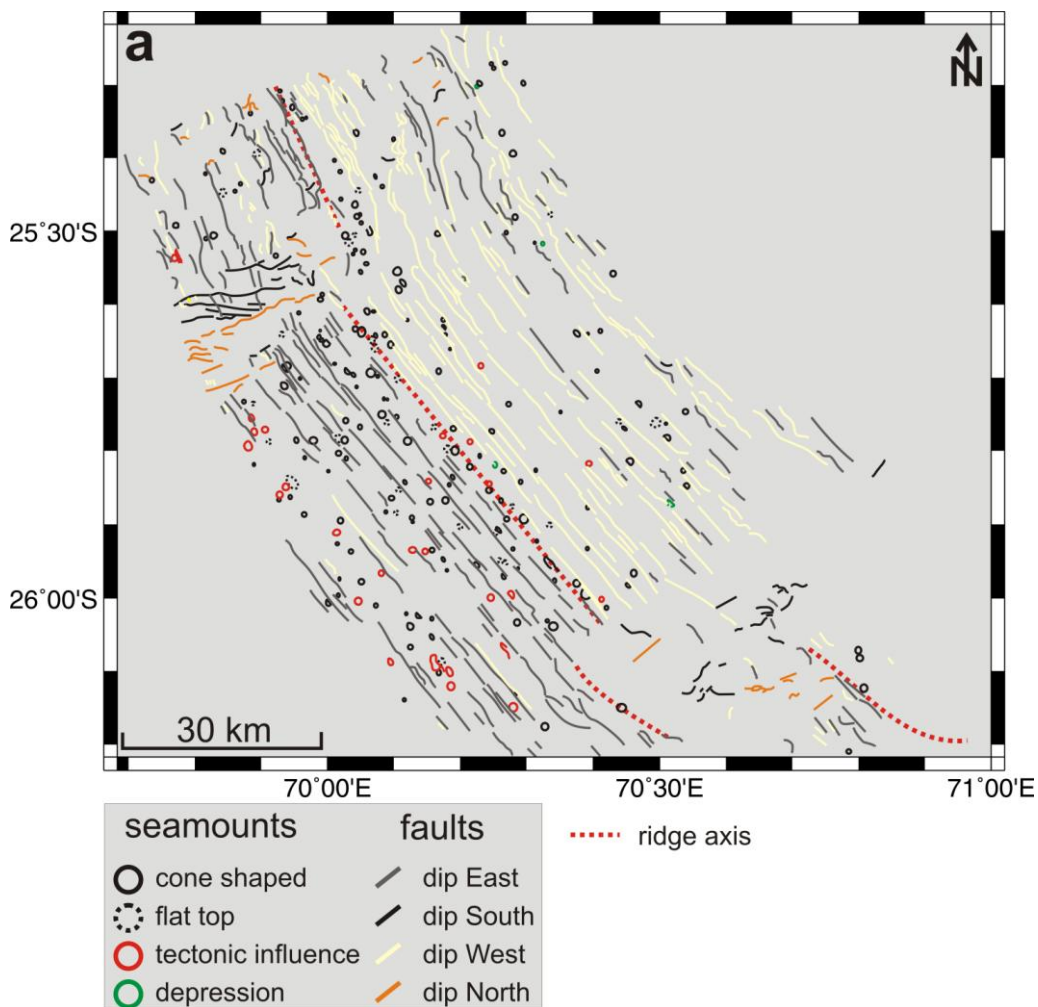


Figure 53: Bathymetric map of Section 1 with structural features like seamounts (circles) and faults (lines).



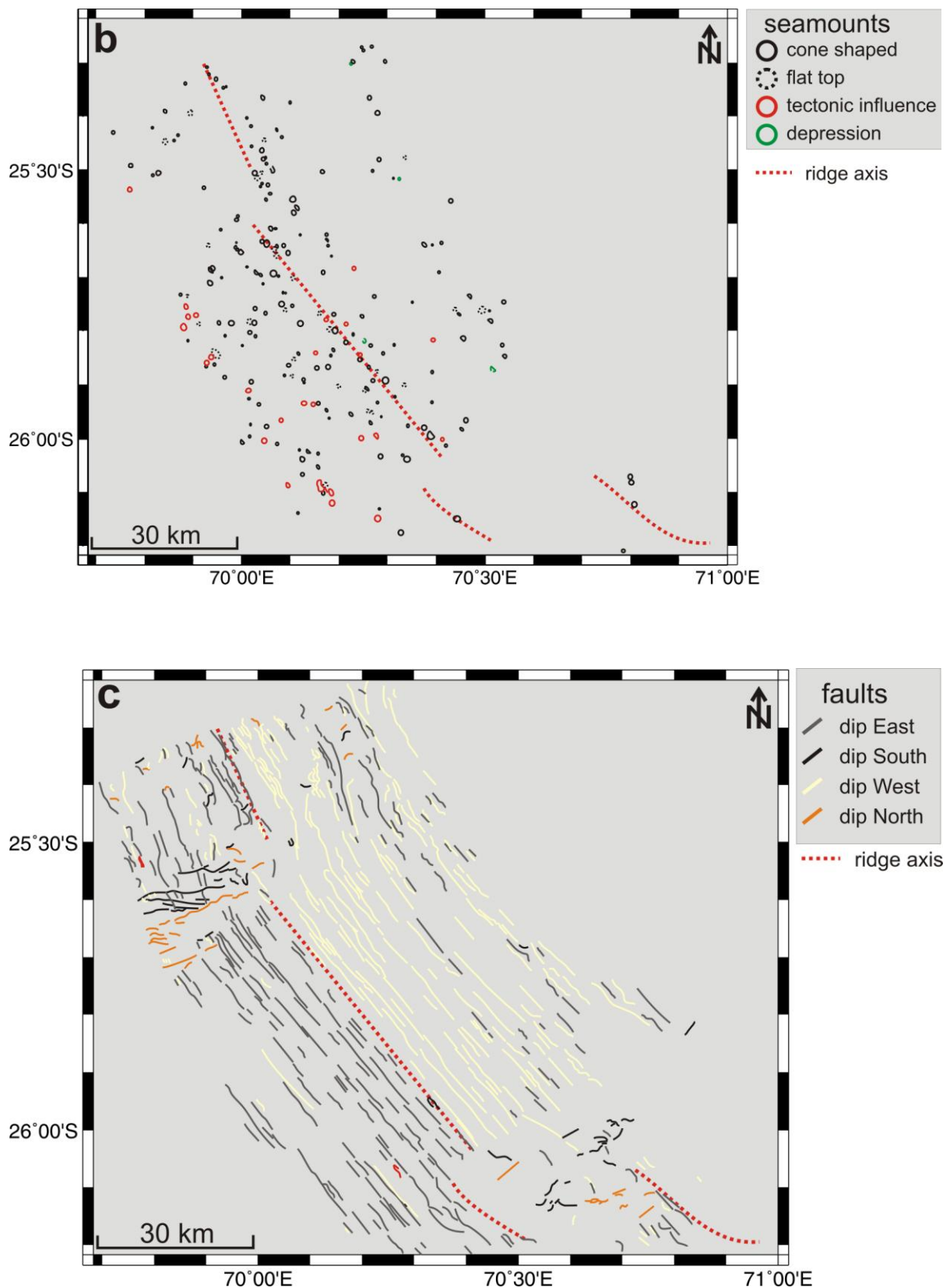


Figure 54: Structural maps of Section 1: **a)** labeled with circles for the seamounts and with lines for the faults; **b)** labeled with circles for the seamounts divided into those who are cone shaped, have a flat top or are tectonically influenced and with green circles for depression structures; **c)** labeled with lines for the faults dipping in different directions.

Adjacent to Section 1 is an accommodation zone Section 2 between 26°09'S and 26°12'S at a length of 43 km (**Figure 55**). The rift valley is well expressed only in the central part of that working area. It has an average water depth of 4300 m and a width of 4 km – 4.6 km. On average the trend of the rift shoulders parallel to the rift valley is missing. Hence, the major faults dip to the north, east, south and west and strike between 50°NE and 130°SE (**Figure 56** and **Figure 57a & c**). There are only a few seamounts which concentrate in the vicinity of the rift valley (**Figure 57b**). Like in Section 1 the seamounts show flat tops. In the north of Section 2 and east of the large OCC another younger oceanic core complex is just starting to develop (**Figure 55** and **Figure 58**). It shows the smooth surface and initial mullions perpendicular to the spreading direction. A line of movement is tentatively marked in the northwestern part (**Figure 58**). Some step faults (**Figure 58**) can be found west of the young OCC. Towards the south there is a deep basin with a water depth of 4600 m and an indicated rhomboid shape, possibly another pull-apart basin (**Figure 55**). As a summary, typical features are another OCC, a pull-apart basin and the fact that the major faults are not striking ridge parallel but rather in every direction.

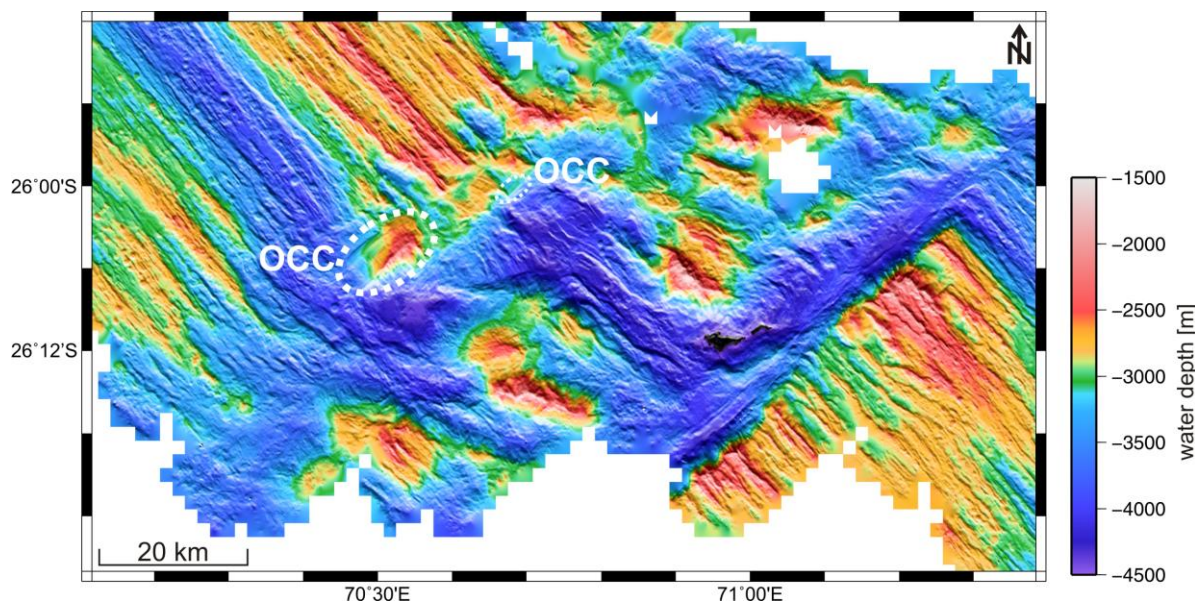


Figure 55: Bathymetric map of Section 2 with two prominent oceanic core complexes.

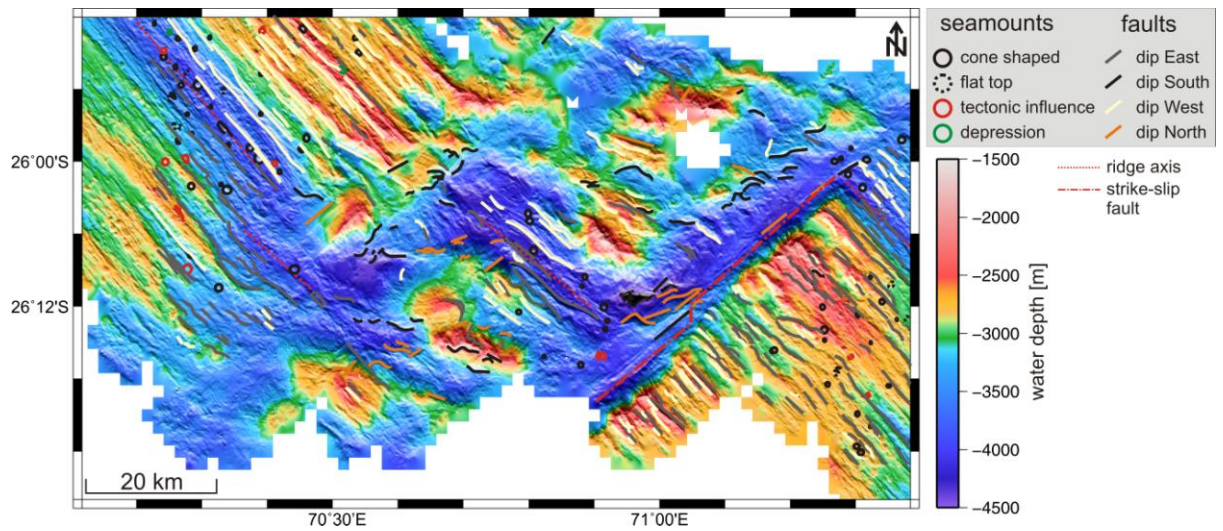
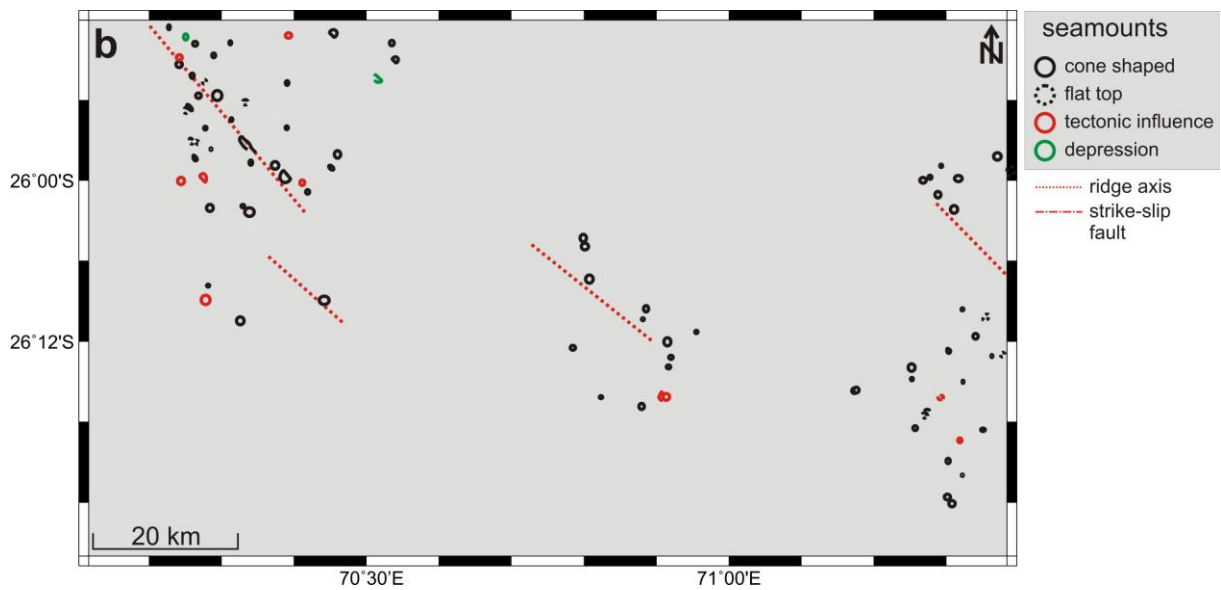
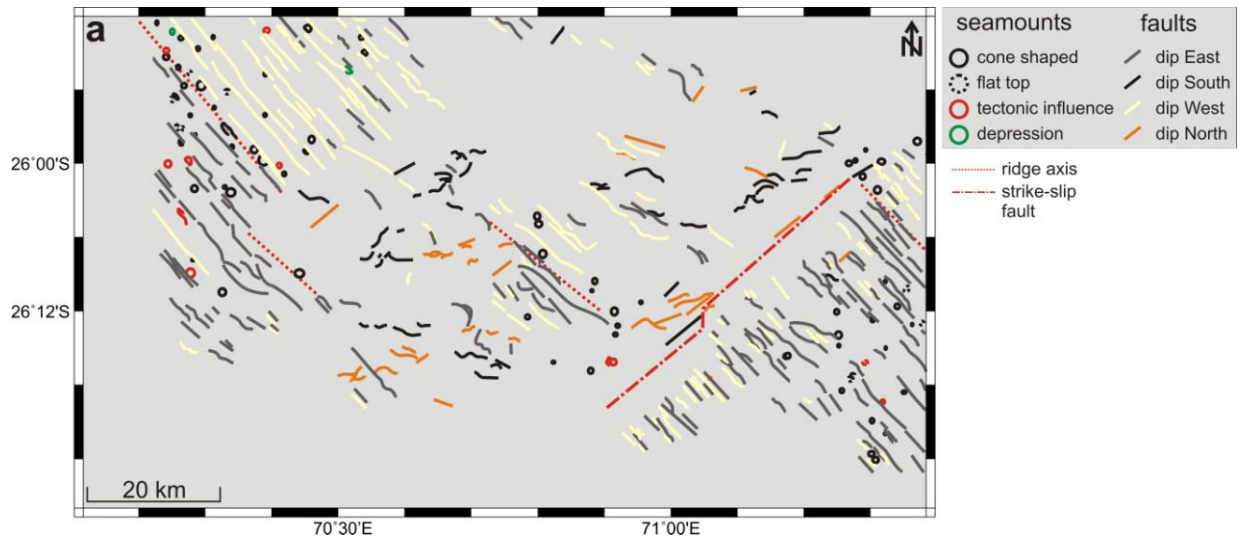


Figure 56: Bathymetric map of Section 2 with structural features like seamounts (circles) and faults (lines).



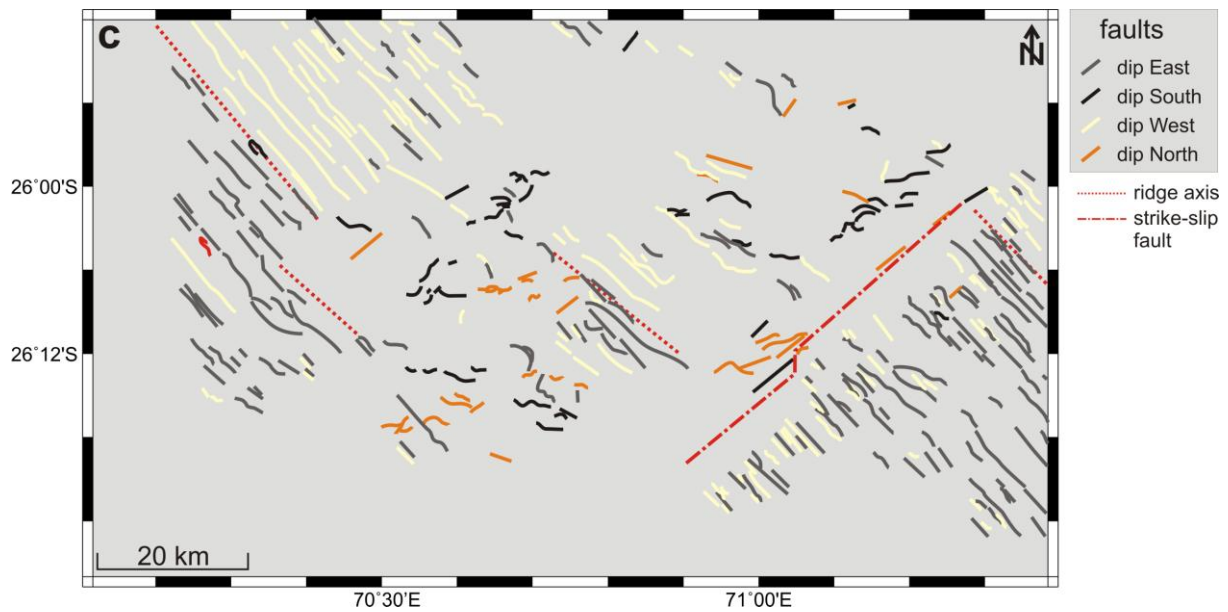


Figure 57: Structural maps of Section 2: **a)** labeled with circles for the seamounts and with lines for the faults; **b)** labeled with circles for the seamounts divided into those who are cone shaped, have a flat top or are tectonically influenced and with green circles for depression structures; **c)** labeled with lines for the faults dipping in different directions.

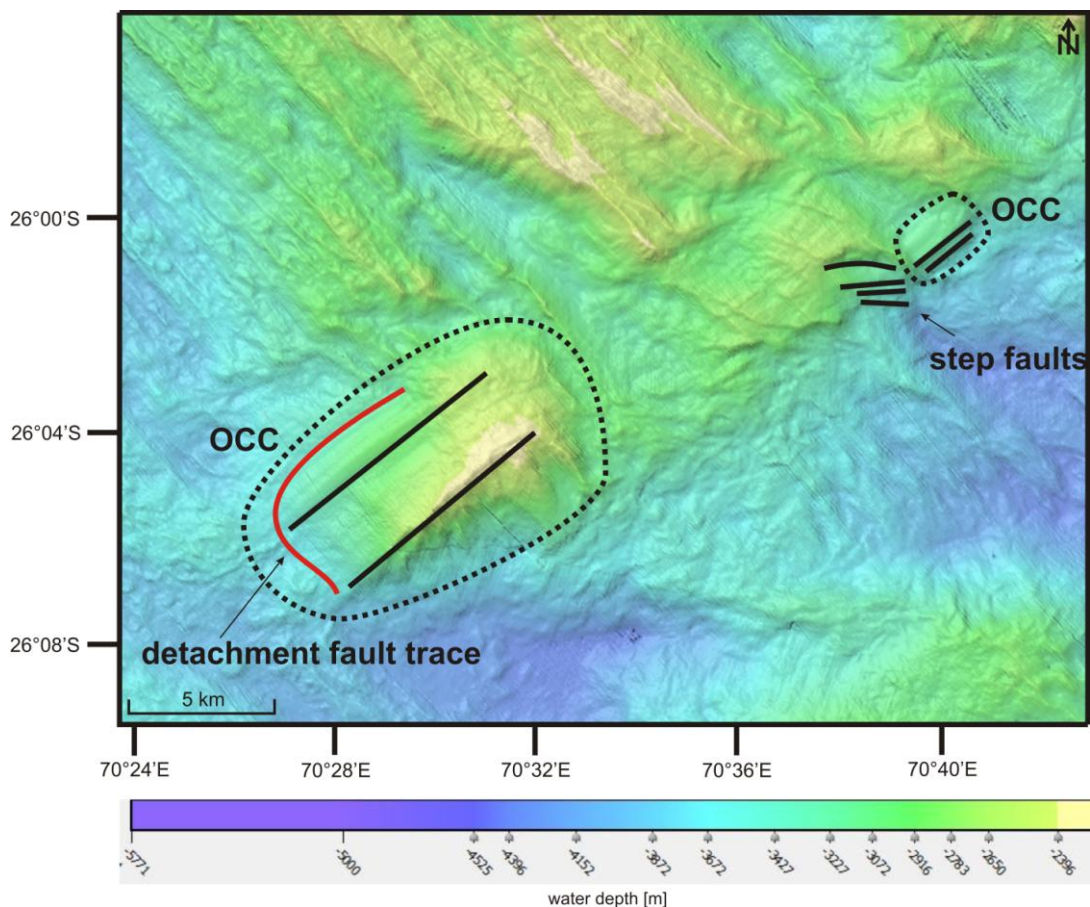


Figure 58: Bathymetric map of two oceanic core complexes in Sections 1 and 2 with structural interpretation. The smaller OCC seems to be still developing.

Working area Section 3 follows between 26°13'S and 26°30'S with a length of ~60 km. In contrast to Section 2 the rift valley is well expressed by the youngest uplifting rift shoulders (**Figure 59**). It has an average water depth of 4100 m and is deepening to the south. The average width is around 5 km. The whole section has the so often seen hourglass morphology where the section is shallower in the middle part (**Figure 60**, left side). With a look at the seamount distribution in **Figure 61** and **Figure 62b** it can be seen that there are many of them on the older rift shoulders. The distribution on both sides of the ridge is relatively equal. In contrast to Section 1, several seamounts located on faults show no offsets. The major faults are running parallel to the rift valley and dip to the west or east (**Figure 62c**). The northern boundary of Section 3 is a large strike-slip fault with an extremely straight trend and a water depth of ~4300 m at the deepest point (**Figure 59**). At this place the ridge axis is offset by ~43 km in a right-lateral sense but the plate boundaries are characterized by a left-lateral movement (**Figure 63**). At 71°02'E/26°13'S the strike-slip fault shows a left stepping transfer shown in **Figure 62a & c** (red dot-line line). There is a difference in height of ~2000 m from the older ridge segments of Section 3 to the strike-slip fault. The recent rift valley and older rift shoulders in the east show a bending to the west towards the strike-slip fault. The uplift of the older rift shoulders is asymmetric from north to south and from east to west (**Figure 60**, right side). That means that where the rift shoulders show a higher uplift on the western flank of the rift valley then the rift shoulders on the opposite side (east of the rift valley) are

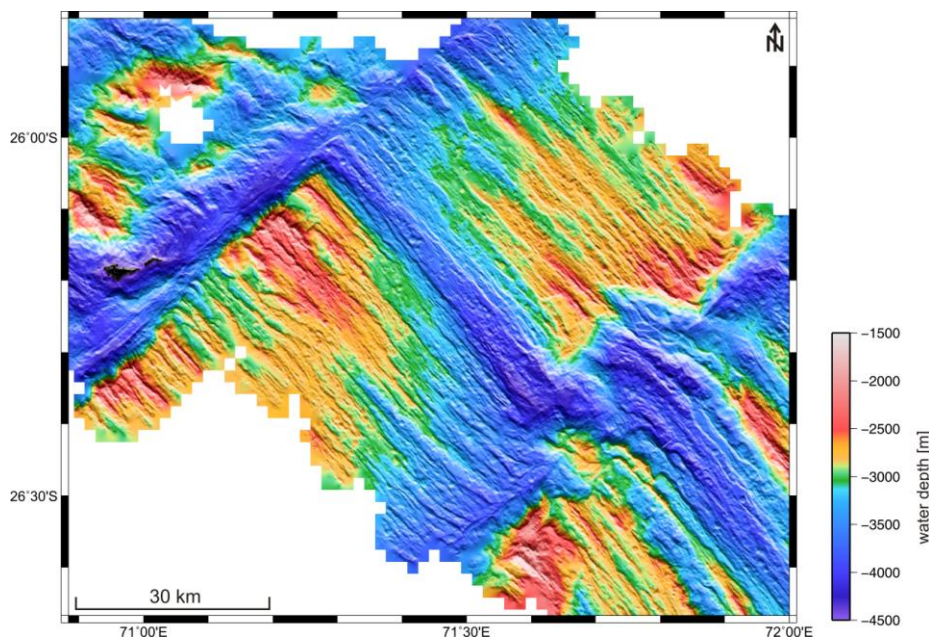


Figure 59: Bathymetric map of Section 3.

depressed. To the south of Section 3 that behavior changes in a way that the rift shoulders on the eastern rift valley flank are higher uplifted than the rift shoulders on the western side (**Figure 60**, right side). To the south a discontinuity

offsets the rift valley left-laterally and the rift shoulders show a slight bending. Typical features of this Section 3 are the strike-slip fault in the northern area, alternating elevated and depressed ridge shoulders and, as in Section 1, ridge parallel faults.

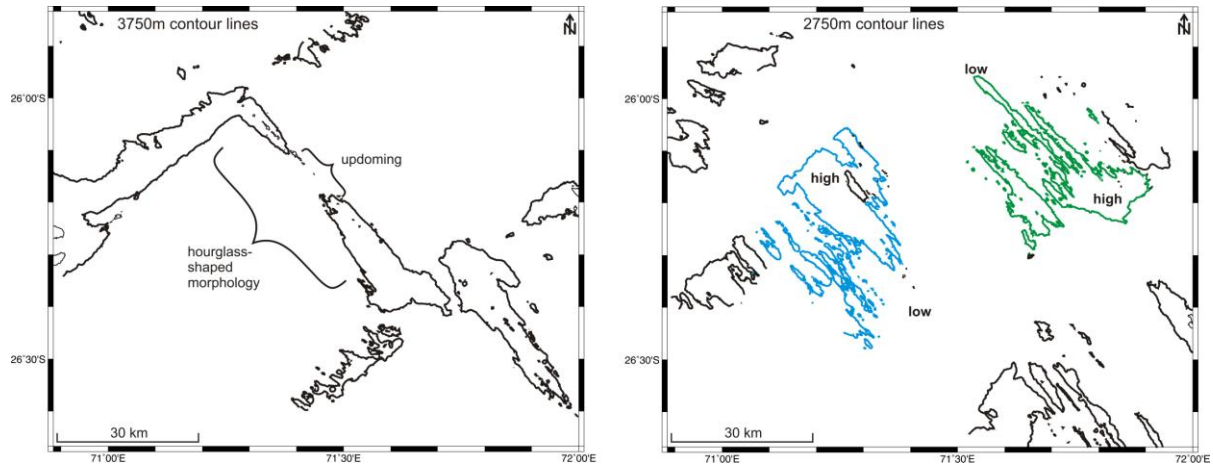


Figure 60: Map of the contour lines of Section 3. On the left side the 3750 m contour lines which mark the rift valley and typical hourglass-shaped morphology of the section. On the right side the 2750 m contour lines characterizing the more uplifted parts of the ridge flanks where the green lines represent the eastern ridge flanks and the blue lines the western flanks.

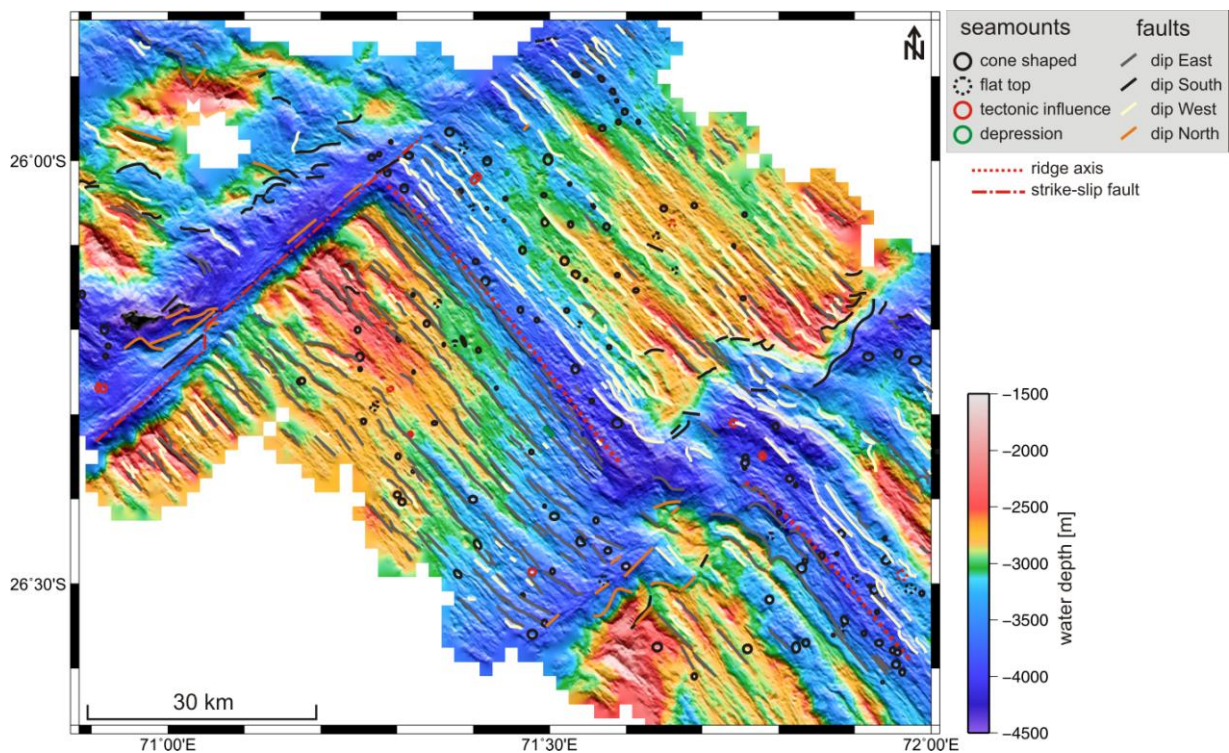
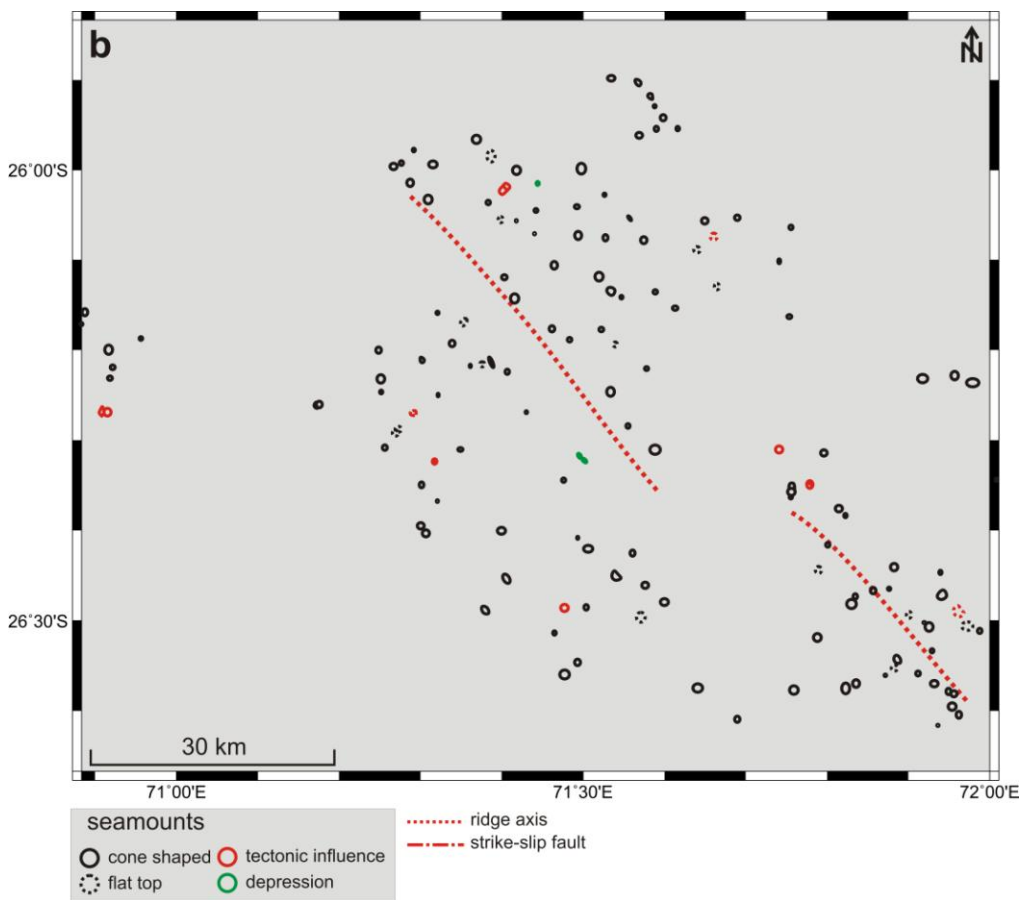
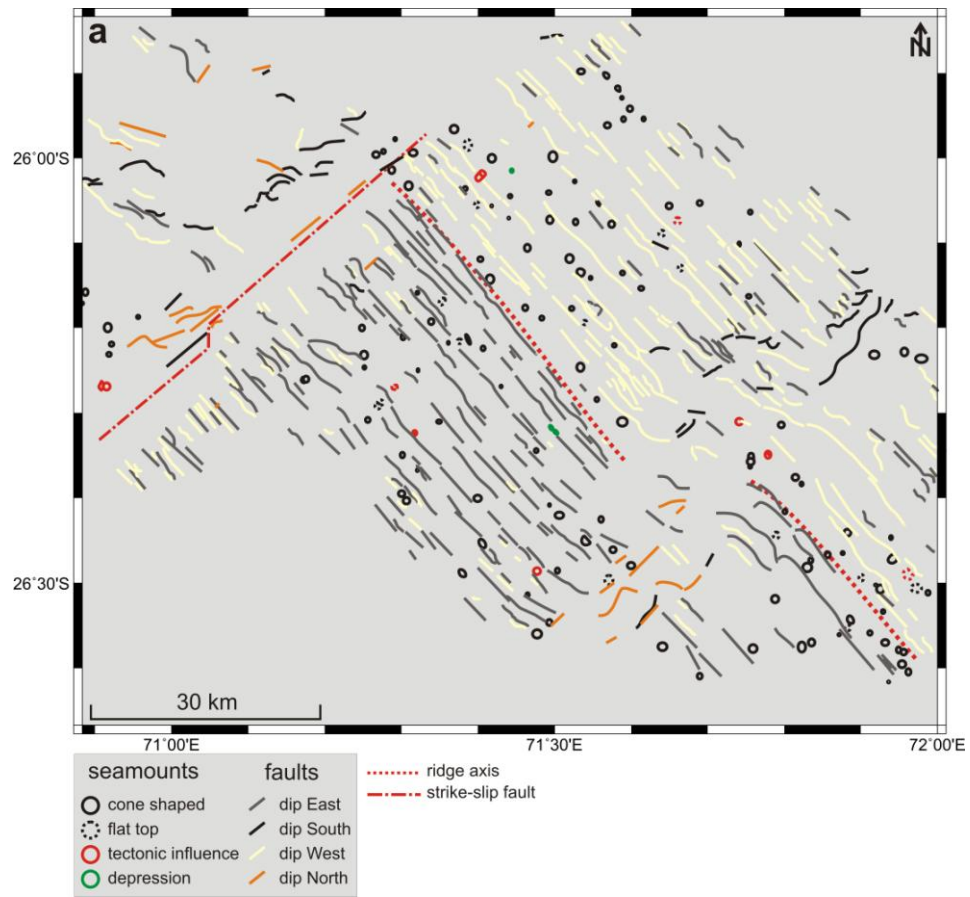


Figure 61: Bathymetric map of Section 3 with structural features like seamounts (circles) and faults (lines).



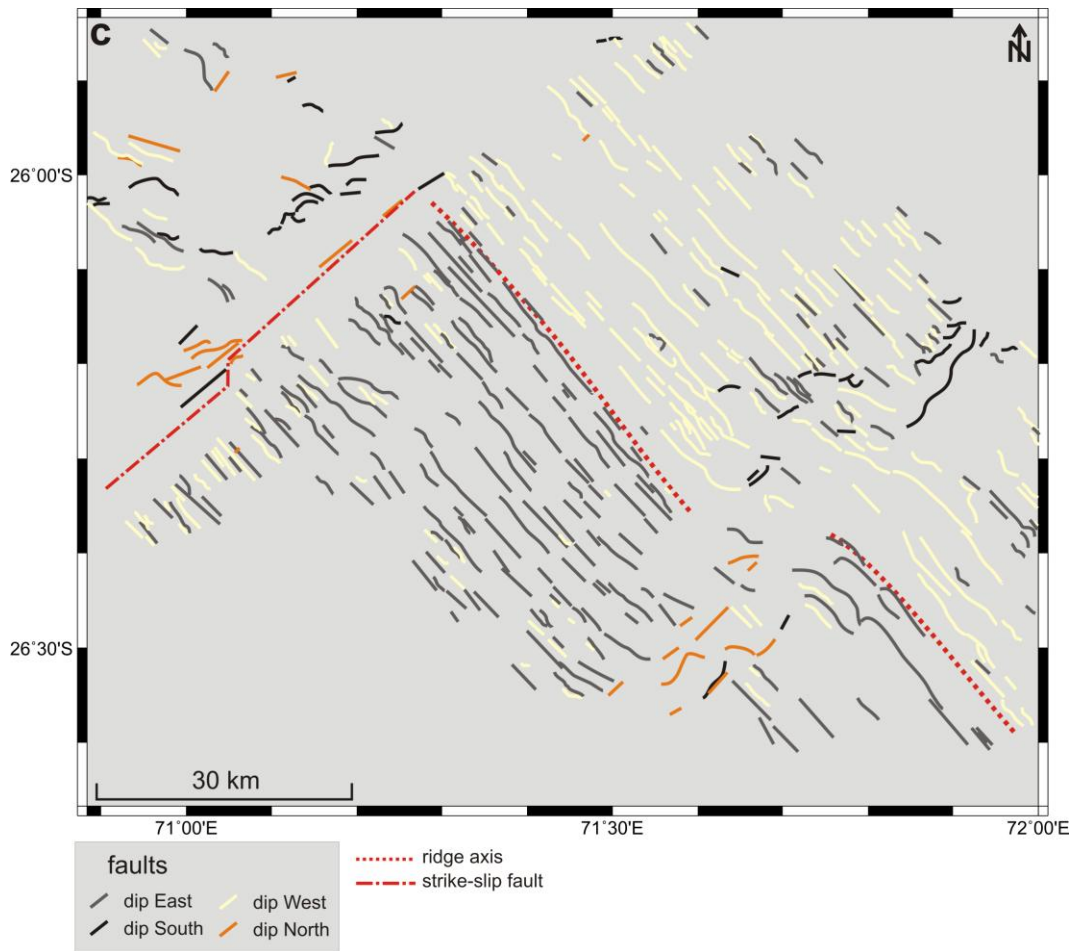


Figure 62: Structural maps of Section 3: **a)** labeled with circles for the seamounts and with lines for the faults; **b)** labeled with circles for the seamounts divided into those who are cone shaped, have a flat top or are tectonically influenced and with green circles for depression structures; **c)** labeled with lines for the faults dipping in different directions.

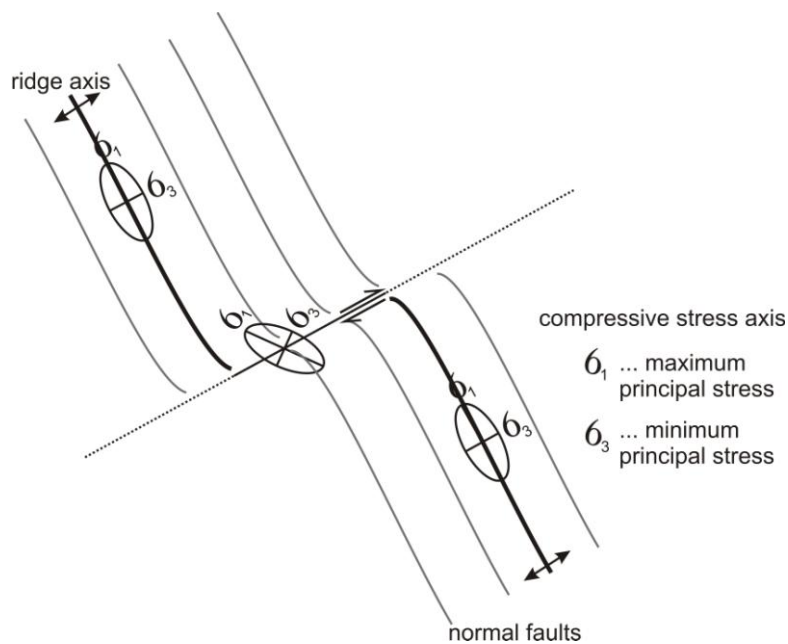
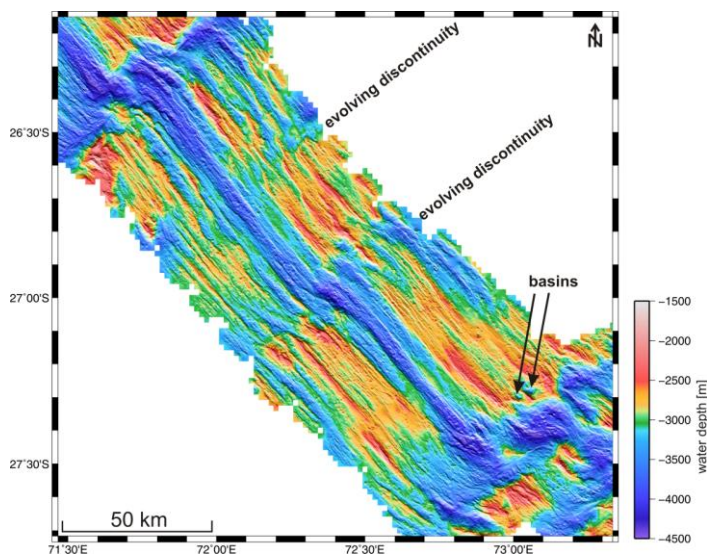


Figure 63: Schematic sketch of the strike-slip fault with the stress ellipse (after SEARLE, 2013, modified).

Working area Section 4 extends from 26°30'S to 27°30'S along the SEIR (**Figure 64**). At a length of ~167 km it is the longest section and shows an area of possibly an evolving discontinuity in the northern and middle part. At this place the rift valley and also the rift shoulders seem to be thinned and have a slight bending (**Figure 64** and **Figure 65**). This becomes clear with the 2750 m contour lines in **Figure 66** (right side). The contour lines are interrupted in the areas of the probably evolving discontinuities. The rift valley is well defined with an average water depth of ~3750 m - 3900 m and a width of ~5 km. It can be outlined with the 3500 m contour lines shown in **Figure 66** (left side). Many seamounts are observed on the rift shoulders as well as in the rift valley (**Figure 67a & b**). In the area of the two evolving offset structures the number of the seamounts decreases. There are more tectonically influenced seamounts in the south of Section 4 (**Figure 67b**). In the northern part the seamounts in the rift valley are aligned along the ridge axis. All in all a strong magmatic activity takes place at the rift valley and the western ridge flank. It is also worth noting that there are many seamount clusters or groups. The uplift behavior of the rift shoulders seems to be the same as in Section 3. Where the eastern shoulders show a high uplift, the western shoulders do not and the other way around (**Figure 64**). On average the eastern ridge side is more uplifted. To the south, between the evolving offset and the end of Section 4, the rift valley shows the typical hourglass morphology. The major faults are running subparallel to the rift valley and dip towards it (**Figure 67c**). Where other dipping faults are observed these are located at or near the evolving offsets. In the transition to Section 5 some basin structures occur on the eastern flank (**Figure 64**). Summarizing features are two evolving discontinuities, stronger uplifted eastern ridge flanks, two basin structures and again ridge



parallel faults.

Figure 64: Bathymetric map of Section 4 with prominent structural features such as evolving discontinuities and basins.

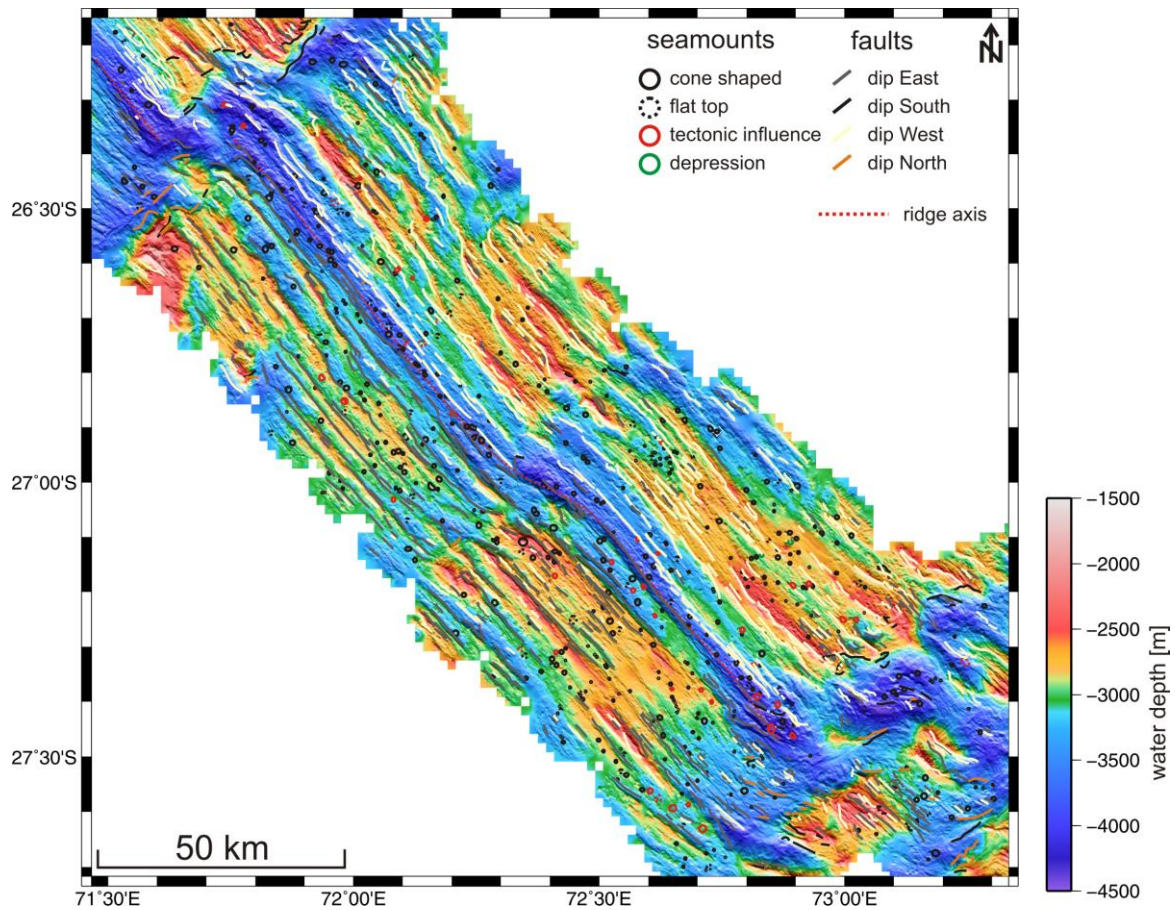


Figure 65: Bathymetric map of Section 4 with structural features like seamounts (circles) and faults (lines).

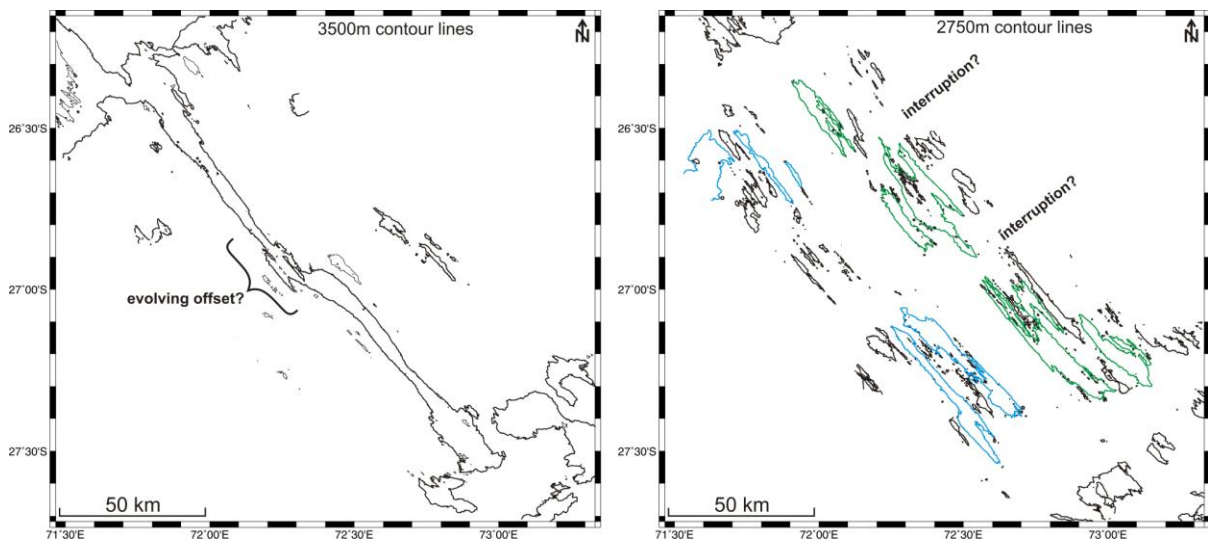
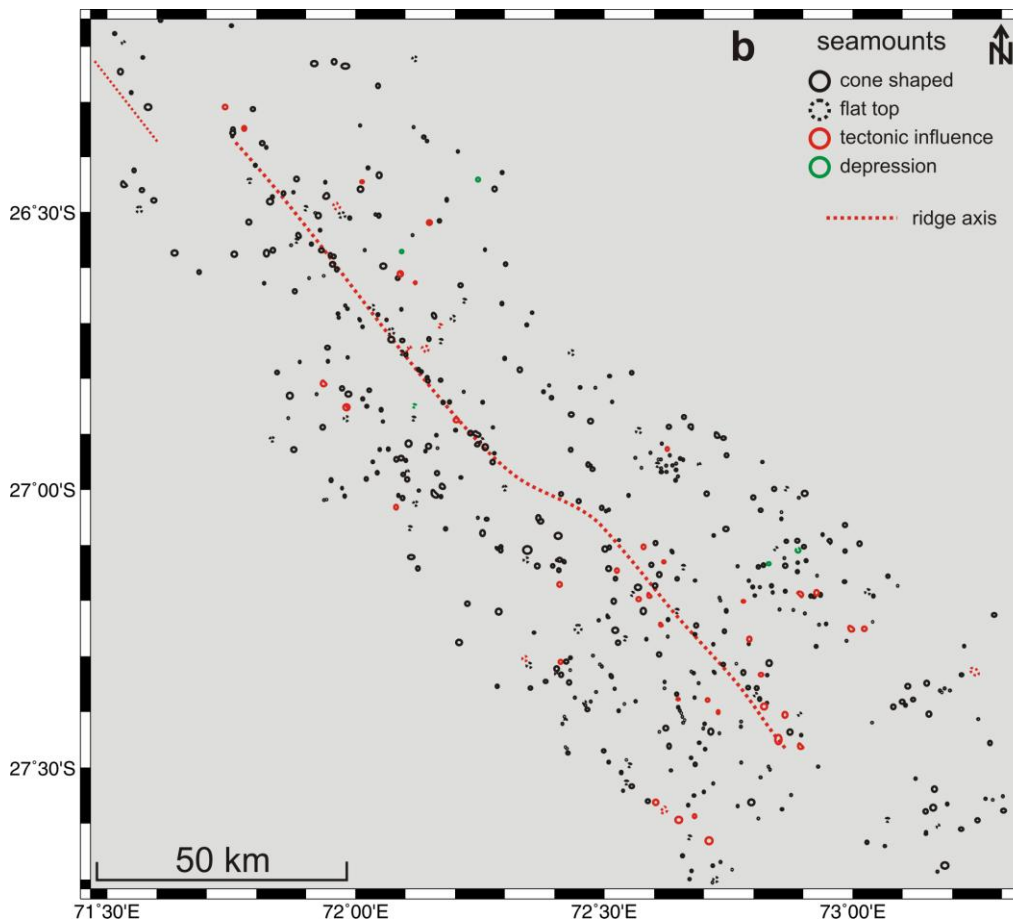
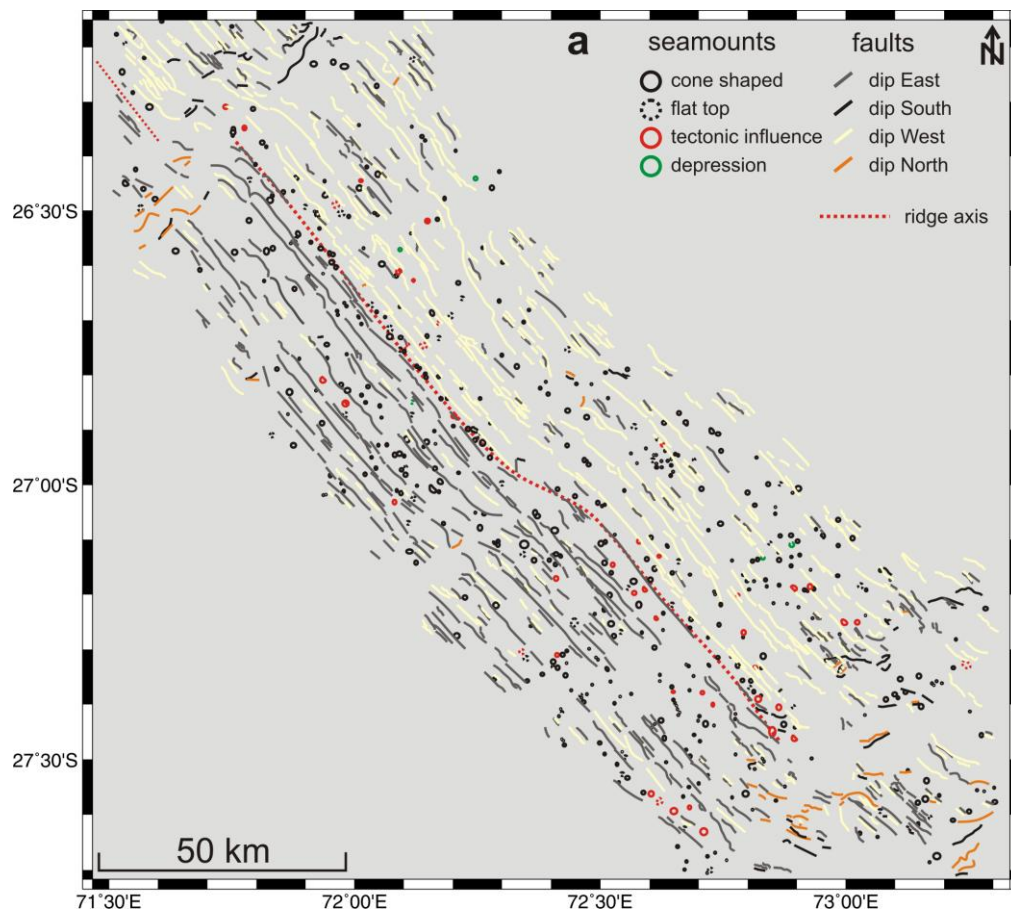


Figure 66: Contour line map of Section 4. On the left side the 3500 m lines which mark the rift valley. On the right side the 2750 m contour lines characterizing the more uplifted eastern flank (green lines) and the areas which are interrupted by evolving discontinuity structures.



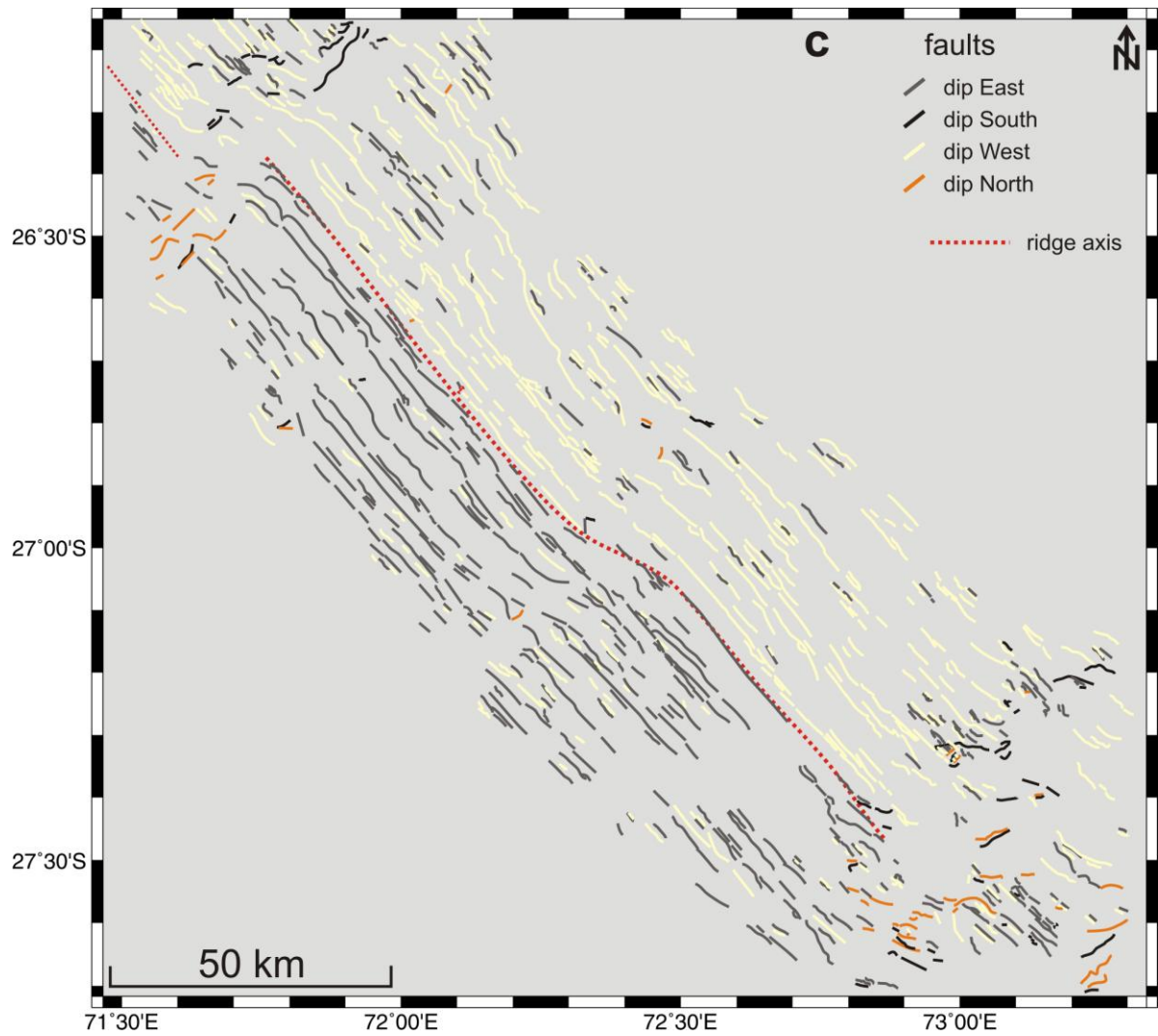


Figure 67: Structural maps of Section 4: **a)** labeled with circles for the seamounts and with lines for the faults; **b)** labeled with circles for the seamounts divided into those who are cone shaped, have a flat top or are tectonically influenced and with green circles for depression structures; **c)** labeled with lines for the faults dipping in different directions.

Working area Section 5 follows at a length of ~36 km between 27°30'S and 27°43'S (**Figure 68**). The section represents the second accommodation zone which means that there is a lack of faults running parallel to the rift valley (**Figure 69**). Besides the east and west dipping faults there are also north and south dipping ones (**Figure 70a & c**). The faults strike between 35° NNE and 135° SE. The course of the rift valley is not clear and not well defined. There is an obvious increase in width at the ends of the rift valley and a narrow middle part. At the center of the section another OCC is located with mullions running perpendicular to the rift valley (**Figure 68**). The OCC is relatively small and it seems that like the small OCC in Section 2 it is in a developing stage. With the given resolution of the bathymetry data no clear line of movement can be seen. Typical for the accommodation zone, only a few seamounts can be found on the older rift shoulders. The few seamounts which have developed in the rift valley are located in the northern part (**Figure 70b**). The deepest point has a water depth of ~4400 m. To the west and east there are some basin structures observed. To sum up the most typical structures for this section are faults running in every direction and a third small, young OCC.

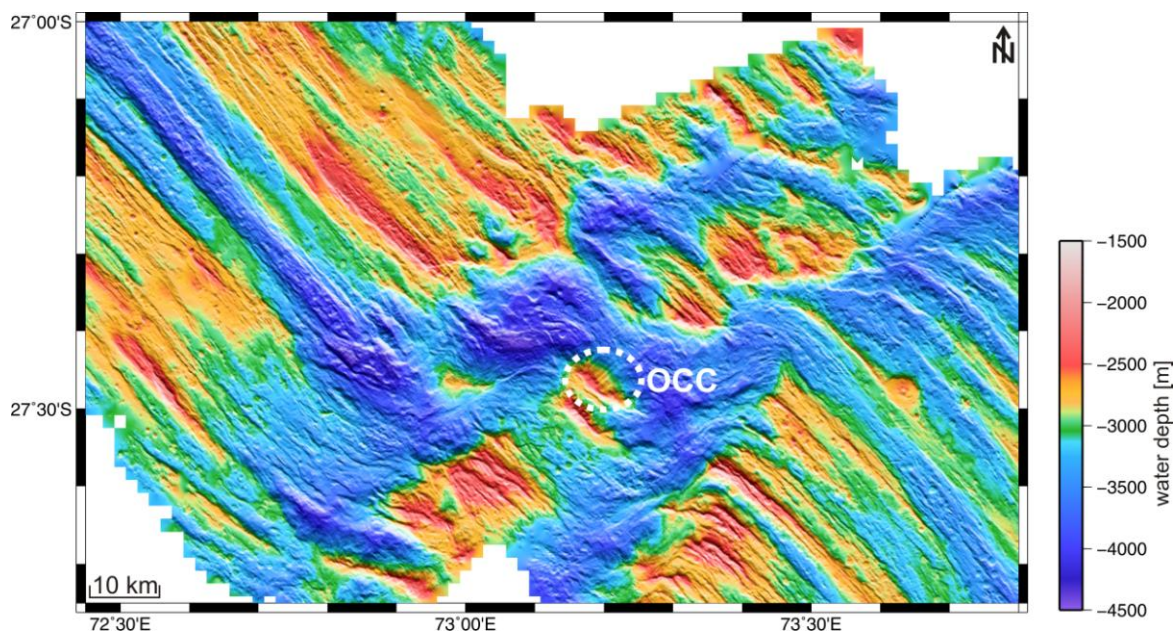


Figure 68: Bathymetric map of Section 5 with a prominent OCC at the center of the section.

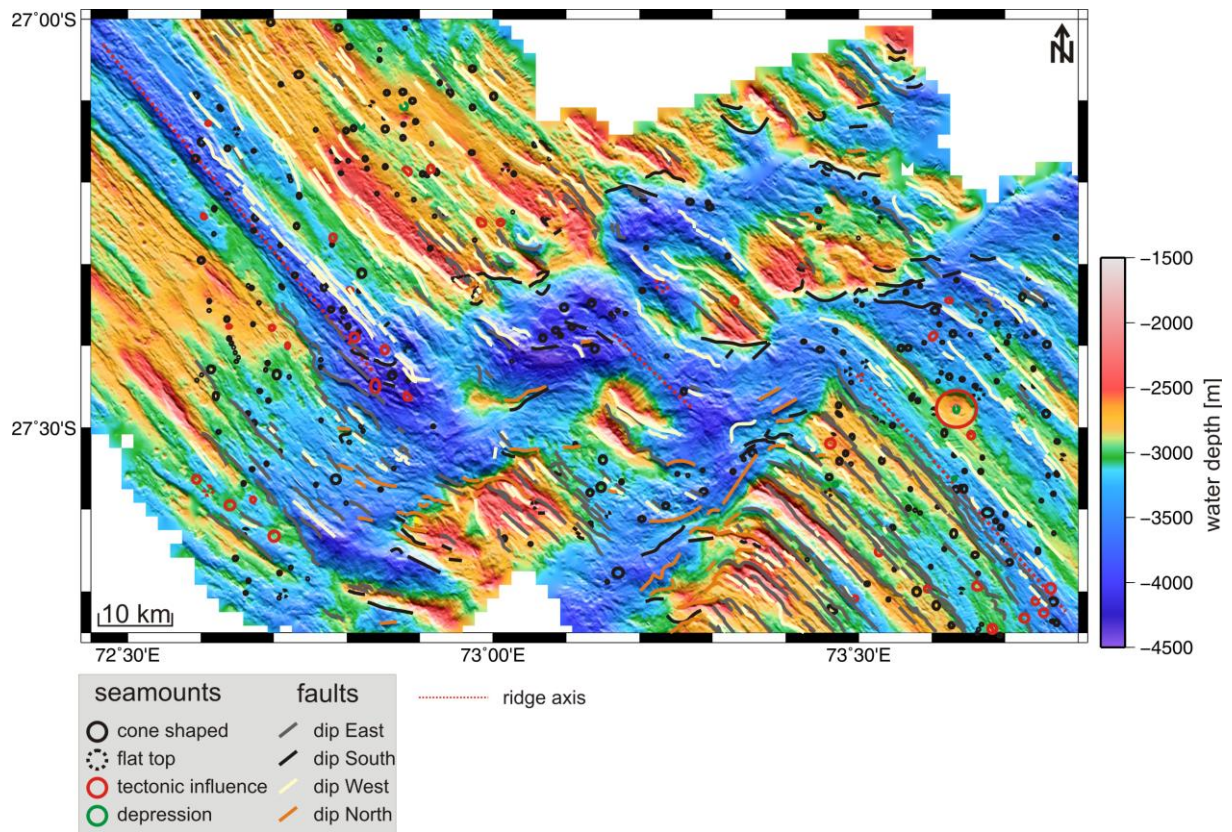
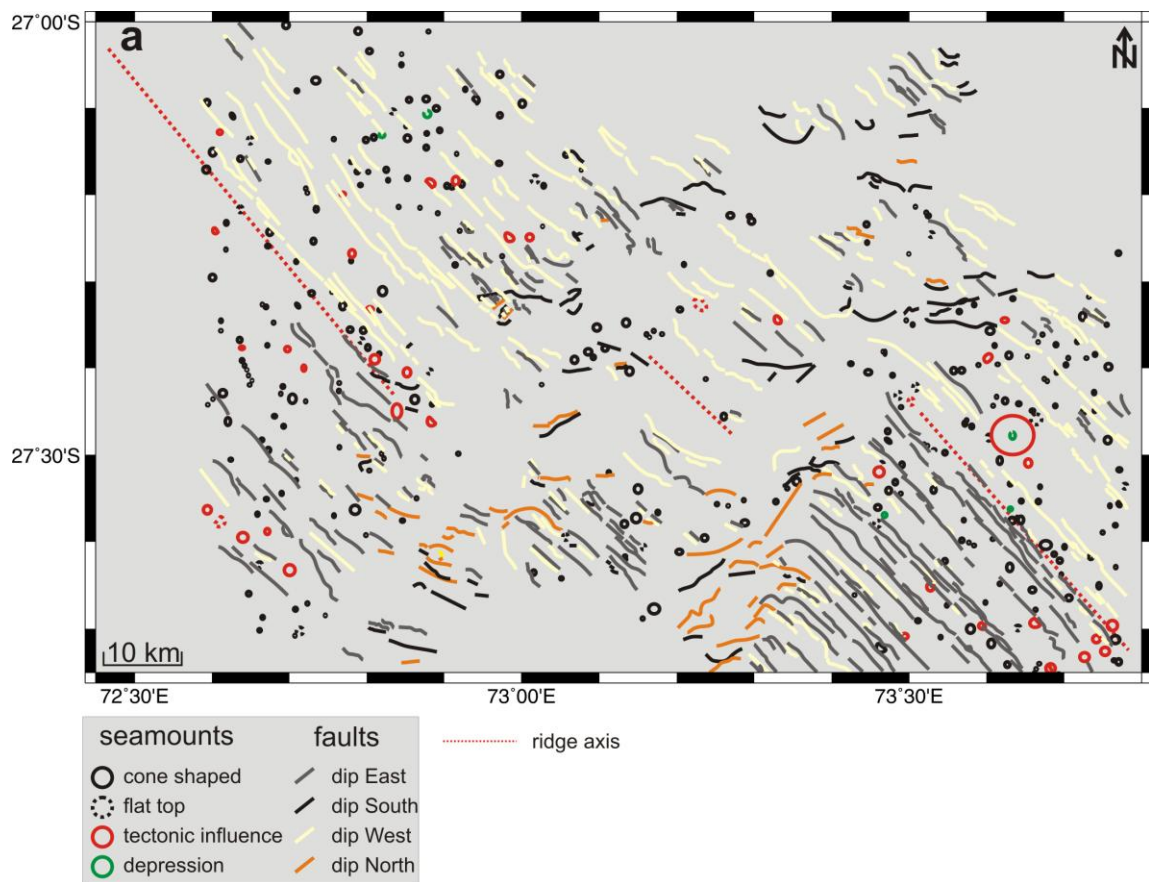


Figure 69: Bathymetric map of Section 5 with structural features like seamounts (circles) and faults (lines).



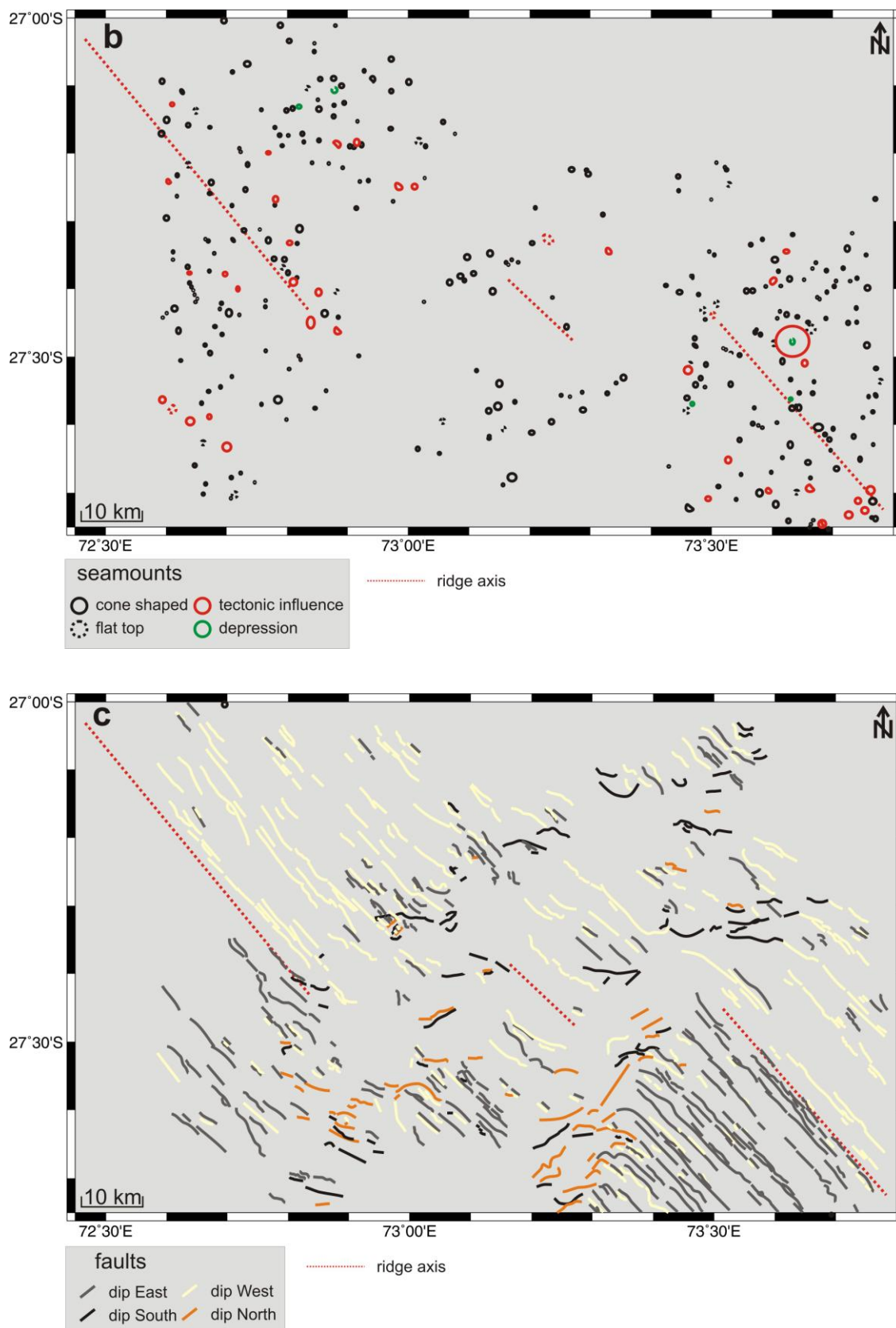


Figure 70: Structural maps of Section 5: a) labeled with circles for the seamounts and with lines for the faults; b) labeled with circles for the seamounts divided into those who are cone shaped, have a flat top or are tectonically influenced and with green circles for depression structures; c) labeled with lines for the faults dipping in different directions.

The southern end of the mapped part of the SEIR between 27°44'S and 28°13'S is represented by working area Section 6 at a length of ~65 km (**Figure 71**). The rift valley is relatively well developed with a width of 4.8 km - 5 km and has an average water depth of 3600 m which increases to the south. This is also an area where again the rift shoulders become thinned and show a bending (**Figure 71** and **Figure 72**). The typical parallelism of the major faults to the rift valley is interrupted there. Possibly like in Section 4 a new offset develops at this place. In the northern part at the boundary to the accommodation zone of Section 5 the rift shoulders bend towards northwest (**Figure 73a & c**). Again the section is characterized by a morphology which looks like an hourglass, shallowest in the middle and deeper at the ends. Many seamounts can be found in the rift valley as well as on the older rift shoulders (**Figure 73b**). On the rift shoulders in the east the seamounts show a cone shape and only a few indications for offsets. On the western ridge flank more seamounts are tectonically influenced. The volcanic activity is concentrated in the vicinity of the rift valley. Two obvious large seamounts are located on faults and the larger one shows a shear movement together with a caldera structure (**Figure 73b**). The larger of these two seamounts with a diameter of ~9-10 km is situated on the western flank (**Figure 73a & b**). The smaller seamount with a diameter of ~6 km is close to the rift valley in the northern area (**Figure 73a & b**). Similar to

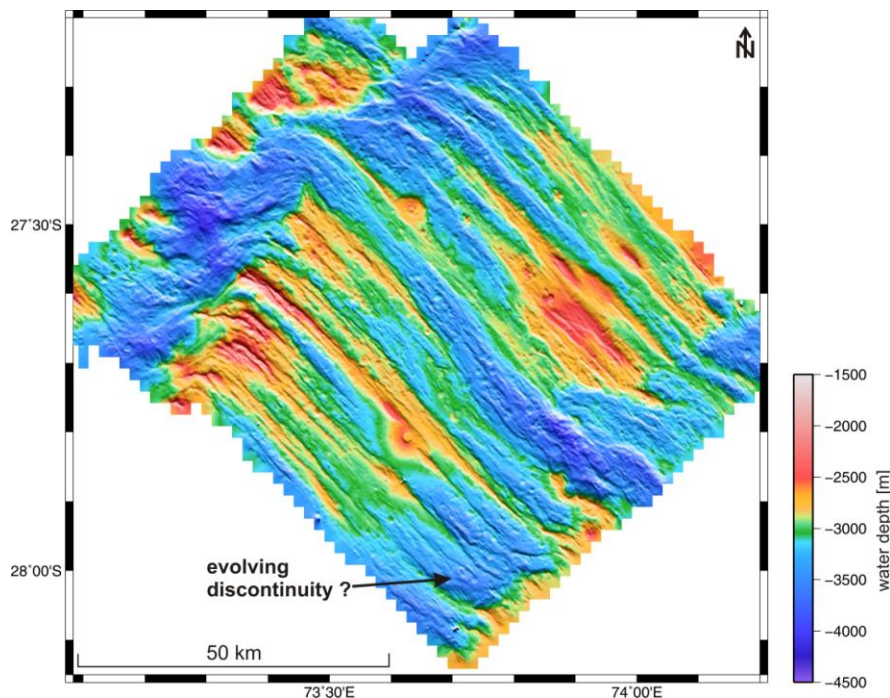


Figure 71: Bathymetric map of Section 6 with an evolving discontinuity structure in the southern part.

Section 3, where the rift shoulders show a higher uplift on the western flank, the rift shoulders on the eastern flank are lower and the other way around (**Figure 74**). In summary, typical features for working area Section 6 are alternating elevated and depressed rift shoulders, two

prominent large seamounts and faults running parallel to the ridge axis.

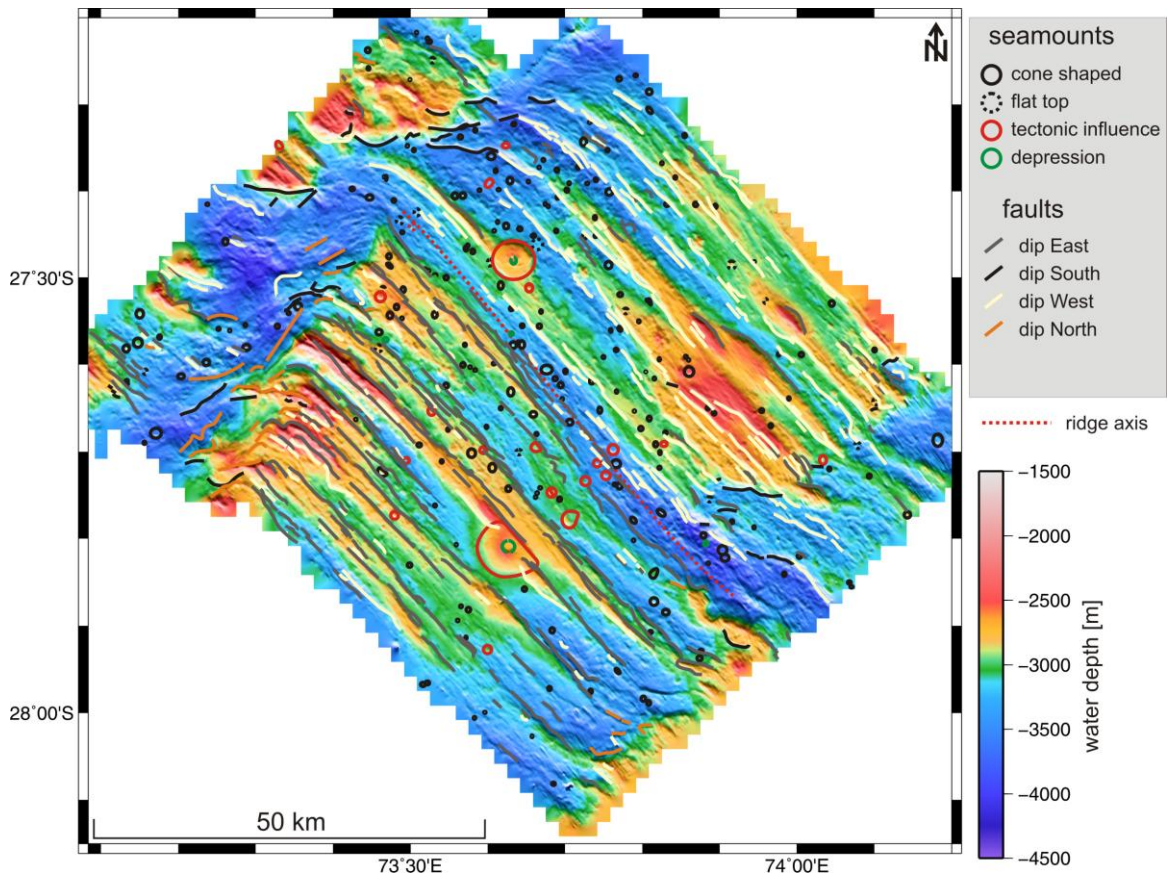
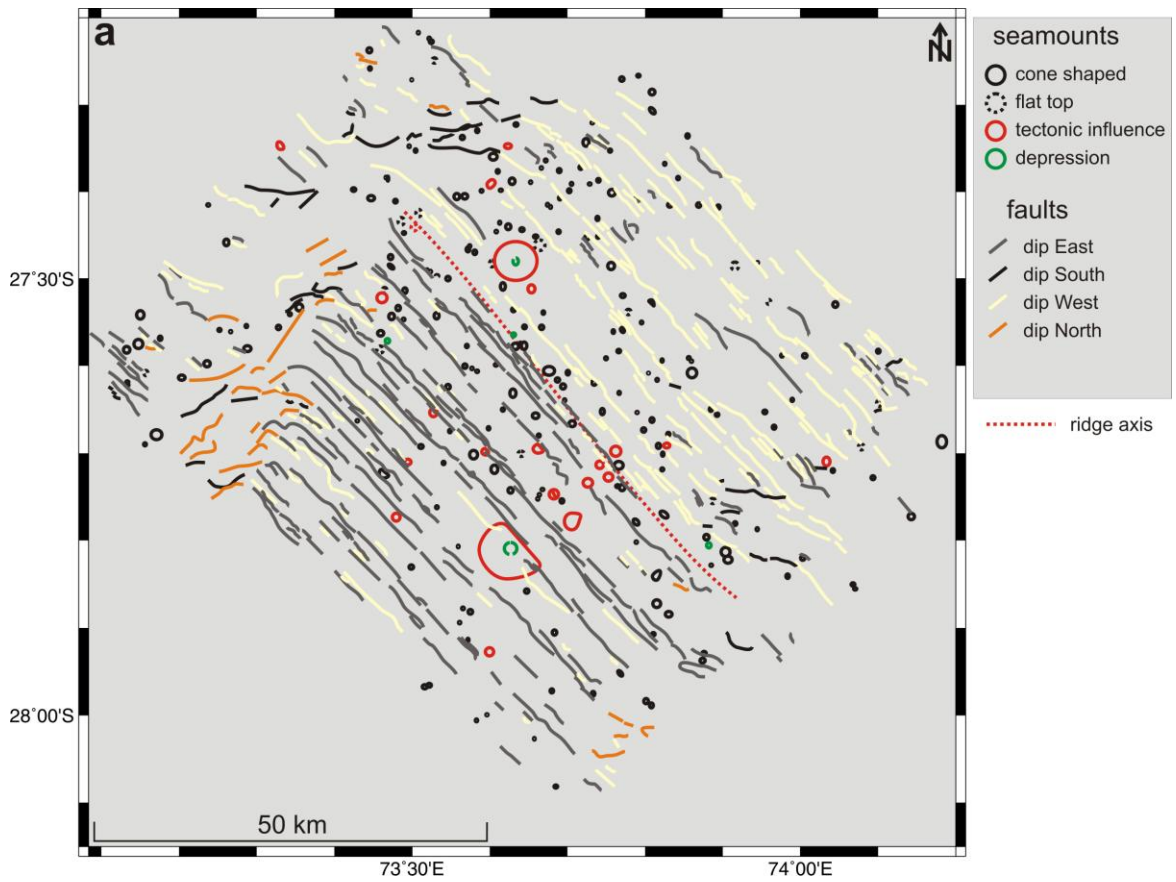


Figure 72: Bathymetric map of Section 6 with structural features like seamounts (circles) and faults (lines).



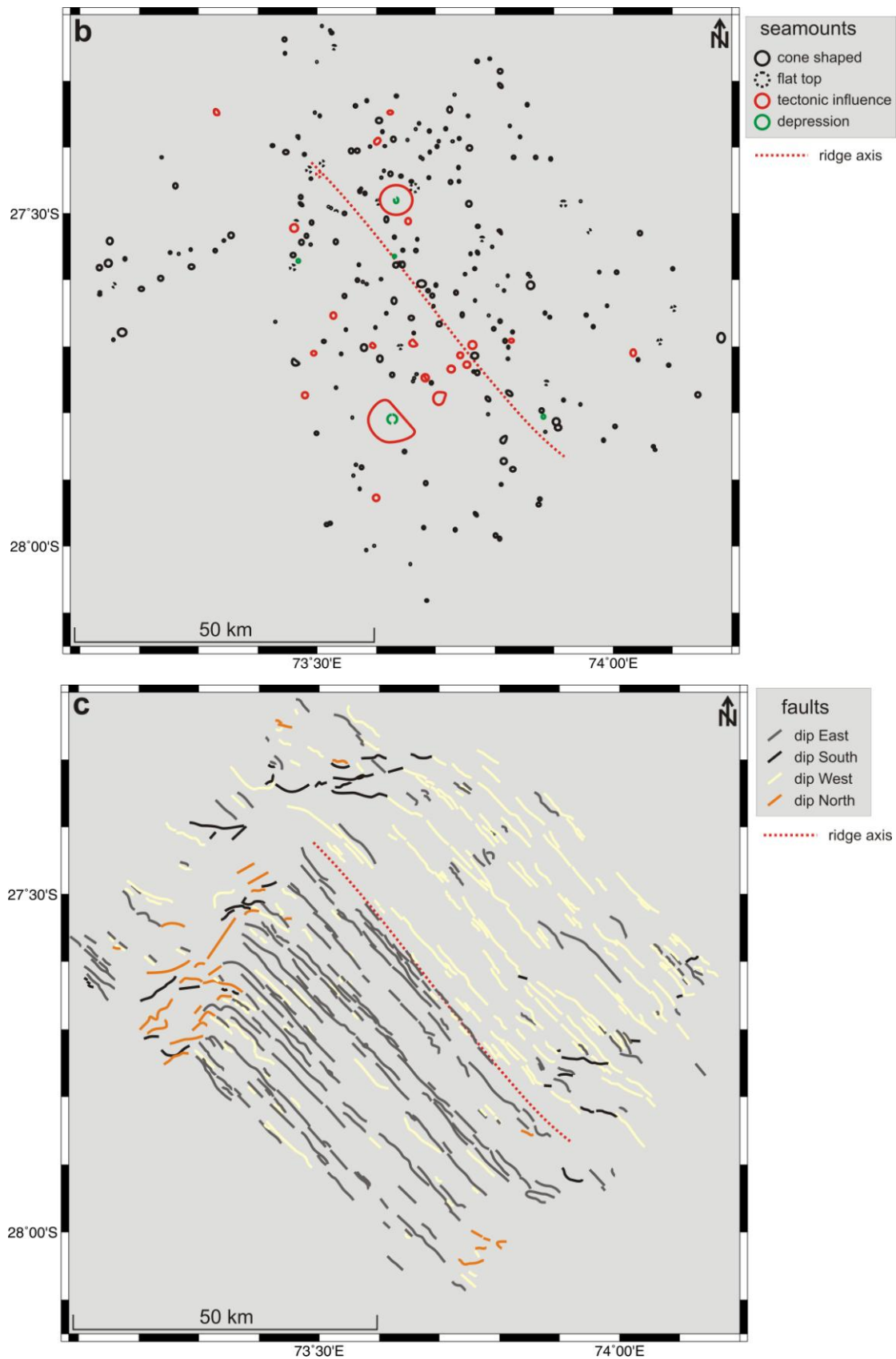


Figure 73: Structural maps of Section 6: **a)** labeled with circles for the seamounts and with lines for the faults; **b)** labeled with circles for the seamounts divided into those who are cone shaped, have a flat top or are tectonically influenced and with green circles for depression structures; **c)** labeled with lines for the faults dipping in different directions.

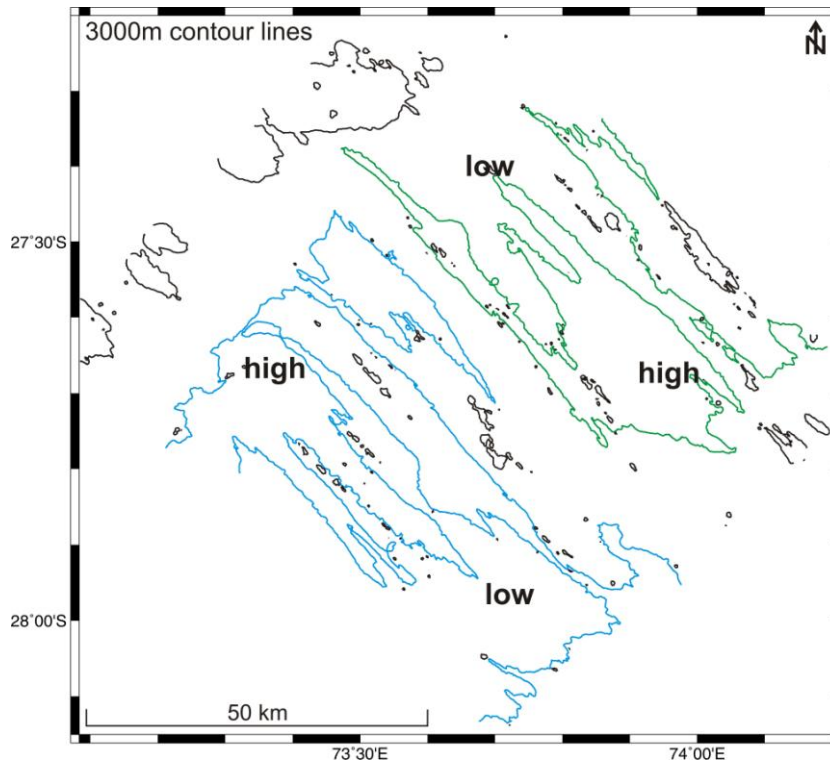


Figure 74: 3000 m contour lines of Section 6 which emphasize the more uplifted ridge flanks and the corresponding lower sides. The green lines represent the eastern ridge flank and the blue lines the western one.

4.2.2) Magnetic observations

Along the intermediate spreading SEIR with 5.7 cm/a full spreading rate on average, 64 magnetic profiles were measured in total. The position and numbering of the individual profiles can be found in **Figure 75**. The profiles strike 50° E perpendicular to the spreading axis. In general the intermediate spreading ridge is characterized by an asymmetric spreading behavior (**Figure 76**). The eastern ridge flank spreads faster in the northern and central part of the surveyed area. That changes to the south where the spreading velocities on the eastern flank decreases and the western ridge side becomes faster. In each case within the area of the discontinuities the individual spreading velocities of the profiles increase. This also applies to the areas of the two probably evolving discontinuities.

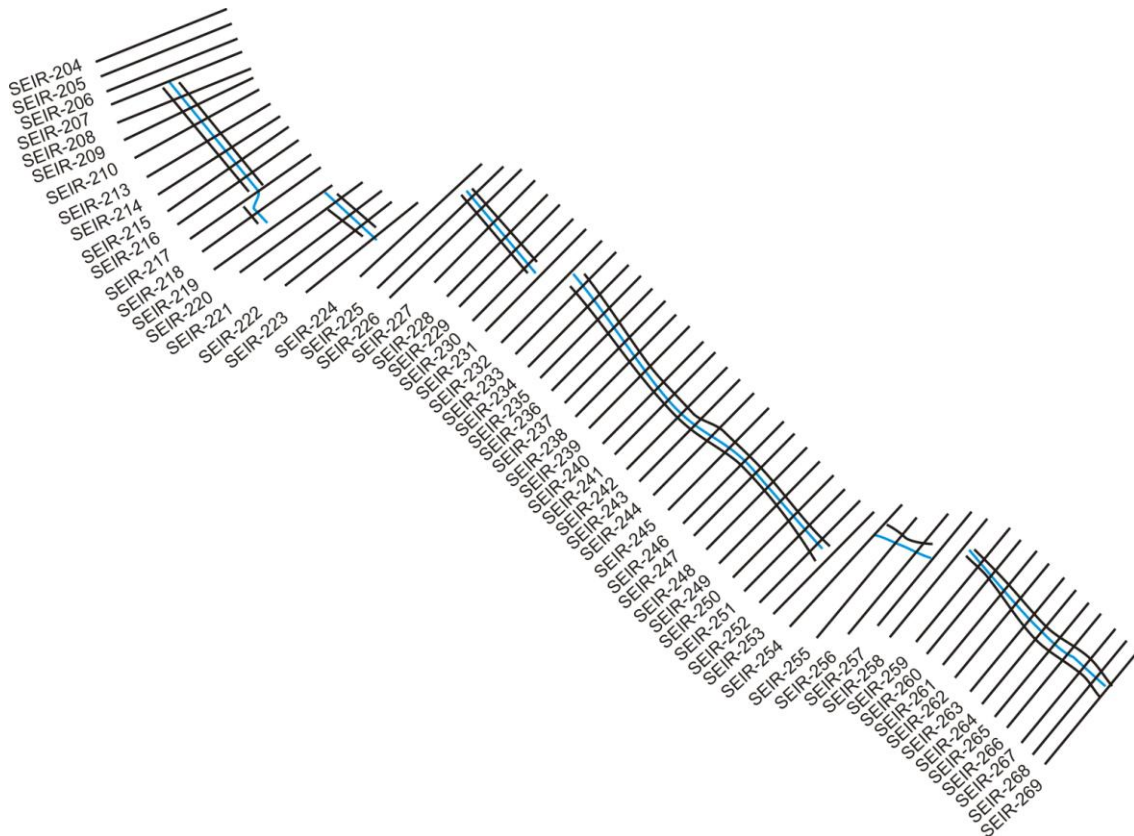


Figure 75: Schematic sketch of the profiles along the Southeast Indian Ridge running from northwest to southeast.

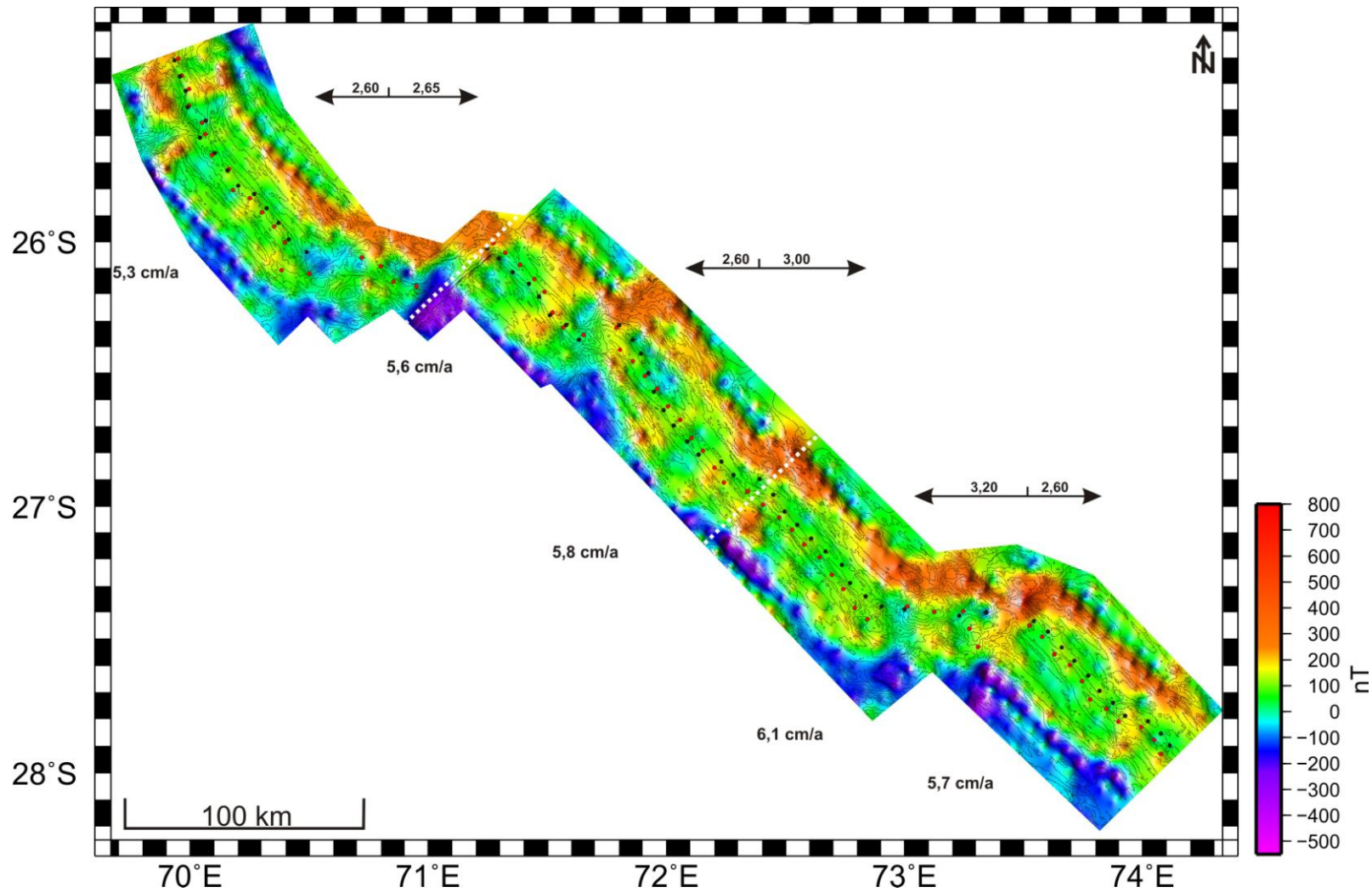


Figure 76: Magnetic map of the northern SEIR including the full spreading rates for the Sections 1-6 on the left side and the model results for each ridge flank on the right side. The black circles mark the center of magnetic Anomaly 1 and the red circles the ridge axis. The map is superimposed with the bathymetric contour lines every 500 m.

The first profiles 204 to 219 south of the RTJ have an average full spreading velocity of 5.3 cm/a and correspond to the working area Section 1. Except for profile 208 which is situated directly within the RTJ all profiles show the boundaries of Anomaly 1 (0-0.78 Ma). The complete Jaramillo event on both sides was mapped within the profiles 204, 206, 207, 213-216. The remaining profiles only cover the Jaramillo event on one ridge flank. All profiles in that area have maximum nT values of around +/- 400 nT. The bathymetric minimum is located on the western side of the center of Anomaly 1. For most profiles the center of Anomaly 1 and the bathymetric minimum correlate very well or they just have a distance of around 2 km. On profile 219 the distance of the center of Anomaly 1 and the bathymetric minimum is highest because the profile is located in the direct vicinity of the large OCC. From the data an asymmetric spreading behavior was deduced where the western flank spreads with 2.60 cm/a and the eastern flank with 2.65 cm/a (**Figure 77**, Model 1).

Section 2 consisting of the profiles 220-225 is defined as an accommodation zone. For the spreading rate calculation the boundaries of Anomaly 1 are necessary. In that case the boundaries could not be clearly identified, therefore no spreading rates can be given. The nT values range about +/- 400 nT. Profile 225 is defined by the boundary of Anomaly 1 on the western flank and the Jaramillo event.

Section 3 with the profiles 226 to 232 is defined by an average full spreading rate of 5.6 cm/a. In all profiles the boundary of Anomaly 1 was localized but only profile 226 also covers the Jaramillo event on both flanks. More clearly the center of magnetic Anomaly 1 and the bathymetric minimum lie apart with the bathymetric minimum located east of the center of magnetic Anomaly 1. Profiles 266 and 231 (**Figure 78**) show indications for the Central Anomaly Magnetic High (CAMH). The former profile also has a double Jaramillo event on its western flank. It is located directly beneath the strike-slip fault. For the spreading behavior in this part an asymmetric spreading can be seen like before but in this case the eastern flank spreads faster with 3.00 cm/a than the western flank with 2.60 cm/a (**Figure 77**, Model 2).

Profiles 233-253 define Section 4 with an average full spreading rate of 5.8 cm/a. There individual nT values with a maximum of +500 nT are reached. Except for profile 241, both boundaries of Anomaly 1 can be observed on all profiles. In addition the profiles 242, 243, 246-249 cover the Jaramillo event on both flanks. A double Jaramillo event can be found in profile 234 which is located south of the third discontinuity which separates Sections 3 and 4.

On profile 247 another Central Anomaly Magnetic High was identified (**Figure 79**). In the area of the first northern evolving discontinuity a change in the position of the bathymetric minimum and the center of magnetic Anomaly 1 takes place. North of this discontinuity the bathymetric minimum is located west of the center of magnetic Anomaly 1 and to the south the bathymetric minimum changes its position to the east. Also at the segment ends the distance between them increases. Profiles 233 to 244 are characterized by an asymmetric full spreading with 2.60 cm/a spreading to the west and 3.00 cm/a to the east (**Figure 77**, Model 2). Profiles 245 up to 253 spread faster to the western side with 3.20 cm/a and slower to the east with 2.60 cm/a (**Figure 77**, Model 3). An exception are the profiles 236-238 which show also an asymmetric full spreading but with 2.50 cm/a to the west and 3.70 cm/a to the east (**Figure 77**, Model 2). These latter profiles are located north of the first evolving discontinuity and the highest spreading values for the eastern ridge flank are reached.

A further accommodation zone covered by profiles 254 to 258 is defined by a full spreading rate of 6.1 cm/a. Some caution is necessary with respect to this value because only three profiles (254, 256 and 257) show the boundaries of Anomaly 1 and the Jaramillo event and thus can be used for the spreading rate calculations. At the beginning and end of this accommodation zone high full spreading rates are observed. The asymmetric spreading continues with 3.20 cm/a to the west and 2.60 cm/a to the east (**Figure 77**, Model 3). One exception is profile 254 with 3.30 cm/a to the west and 3.00 cm/a to the east (**Figure 77**, Model 3). A +700 nT spike was measured on profile 258 at the eastern ridge flank.

Section 6 with the profiles 259-269 has an average full spreading rate of 5.7 cm/a. As before the spreading behavior still remains asymmetric with 3.20 cm/a to the west and 2.60 cm/a to the east (**Figure 77**, Model 3). With the exception of the last three profiles both boundaries of Anomaly 1 and the Jaramillo event could be identified.

Summarizing the spreading behavior along the SEIR with **Figure 80** and **Figure 76** it becomes clear that, with exception of the RTJ, there is no conspicuous increase or decrease in the spreading rates from 70°E to 74°E. A slight increase in spreading rates can be seen at the discontinuity structures and the two evolving discontinuities. The interruptions at Sections 2 and 5 result from the fact that in these areas not the complete Anomaly 1 was measured.

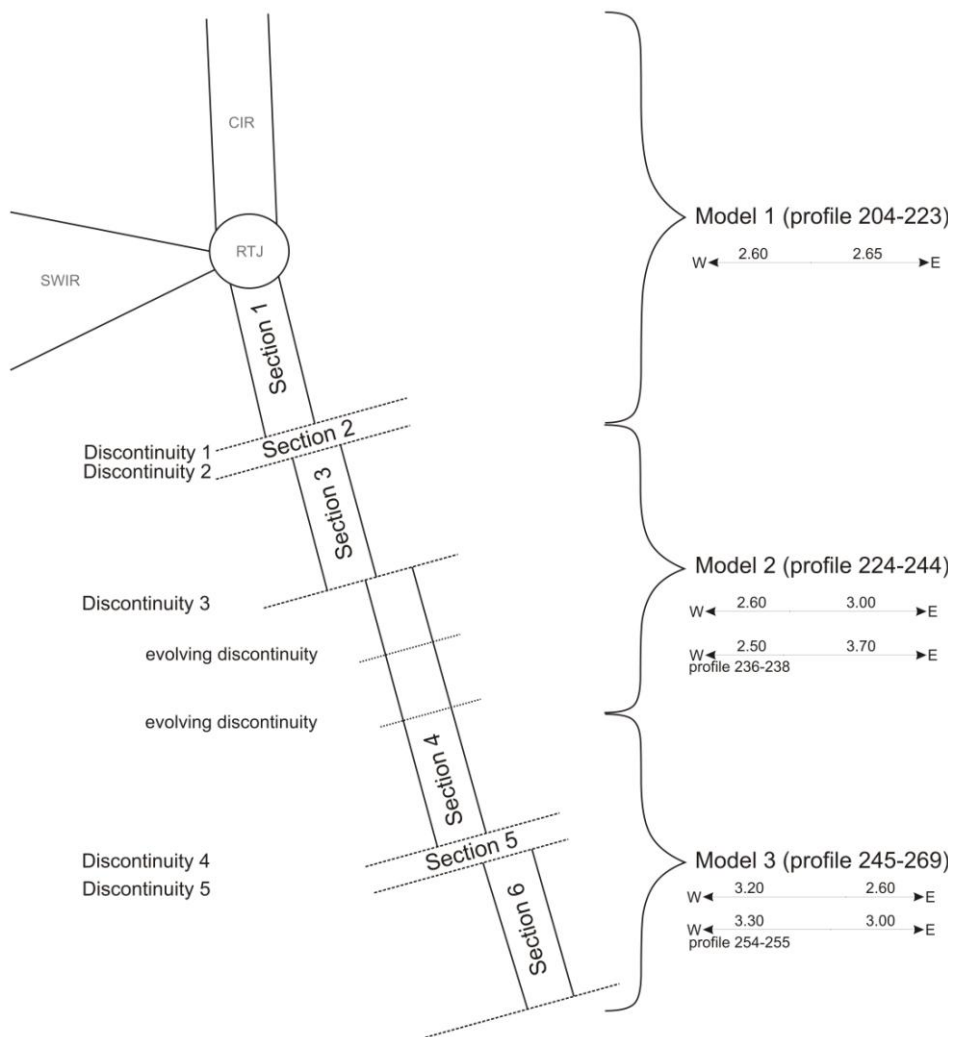


Figure 77: Schematic sketch of the SEIR with the working areas and discontinuities on the left side and the magnetic modeling results with different full spreading rates in cm/a on the right side.

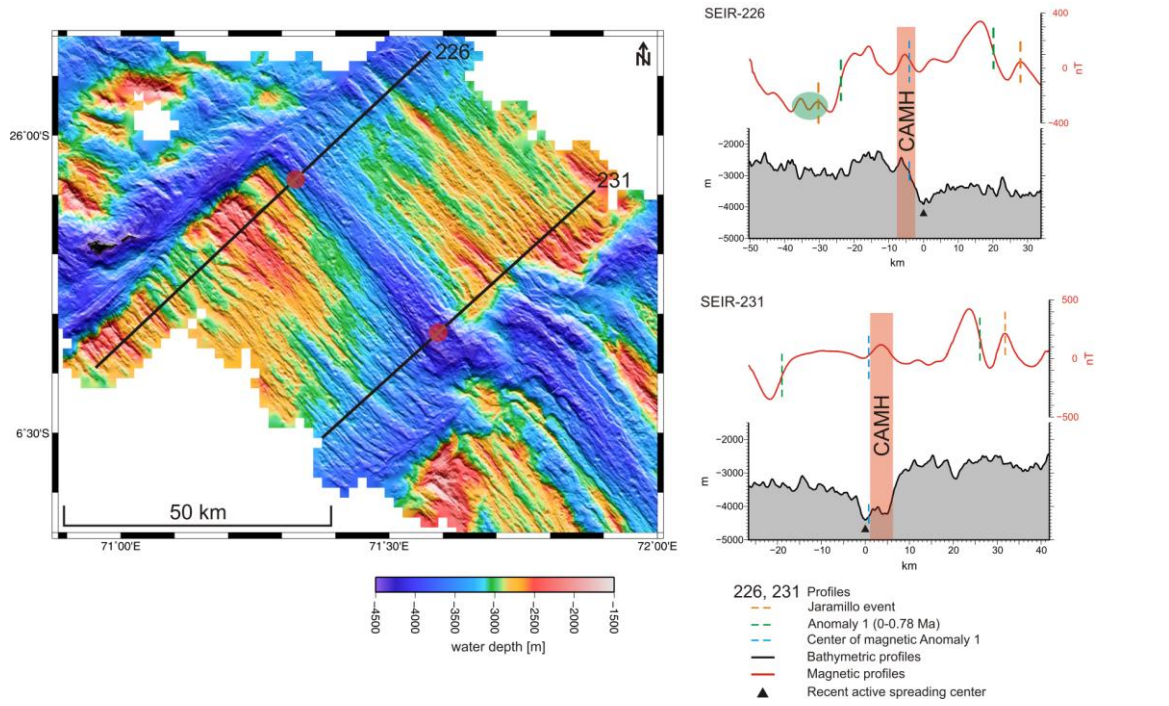


Figure 78: Bathymetric map of Section 3 and two cross profiles containing bathymetry (grey) and magnetic (red) data. The red transparent zone (circle and box) marks the Central Anomaly Magnetic High (CAMH) and the green transparent circle the double Jaramillo event.

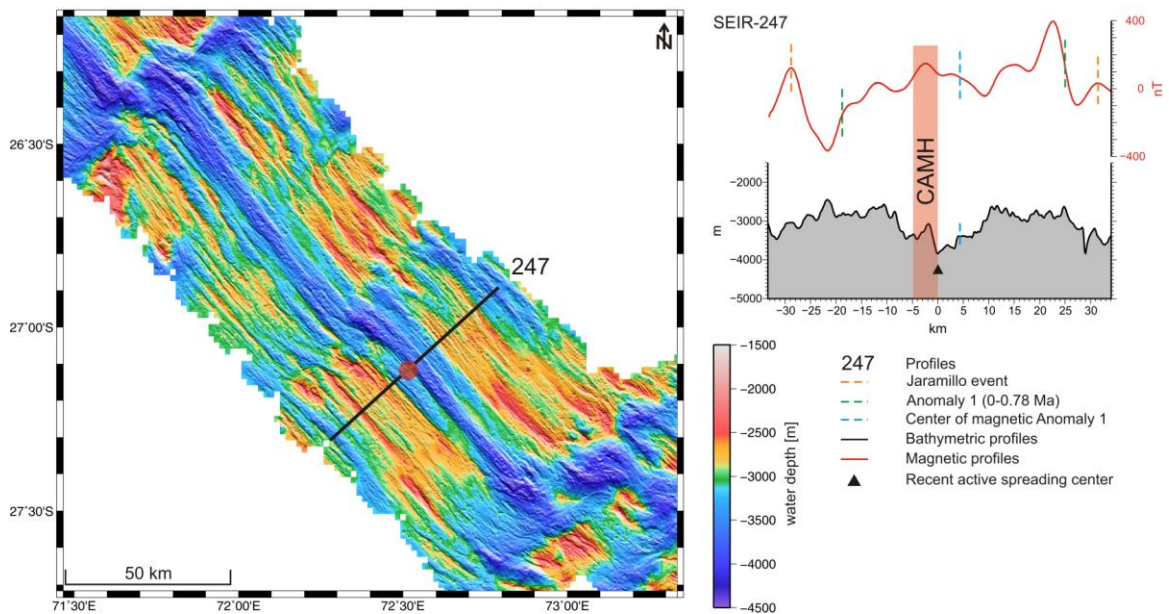


Figure 79: Bathymetric map of Section 4 and one cross profile containing bathymetry (grey) and magnetic (red) data. The red transparent zone (circle and box) marks the Central Anomaly Magnetic High (CAMH).

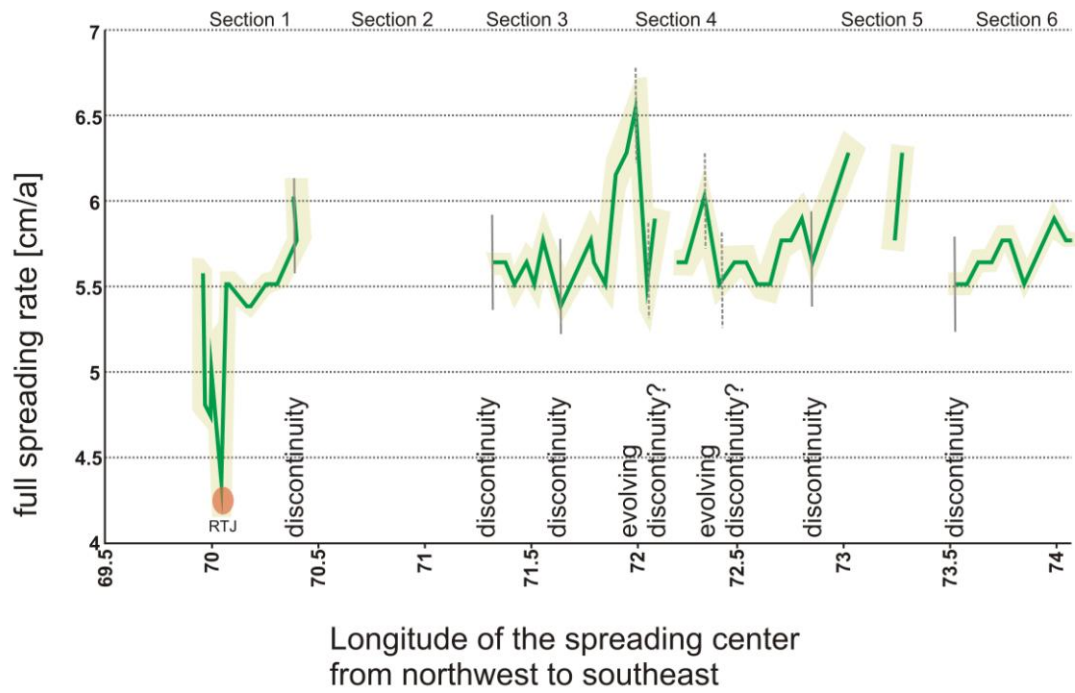


Figure 80: Full spreading rates along the SEIR from northwest to southeast with the location of the discontinuities and sections. Transparent green area marks the estimated error according to **Chapter 3.3**.

4.3) Hydrothermal vent field Sonne

The inactive basalt hosted hydrothermal vent field named Sonne is located at 69°14'E and 23°23'S in a water depth of about 2820 m and rises ~339 m above the ridge axis. It occurs in the central part of the working area Meso on an elongated ridge segment that extends for about 3.5 km and rises between 300 and 350 m above the western valley floor. The distance to the morphologic valley axis is 2400 m. A full spreading rate was determined at 5.0 cm/a and the distance to the center of magnetic Anomaly 1 is 5400 m. On the basis of half spreading velocities (2.5 cm/a) and the distance to the morphological spreading axis (2400 m) an average age of the bedrocks around the hydrothermal field could be estimated with ~ 96, 000 years.

$$\begin{array}{ll} \text{Distance 2400 m} & \frac{1a}{2.5cm} * 240000 \text{ cm} = x \\ \text{Half spreading rate 2.5 cm/a} & x = 96000 \text{ a} \end{array}$$

This does not necessarily reflect the age of the inactive hydrothermal field but it may constrain the period of its formation. In terms of morphology, the Sonne field is located in an area of regional morphological uplift with the formation of axis-parallel elevated ridges within the central valley. Neovolcanic ridges and seamounts imply enhanced magmatic and volcanic activity in this area. The western neovolcanic ridge hosted the vent field in its central part. Noteworthy are two prominent fault zones in the vicinity running subparallel to the valley axis. Investigations with cameras and rock samples showed that the northern part of the hydrothermal vent field is characterized by sheet flow lavas and in the direction of the rift valley axis the pillow basalts often show fractures (SCHWARZ-SCHAMPERA & Shipboard Scientific Party, 2012). The more massive, higher uplifted eastern neovolcanic ridge displays no clear normal faults or shear movements which led to the suggestion that there is probably an asymmetric magma lens beneath (**Figure 81**, schematic sketch).

As summarized in **Table 1** the Sonne hydrothermal vent field is defined by a water depth of 2820 m, is situated 339 m above the ridge axis, has a distance to the ridge axis of 2400 m, and an approximately age of the bedrocks of 96,000 a. It is located in the central part of the working area on a neovolcanic ridge. The full spreading rate at this location is relatively high with 5.0 cm/a. **Figure 82** show the inactivity of the Sonne hydrothermal vent field because no chimney structures are observed, instead only hydrothermally influenced sediments and

sulfide talus are found. An impression of a prominent fault zone which is characteristically for the vent field can be seen in **Figure 83**. Here the fault must be inactive for a while because fine sediment accumulations are observed and a younger magmatic event has taken place expressed in the round shaped pillow basalt directly at the rim of the fault.

water depth	height above ridge axis	position	distance to the spreading axis	full spreading rate	distance to the center of magnetic Anomaly 1	approx. age of the bedrocks	lava type
2820 m	~339 m	central part, on a neovolcanic ridge	~2400 m	5.0 cm/a	~5400 m	96,000 a	sheet flow

Table 1: Summarizing features which are characteristically for the Sonne HTF.

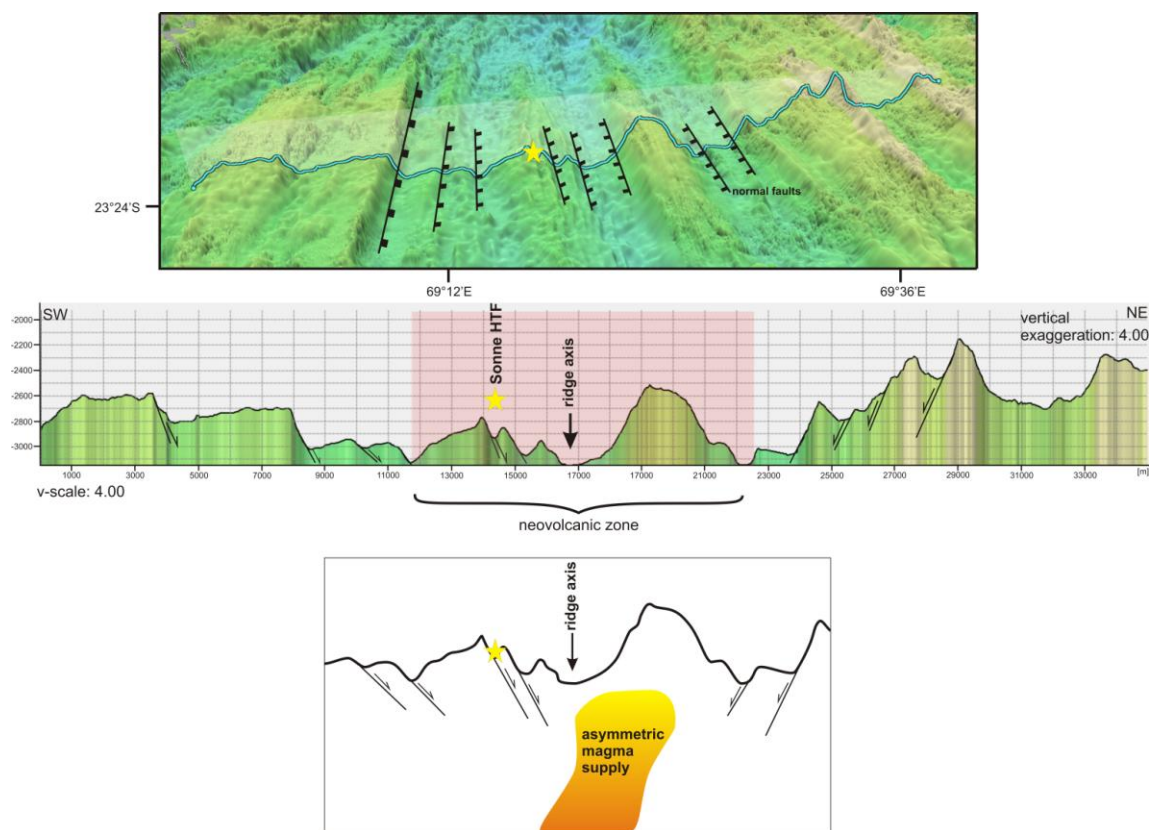


Figure 81: Top: Bathymetric map of the Sonne hydrothermal vent field. Middle: A cross section along the blue line in the top panel. Bottom: Schematic sketch of the Sonne vent field and a probably asymmetric magma supply.

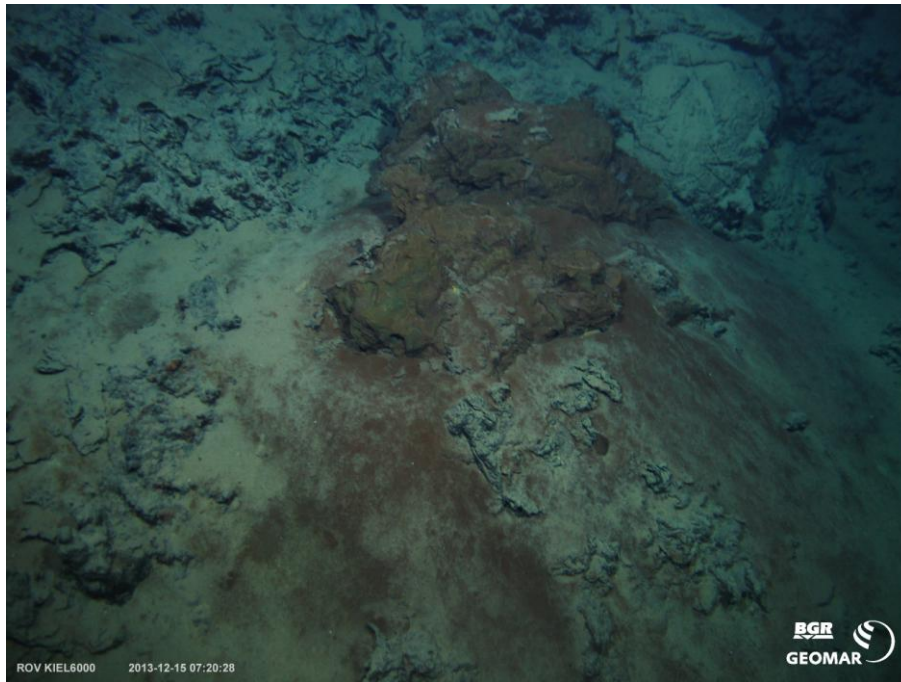


Figure 82: Hydrothermally influenced sediments and sulfide relicts of the inactive hydrothermal vent field Sonne observed with a remotely operated vehicle (ROV) 6000 Kiel (SCHWARZ-SCHAMPERA & Shipboard Scientific Party, 2014).

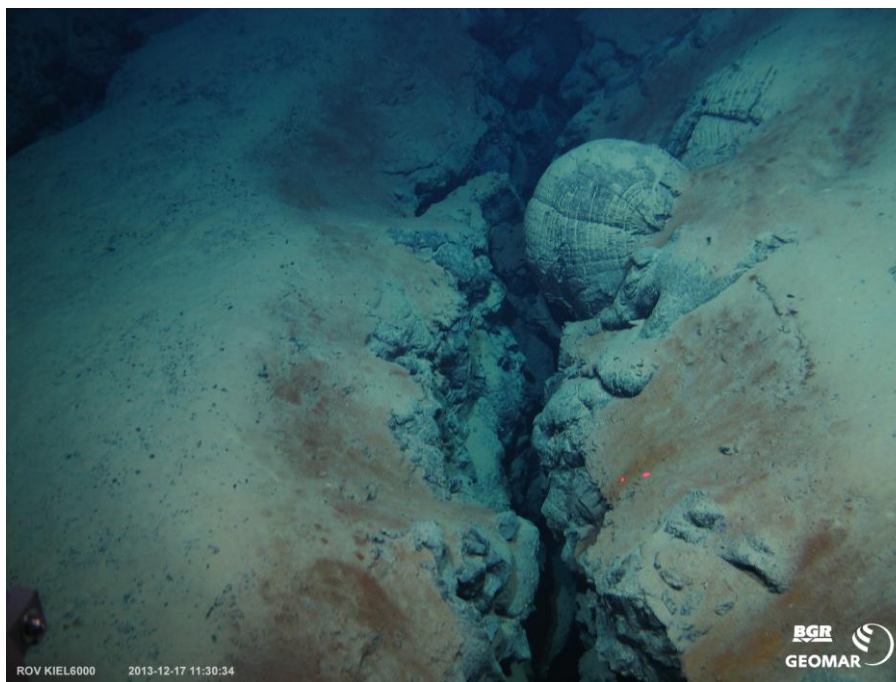


Figure 83: A fault structure at the inactive hydrothermal vent field Sonne. The large pillow basalt leads to conclude that there was a magmatic event younger than the tectonic event which causes the development of the fault. This underwater photo was observed with a remotely operated vehicle (ROV) 6000 Kiel (SCHWARZ-SCHAMPERA & Shipboard Scientific Party, 2014).

4.4) Hydrothermal vent field Edmond

The active basalt hosted Edmond hydrothermal vent field (**Figure 84**) is located at 69°35'E and 23°52'S in a water depth of ~3290 m. It is situated about 5200 m away from the well expressed valley axis, 868 m above the axis and on the steeper eastern side. In the direct



Figure 84: Chimney structure and shrimps at the active hydrothermal vent field Edmond. The photo was observed with a remotely operated vehicle (ROV) 6000 from Kiel (SCHWARZ-SCHAMPERA & Shipboard Scientific Party, 2014).

vicinity of the field at the eastern flank there is a depression and young neovolcanic ridges showing sigmoidal orientation and suggesting the ongoing evolution of a discontinuity and tectonic activity. That prefers the evolution of pathways for the hydrothermal fluids.

Additionally, the pull-apart basin north of Edmond is a hint for extensional movement and the dominance of tectonic activity. With a look at the whole section the hydrothermal vent field is located in the northern part of the ridge segment, close to an evolving discontinuity and on the inside corner. From the magnetic dataset full spreading rates of ~5 cm/a are calculated and the distance between the field and the center of magnetic Anomaly 1 is approximately 100 m. A calculation of the bedrock ages around the hydrothermal vent field (compare **Chapter 4.3**) gives an age of ~208, 000 years. From dredging results basalts as well as gabbros have been recovered (SCHWARZ-SCHAMPERA & Shipboard Scientific Party, 2014) which lead conclude that there must be a fault structure or another mechanism which causes the gabbros to be exhumed at the seafloor. During the research cruise INDEX2013 fluid temperatures of +418°C were measured out of a chimney of massive copper ore (SCHWARZ-SCHAMPERA & Shipboard Scientific Party, 2014). The sulfides have a copper rich composition. Edmond

represents a structurally controlled vent field because eight different strike directions, between 10 and 170 degrees, of the major faults in the vicinity of the field are observed (**Figure 85**). At least two fault structures striking between 60° and 65° northeast influence the hydrothermal vent field as pointed out in **Figure 85**. Video observations during INDEX2013 showed that the actual outflow of hydrothermal fluids takes place at one single chimney complex with a 29 m high chimney. Approximately 1.5 km away from Edmond in the northeast the inactive vent site Gauss was found in a water depth of ~3052 m (**Figure 85**). It has a distance to the center of magnetic Anomaly 1 of ~1005 m and rises 1100 m above the rift axis. With a spreading rate of ~5 cm/a and a distance of ~6500 m to the valley axis the average age for the bedrocks is calculated at 260,000 years. The field is copper rich as well and defined by an oxidation layer of a few centimeters (SCHWARZ-SCHAMPERA & Shipboard Scientific Party, 2014). High concentrations of amorphous silicic acid are responsible for a good preservation of the complexes. South of these two locations another inactive field named Score (Seafloor Confirmed ORE) was found during INDEX2013. It is located ~1.2 km southeast of Edmond and has a lateral extension of ~200 m. The short distance of those three locations led to conclude that it is one large hydrothermal vent field (named Edmond) with three localized outflows at the seafloor, two of them inactive. During a detailed magnetic survey in 2012 a clear decrease in the magnetic values right above the hydrothermal vent field was measured. This behavior will be explained and modeled in more detail in **Chapter 5.6**. To summarize the characteristics for the Edmond hydrothermal vent field (**Table 2**), it is located in a water depth of 3290 m, at the northern end of the working area in the vicinity of an evolving discontinuity on the steeper eastern ridge shoulder. The hydrothermal vent field lies approximately 868 m above the ridge axis and in a distance of 5.2 km. With 5.0 cm/a the full spreading rate is again relatively high and the distance to the center of magnetic Anomaly 1 is just 100 m. It is characterized by sheet flows and the bedrocks have an age of approximately 208,000 a.

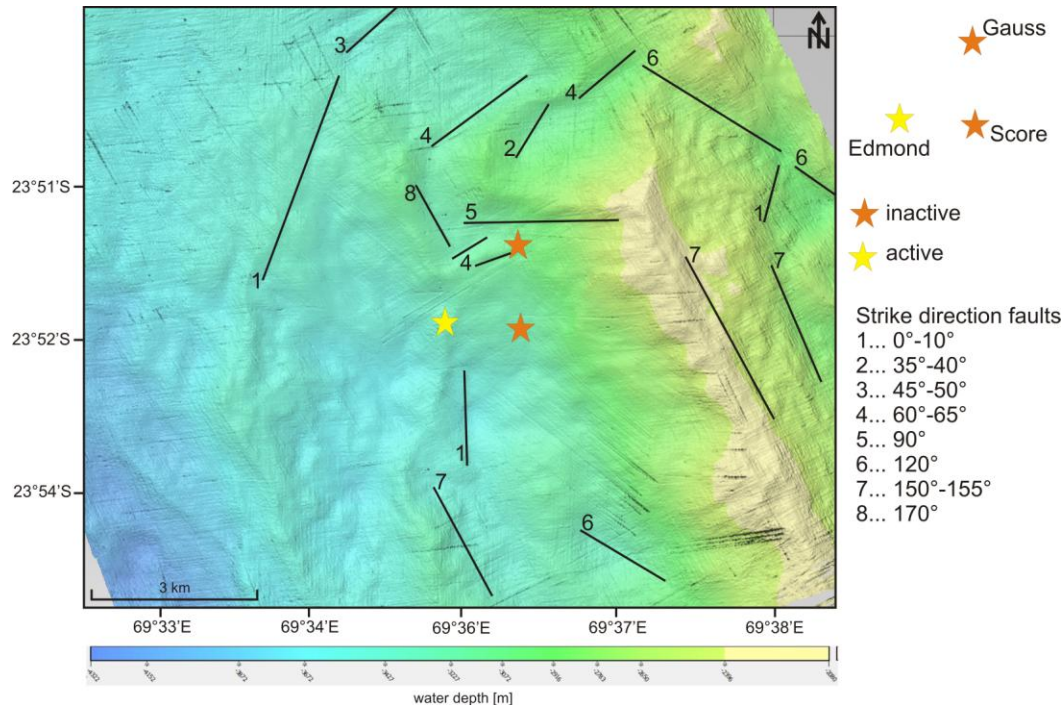


Figure 85: Detailed bathymetric map of Edmond, Gauss and Score (labeled with stars). The lines show the main faults with their corresponding strike directions.

water depth	height above ridge axis	position	distance to the spreading axis	full spreading rate	distance to the center of magnetic Anomaly 1	approx. age of the bedrocks	lava type
3290 m	~868 m	northern end, steeper eastern flank, vicinity of an evolving discontinuity	~5200 m	5.0 cm/a	~100 m	208,000 a	sheet flow

Table 2: Summarizing features which are characteristically for the Edmond hydrothermal vent field.

4.5) Hydrothermal vent field Kairei

Kairei is located in the southernmost part of the Central Indian Ridge at the steeper eastern flank of the rift valley at 70°02'E and 25°19'S in a water depth of 2521 m. It has a distance of ~8000 m to a prominent local discontinuity in the north and is located ~1800 m above the ridge axis at the inside corner. The field developed on the shoulder of a westward dipping slope of a recently formed abyssal hill which is named Hakuho Knoll (KUMAGAI et al., 2008). The rift valley reaches the greatest depths at 4240 m and largest width between 5000 m and 6000 m. Smaller normal faults can be found between the hydrothermal field and the deepest part of the rift valley. In contrast to Edmond, the majority of the identified faults (**Figure 86**) strike ridge parallel between 140 and 150 degrees. There are no obvious cross-cutting faults in the vicinity of the hydrothermal vent field. Just a small number strikes 110° or 170° and there is far less variability in strike directions compared to Edmond. Furthermore, Kairei is located at a large, massive structure of the older ridge shoulder which is not as influenced by faults as the Edmond field. With a distance of 7000 m Kairei is characterized by the greatest distance to the morphological ridge axis. A small evolving neovolcanic ridge inside the rift valley leads suggest that in recent times magmatic activity takes place. The full spreading rate is 5.58 cm/a and the distance from the hydrothermal vent field to the center of magnetic Anomaly 1 is ~5000 m. The age of the bedrocks has been determined at 251,000 years, based on the distance to the ridge axis. Video observations of INDEX2013 have shown that the field is characterized by sheet flows, a lot of talus on the flanks, and collapsed dead chimneys at the sulfide mound. It is a large widespread sulfide mound where the active fluids come out of three chimneys. Fluid temperatures between +270 and +370 °C were measured and the copper rich composition of the sulfides led to conclude that the formation temperatures must be very high (SCHWARZ-SCHAMPERA & Shipboard Scientific Party, 2014).

Table 3 summarizes the main characteristics for the Kairei hydrothermal vent field. It is located in a relatively shallow water depth of 2521 m on the steeper eastern ridge flank in the northern end of the working area. Like the Edmond hydrothermal vent field previously it is located close to a discontinuity structure. The hydrothermal vent field rises 1800 m above the ridge axis and shows the highest distance to the ridge axis with ~7 km. With 5.58 cm/a the highest full spreading rate is reached at this hydrothermal vent field. The average age of the bedrocks is 251,000 a and the field is again characterized by sheet flows.

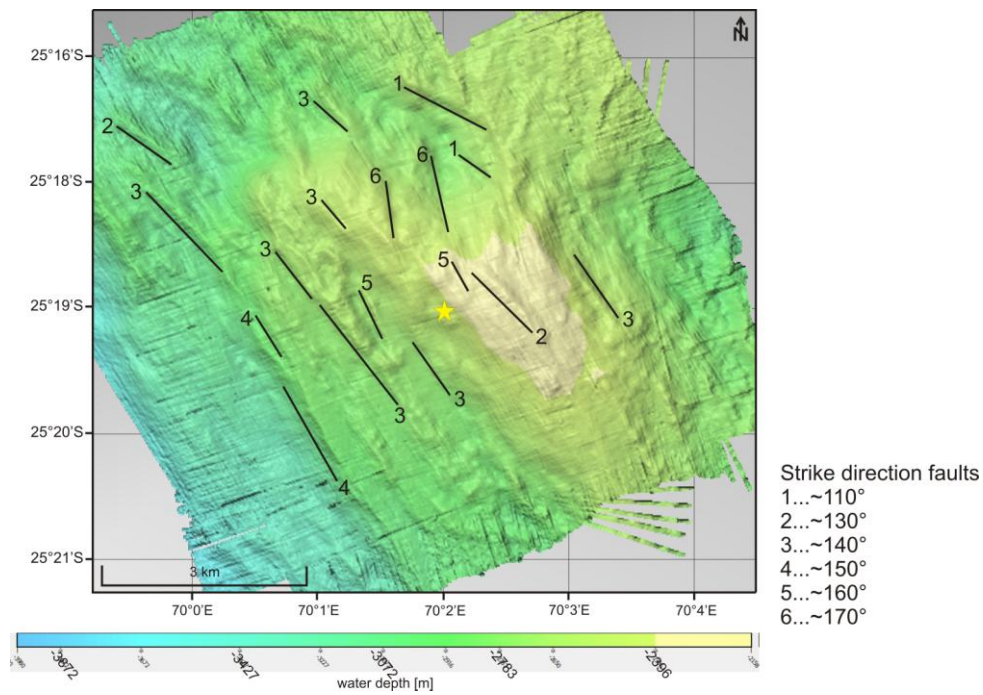


Figure 86: Detailed bathymetric map of Kairei (marked with a yellow star) and main faults with corresponding strike directions.

water depth	height above ridge axis	position	distance to the spreading axis	full spreading rate	distance to the center of magnetic Anomaly 1	approx. age of the bedrocks	lava type
2521 m	~1800 m	northern end, steeper eastern flank, vicinity of a discontinuity	~7000 m	5.58 cm/a	~6000 m	251,000 a	sheet flow

Table 3: Summarizing features which are characteristically for the Kairei hydrothermal vent field.



Figure 87: A chimney structure at the active hydrothermal vent field Kairei characterized by a large amount of shrimps. The underwater photo was observed with a remotely operated vehicle (ROV) 6000 from Kiel (SCHWARZ-SCHAMPERA & Shipboard Scientific Party, 2014).

5) Discussion

First of all in this chapter a short review of the previously described two ridge systems and the three hydrothermal vent fields will be given. Afterwards the main features of the slow spreading Central Indian Ridge and the intermediate spreading Southeast Indian Ridge will be interpreted and discussed. Finally an outlook on characteristic areas of other hydrothermal vent sites is given.

5.1) Review of the two active spreading systems

As a short summary for the two active spreading ridge systems **Table 4** and **Table 5** show the main characteristic features divided into the working areas and the discontinuities from north to south. The strike direction of the working areas of one ridge system remains constant and the values of both ridges are very similar as well. On the Central Indian Ridge, EXFX and Edmond are the longest working areas with the highest rift valley width between 6 km – 13 km. The highest average water depth of the rift valley can be observed in the working area Kairei at ~4200 m. Along the whole Central Indian Ridge the older ridge shoulders have on average the shallowest water depth at ~2100 m. In all working areas of the slow spreading ridge system a more or less well pronounced neovolcanic ridge was observed. From north to south the Central Indian Ridge is characterized by an overlapping spreading center, a bending of the ridge axis, the Gemino transform fault, the Sonne hydrothermal vent field, neovolcanic ridges, the Knorr rise, an evolving discontinuity, the Edmond hydrothermal vent field, an oceanic core complex, the Kairei hydrothermal vent field, several pull-apart basins, and on average a stronger uplifted northeastern ridge flank.

At the Southeast Indian Ridge Section 4 has the highest length and in contrast to the Central Indian Ridge the width of the rift valley in all working areas is almost the same with ~5 km and shows not such large variations. Section 1 is defined by the shallowest water depth of the older ridge shoulders (1700 m). Similar to the Central Indian Ridge the northeastern ridge shoulders are on average stronger uplifted. A prominent behavior at the intermediate spreading Southeast Indian Ridge is the alternating elevated and depressed ridge shoulder. Again oceanic core complexes are observed as well as pull-apart basins and evolving discontinuities.

From 21°S to 27°30'S 11 discontinuities are observed as shown in **Table 5** where two of them represent transform faults. They show the highest ridge axis offset values with 35 km and 43 km. The remaining discontinuities offset the ridge axis by on average 15 km. No clear trend or dependency can be observed in the amount of the ridge axis offset along both ridge systems.

segment	strike direction	length	rift valley width	rift valley depth	shallowest water depth	height neovolcanic ridge above ridge axis	special features
EXFX	145°SE	130 km	6 km – 9 km	~3450 m	2000 m	500 m – 600 m (bending area)	OSC, bending ridge axis, pull-apart basin, stronger uplifted northeastern ridge shoulders
JX	145°SE	88 km	4.5 km – 8 km	~3800 m	2100 m	450 m	Gemino transform fault, strongly pronounced ridge parallel normal faults
Meso	145°SE	8.4 km	1.6 km – 9 km	~3900 m	2200 m	400 m – 600 m	Sonne hydrothermal vent field, two neovolcanic ridges, stronger uplifted NE ridge shoulders
Edmond	145°SE	170 km	7 km – 13 km	~3700 m	2100 m	1200 m (Knorr rise) 400 m – 600 m (southern part)	Knorr rise, two pull-apart basins, two neovolcanic ridges, one evolving discontinuity, highest amount of seamounts in the southern area
Kairei	145°SE	43 km	5 km – 6 km	~4200 m	2200 m	300 m	OCC, stronger uplifted northeastern ridge shoulders
Section 1	135°SE	85 km	4 km – 6 km	~3800 m	1700 m		stronger uplifted northeastern ridge shoulders, sheared seamounts, OCC, two basins
Section 2	135°SE	43 km	4.5 km	~4300 m	1800 m		OCC, pull-apart basin, diffuse striking direction of major faults
Section 3	135°SE	60 km	5 km	~4100 m	2200 m		strike-slip fault, alternating elevated and depressed ridge shoulders
Section 4	135°SE	167 km	5 km	~3800 m	2000 m		two evolving discontinuities, stronger uplifted northeastern ridge shoulders, two basins
Section 5	135°SE	36 km	7 km	~4100 m	2100 m		young OCC, diffuse striking direction of major faults
Section 6	135°SE	65 km	5 km	~3600 m	2250 m		alternating elevated and depressed ridge shoulders, two prominent large seamounts

Table 4: A summary of the main features characterizing first the slow spreading Central Indian Ride (EXFX – Kairei) and second the intermediate spreading Southeast Indian Ridge (Section 1-6).

discontinuity	Offsets the segments	sense	Ridge axis offset
21°09'S	EXFX		
22°08'S	EXFX - JX	dextral	13 km
22°50'S	JX – JX Gemino TF	sinistral	35 km
23°05'S	JX - Meso	dextral	14 km
24°41'S	Edmond (north) – Edmond (south)	dextral	12 km
25°14'S	Edmond - Kairei	dextral	17 km
26°02'S	Section 1 – Section 2	sinistral	19 km
26°10'S	Section 2 – Section 3	dextral	43 km
26°21'S	Section 3 – Section 4	sinistral	13 km
27°23'S	Section 4 – Section 5	sinistral	15 km
27°29'S	Section 5 – Section 6	sinistral	16 km

Table 5: Summary of discontinuities along the Central- and Southeast Indian Ridge with main characteristics such as offset sense and amount.

5.2) Review of the HTFs along the CIR

Hydrothermal vents strongly correlate with the ridge geometry and that of magma chambers, their depth and size, and the valley morphology. Structurally controlled environments with cross cutting fault systems play an important role as outlined in the case of the Edmond hydrothermal field. Such structures represent pathways for the fluids to reach the seafloor and react with the seawater to build hydrothermal system.

A regional uplift behavior can be seen at the Sonne field and the Knorr rise. It is related to intense magmatic activity at the central rift and in the entire region. This magmatic activity obviously has an impact on the spreading rates, likely related to higher melting rates and intermittent spreading. SEARLE (2013) published that water is not able to penetrate magma which leads to the conclusion that the enhanced magmatic activity at the Sonne field could possibly block important channel ways and hinder the hydrothermal fluids to reach the seafloor. This seems to be an explanation for the inactivity of the Sonne field. From video observations at Sonne, Edmond, and Kairei it becomes clear that all these fields are dominated by sheet flows (SCHWARZ-SCHAMPERA & Shipboard Scientific Party, 2012). Seamount distribution maps point out that there is a lack of seamounts at and around the hydrothermal vent fields.

Figure 88 points out the large distance of the active vent fields Edmond (5200 m) and Kairei (7000 m) from the bathymetric low. The inactive Sonne field (2400 m) and Gauss (6500 m) occur at variable distances from the morphological low. However, the distance of the Sonne field to the bathymetric low east of the second active neovolcanic ridge is 7700 m. This equidistance between 5 and 7 km from the active spreading axis may indicate a distinct structural control of sustainable fluid upflow and discharge at the seafloor. It seems possible to define structural fault zones and, or detachment faults that are responsible for focusing the fluid flow. An increasing elevation of the vent sites with increasing distance from the bathymetric low (**Figure 88**) is likely related to the fact that hydrothermal fluids are tapped by regional detachment faults (where present) and that these detachment faults may allow for the presence of hydrothermal activity at a great distance to the spreading axis. Also dykes can transport mass and heat vertically as well as laterally through the crust (BEHN & ITO, 2008). The formation of detachment faults in oceanic crust is supported by tectonic extension as a result of magma supply to the ridge axis (PETERSEN et al., 2009). This statement is confirmed

by the fact that detachment faults preferably occur at the segment ends. They could be pathways for the circulation and transport hydrothermal fluids away from the heat source (PETERSEN et al., 2009). This process is very important for the fluid flow at a black smoker along slow spreading ridges. Detachment faults make it possible that hydrothermal vent sites like Edmond and Kairei are situated relatively close to a discontinuity structure.

There is a very good correlation between basalt ages, distances and elevation. Kairei and Edmond/Gauss are associated with the oldest basaltic rocks, have the greatest distance from the active spreading center and they occur at the highest elevation above the bathymetric low. The age of Kairei is a little bit younger because here the spreading rates are comparatively high. As a consequence the vent field moves further away from the rift valley in a relatively short time period. Sonne is hosted by the youngest basalts and shows the lowest elevation.

The location of the prospective areas EXFX and JX as well as the active Edmond and Kairei fields is close to discontinuities at the segment ends. This may suggest enhanced heat flow at fault intersections, shallower magma chambers towards the discontinuities, limited volcanic activity, and enhanced channel ways for hydrothermal fluids. The locations, however, differ from the Sonne field which shows a larger distance to the discontinuity of the ridge. In general, the active vent fields are situated on the steeper eastern ridge flank.

Another evidence for the occurrence of detachment faults are oceanic core complexes as found north of Kairei. VAN WIJK & BLACKMAN (2005) and other authors (KARSON, 1990; TUCHOLKE & LIN, 1994) suggest that oceanic core complexes were built by a slip movement along detachment faults which are rooting below the rift valley. Exhumation from the valley rift might be an additional critical factor for massive sulfide potential. All in all four OCCs have been observed, one at the slow spreading ridge and three at the intermediate spreading ridge.

It seems possible that the acoustic signals of the multibeam echo sounder are not able to detect the seafloor where hydrothermal activity takes place. They will be reflected in an erroneous way and produce “holes” in the bathymetric map. Such a seemingly wrong beam fits perfectly to the Edmond hydrothermal vent field in the data of cruise INDEX2011. Possibly in combination with other investigations this could be a hint for prospective areas.

The known hydrothermal vent sites from the Central Indian Ridge are associated with full spreading rates between 4.87 cm/a and 5.6 cm/a. This is the upper spectrum of the full spreading rates along that ridge. It indicates potential especially for the JX area but also for other areas around Sonne, Edmond and Gauss. It is also evident that the inactive Sonne hydrothermal vent field is situated within an area of lower spreading rates. The range leaves a significant number of areas with similar spreading rates. After FONTAINE et al. (2008), statistical analysis showed that there is a decrease in numbers of axial hydrothermal vent sites with decreasing spreading rates. WILCOCK & DELANEY (1996) suggest that the dimensions of high-temperature hydrothermal sulfide edifices vary with the spreading rate. On the basis of detailed magnetic surveys local minimum areas of magnetic values are recognized around the Edmond and Kairei hydrothermal vent fields. This decrease could probably be a result of hydrothermal interactions and a process called metal leaching. The mineral Titanomagnetite of the basalts will be replaced by non-magnetic sulfide minerals caused by the hydrothermal fluids on their way up to the seafloor (TIVEY & DYMENT, 2010).

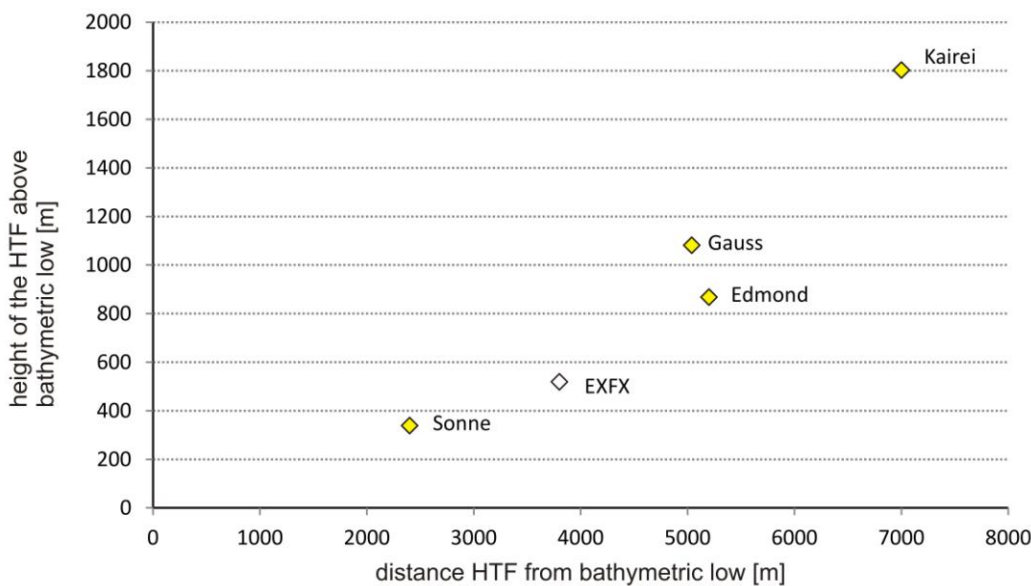


Figure 88: Elevation of the hydrothermal vent sites along the CIR above the bathymetric low with respect to the distance towards the bathymetric low. The white rhombus shows the methane anomaly of EXFX. The yellow rhombuses are the active and inactive HTF known so far.

To summarize, from bathymetric data parameters like fault distributions, crossing faults, seamount distribution, distances to the spreading axis, height above the rift valley, discontinuities, oceanic core complexes, and seemingly bad measured beams can be deduced. Magnetic measurements give information about the spreading rates and areas with a decrease in magnetic values.

5.3) Slow spreading Central Indian Ridge system

At slow spreading ridge systems mechanical deformation and tectonic processes play an important role (MUTTER & KARSON, 1992). An asymmetric ridge morphology as can be seen at the slow spreading Central Indian Ridge is the result of primary volcanic activity modified by tectonic activities (BALLARD & VAN ANDEL, 1977). With decreasing spreading rates the tectonic processes are getting more and more important. In the following, after a short analysis of the main prominent structural features (OSC, bending and OCC), a differentiation will be done between these magmatic and tectonic activities along the CIR.

A very prominent structural feature of the slow spreading ridge system is the overlapping spreading center in the northern part of EXFX (**Figure 89**). Here, the ridge axis overlaps by about 9.5 km. BRIAIS (1995) published an evolution chronology of the tectonic deformation for the 21°45'S offset (**Figure 90**). At time t_0 a straight ridge axis exists, which is interrupted at time t_1 around 0.7 Ma. 0.4 m.y. later a valley developed and the ends of the rift valley bend to the sides which causes an increase in offset. At recent time t_3 the extremely bended morphology reduces the offset and the overlapping zone.

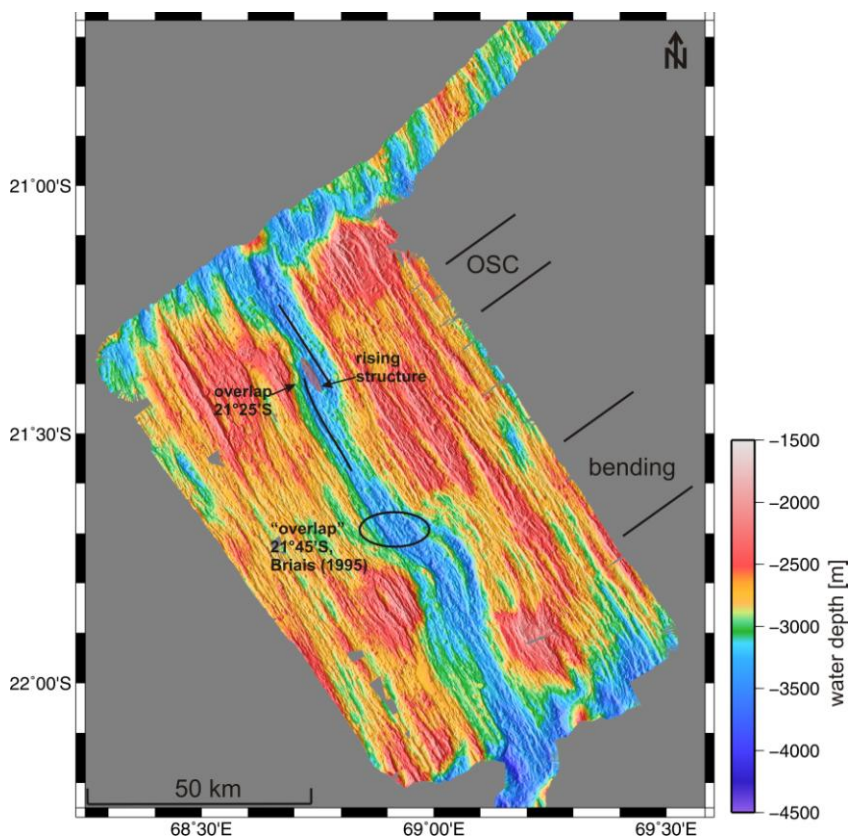


Figure 89: Interpretation of the working area EXFX. Prominent structural features identified from INDEX2011 are labeled as well as the “overlapping spreading center” noticed by BRIAIS (1995).

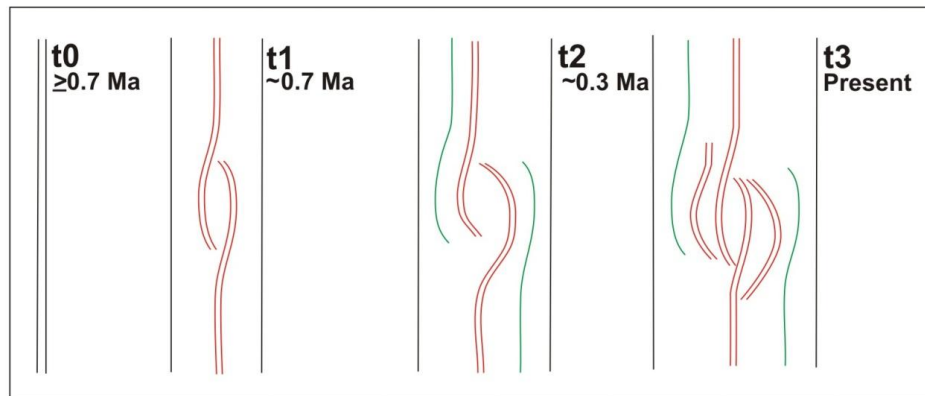


Figure 90: Evolution of the 21°45'S offset in four stages (BRIAIS, 1995, modified). During INDEX2011 this was identified as the tip of a bending structure.

With the new high resolution bathymetric data the area at 21°45'S described by BRIAIS (1995) as an OSC cannot be confirmed. Newest data show the location of the OSC at 21°25'S (**Figure 89**). The area at 21°45'S is the northern tip of the bending structure in the southern part of EXFX. Moreover, this bending structure does not represent an offset of the ridge axis. Instead, it is a slight curving of the ridge axis and the youngest ridge flanks to the east, but without any interruption. The term "21°45'S offset" used by BRIAIS (1995) is false at this location. At the real OSC there are no hints for a propagation of the ridge segment ends, instead this section seems to be defined by a ridge jump. A second study exists for overlapping spreading centers compiled by SEARLE (2013). Some authors like MACDONALD & FOX (1983) and SEARLE (2013) describe OSCs as characteristic for fast spreading ridge systems, but in the case discussed here it is definitely a part of a slow spreading ridge system. That means OSCs are not only typical for and limited to fast spreading ridges. In the evolution model of SEARLE (2013), the ends of the offset spreading segments overlap each other by about three times the offset length and between them an 'overlap basin' will be formed. Such a basin could not be found at the OSC of EXFX. Instead, between the two overlapping spreading segments a ridge evolves. Probably that is the difference between OSCs at fast and slow spreading ridges: fast spreading ridges are characterized by an 'overlap basin' between the overlapping spreading centers (SEARLE, 2013) and slow spreading ridges show an 'overlap rise' between the spreading centers. After SEARLE (2013) the overlapping process must lead to either a deformation or rotation in the region of the overlap. The author suggests that the propagation of an OSC along the ridge axis causes a material transfer from one plate to the other one. This material leads to a time-averaged asymmetric spreading and can also provide a mechanism for ridge reorientation following a change in spreading direction (SEARLE, 2013). This assumption of the author of an asymmetric spreading behavior cannot be reconstructed in

this case. With a look at the magnetic data and the spreading rates in that area the ridge spreads symmetrically with half spreading rates of 2.30 cm/a. Possibly that is another difference to OSCs along fast spreading ridges. Referring to the time development model presented by BRIAIS (1995), the OSC at 21°25'S could be in stage t_1 because the overlapping segments show not such a strong curvature as this is the case at time t_2 and additionally no old overlapping segments east and west of the OSC can be seen as the typical feature for stage t_3 . SEARLE (2013) argued that it is typical for slow spreading ridges to develop oblique offsets rather than OSCs, because the axial lithosphere at slow spreading environments is thicker and stronger, hence it withstands rotations or deformations typical for OSC. Considering that the OSC evolves at a slow spreading ridge this probably means that the axial lithosphere is not thicker in this area proved by the bending structure and pull-apart basin which are hints for extensional movements.

It seems possible that in a slow spreading environment the development of OSCs is characterized by a ridge jump, an evolving rise between the spreading centers, and symmetrical spreading. Furthermore, there is no deformation or rotation, it is just a shifting because the strike direction of the ridge axis still remains the same.

With a look at structural analysis of SAUTER et al. (1996) it becomes clear how important actual high resolution bathymetry data are. SAUTER et al. (1996) described an area between 21°10'S and 22°25'S, corresponding to the working area EXFX, with the help of bathymetry data from 1984 (Rodriguez project) (MUNSCHY & SCHLICH, 1990), 1986 (Gemino-2) (HERZIG & PLÜGER, 1988) and 1987/88 (Gemino-3) (HERZIG & PLÜGER, 1988). These data have a resolution of 120 m. They identified second-, third- and fourth-order discontinuities along the slow spreading ridge. The authors defined second-order discontinuities as small non-transform offsets below 30 km. The third-order discontinuities have offsets below 10 km and fourth-order discontinuities are just fine forms of segmentation without an interruption of the ridge axis. Between the discontinuity in the southern part and the bending structure of EXFX SAUTER et al. (1996) described the rift valley as hourglass shaped. With the high resolution bathymetry (~50 m) of INDEX2011 this behavior cannot be confirmed. Also the described second- and third-order discontinuities in that area could not be reproduced. The authors identified two non-transform discontinuities (NTD) at 21°47'S and 22°15'S. The first one at 21°47'S corresponds with the northern end of the bending structure in the modern bathymetry and the interpretation as a discontinuity must be rejected. It is more a bending of the recent

ridge valley. Following the definition of SAUTER et al. (1996), this means that the bending area is not an offset structure but rather a fourth-order discontinuity because the rift valley is not interrupted. At such places the segments can behave like fractures, because the lithosphere is thin enough and such fractures are able to cause a bending to neighboring segments (BRIAIS, 1995). The second NTD described at 22°15'S by SAUTER et al. (1996) is the location of the discontinuity which bounds the southern part of the working area EXFX. Petrographic and geochemistry studies from the basalts north and south of the bending structure show different textures (SAUTER et al., 1996). The different grades and processes of fractionation makes the authors believe that there is also a segmentation of the magma reservoir along the rift axis. To sum up, not all results of SAUTER et al. (1996) can be confirmed with the newest dataset. The interpreted NTD at 21°47'S is in agreement with the interpretation of BRIAIS (1995) but is not true. Definitely the ridge axis shows no offset structure, instead it is just a curving behavior. The second NTD defined by SAUTER et al. (1996) at 22°15'S correlates with the newest data. This observation makes clear that there is a great difference in the interpretation of the dataset with a resolution of 120 m and the newest one with 50 m resolution. Large offset structures could be identified before but smaller structures are occasionally interpreted in a wrong way. The assumption of a segmented magma reservoir along the rift axis should be clarified with further investigations and specific rock sampling north and south of the bending structure.

Along detachment faults, representing large offset normal faults, plutonic lower crust can be exhumed so that mantle rocks are exposed on the seafloor forming an oceanic core complex (RESTON & RANERO, 2011). Oceanic core complexes are typical for magma-starved conditions as prevalent at the slow spreading CIR and can be generated by a ridge jump or asymmetric spreading (KUMAGAI et al., 2008). The detachment fault serves as the pathway for fluids and is a connection to the heat regime deep beneath. Thus it is not unusual to find hydrothermal vent fields at the flanks of oceanic core complexes. OCCs mostly occur at inside corner (IC) highs of ridge offsets (**Figure 91**) and evolve during periods of tectonic extension (BOSCHI et al., 2006). Typical for oceanic core complexes are the lineations running perpendicular to the spreading axis. They can be outlined very well with a map of the slopes seen in **Figure 91**. Here, also the line of movement can be seen in the western part of the OCC (red line). Several OCC structures exist in the Atlantic Ocean at segment ends which are very well investigated. The knowledge of these OCCs should be used to explain the OCC in

the southern part of the slow spreading ridge system near the Rodriguez Triple Junction. After RESTON & RANERO (2011), OCCs represent the exhumed footwalls of oceanic detachment faults that extend into the basement. GRÁCIA et al. (2000) suggest that OCCs occur where a high amount of extension is present because that results in lithospheric stretching and thinning which favors the exposure of mantle rocks. SATO et al. (2009) published a study of the OCC at the slow spreading ridge system at 25°S. The oceanic core complex is located off-axis on the western ridge flank and evolved during the Matuyama reversal chron. This structure is characterized by megamullion morphology and developed probably 0.8 Mio years ago. That is a shorter period of time than the oceanic core complexes along the Mid-Atlantic Ridge need to evolve. Compared with the surrounding seafloor of the same age the magnetization intensity over the OCC is poorly developed. This indicates that the OCC mainly consists of gabbros, which have a lower magnetization than basalts. From the morphology of the OCC the following origin can be concluded: after the OCC developed, the segment north of Kairei and south of the Knorr rise migrated south-southeast. The OCC itself migrated off-axis as a result of seafloor spreading in this segment. The Kairei working area propagated north-northwest and so the OCC is located at the western side of the recent ridge axis of this segment. A second OCC location was published by KUMAGAI et al. (2008). They suggest that the Uraniwa hills (KUMAGAI et al., 2008) east of Kairei also represent an OCC because of olivine-abundant mafic plutonic rocks (**Figure 91**, small dotted red box). From the bathymetric data of INDEX2011 and structural analysis no indication was found that these hills could be an OCC. Also the map of the slopes shown in **Figure 91** does not give any hints for such an assumption since there are no lineation structures perpendicular to the spreading axis or lines of movement.

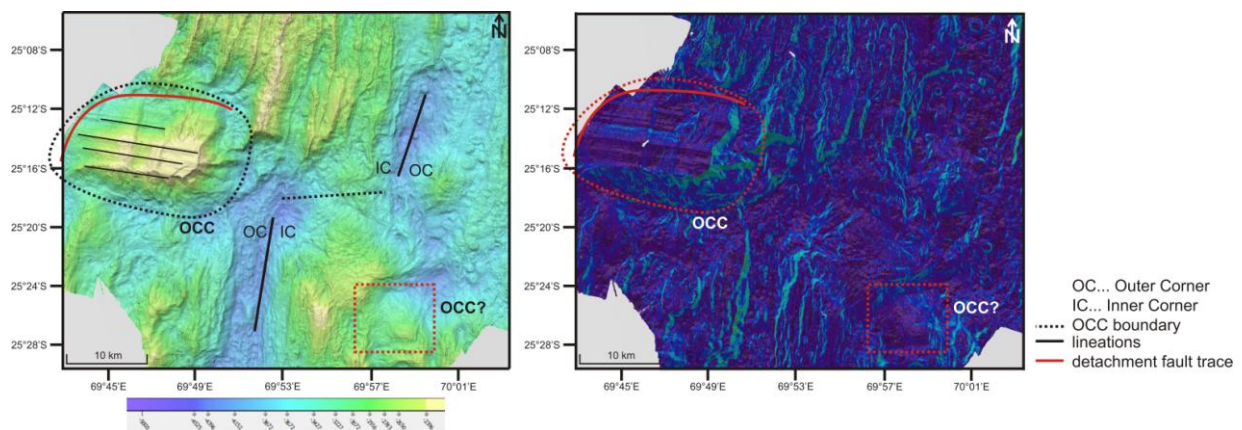


Figure 91: Bathymetric and slope inclination map of the working area Kairei. The large red box marks the OCC and the small dotted red box marks the identified OCC after KUMAGAI et al. (2008) which cannot be confirmed with the data today.

The pattern of magmatic activity along mid-ocean ridges can be shown with maps of the seamount distribution because seamounts are an expression for magmatic activities. Furthermore, in the following a time differentiation between tectonic and magmatic phases can be made. The division of seamounts which are typically cone shaped and those which are

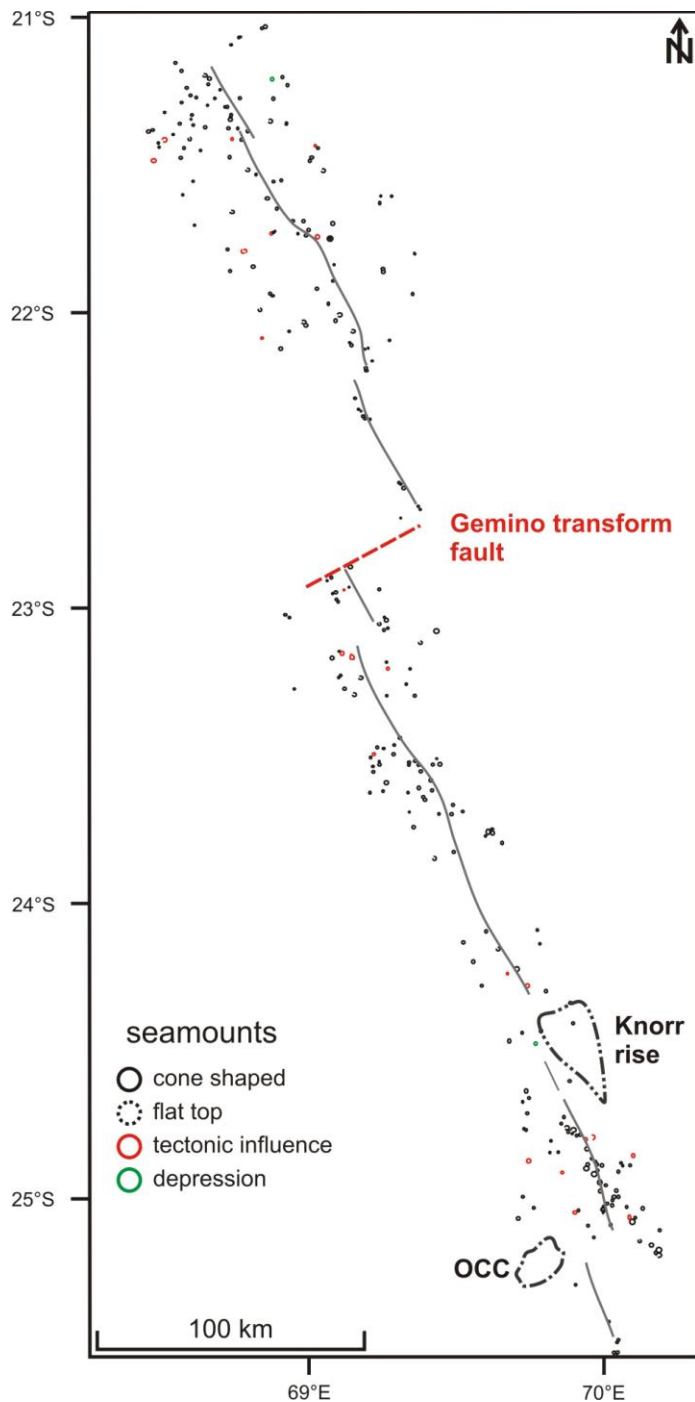


Figure 92: Seamount distribution map of the whole mapped CIR. The grey line represents the ridge axis and some prominent features are labeled for orientation like the Gemino transform fault, the Knorr rise and the OCC.

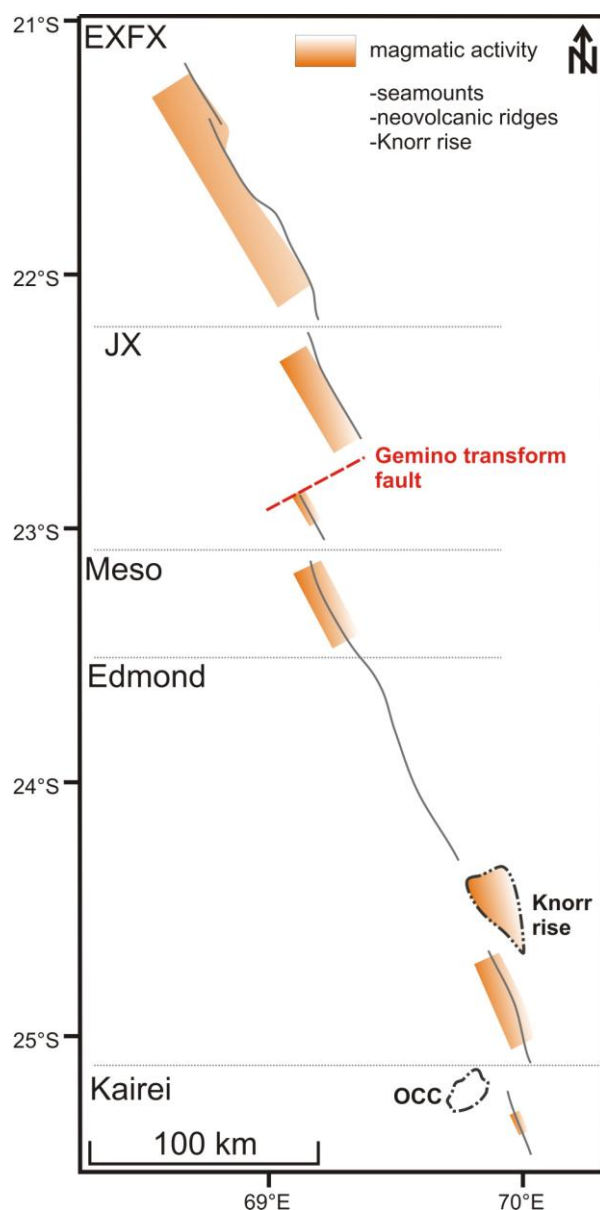
tectonically influenced by faults makes it possible to distinguish between areas where the magmatic activity must be younger than the tectonic one and vice versa. In the previous **Chapter 4.1.1** detailed seamount distribution maps have been shown for every single working area. **Figure 92** summarizes these results in one large overview map. From the fact that several cone-shaped seamounts occur on the ridge flanks far away from the rift valley it is possible to conclude that the magmatic source beneath the spreading center is not limited to the ridge axis. That is especially true for the working area EXFX, where more seamounts are concentrated in the northern part as well as on the western ridge flank. This distribution of seamounts on the western flank and along the rift valley can also be found in the working area JX. That means that EXFX and JX are possibly characterized by an

asymmetric magma chamber beneath shifted to the western side (**Figure 93**). That observation correlates with a study of BUCK et al. (2005). They found out that in slow spreading ridge systems most of the magmatic accretion takes place on one side of the ridge. Mostly it is the side with smaller fault offsets which result in asymmetric magmatic accretion along the ridge system (BUCK et al., 2005). For such high resolution detailed studies of fault offset measurements deep-towed bathymetric data are needed. A very high magmatic activity must exist in the working area Meso beneath the ridge axis, expressed by two large neovolcanic ridges (**Figure 92** and **Figure 93**). A conspicuity of the seamount distribution is a lack of them around these neovolcanic ridges and hence at the inactive hydrothermal vent field Sonne. Possibly the neovolcanic ridges are a consequence of a magma chamber which is bigger and hotter or just shallower in the crust. Thus there are no small seamounts in that area and the hydrothermal vent field becomes inactive because the magmatic activity is very high and the fluid pathways become blocked. Also the Knorr rise and the larger number of seamounts and the neovolcanic ridge in the southern part of Edmond are an expression for enhanced magmatic activity. Elevated heat flow through shallower magma chambers exactly beneath the ridge axis may be suggested.

BALLARD & VAN ANDEL (1977) found out that several seamounts in one area occurring at more or less the same water depth suggest the same hydrostatic level and one individual magma chamber. That could be true for EXFX where the seamounts near the rift valley occur in a water depth between 3100 and 3200 m. With respect to the time development between magmatic and tectonic activity deduced from the seamount maps, it becomes clear that where the present magmatic activity is expressed by cone-shaped seamounts this must be younger than the tectonic activity. A very nice example can be seen at the Gemino transform fault, where one single, large seamount is round and cone-shaped with no pattern of a shear movement. Only in the working areas EXFX, Meso and Edmond a few seamounts are sheared by fault structures.

The small neovolcanic ridge in the working area Kairei is located in a very deep part of the slow spreading ridge system near the RTJ. Those neovolcanic ridges which are located in the deepest part of the ridge could be the expression for regions of crustal thinning (MUTTER & KARSON, 1992).

Apparently higher nT values within the boundaries of Anomaly 1 seem to correlate with zones of neovolcanic ridges or higher numbers of seamounts along the slow spreading ridge system. TIVEY et al. (2003) showed that an axial volcanic ridge seems to be correlated with a high crustal magnetization of the Brunhes anomaly. That behavior is typical for the locus of volcanic accretion, because very young basalts have the highest magnetization as found out by JOHNSON & TIVEY (1995) and SEARLE (2013). POULIQUEN et al. (2001) called the zone of most recent volcanism, where frequently higher magnetic values are observed, the Central Anomaly Magnetic High (CAMH). In their study most of the CAMH locations correspond to the bottom of the axial bathymetric valley. TIVEY & JOHNSON (1987) as well as POULIQUEN et al. (2001) have shown from the Juan de Fuca Ridge that newly erupted basalts locally



coincide with a magnetic low as a result of extensive low-temperature alteration. As described in **Chapter 4.1.2** the peak in the magnetic values within Anomaly 1 (CAMH) does correlate in many cases with the bathymetric minimum, the rift valley. On the profiles of Meso and Edmond the CAMH is not observed directly above the bathymetric minimum, instead it is located above neovolcanic ridges or seamounts which are also expressions for high magmatic activities. As a result from this, it is possible to identify zones of recent volcanism from the magnetic data analysis.

Figure 93: Schematic sketch of magmatically active zones and a possible trend of the magma chamber underneath to the western ridge flank (EXFX and JX) or more central directly beneath the ridge axis (Meso and southern part of Edmond).

For the analysis of tectonically active areas along the CIR it is important to analyze the fault behavior and to understand how faults evolve along a slow spreading ridge. BUCK et al. (2005) showed that the dip angle of normal faults at mid-ocean ridges shows systematic variability as a function of the spreading rate. Thus more or less all faults at slow spreading ridges dip in the direction of the ridge axis called inward-facing faults because they develop due to extension. That behavior can be observed in the fault distribution figures of **Chapter 4.1.1**. There the main ridge parallel faults dip to the east or west towards the ridge axis and strike between 140° - 145° E. Faults which dip or strike in a different way are located near discontinuity structures and indicate tectonic movements. Long-lived faults produce an asymmetrical axial thermal structure, consequently the thinner lithosphere can be found on the side of the ridge with the active faults (BEHN & ITO, 2008). The along-axis variations in crustal thickness are expressed by the hourglass shaped morphology of the individual ridge segments. That implies thinner, warmer crust at the segment centers and thicker, colder crust towards the ends. BEHN & ITO (2008) found out that these crustal variations correspond to along-axis changes in the fault style. Hence, small closely spaced faults can be found at segment centers and the larger more widely spaced and long-lived faults near the segment ends. The magma supply influences the faulting style predominantly by varying the amount of magmatic extension (BEHN & ITO, 2008). BEHN & ITO (2008) constructed a model for the sequential fault development at mid-ocean ridges as shown in **Figure 94**. The model works as follows: faulting at mid-ocean ridges occurs sequentially and starts near the axis because there the lithosphere is thinnest. Due to continued magma accretion the initiated fault rafts off-axis until the stress which is required to continue the initial fault exceeds the stress required to break a new fault. The first fault becomes inactive and a new active fault will develop. This new fault will often become antithetic and develops on the opposite side of the ridge axis. That mechanism results in asymmetric spreading rates of off-axis fault transport. After BEHN & ITO (2008) there are four parameters which influence the distance to which a fault remains active. These are the lithospheric thickness, the off-axis slope of the lithosphere, the fault dip, and frictional properties of the lithosphere. The fault behavior itself is mechanically controlled by the balance between the pulling force needed to keep a fault active and the force needed to break a new fault closer to the axis (ITO & BEHN, 2008). Generally five parameters control the fault characteristics, first the duration of the tectonomagmatic cycle, second the magmatic time fraction, third the axial lithospheric thickness, fourth the topographic growth during magmatic phases, and finally the spreading rate (ITO & BEHN, 2008). These authors indicate

that during a tectonic phase faults develop and remain active while with a magmatic phase they rift away from the axis.

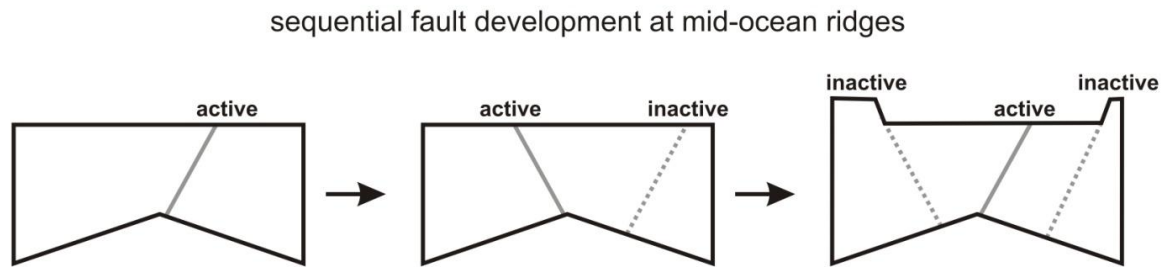


Figure 94: Sketch for the sequential fault development at a MOR (after BEHN & ITO, 2008, modified).

Profiles across the ridge axis point out the inward-facing behavior of the faults (**Figure 95, 96, 97, and 98**). In addition, the behavior of the ridge flanks is pointed out when one ridge side is elevated more than the corresponding one. That observation implies an isostatical compensation behavior of the slow spreading ridge system. In a more general view the profiles point out that the eastern ridge flanks are stronger uplifted along the entire ridge segment analyzed here.

Increasing water depth at segment ends as can be found along the CIR expressed in the hourglass shaped morphology, reflects a lower magmatic influence and a greater tendency to a rifting behavior (SEARLE, 2013).

Second-order discontinuity structures occur more often along slow spreading ridges than transform faults, representing first-order discontinuities. The structural features which develop at those discontinuities are not stable in time because they are influenced by strike-slip movements and oblique extensional faulting (GRÁCIA et al., 2000). There are two mechanisms described by ABELSON & AGNON (1997) which cause ridge segmentation. First the along-axis variations in mantle upwelling and melting, and second lithospheric extension in a region where mantle upwelling and crustal supply is oblique to the spreading direction.

To sum up, the tectonically active areas as pointed out in **Figure 99** can be found first of all at the discontinuity structures along the whole mapped CIR. One first order discontinuity, the Gemino transform fault, offsets the ridge by about 35 km. Furthermore, the OSC as well as the bending structure are characteristic for tectonic activities. Inside of the bending structure a pull-apart basin as a hint for strike-slip movement, proves this assumption. Such pull-apart

basins can be found additionally in the northern part of the Edmond area with its evolving discontinuity and in the southern part of Edmond close to the discontinuity separating the working areas Edmond and Kairei and the OCC. The latter pull-apart basin has one specialty because a cone-shaped seamount evolves directly inside of this basin. That underlines the recent magmatic activity further north with the highest amount of seamounts and the neovolcanic ridge. Hence, that is an area where tectonic and magmatic activity takes place at the same time.

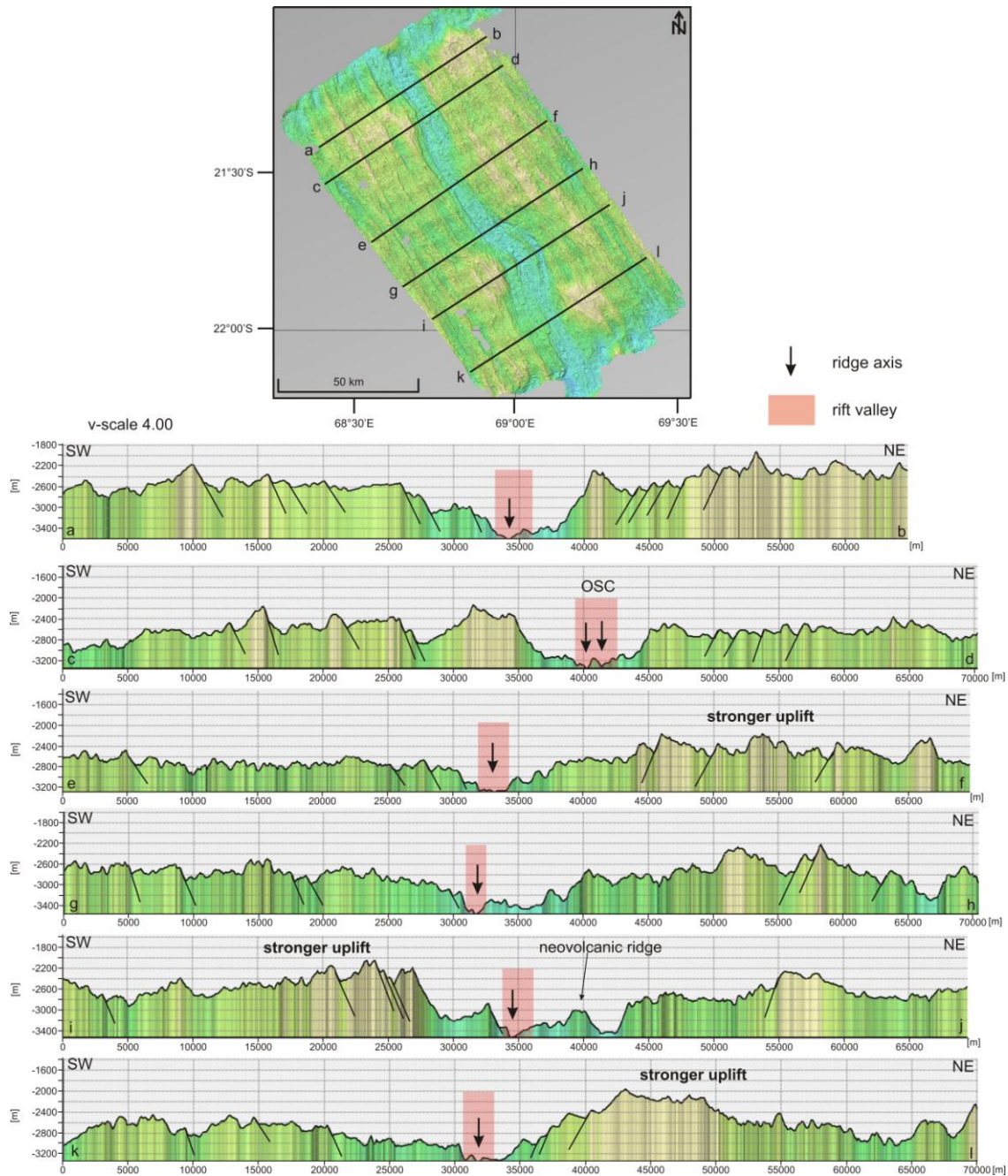


Figure 95: Profiles across the ridge axis of the working area EXFX striking from southwest to northeast. The vertical exaggeration of the profiles is 4.0.

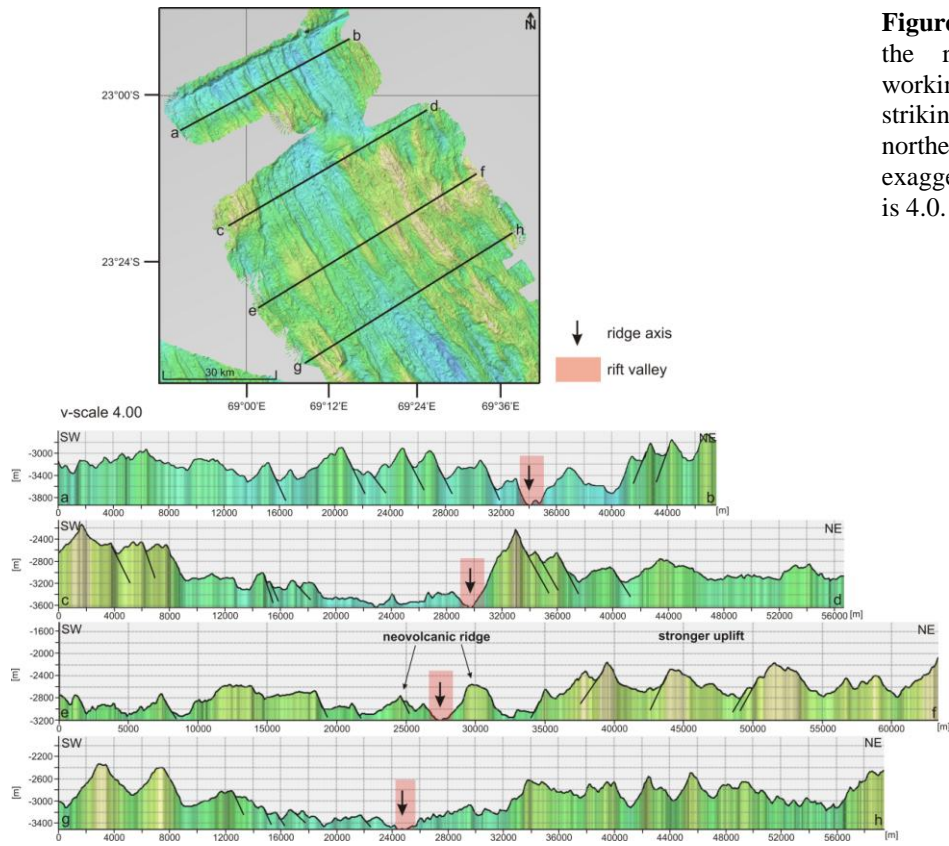


Figure 96: Profiles across the ridge axis of the working area JX and Meso striking from southwest to northeast. The vertical exaggeration of the profiles is 4.0.

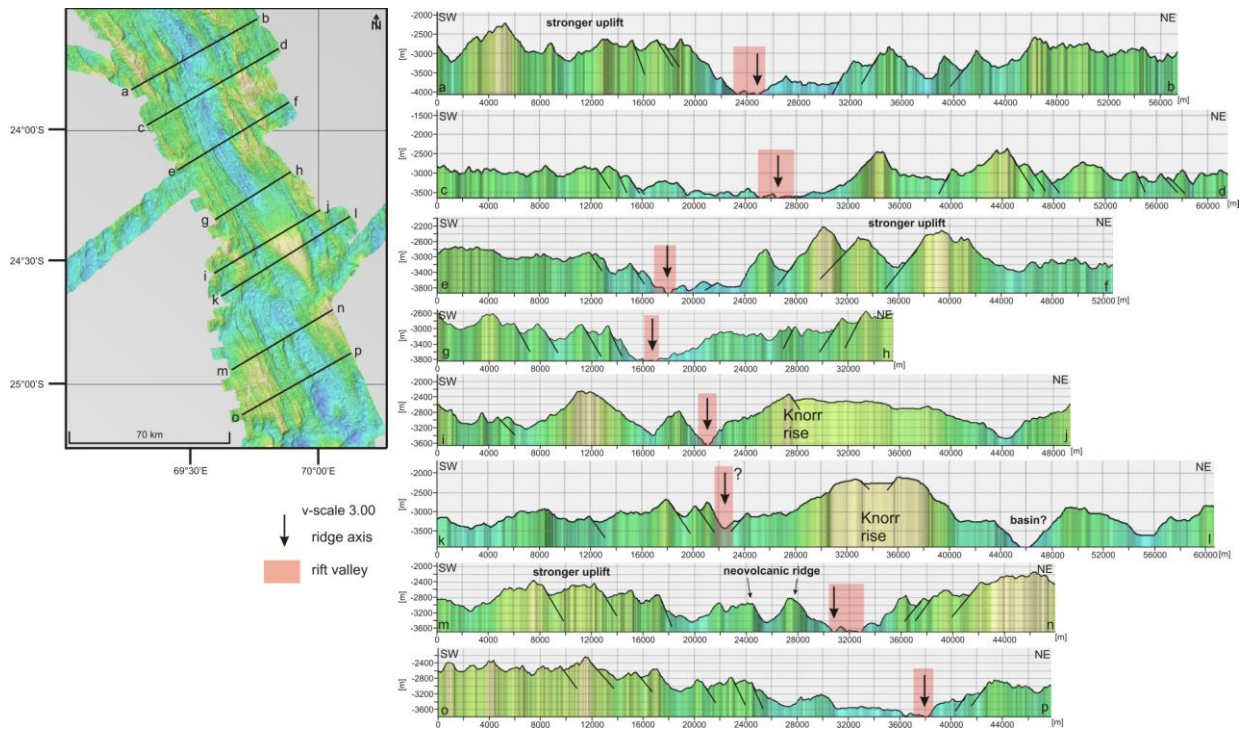


Figure 97: Profiles across the ridge axis of the working area Edmond striking from southwest to northeast. The vertical exaggeration of the profiles is 3.0.

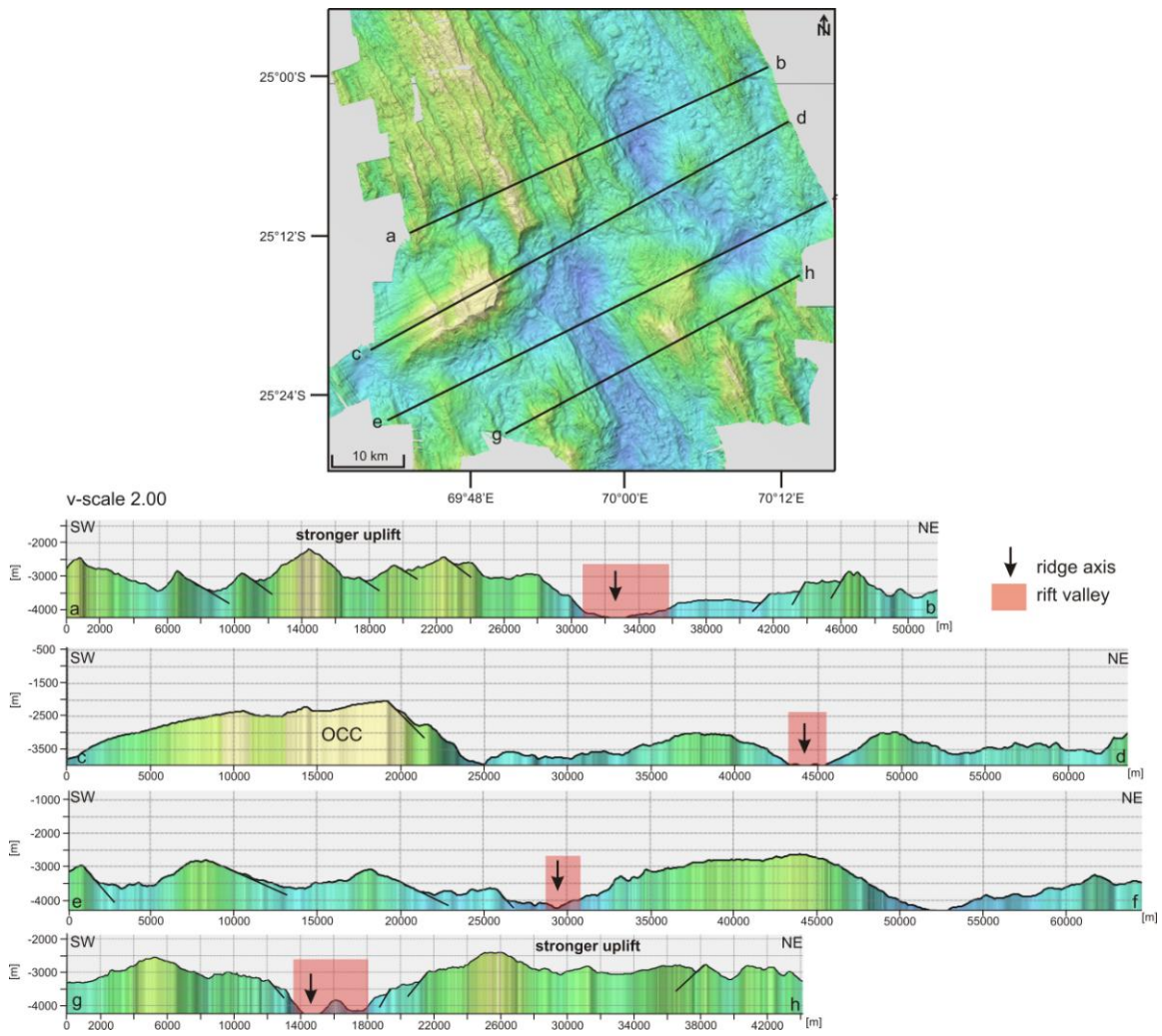


Figure 98: Profiles across the ridge axis of the working area Kairei striking from southwest to northeast. The vertical exaggeration of the profiles is 2.0.

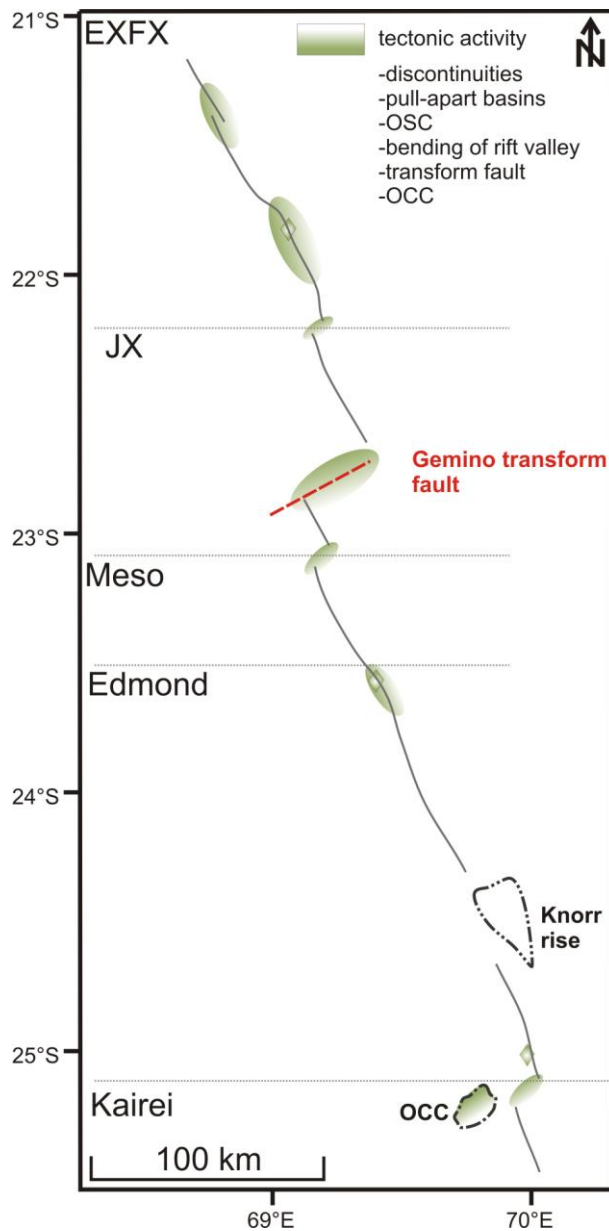


Figure 99: Schematic sketch of the total mapped CIR with outlined areas of tectonic activity in terms of discontinuities, OSC, bending of the rift valley, pull-apart basins, and an OCC.

With figures of the contour lines it is possible to get hints for the spreading direction and the sense of movement whether there was a simple spreading movement to the west and east or additionally a strike-slip movement. At the first working area EXFX the 3000 m contour lines shown in **Figure 100a** represent the boundaries of the rift valley. In **Figure 100b** the closure of the rift valley is shown for the case that the northeastern valley flank is moved back to the southwest. The spreading in the northern part is now closed, but the bending structure still remains open. This structure can be closed if the northeastern flank moves to the north as shown in **Figure 100c**. This means that there must have been a strike-slip movement active which is also expressed in the pull-apart basin located directly at the bending structure. The

assumed movement direction of the eastern plate to the north-east can also be supported by the seamount chain in the vicinity of the OSC which strikes in a northern direction. That the eastern plate in the vicinity of the bending structure is moving faster has been shown with the magnetic results (see **Chapter 4.1.2**).

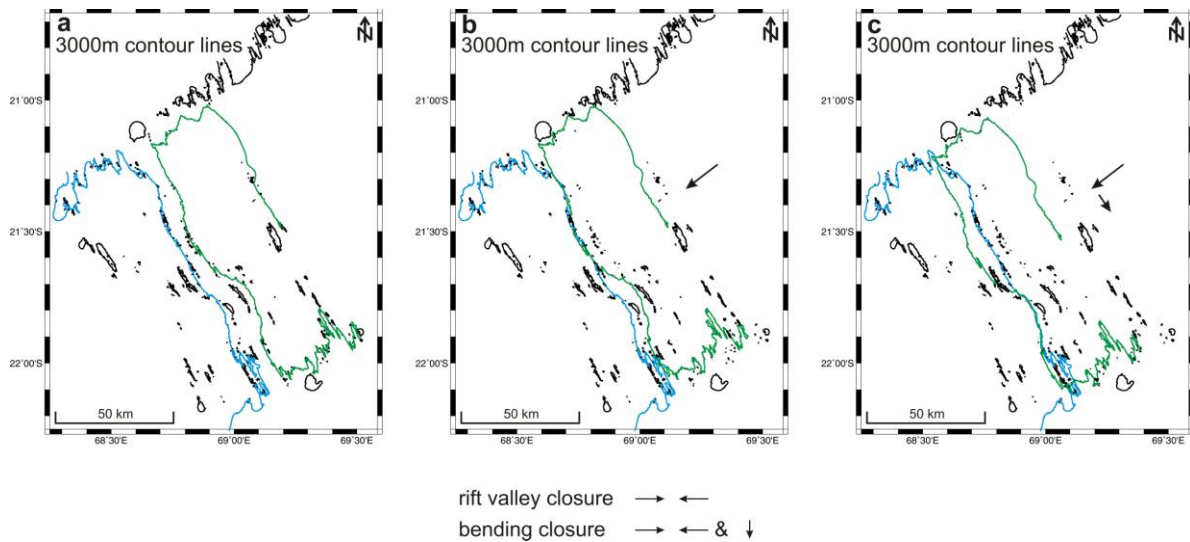


Figure 100: 3000 m contour lines of EXFX and the movement process to reconstruct the spreading movement. Blue lines mark the western flank and the green lines the eastern one.

In the working area Meso and Edmond the 3250 m contour lines shown in **Figure 101** represent the boundaries of the rift valley. In the area of the Sonne hydrothermal vent field the contour lines are interrupted due to the updoming structures where the hydrothermal vent field is located. North of Edmond hints exist for the development of a new discontinuity. There the contour lines bend and the rift valley continues more to the west. Again with the 3250 m contour lines the spreading can be reconstructed (**Figure 101**). The northeastern flank must be moved to the southwest to close the rift valley. From this analysis there are no obvious hints for a movement to the north or south. Possibly a slight strike-slip movement exists expressed in the pull-apart basin near the Edmond hydrothermal vent field. Furthermore, the rift shoulder which bends into the rift valley could also be an indicator for changing states of stress and an evolving discontinuity structure in the future.

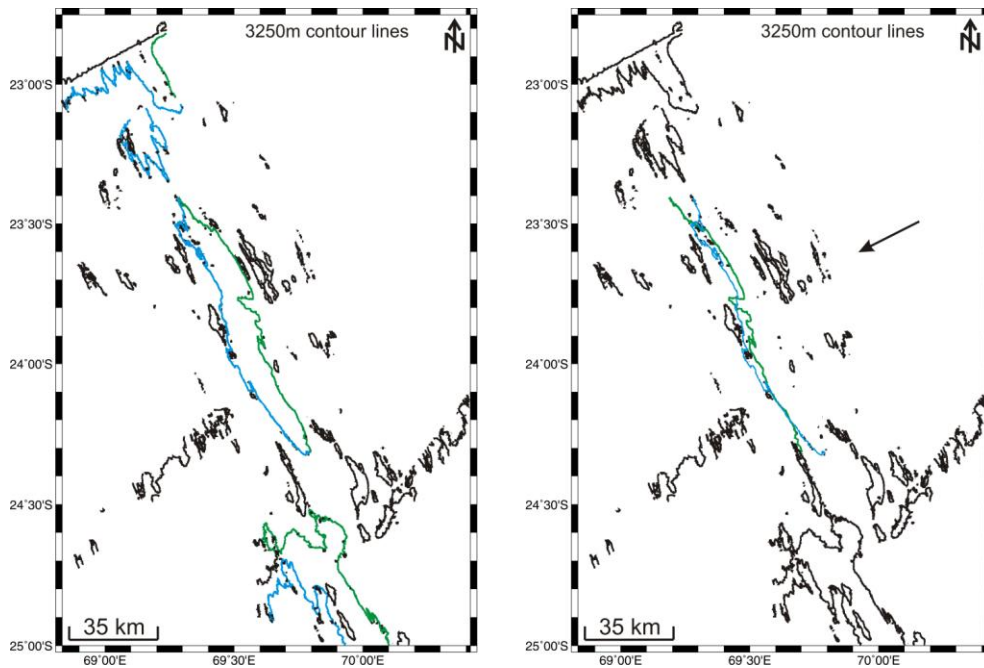


Figure 101: 3250 m contour lines of Meso and Edmond and the movement process to reconstruct the spreading movement. Blue lines mark the western ridge flank and the green lines the eastern one.

On a global scale BRIAIS (1995) found out that the relief across the rift valley decreases with increasing spreading rates. That is applicable to the working area Meso. At this place the spreading rate is highest along the slow spreading ridge with 5.0 cm/a and the rift valley morphology is very smooth with the two neovolcanic ridges inside of the valley. Also the magmatic activity increases with increasing spreading rates as the location Meso shows. Where the spreading rates decrease to 4.5 cm/a south of the Knorr rise the rift valley morphology becomes rougher.

SAUTER et al. (1996) published the spreading rate evolution over the CIR between 21°40'S and 22°10'S from 0-1.049 Ma as shown in **Table 6**. That area corresponds to the southern part of the working area EXFX including the bending section of the rift valley. For the time span 0-0.780 Ma the newest results of INDEX2011 show some deviations in the total spreading rates. The total spreading rate is 4.8 cm/a with 2.3 cm/a at the southwestern flank and 2.5 cm/a at the northeastern flank. The newest data show slightly higher values than the data from SAUTER et al. (1996), but these are just minimal variations and the results overlap within the error margins. As an important message the fact that the northeastern flank spreads faster can be seen in both datasets. During INDEX2011 only both flanks of Anomaly 1 were measured, that is why it is not possible to give a comparison with the data of SAUTER et al. (1996) for ages older than 0.780 Ma.

Time span [Myr]	Total spreading rate [mm/a]	SWflank [mm/a]	NEflank [mm/a]
0-0.780	45.5 +/- 2.4	20.8 +/- 1.5	24.7 +/- 0.9
INDEX2011	48.0 +/- 0.5	23.0	25.0
0.780-0.984	46.0 +/- 7.8	23.6 +/- 5.8	22.4 +/- 2.0
0.984-1.049	110.3 +/- 11.9	52.8 +/- 4.5	57.5 +/- 7.4

Table 6: Spreading rate evolution over the CIR between 21°40'S and 22°10'S from 0-1.049 Myr (after Sauter et al., 1996).

PARSON et al. (1993) described the evolution history of the CIR and the fracture zones in the vicinity of the RTJ as influenced by a complex development of short-lived discontinuities. They suggest that the regional trend of the CIR and its recent geometry evolved during the reorganization of the plate boundaries resulting from the collision of India with Asia. In this context it was necessary that the ridge developed its new geometry because the spreading direction changed at that time by about 30° clockwise. Further small-scaled reconfigurations of the ridge modified the geometry in the following time periods. PARSON et al. (1993) are convinced that the ridge system between the Gemino transform fault and the RTJ developed by an extension of the CIR since Anomaly 20 times (~45 Ma) and the orientation was controlled by the local tectonic evolution of the RTJ. Ductile, tectonic processes of the plate geometry arrangement take place within the warm, central parts of each segment. These processes facilitate the development of short, oblique offsets and overlapping spreading centers. A popular explanation for second order discontinuities like offsets is after PARSON et al. (1993) a new spreading direction which forces itself on existing ridge geometry. Responsible for variations in the character of offsets, their evolution and extinction are changes in spreading direction and/or spreading rate. Studies of SAUTER et al. (1996) have shown that south of 21°S to the RTJ the segments become younger in age and the last segment north of the RTJ evolved around 12 m.y. ago. In their analysis the average spreading rate for the last 50 m.y. (Anomaly 21) is 4.3 cm/a close to the RTJ and 3.4 cm/a to the north. The findings from their study seem to indicate that the CIR first developed during the late Cretaceous, 63 m.y. ago (Anomaly 29).

5.4) Intermediate spreading SEIR system

First of all the Rodriguez Triple Junction, defined by three ridge systems, two of them described during this study, will be analyzed from its evolving history. Afterwards the main characteristic features for the intermediate spreading SEIR such as the OCCs and the uplift behavior of the older ridge shoulders will be described. Finally, magmatically and tectonically active areas are shown.

Several authors like TAPSCOTT et al. (1980), PATRIAT & SEGOUFIN (1988), MÜNCH (1995) and HONSHO et al. (1996) have studied the evolution of the Rodriguez Triple Junction and believe that it evolves as a Ridge-Ridge-Ridge type triple junction since 60 Ma. For the last 10 m.y. the RTJ evolution can be described with such an R-R-R type velocity diagram where the CIR and SWIR are lengthening obliquely (TAPSCOTT et al., 1980; HONSHO et al., 1996). These authors argued that the SEIR segment nearest to the RTJ still remains constant in its length. With a look at the CIR and SEIR at the RTJ, a small offset between them becomes obvious (**Figure 49**). The size of this offset is important for the configuration mode of the RTJ. HONSHO et al. (1996) published an evolution cycle containing a continuous R-R-R mode and a discontinuous phase. They believe that if the offset between the CIR and SEIR remains small then the RTJ is in the continuous mode. When that offset gets larger, the phase of the RTJ changes into the discontinuous mode, which lasts until the CIR segment is completely separated from the RTJ. After HONSHO et al. (1996) one whole cycle over these two phases creates one CIR segment. The small ridge structure inside of the RTJ (**Figure 49**) can be explained as being previously a part of the Australian plate, which has been transferred to the African plate by recent rifting of a small segment of the southern end of the CIR (HONSHO et al., 1996). Today the RTJ is a stable R-R-R type triple junction as believed by MITCHELL & PARSON (1993) and MÜNCH (1995). Other authors like MUNSCHY & SCHLICH (1989) published that the RTJ can be explained by an instable Ridge-Ridge-Transform model. PATRIAT & COURTILLOT (1984) suggest that the RTJ evolved out of two different phases, first the effusive one which represents the R-R-F model and second a tectonic one representing the R-R-R model. These two phases alternate with a frequency of 1 m.y. depending on the dominance of magmatism or tectonism (PATRIAT & COURTILLOT, 1984; SEARLE, 2013). The stability of the configuration of the RTJ whether it is in a R-R-F or R-R-R mode depends on the geometry of the three spreading ridges and the relative velocities between them (SEARLE, 2013). To summarize, with the new bathymetric map of the RTJ and the resulting

structural analyze a R-R-R configuration of the triple junction can be confirmed. An indication for this assumption is the offset between the CIR and SEIR, seen in the newest dataset, as well as the identification of indicators for tectonic activity such as the inward-facing faults at the CIR and SEIR and the step faults at the SWIR.

The prominent oceanic core complexes of the intermediate spreading ridge system are located at the inside corners (**Figure 102**, schematic sketch) of the discontinuity structures. They can build when the melt supply falls to a critical level of approximately half the crustal accretion rate and end when the melt supply resumes (TUCHOLKE et al., 2008; SEARLE, 2013). In the case of the largest OCC in Section 1, the ridge flanks nearby bound to the east because of the uplift movement of the OCC. A detachment fault trace becomes very clear in the north-west of the OCC (**Figure 102**), where lower crust can be exhumed. The evolution of detachment faults is supported by tectonic extension due to magma delivery to the ridge axis, which is confirmed by the fact that detachment faults occur at segment ends (PETERSEN et al., 2009). The two smaller OCCs just start to evolve because their lineations and line of movement are not very well pronounced yet. With the help of bathymetric slope maps which mark out the lineations running perpendicular to the spreading axis it is easier to identify them. Lineation or mullion structures develop due to the movement of the ductile footwall, which is pulled

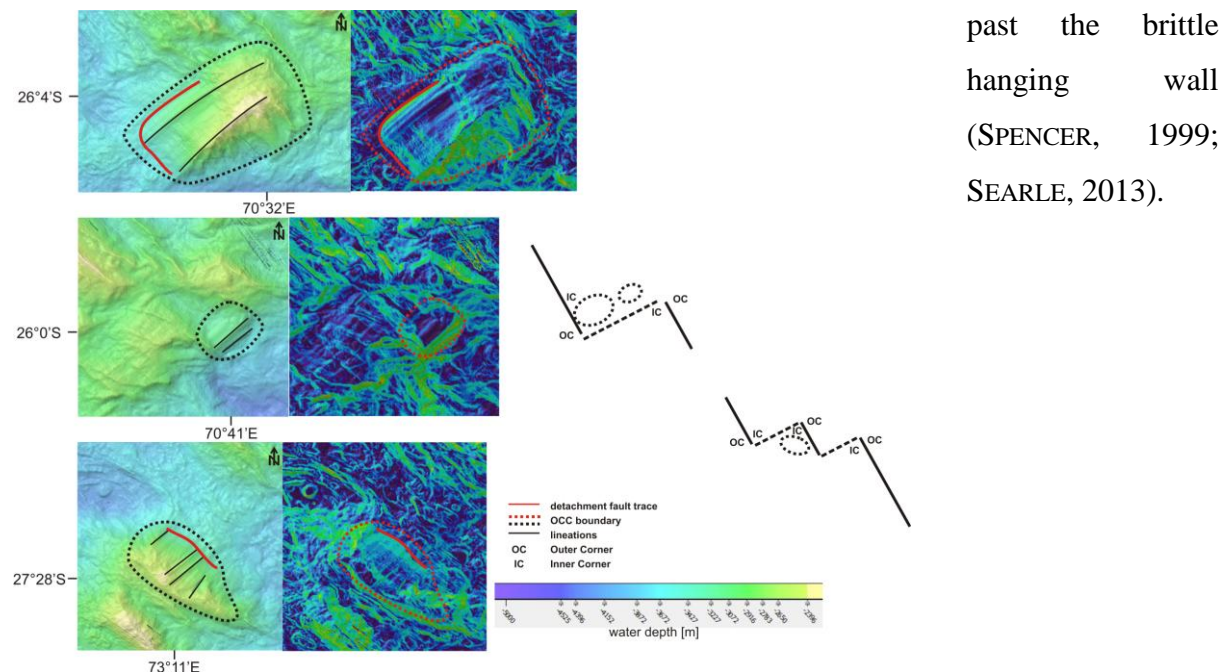


Figure 102: Bathymetric and slope inclination map of the three oceanic core complexes at the intermediate spreading ridge system. A schematic sketch of the location and the inner and outer corners is shown on the right side.

A very prominent feature along the mapped intermediate spreading SEIR is the more and less elevated behavior of the ridge shoulders corresponding to each other. As previously described for Sections 3, 4 and 6, the isostatical compensation behavior of the ridge is expressed in a stronger elevated ridge shoulder than the corresponding one on the other side. One explanation for stronger uplifted ridge shoulders could be an underlying magma chamber and the resulting difference in density. With a look at the maps of the seamount distribution this seems not to be the reason, because several seamounts occur on both sides of the rift valley. There is no pattern of seamount numbers increasing at the elevated rift shoulders. In contrast, many tectonically influenced seamounts lead to the conclusion that a tectonic process might be responsible for the uplift behavior. TUCHOLKE & LIN (1994) and previously

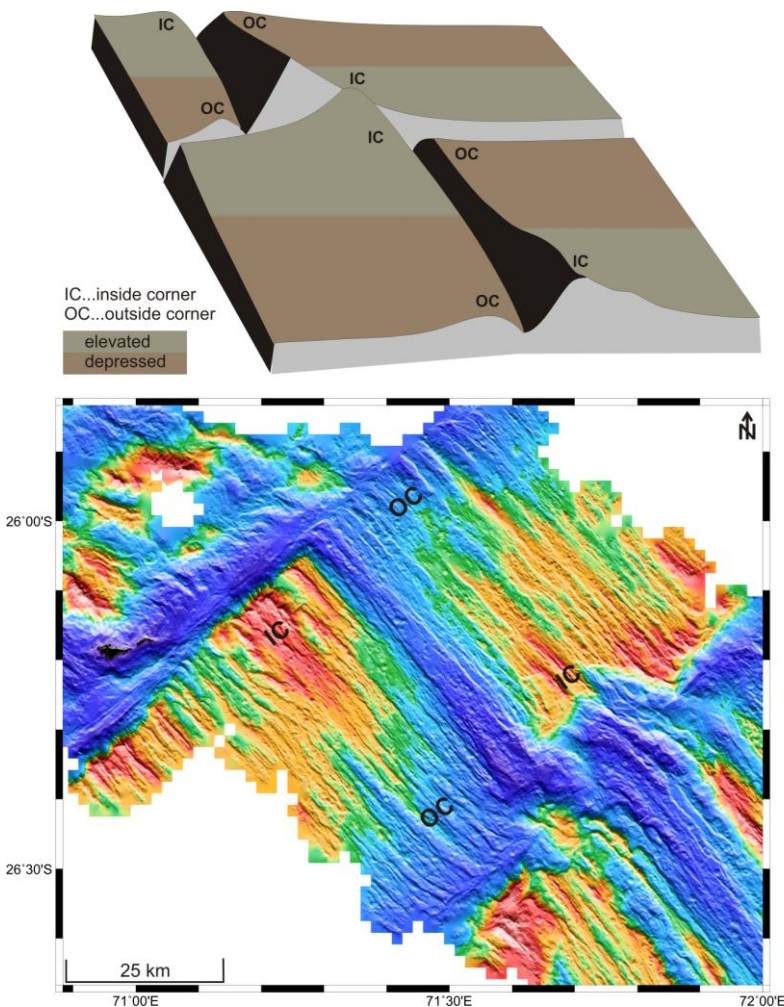


Figure 103: Uplift behavior of the ridge shoulders in a schematic sketch at the top (after TUCHOLKE & LIN, 1994, modified) and as an example Section 3 of the SEIR below.

(TUCHOLKE & LIN, 1994). SEARLE (2013) published that outer corners are defined by relatively old, cold lithosphere which lies deeper because of its greater density while on the

SEVERINGHAUS & MACDONALD (1988) have noted that along mid-ocean ridges the inner corners (IC) of a segment are elevated whereas the outer corners (OC) are depressed (Figure 103 top). They suggest that the surface of the oceanic crust slopes downward from inside to outside corners. An explanation for the elevating behavior at inner corners includes static and dynamic components

contrary inner corners are decoupled from the older lithosphere by detachment faults and thinner, thus more uplifted.

SAUTER et al. (1991) found out for the evolution of the segments that magmatic and tectonic phases vary episodically. During magmatic periods, volcanic and thermal processes take place in the axial zone above the melt reservoir where the crust is weakened. In these periods the axial valley is filled up with lavas and bulges under thermal effects. When the melt reservoir becomes empty this bulged zone collapses by thermal subsidence. The second period defined by SAUTER et al. (1991) is the tectonic phase. During this phase the axial zone is no longer melt enriched. Tectonic processes like active faulting and block tilting take place and extend over tens of kilometers away from the ridge axis.

Indicators for magmatic activities are seamounts. In contrast to the slow spreading CIR, obviously more seamounts occur at the intermediate spreading SEIR. It becomes clear that with increasing spreading rates magmatic processes also occur more frequently. With a look at the seamount distribution maps of **Chapter 4.2.1** and the summarizing **Figure 104** the first obvious matter of fact is a decrease in seamount occurrence at the two accommodation zones

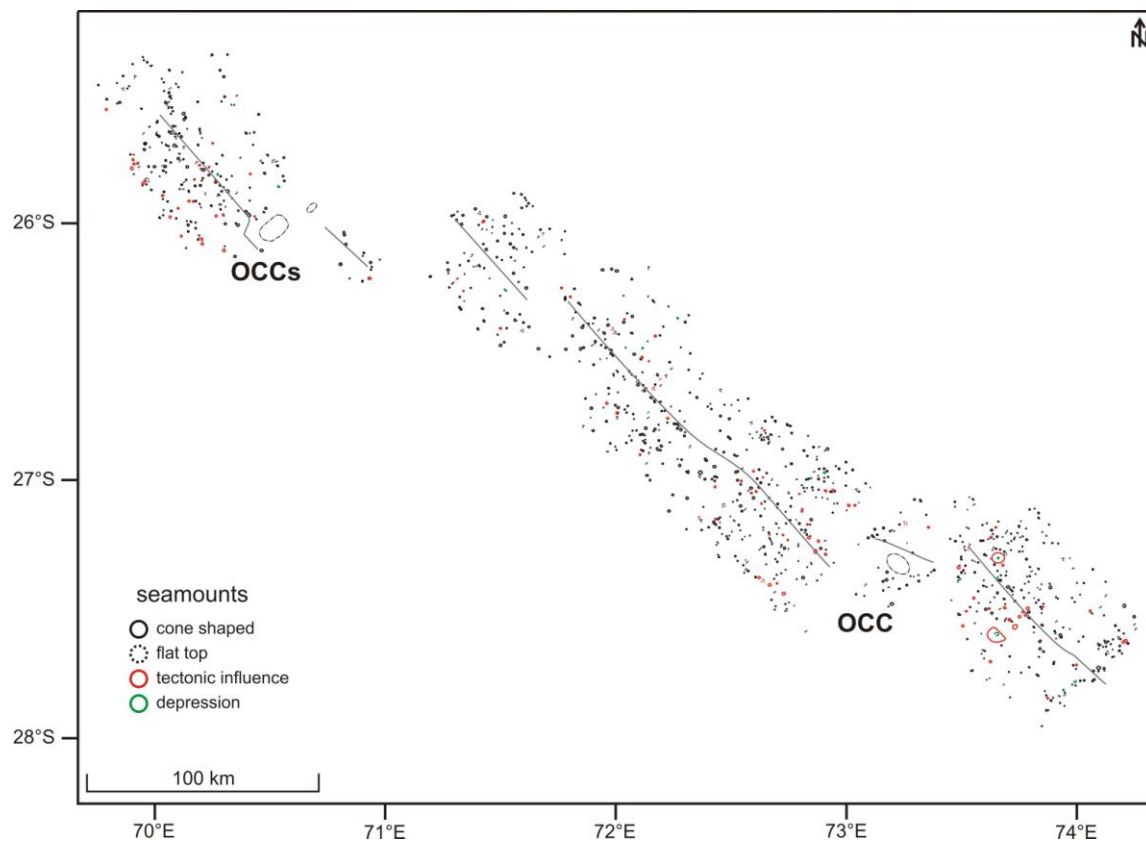


Figure 104: Seamount distribution map along the whole mapped SEIR divided into those who are cone shaped, have a flat top or are tectonically influenced. The green circles mark depression structures.

Sections 2 and 5. This observation results in the assumption that these areas are influenced by tectonic processes described later. The other sections are characterized by a high number of seamounts where on average the majority of seamounts is located on the western ridge flank and leads to the assumption that the magma chamber has a western trend (**Figure 105**). Furthermore, in contrast to the CIR many seamounts show tectonic influences, they are sheared. In those areas (western flank of Section 1 and central part of Section 6) the tectonic event must be younger than the magmatic activity. Section 3 is defined by many seamounts which are located directly on faults but showing no shear movements. That implies a recent magmatic activity which is younger than the tectonic phase. Flat-topped volcanoes which do not occur systematically, but show a slight tendency to the segment ends, are formed by long-lived eruptions which produce a lava lake and surrounding levees (CLAGUE et al., 2000, SEARLE, 2013).

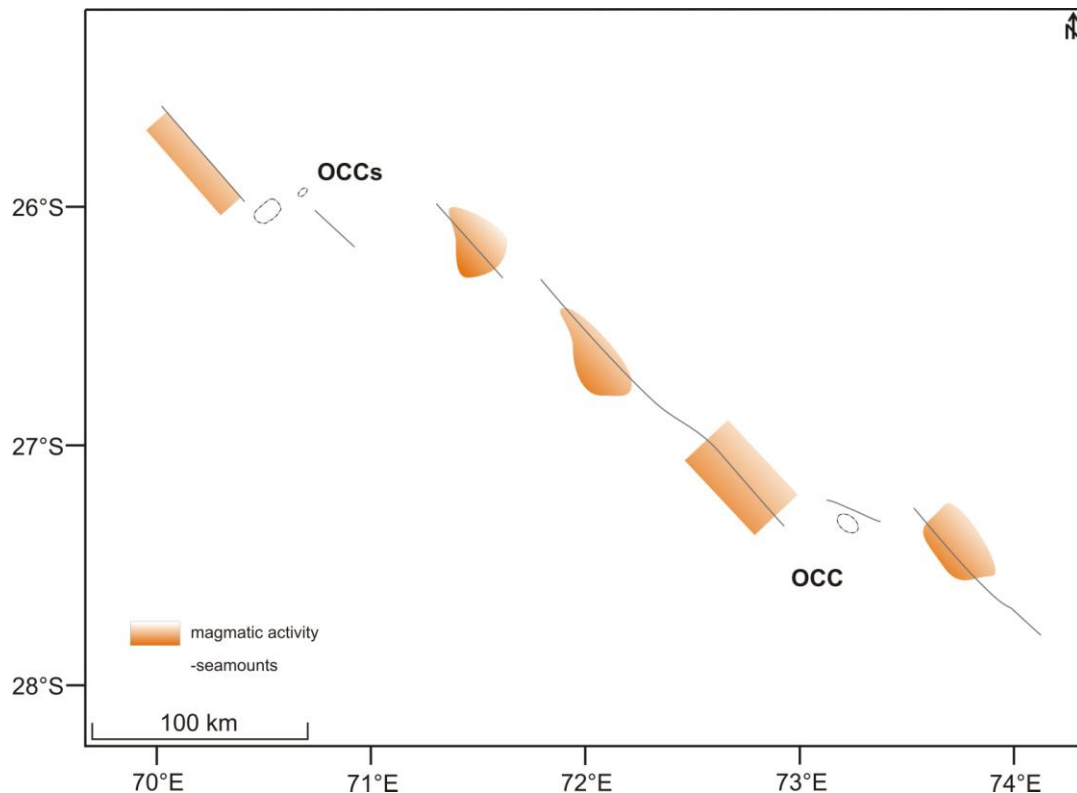


Figure 105: Estimations of the magmatically active zones resulting from the seamount distribution maps and the tendency of a magma chamber beneath the ridge axis or to the ridge flanks.

To summarize, the intermediate spreading ridge seems to be characterized by a magma chamber which is in general more pronounced to the western ridge flanks. Within the magmatically active areas some local tectonic activities take place identified with sheared seamounts.

Tectonically active areas like Sections 2 and 5, defined as accommodation zones, show less volcanic activity and increasing water depths. It can therefore be concluded that these sections have no magma lens beneath. At these places the tectonic influence is highest, causing the ridge axis to be offset. In each case two basin structures can be observed in the northern part of the accommodation zones which also lead to conclude that extensional movements take place (**Figure 107** i-j). From the fault distribution in these areas many different strike and dip directions could be determined. SAUTER et al. (1991) argued that local variations in the facing direction of faults and their strike correspond to a change in the strike of the axial valley which can be seen in Sections 2 and 5. This can be summarized under the keyword microsegmentation (SAUTER et al., 1991). An increase in spreading velocities near and at the discontinuities along the whole mapped SEIR confirms the tectonic influence as well. Magnetic data of profiles 226 and 234 both show a double Jaramillo event. SCHULZ et al. (1988) as well as CONDER & FORSYTH (2001) attributed such double Jaramillo events to small ridge jumps of less than 10 km (MITCHELL, 1991). This explanation can be supported with a look at the location of both profiles. Profile 226 is situated in direct vicinity of the strike-slip fault and profile 234 lies south of the discontinuity which separates Sections 3 and 4. Ridge jumps are caused by a reheating and thinning of the lithosphere in the vicinity of the ridge axis (ROYER & SCHLICH, 1988). The inward-facing faults which are typical for Sections 1, 3, 4, and 6 (**Figure 106** and **Figure 107**) and which run parallel to the rift valley evolve at the ridge axis. As shown in **Figure 94**, they are transported away by rifting processes afterwards. These older faults reflect neovolcanic zones linked to intense periods of magmatism (SAUTER et al., 1991). Like CAMHs they would correlate to positive magnetic peaks. An increasing tectonic influence can be seen on the western flank at the end of Section 6. Here, the seamounts get more influenced by faults and the seamount distribution decreases. Additionally, from the magnetic data it is obvious that the western flank starts to spread faster than the eastern side. The strike-slip fault at 71°E is referred to by TAPSCOTT et al. (1980) and MÜNCH (1995) as an indicator for the relative movement between Indian and the Antarctic plate.

Figure 108 summarizes the areas which are tectonically active at the intermediate spreading SEIR. Mainly these are the two accommodation zones with the OCCs and the other discontinuity areas. Also some basin structures are hints for the tectonically active regions.

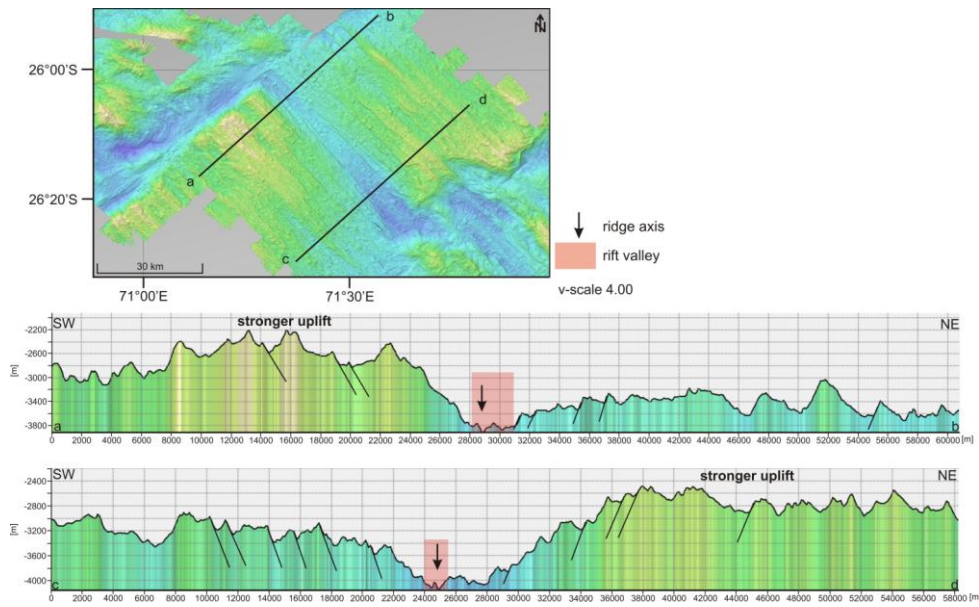


Figure 106: Profiles across the ridge axis of Section 3 which points out the elevated and depressed rift shoulders as well as the inward facing normal faults.

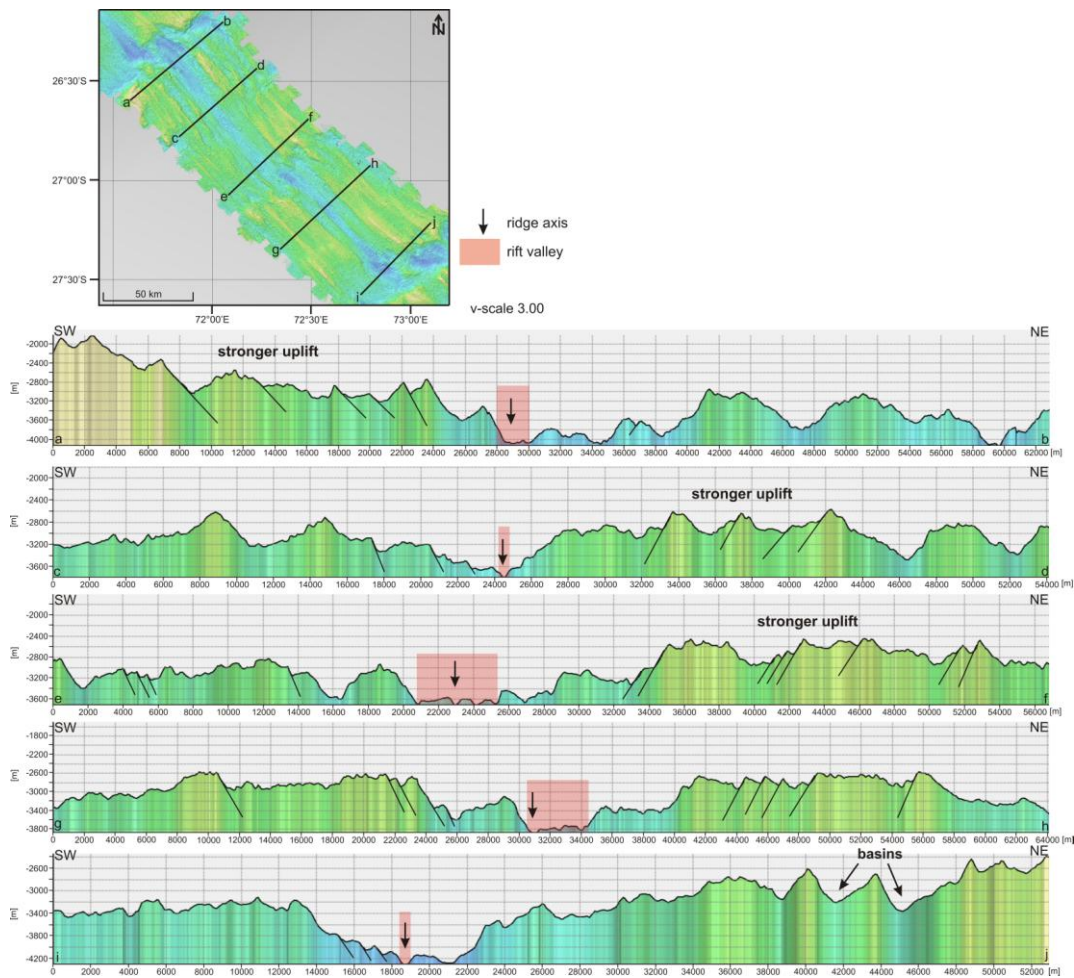


Figure 107: Profiles across the ridge axis of Section 4 from southwest to northeast with major faults and two basin structures at the end of this section as an expression for extensional movements.

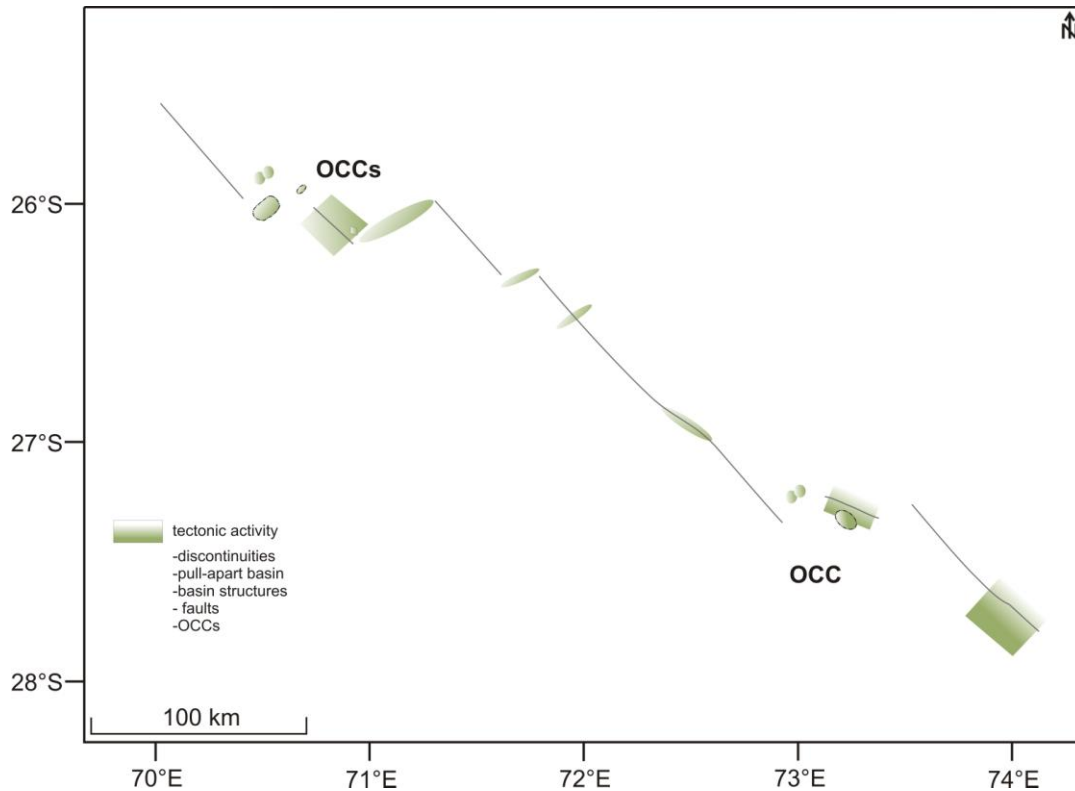


Figure 108: Tectonically active areas of the whole mapped SEIR resulting from the appearance of discontinuities, basins, faults and OCCs.

The process of spreading in Section 1 can be reversed in a model with the 3500 m contour lines as shown in **Figure 109**. With the northeastern plate moved back to the southwest the rift valley can be closed. Only a small area in the south still remains open. This is the location of the OCC where the ridge axis is offset by 7 km.

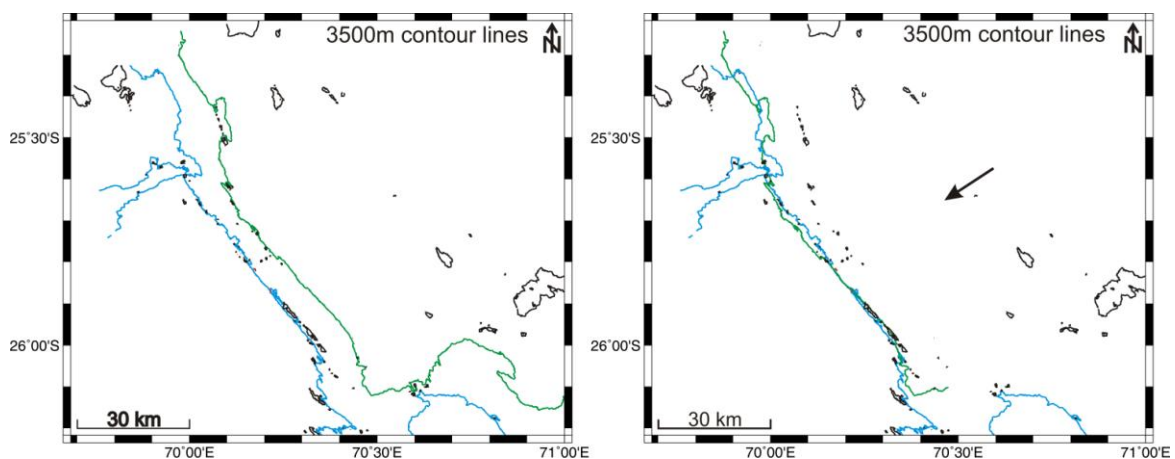


Figure 109: 3500 m contour lines of Section 1 and the movement process to reconstruct the spreading movement. Blue lines mark the western flank and the green lines the eastern one.

A simple spreading movement was identified in Section 3 using the 3500 m contour lines (**Figure 110**). There the spreading of the ridge flanks can be reversed with a simple movement of the northeastern plate to the southwest. In the southern part the area near the evolving discontinuity still remains open. Possibly at this place the first extensional movements took place.

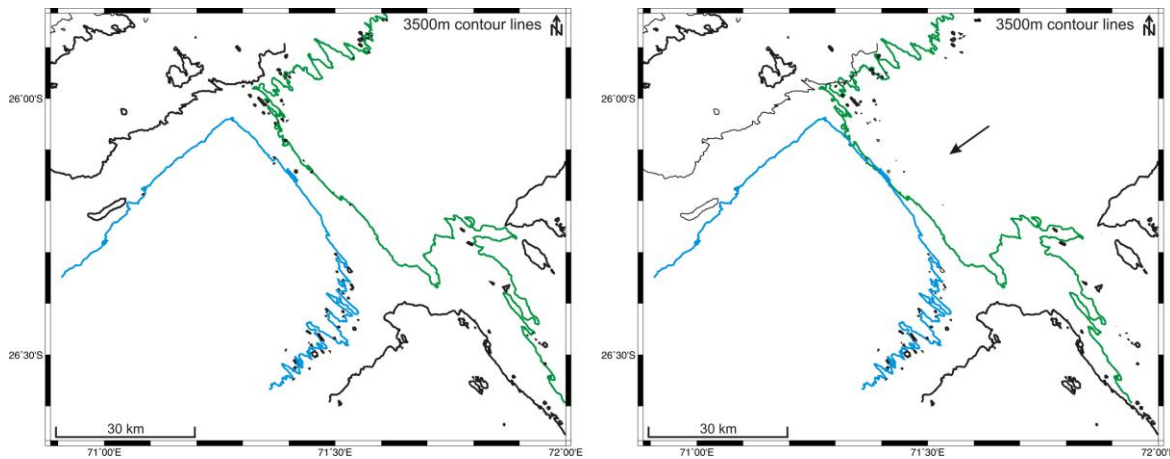


Figure 110: 3500 m contour lines of Section 3 and the movement process to reconstruct the spreading movement. Blue lines mark the western flank and the green lines the eastern one.

With a simple spreading SW-NE movement in Section 4 (**Figure 111**, 3250 m contour lines), the area of the second evolving discontinuity remains open. That part can be closed if an additional shear movement is assumed.

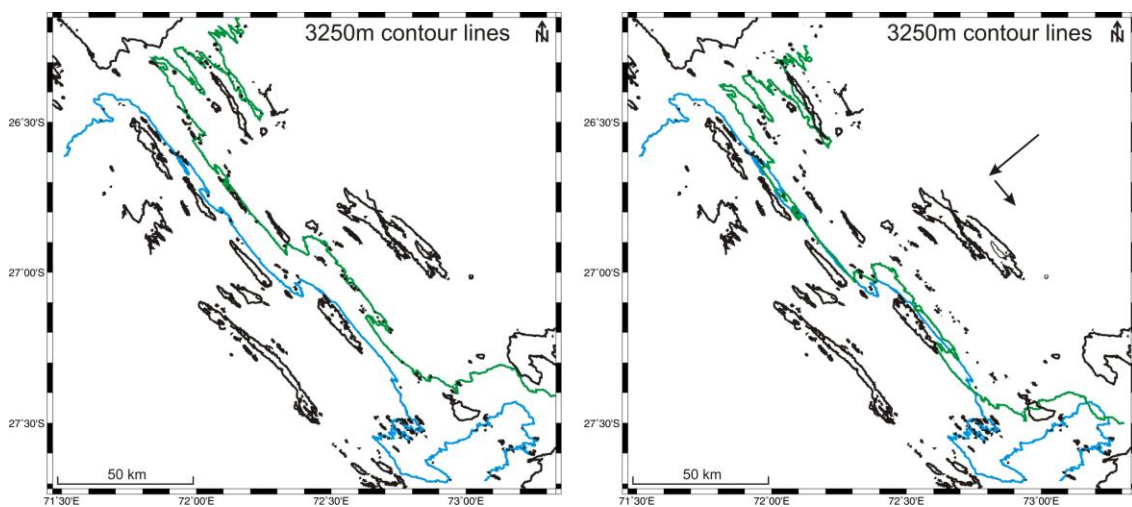


Figure 111: 3250 m contour lines of Section 4 and the movement process to reconstruct the spreading movement. Blue lines mark the western flank and the green lines the eastern one.

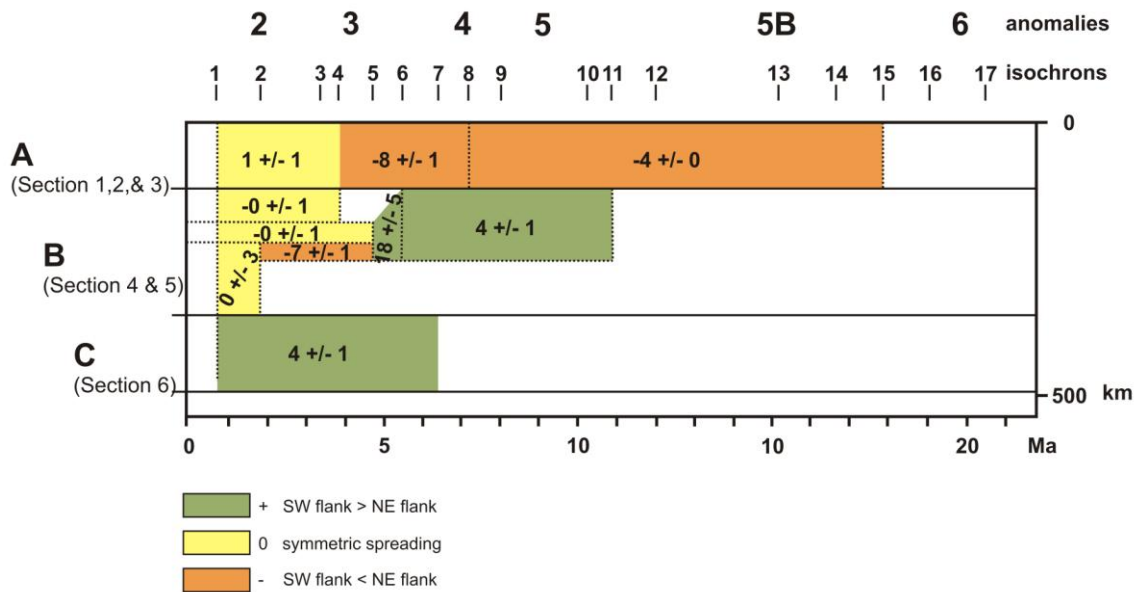


Figure 112: Spreading rate development over the SEIR (after ROYER & SCHLICH, 1988, modified).

For the interpretation of the spreading rate history ROYER & SCHLICH (1988) used magnetic data from cruises between 1961 and 1984 and the reversal time scale of LOWRIE & ALVAREZ from the year 1981, where Anomaly 5 starts at 10.3 Ma and Anomaly 6 begins at 24.6 Ma (boundary Miocene/Oligocene). The spreading rates along the SEIR vary considerably which can be seen in the profiles measured at the same ridge flank and ridge segment. ROYER & SCHLICH (1988) identified three spreading episodes for the SEIR. The first episode between Anomaly 18 and 11 was characterized by full spreading rates of 6.0 and 8.0 cm/a. During the second phase between Anomaly 11 and 5 the spreading rates decreased to an average value of 2.5 cm/a. In the third, the recent episode, the spreading rates show a slight increase to 3.0-3.5 cm/a. Since 20 Ma the northeastern ridge flank has higher spreading rates than the southwestern flank. The spreading along the SEIR is asymmetrical since the Miocene. **Figure 112** represents the evolution of symmetric or asymmetric spreading along the SEIR. The letters A, B and C can be compared to the working areas of INDEX2012 (A = Section 1, 2 and 3; B = Section 4 and 5; C = Section 6). After ROYER & SCHLICH (1988) region A is defined by a symmetric spreading until Anomaly 2, but the results from the INDEX cruise show a slight asymmetric spreading with 2.60 cm/a to the west and 2.65 cm/a to the east (**Figure 113**). Area B should spread symmetrically after ROYER & SCHLICH (1988) while the results from INDEX definitely show an asymmetric spreading of 2.60 cm/a west and

3.00 cm/a east and more to the south 3.20 cm/a west and 2.60 cm/a east (**Figure 113**). The results of area C agree with the results from INDEX, here the southwestern ridge flank spreads faster with 3.20 cm/a than the northeastern ridge flank with 2.60 cm/a. After a massive change in spreading direction during the Middle Eocene (Anomaly 22-19) the SEIR spreads with medium spreading rates of 5-7 cm/a at a stable direction of N045°. Magnetic profiles between 25.5°S (RTJ) and 41°S (southeast of Saint-Paul island) show half spreading rates of 2.7-3.5 cm/a between 0 and 8 Ma and 2.4-3.1 cm/a between 8 and 20 Ma (ROYER & SCHLICH, 1988). With increasing distance from the RTJ to the south the spreading rates also increase. This behavior can be seen with the recent magnetic data as well (**Figure 76**) where the spreading rates increase from 5.3 cm/a at the RTJ up to 5.7 cm/a at 74°E.

	0-2 Ma	2-4 Ma
Section 1+2	SW < NE 2.6 cm/a < 2.65 cm/a	SW < NE 2.55 cm/a < 2.65 cm/a
Section 3+4 <small>(Section 4 northern part to central)</small>	SW < NE 2.6 cm/a < 3.0 cm/a	SW = NE 2.9 cm/a = 2.9 cm/a
Section 4+5+6 <small>(Section 4 central part to southern end)</small>	SW > NE 3.2 cm/a > 2.6 cm/a	SW < NE 2.8 cm/a < 4.0 cm/a

Figure 113: Overview of the spreading rate evolution from 0 to 4 Ma and the behavior of the ridge flanks spreading faster or more slowly, based on INDEX magnetic data and a new analysis of three older magnetic profiles from the GEODAS database.

To sum up the results of both studies the first obvious fact is the time in which the data were collected. ROYER & SCHLICH (1988) used data from 1961-1984 and the magnetic data of INDEX2012 were measured in 2012. Hence, there is a great difference in resolution and accuracy which further develops with time. A second fact is the used time reversal scale which differs between the one from LOWRIE & ALVAREZ (1981) and the one from CANDE & KENT (1995). The general trend that the northeastern flank spreads faster than the southwestern flank can be observed in both data sets. In case of INDEX 2012 only a time span of 0 to 4 Ma can be covered and the time interval 2-4 Ma just with reprocessed transit profiles from the GEODAS database. However, the large number of profiles and high data quality make clear that for the younger time the INDEX results are more reliable.

5.5) Slow vs. Intermediate

To sum up the most prominent characteristics of the slow spreading CIR and the intermediate spreading SEIR they will be compared in the following. The sketch of **Figure 114** summarizes the most important results deduced from bathymetric and magnetic data. First of all it becomes clear that the intermediate spreading ridge shows more discontinuities or evolving ones. It is more segmented and thus more tectonically influenced. Both ridges have in common that their eastern ridge flank is more uplifted in total and steeper than the western flank. As shown with the fault distribution maps, the slow spreading ridge is characterized by normal faults which face towards the rift valley, so called inward-facing faults, also described by several authors (TAMSETT & SEARLE, 1988; WHITMARSH & LAUGHTON, 1976; MITCHELL, 1991). The intermediate spreading ridge in contrast has besides inward-facing faults also faults which dip away from the rift valley, defined as outward-facing faults (HUMLER & WHITECHURCH, 1988; MITCHELL, 1991). A lower amount of magma intrusion and off-axis lithosphere thickening produces larger, widely spaced faults at magmatically starved ridges like the slow spreading one (ITO & BEHN, 2008). Large magma intrusions and rapid off-axis cooling of the crust is responsible for small, closely spaced faults and magmatically robust ridges like the intermediate spreading ridge (ITO & BEHN, 2008). The two ridge systems have prominent structures of oceanic core complexes, one at the slow spreading ridge and three at the intermediate spreading ridge (**Figure 115**). They are located relatively close to the RTJ with exception of the third, small evolving OCC at the SEIR, and they are situated at the inside corners of discontinuity structures. With a look at the magmatic activity, the slow spreading ridge shows on average less seamounts than the intermediate spreading one. At this point it has to be emphasized that the two ridge maps were acquired with different multibeam echo sounder systems. The EM122 used in the case of the intermediate spreading ridge provides significantly higher data quality and resolution. From the global view, the majority of the seamounts are located on the western ridge flanks on both ridges leading to the assumption that there are asymmetric magma lenses beneath the rift valley (**Figure 115**). Outstanding features regarding the volcanic activity are the neovolcanic ridges at the slow spreading ridge. The intermediate spreading ridge has more seamounts but no indications of neovolcanic ridges are observed, at least no distinct evolved neovolcanic ridges like the ones at the Sonne field or in the southern part of the working area Edmond. A reason for the lack of neovolcanic ridges along the intermediate spreading SEIR could be the behavior of the

magma chamber. With decreasing spreading rates the magma lens will become deeper (PHIPPS MORGAN & CHEN, 1993; BARAN et al., 2005). Consequently, the slow spreading CIR must be characterized by a deep magma chamber. When magmatic activity takes place along the slow spreading CIR, the magma source lies very deep and hence, at the seafloor it occurs more like a point source resulting in neovolcanic ridges and less seamounts. At the intermediate spreading SEIR the magma chamber has a shallower depth and a broader expansion hence, magmatic activity can occur over a wider area. Slow spreading ridges are defined by a small width of the rheological weak zone where the lithospheric deformation occurs (SMALL et al., 1999). In contrast to this, at intermediate spreading ridges age dependent strengthening does not create a narrow weak zone and deformation can occur over a broader plate boundary zone (SMALL et al., 1999). In terms of the spreading velocities both ridges spread asymmetrically with a faster eastern ridge side except for the southern part of the intermediate spreading ridge where this behavior changes and the western ridge flank gets faster (**Figure 114**). This behavior can be explained with the relative movement directions

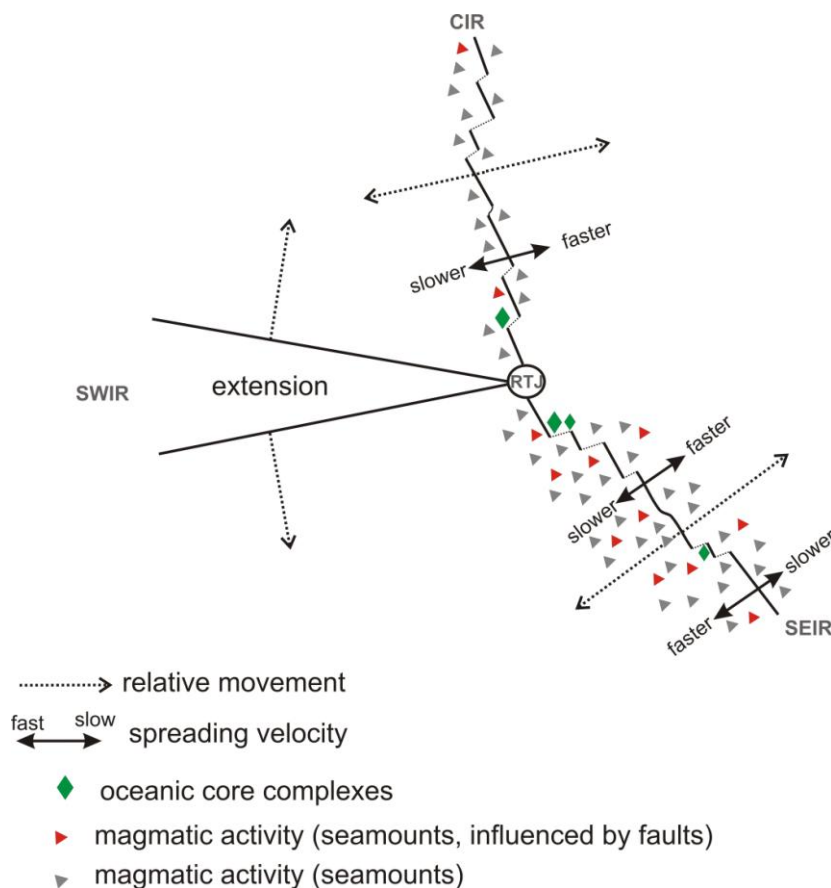


Figure 114: Schematic sketch of the three ridge systems at the RTJ and their relative movement as well as the spreading velocity behavior and magmatic activity at the CIR and SEIR.

(**Figure 114**, dotted arrows) of the ridges. Because the SWIR extends like a wedge there is not much space for the western ridge sides of the CIR and SEIR. The only way to move faster is the northeastern side because there is over a long distance no structure which could block the spreading movement of the ridges.

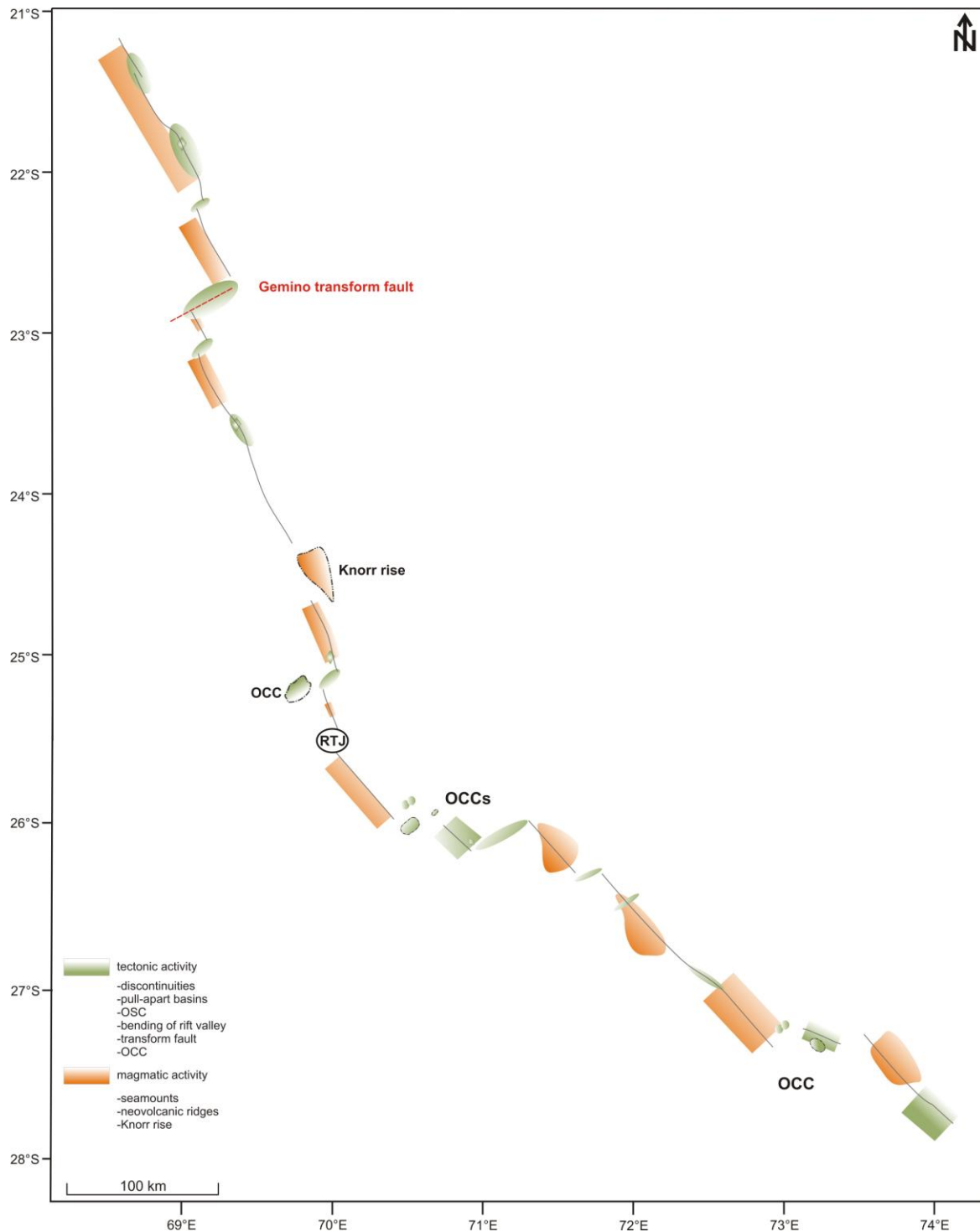


Figure 115: Schematic sketch of the CIR and SEIR with tectonically and magmatically influenced areas. The estimation of the magmatically influenced areas results from the seamount distribution along both spreading ridges. Tectonically active areas are characterized by discontinuities, pull-apart basins, overlapping spreading centers, transform faults, and oceanic core complexes.

The summarizing **Figure 115** makes clear, that both spreading ridges are strongly tectonically influenced. The observation is supported by discontinuities, inward-facing faults, OCCs, and pull-apart basins. Nevertheless, there are some exceptional areas where magmatic activity

takes place. In the mapped area the SEIR obviously shows more well developed discontinuities and OCCs, furthermore the magmatic activity expressed by seamounts increases at the intermediate spreading ridge. Conspicuous is the fact that the asymmetric location of the magma chamber is opposed to the asymmetric spreading behavior. The northeastern ridge flank spreads faster but the magma chambers seem to be more pronounced to the southwestern ridge flanks as concluded from the seamount distribution maps. Hence, the magma chambers are located beneath the slower spreading southwestern ridge flank. Due to the faster movement of the northeastern ridge side there is no time for so many seamounts to evolve.

5.6) Magnetic modeling of Edmond

During a detailed mapping survey a bathymetric and magnetic grid was taken over Edmond (**Figure 116**). Three profiles were measured in E-W and N-S direction with a distance of ~1.3 km. This detailed magnetic survey with a reduced vessel velocity and closely spaced profile lines in different directions reveals a decrease in the magnetic susceptibility of the basalts, caused by the process of metal leaching right above the hydrothermal vent field and extends also to the south (**Figure 117**). That makes it possible that south of Score also hints for hydrothermally activity can be found. To get an idea of the dimensions of this hydrothermally influenced body a 3D forward modeling was done. Model and system parameters are explained in **Chapter 3.3**.

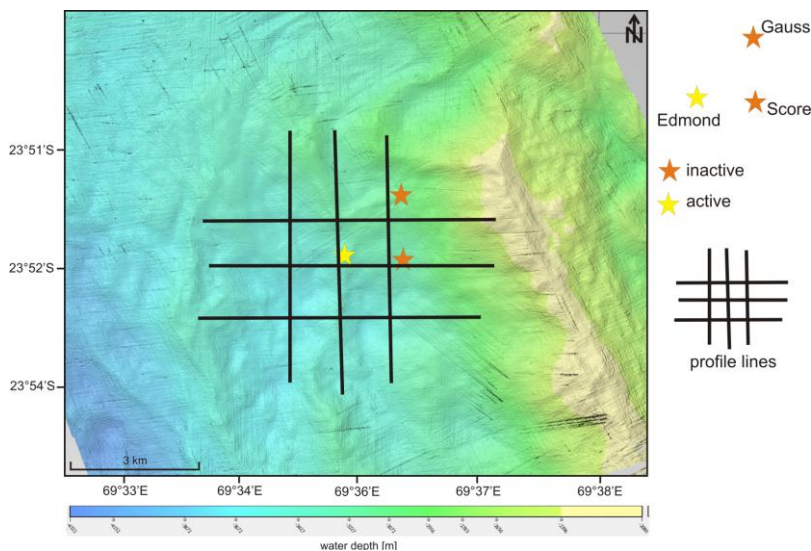


Figure 116: Bathymetric map with the detailed survey lines for Edmond.

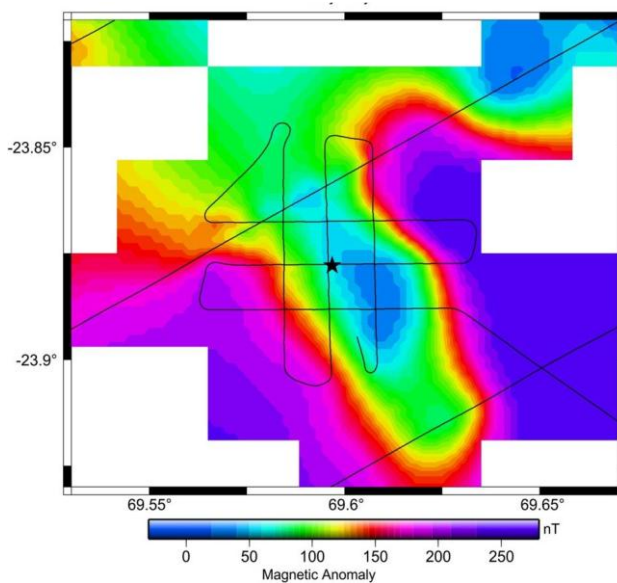


Figure 117: Magnetic map with superimposed survey lines of Edmond. The 50 nT line has a width of ~1.5 km. The blue area represents the decrease in magnetic values due to the process of metal leaching caused by the hydrothermal fluids.

According to the literature, Layer 2 of the oceanic crust consisting of basalts has normally the highest magnetization (LOWRIE, 2007). That does not mean that the gabbros are not magnetized. They show the same composition but are coarse grained. For the magnetic measurements structures close to the seafloor are of highest interest. That means the basalts are the primary source for the observed values in the total magnetic field and right above the hydrothermal vent field they seem to be demagnetized.

Figure 118 shows the results of the modeling process in 2D in summary. On the left side the measured magnetic values are illustrated and on the right side the calculated ones out of the modeling process. The blue area represents the decreased magnetic values with 50 nT as previously shown in **Figure 117**. It can clearly be seen that there is no 100% match especially at the northern edge but the area of interest fits very well. Modeling results indicate that the lateral extension of the hydrothermally influenced body increases from 1.5 km at Section 11 (**Figure 119**) to 2.5 km at Section 12 (**Figure 119**). At Sections 13 and 14 that lateral extension decreases to 2.3 km (**Figure 119**). More generally, there is a decrease in width to the north and south. The body has a minimum thickness of 4 km as pointed out in Section 12 (**Figure 120**). Section 14 reveals the rise of gabbros to the seafloor which can be proved with rock samples from that area including basalts and gabbros. The modeled dimensions of this body do not mean that the hydrothermal vent field or the sulfide mound have such dimensions. It is just the size of the rocks which are influenced by hydrothermal activities. With the dimensions of the modeling a simple volume estimation can be done in which the hydrothermally influenced body could have a volume of at least 35 km³ (**Figure 120**).

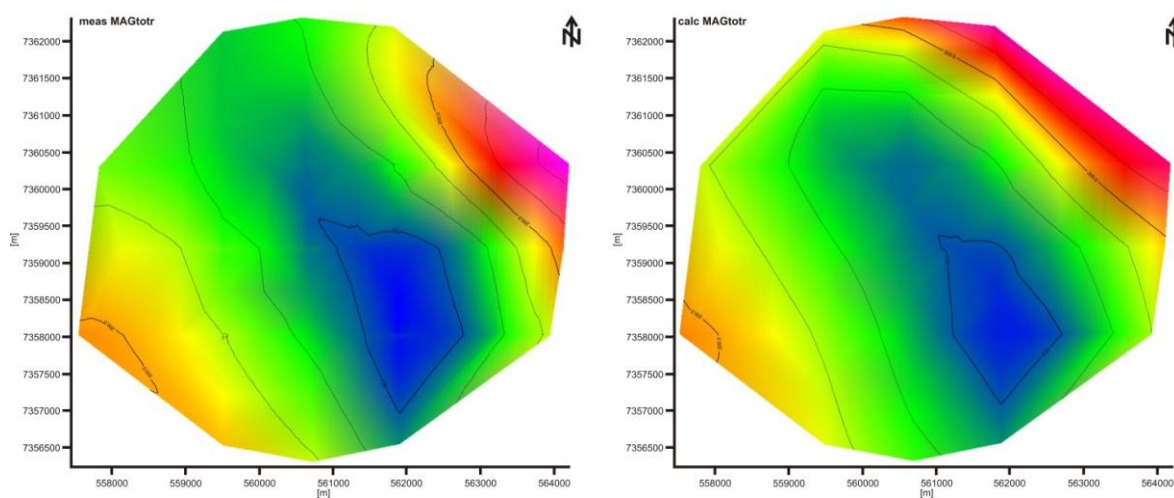


Figure 118: 2D view of the measured magnetic data on the left side and the calculated magnetic data on the right side. The blue area marks the decrease of the magnetic values due to hydrothermal influence.

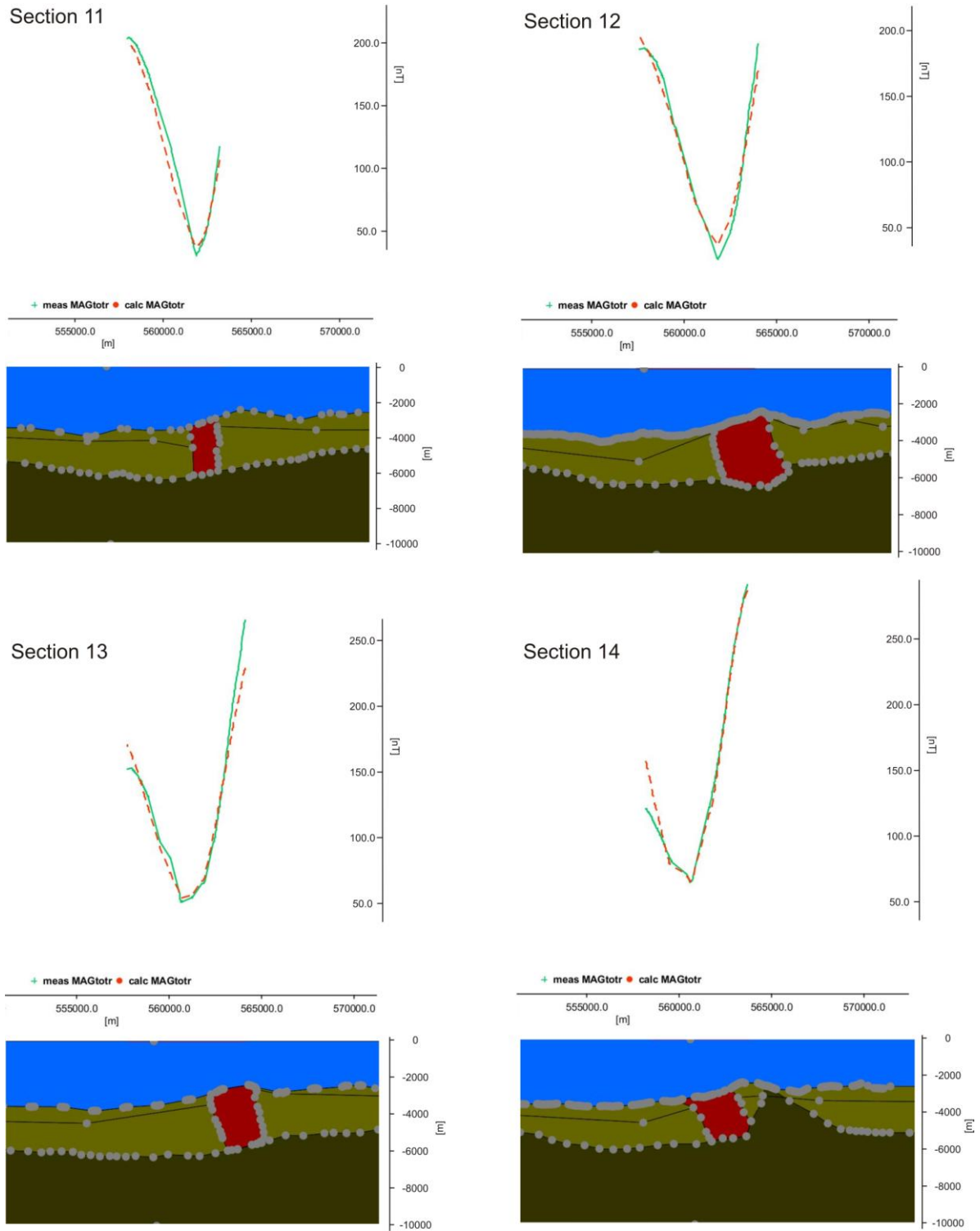


Figure 119: Modeled Sections 11 – 14 with the measured magnetic values (green line) and the magnetic values calculated from the model (red dotted line). Beneath each magnetic line the corresponding 2D section is shown with the basalts (light green), the grabbos (dark green), and the hydrothermally influenced body (red).

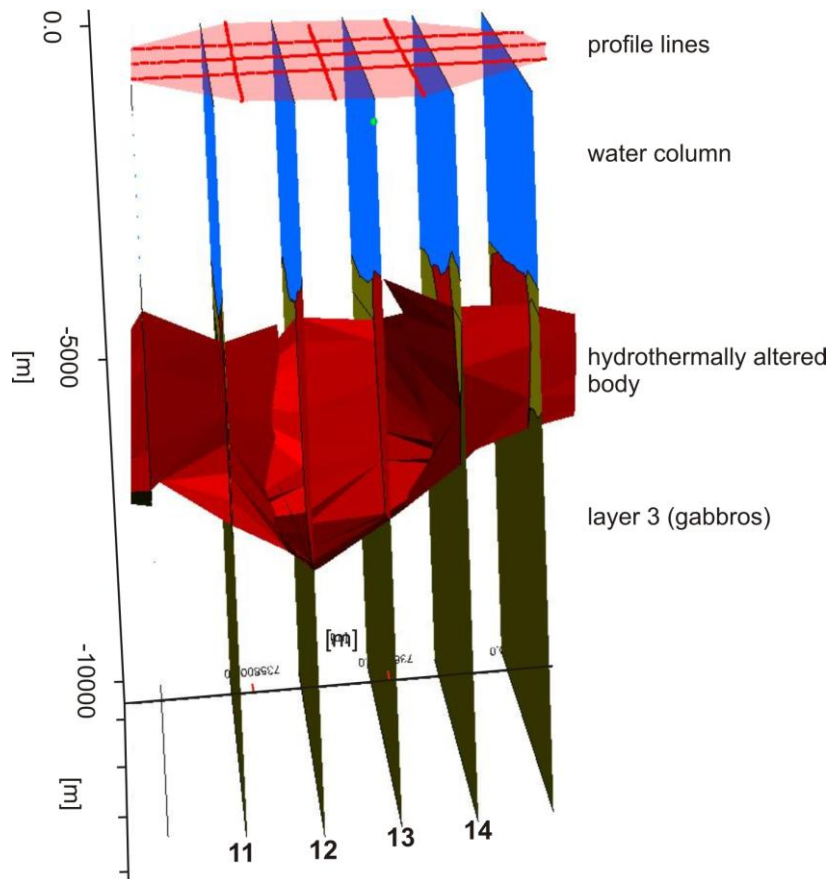


Figure 120: Hydrothermally altered body in a three dimensional view with the previously shown cross sections 11 to 14.

Deep-towed magnetic studies of TIVEY et al. (2003) show a decrease in magnetic values south of the TAG hydrothermal vent field in the Atlantic. They present two hypotheses for the evolution of these decreased magnetic values. First they argue that the decrease in magnetic values exists because of thermal demagnetization of the crust due to a broad thermally active region beneath the hydrothermal vent field. Secondly, and that is what the authors favor, the magnetic decrease could develop because of a thinned magnetic crust due to tectonic extension on a normal fault for example. With the modeled results of IGMAS+ the second hypotheses can be ruled out for the Edmond HTF because the thickness of Layer 2, the “magnetic layer”, does not decrease and remains more or less constant in thickness. Another difference in the measured values of Edmond is that the decreased values are situated directly above the hydrothermal vent field with expansion to the south. The data from TIVEY et al. (2003) show all in all a decreased magnetic zone which is shifted to the south and does not occur over the hydrothermal vent field. Attention must be paid to the data acquisition because the study of TIVEY et al. (2003) was done with deep-towed magnetics and the data from Edmond derived from sea surface measurements.

With detailed magnetic surveys at massive sulfide complexes on land TIVEY & DYMENT (2010) found out that strong demagnetization areas above the stockwork zone exist caused by the replacement of titanomagnetite with non magnetic sulfide minerals. TIVEY & DYMENT (2010) postulate that not all types of hydrothermal activity cause reduced magnetization. They have the opinion that in some cases hydrothermal activity can be the reason for the development of magnetite caused by a process called serpentinization and result in an increase of the measured magnetic values. At basalt-hosted hydrothermal systems, as it is the case for Edmond, the crustal magnetization is influenced by hydrothermal fluid circulations especially along upflow zones where high temperature fluids rise to the seafloor (TIVEY & DYMENT, 2010).

A combination of the bathymetric dataset with the mapped major faults and the magnetic dataset with the decreased magnetic susceptibility of the basalts right above the HTF result in a schematic sketch striking from southwest to northeast as shown in **Figure 121**. Seawater (blue lines) is able to migrate through the oceanic crust along fault zones and reaches the high-temperature zone of a magma chamber (yellow-orange body). Along at least two fault zones (red lines), mapped with the bathymetry, the seawater interacts with the surrounding rocks and leaches out the metals on its way up to the seafloor (orange lines). The now called fluids reaches the seafloor and due to the great temperature difference between fluids and seawater metals fall out and black smokers as observed for the Edmond hydrothermal vent field can evolve. The hydrothermally altered rocks (transparent red zone) produce the zone of decreased magnetic values as shown with the schematic magnetic behavior (black line) in the upper part of **Figure 121**. It is a decrease of the magnetic susceptibility of the basalts compared to the surrounding basalts which are not hydrothermally influenced. Dredging results have shown that beside basalts also gabbros can be observed at the seafloor. A possible mechanism for the exhumation of these gabbros to the seafloor could be one of the fault zones (red lines). In the schematic sketch the normal fault northeast of Gauss could be the place where the gabbros reach the seafloor. As the detailed magnetic survey has shown it seems to be very likely that south of Edmond and Score hydrothermal activity can be found as well.

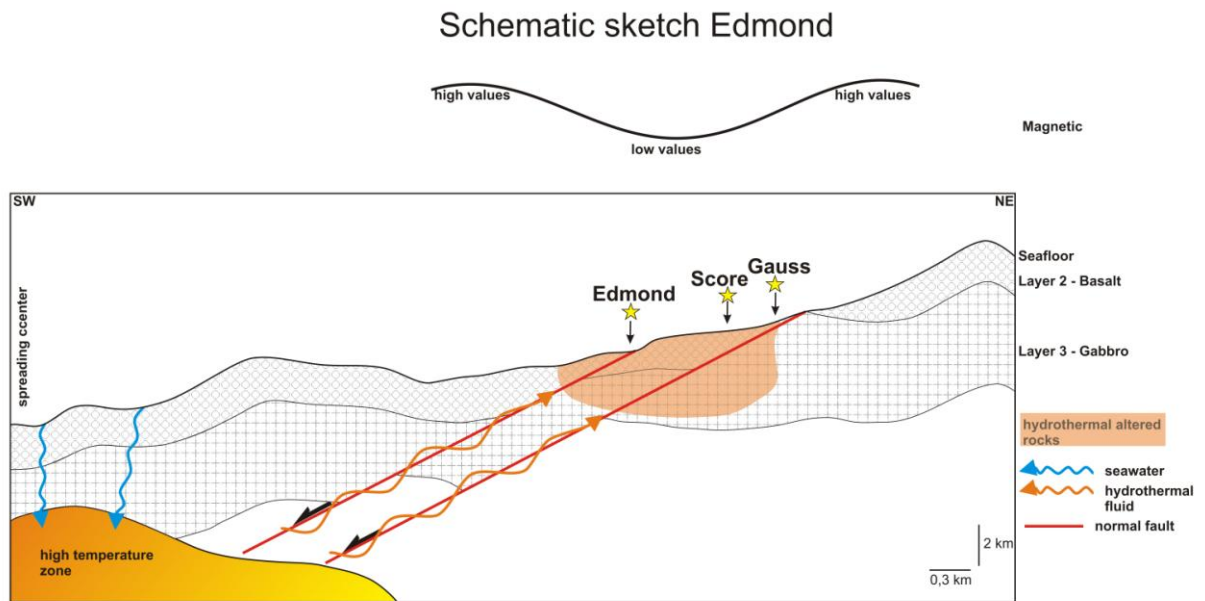


Figure 121: Schematic sketch of the Edmond HTF out of bathymetric and magnetic data and analysis.

Further investigations should include deep-towed magnetic and bathymetric surveys to get higher resolution data and seismic studies or drilling to get precise insight into the dimensions of the hydrothermally influenced body.

5.7) Characteristic areas of other HTFs

After a structural and magnetic interpretation of both ridge systems and a presentation of three hydrothermal vent fields an outlook will be given for further potential areas with hydrothermal activities. As summarized in **Table 7** several characteristic features exist which can be hints for hydrothermal activities and limit areas of interest along both ridge systems. From the magmatic point of view the most interesting observation is the lack of seamounts in the direct vicinity of the known hydrothermal vent fields. In the case of the Sonne field the neovolcanic ridge is an expression of high magmatic activity which presumably hinders the fluids to reach the seafloor (SEARLE, 2013) and results in an inactive hydrothermal vent field. From the tectonic point of view many characteristic features can be observed such as cross-cutting faults, the location at segment ends at discontinuities and a location on the steeper eastern ridge flanks. With a look at **Table 7** it becomes obvious that many more tectonic features play an important role for hydrothermal activities. This observation was previously made by several authors like GERMAN & PARSON (1998), PARSON et al. (2000), and GRÁCIA et al. (2000). They published studies from slow spreading environments where the magmatic activity is not the primary control for the distribution of hydrothermal vent fields. BAKER et al. (2001) have shown the same result for an area in the Pacific at 15°-18°N. Where less tectonic activity takes place, the axial surface appears smooth and not influenced by faults resulting in weak and sparse hydrothermal activities (BAKER et al., 2001). The authors also found out that on the other hand a well developed rift valley or deep faults cause increased permeability and hydrothermal activity. Measurement investigations have been done by GERMAN et al. (2010, 1998) and they argued that high-temperature vents will occur at least every 100 km along slow spreading ridge systems. This prediction could not be verified for the slow spreading Central Indian Ridge and its known hydrothermal vent fields. However, until now only three locations for hydrothermal activities are known which is not enough for such a statistic analysis.

An obvious tectonic feature ideally suited for hydrothermal vent fields are oceanic core complexes. As described in **Chapter 5.3** they develop with a detachment fault representing an ideal pathway for hydrothermal fluids. Furthermore, OCCs are characteristic for a high asymmetric form of lithospheric accretion and hydrothermal activity is more common at asymmetric segments (SEARLE, 2013). Thus it is likely that in the vicinity of the four OCCs of both ridge systems hydrothermal activity can be found.

In the following further potential areas for hydrothermal activity are shown primary based on areas with decreased magnetic values along both ridge systems (**Figure 122**, **Figure 123**, and **Figure 124**). In doing so only small, limited areas with decreased magnetic values are taken into account which make sense in terms of the dimensions of HTFs. Large areas with such decreased magnetic values are unrealistic and also edge effects next to prominent positive magnetic anomalies must be excluded. A special attention must be paid to those days during the measurements which are characterized by high Kp-values (Planetary index number K for magnetic activity). Introduced by BARTELS in 1939 (BARTELS, 1957) a planetary 3-hour Kp-Index can be calculated for each day. This index represents the effect of solar particle radiation on the Earth's magnetic field (BARTELS, 1957). High Kp-values mean increased magnetic activity which results in variations of the Earth's magnetic field within short time intervals. At the mid-latitude position of the survey areas it must be suspected that at Kp-values of 5 and more small observed magnetic anomalies on the order of 50 nT could be entirely the effect of the magnetic variations. After the selection based on the magnetic observations these areas are analyzed in terms of cross-cutting faults and other hints for tectonic activities with the goal that as many as possible observed features summarized in **Table 7** apply. Past studies of SCOTT et al. (1974) have shown that magnetic lows are caused by hydrothermal alteration of the magnetic minerals of the basalts. The authors postulate at that time that this observation could be a future exploration tool for the fast identification of hydrothermal vent sites.

Magmatic	Tectonic	Other
neovolcanic ridge (inactive Sonne field, too much heat)	inner corner (decoupling from lithosphere by detachment faults after SEARLE, 2013)	methane anomalies (vicinity of the OSC in EXFX after PLÜGER, 1988)
sheet flows (Sonne, Edmond, Kairei)	spreading rates (4.87-5.6 cm/a at known HTF)	zone of decreasing magnetic values (Edmond and Kairei)
lack of seamounts around the HTF	detachment faults	“wrong” beams (Edmond)
	OCCs	distance measurements (HTF every 100 km after GERMAN et al., 2010)
	segment ends (close to discontinuities; Edmond and Kairei)	large distance to spreading axis (Sonne, Edmond, Kairei)
	steeper eastern ridge flanks	
	cross-cutting faults (Edmond and Kairei)	

Table 7: Summary of features characteristic for the three hydrothermal vent fields along the CIR divided into magmatic and tectonic events and other characteristics.

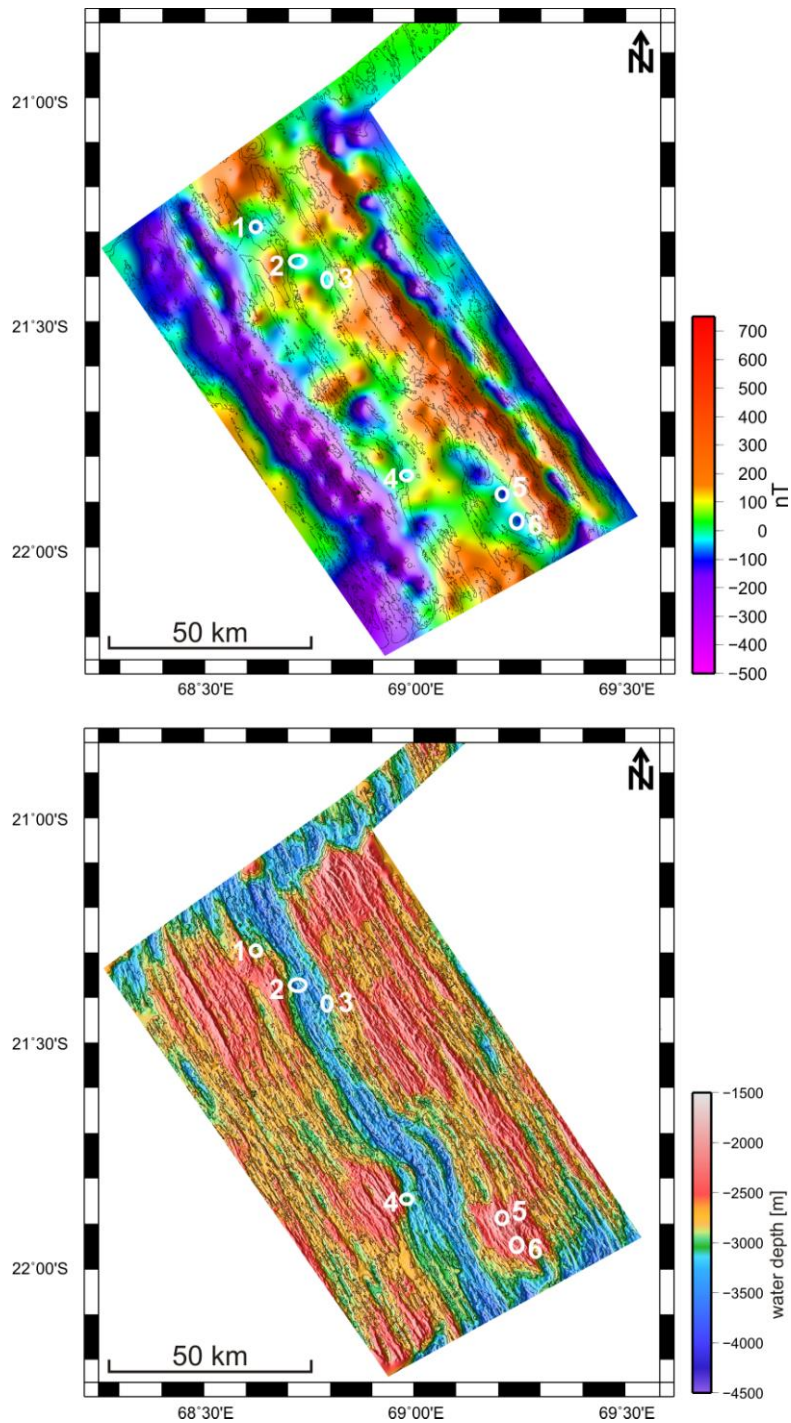


Figure 122: Magnetic (top) and bathymetric (bottom) map of the working area EXFX. Areas with a magnetic low are pointed out by circles and their positions are marked in the bathymetric map below as well.

In the working area EXFX six potential areas are observed from the decreased magnetic value analysis. They are shown in **Figure 122** and are applicable to tectonically active areas. Locations #2 and #3 are situated at the overlapping spreading center and in both cases at the end of the evolving ridge between the overlapping segments. This place is defined by a jump

of the ridge axis and hence an ideal place with pathways for the fluids. Locations #1, #4, #5 and #6 have a great distance to the spreading axis and except for #1 are located at the steeper flanks of the area (#4 on the western flank and #5, #6 on the eastern flank). #5 and #6 show similarities to the known Kairei hydrothermal vent field because they are located at the segment end, on the steeper eastern flank, and on an elevated ridge shoulder. Location #4 is situated at the northern end of the bending structure which with the pull-apart basin represents an area of extensional and strike-slip movement, ideal for evolving faults as pathways. The neovolcanic ridge inside the bending structure is an indicator for a heat source in the vicinity.

Within the working areas JX, Meso, Edmond and Kairei shown in **Figure 123** further seven locations with decreasing magnetic values are observed, counted from #7 to #13. Once again, locations #7 to #10 and #13 are situated in tectonically active areas and at the segment ends. Number 10 roughly corresponds to the known hydrothermal vent field Edmond. At this point it has to be mentioned that it seems to be possible to detect or limit potential areas for hydrothermal activities with magnetic data from the sea surface. The locations #8 and #9 are characterized by an evolving discontinuity, representing a perfect pathway for the fluids and they are far away from the ridge axis on the steeper eastern ridge flank. A heat source for these two locations could be the magma chamber beneath the Sonne field and due to a detachment fault the fluids can be transported away to the positions #8 and #9. Number 7, #11, and #12 are located in magmatically active areas. #11 and #12 are located exactly at the southwestern end of the Knorr rise where the ridge axis has jumped more to the west. Consequently, it can be looked upon as the way that a discontinuity structure would behave. So it is a magmatically active area, but due to tectonic movements pathways exists. As mentioned previously, OCCs are prominent structures for hydrothermal activities. Location #13 is situated directly on the northwestern flank of the OCC in the working area Kairei. That is the place of the detachment fault trace, the line of movement from the OCC structure, and therefore an ideal area for hydrothermal fluids to rise to the seafloor. Resulting from the Kp-Index analysis almost all days during the measurement of the Central Indian Ridge have had relatively calm conditions with Kp-values ≤ 4 with the exception of #11 and #12. These two locations, defined by the profiles CIR355 and CIR356 (Knorr rise), show high Kp-Index values ranging between 5 and 7. Consequently, these two locations must be viewed with caution in terms of the magnetic results. From the geologic point of view especially #12 seems to be promising because of the close proximity to an offset structure.

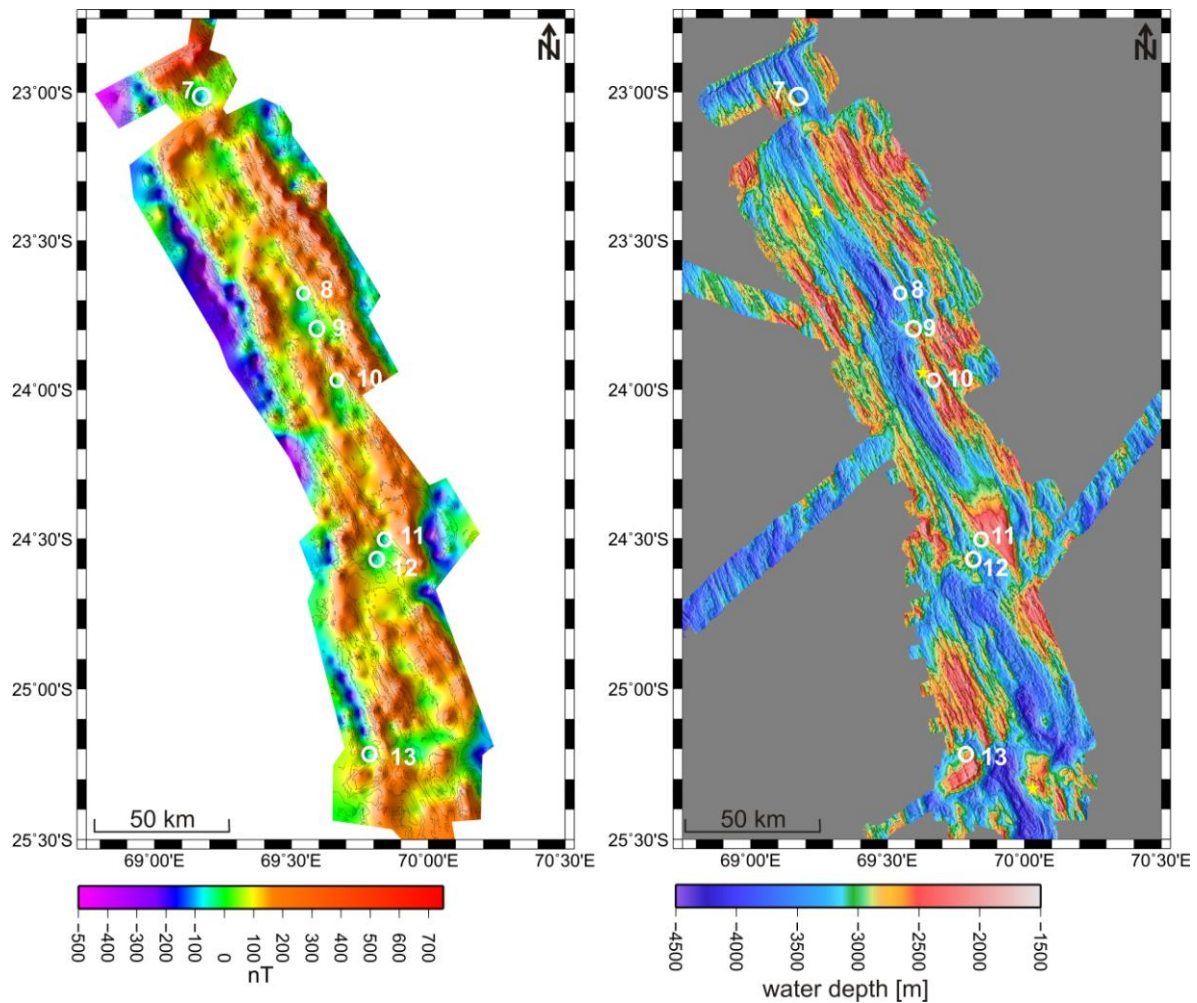


Figure 123: Magnetic (left side) and bathymetric (right side) map of the working areas JX; Meso, Edmond and Kairei. Areas with decreased magnetic values are marked by white circles in the magnetic map as well as in the bathymetric map.

Along the mapped intermediate spreading SEIR no hydrothermal vent field is known today. It is only possible to transfer the results and features observed from the hydrothermal vents of the CIR. 18 promising areas along the SEIR are shown in **Figure 124**. The majority of these locations (#14, #16 - #21, #24, #28 and #31) are situated in tectonically active areas and along the segment ends or evolving discontinuities. Locations #18 to #21 correspond to the inner corners which are strongly elevated and represent a decoupling from the lithosphere by detachment faults (SEARLE, 2013) which could be perfect pathways for the fluids. Especially in Section 4 the zones of decreasing magnetic values are located at the steeper eastern ridge flank (locations #22 - #26). The large OCC structure in the transition between Sections 1 and 2 causes a very large zone of decreasing magnetic values labeled with the red line in **Figure 124**. The locations #14, #19 - #20 and #29 show similarities to the Kairei hydrothermal vent field location from the southern end of the CIR because they are situated along strongly elevated older ridge shoulders. The Kp-Index analyses for the Southeast Indian Ridge also

show relatively calm conditions for the majority of the profiles with Kp-values ≤ 4 . For locations #16 and #17, corresponding to profiles SEIR220-223 (accommodation zone Section 2), the Kp-values increase to 5-6. Compared to the other locations #17 is noticeable because the magnetic low there is much stronger than at the other locations. Another location which could be affected by slightly higher Kp-values of 4-5 is #28 (profiles SEIR256-257, accommodation zone Section 5). To sum up, from the magnetic point of view these three locations must be regarded with caution.

Another interesting area for hydrothermal activity which is not characterized by decreased magnetic values is situated between 69°51'E/24°54'S and 69°56'E/25°03'S, north of Kairei in the southern part of working area Edmond. It is characterized by an asymmetric axial valley with steeper slopes on the eastern valley flank and neovolcanic ridges on the western axial valley flank. Here, on the western flanks normal faults occur which are possible pathways for hydrothermal fluids. The combination of neovolcanic ridges and a large number of seamounts in the rift valley indicates magmatic activity underneath. There are some similarities to the Sonne hydrothermal vent field like tectonic activity through normal faults and magmatic activity represented by neovolcanic ridges. Possibly that is an area to find further inactive hydrothermal vent fields due to the strong magmatic activity in that area which blocks the pathways at recent times. At this point it is worth noting that the inactive Sonne hydrothermal vent field also is not associated with a magnetic low.

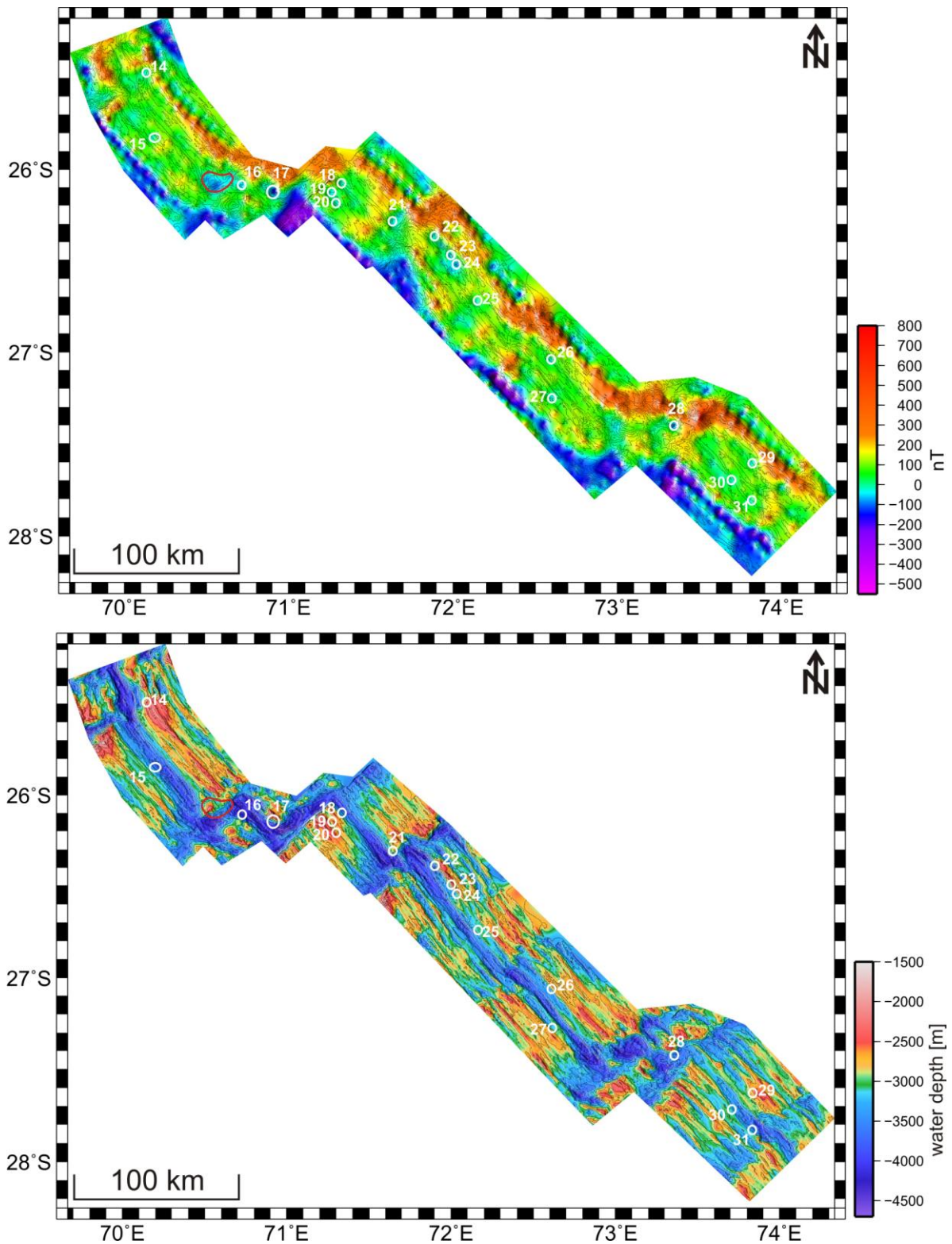


Figure 124: Magnetic (top) and bathymetric (bottom) map of the SEIR. Areas with a magnetic low are pointed out by white circles and their positions are marked in the bathymetric map below as well.

In comparison with the literature of other hydrothermal vent fields, especially those in the Atlantic Ocean, it becomes clear that most of them have been found with luck such as Lucky Strike (LANGMUIR et al., 1997), TAG (SCOTT et al., 1974), and Snake Pit (KARSON et al.,

1988) or by detection of methane anomalies caused by the hydrothermal plumes like Rainbow (GERMAN et al., 1996), Nibelungen (MELCHERT et al., 2008), and Ashadze/Logatchev/Krasnov (FOUQUET et al., 2008). Along the ultraslow spreading Southwest Indian Ridge the first evidence for hydrothermal activities came from water-column anomalies obtained in 1997 (GERMAN et al., 1998; TAO et al., 2012). All these hydrothermal vent fields have been found with measuring tools near the seafloor such as autonomous underwater vehicles (AUVs) with Eh (redox potential) measurement tools or video systems attached, remotely operated vehicles (ROVs) or video cameras mounted on a drill string as it was the case for Snake Pit (KARSON et al., 1988). Resulting from structural analysis it is possible to compare the three hydrothermal vent fields from the Central Indian Ridge with hydrothermal vent fields from the Atlantic in order to find similarities.

The active TAG (TransAtlanticGeotraverse) hydrothermal vent field at 26°N in the Atlantic is hosted on a tectonically-controlled terrain, far away from the ridge axis and on the eastern ridge flank (SCOTT et al., 1974; RONA, 1980; KLEINROCK & HUMPHRIS, 1996; GERMAN & LIN, 2004). Research cruises of the Trans-Atlantic Geotraverse project found the hydrothermal vent field via dredging with good luck between 1972 and 1973 (SCOTT et al., 1974). It has several similarities to the tectonically-controlled active Edmond hydrothermal vent field. At both locations faults and fractures increase the permeability of the rocks (RONA, 1980) and enable the fluids to reach the seafloor.

From analyzing results of the Kairei hydrothermal vent field it correlates with the Logatchev-1 hydrothermal vent field in the Atlantic which was discovered in 1994 (FOUQUET et al., 2008). PETERSEN et al. (2009) published the characteristics for Logatchev-1 which is located ~7 km off-axis in an area with ridges running parallel to the rift axis, ~1000 m above the ridge axis and at an OCC. This description of the Logatchev-1 field supports the assumptions made during this study.

The inactive Sonne hydrothermal vent field can be compared to an inactive hydrothermal vent field at 50°28'E on the Southwest Indian Ridge. There the inactive hydrothermal vent field is located towards the segment center with thick crust and no axial rift valley formed (TAO et al., 2012). TAO et al. (2012) described promising looking areas for hydrothermal activities along slow and ultraslow spreading ridges as areas which are characterized by large heat values due to enhanced magmatism and where the crust has a suitable permeability.

To summarize, in the future work areas should be defined which are tectonically active as seen by faults (especially cross-cutting faults), discontinuities, and pull-apart basins, but also have a heat source in the vicinity expressed by neovolcanic ridges or an increasing number of seamounts. The areas should have a large distance to the ridge axis, a location at segment ends, and ideally a decrease in magnetic values. A more or less sure sign for hydrothermal activity are oceanic core complexes which can be easily identified with slope maps and by their lineation structures running perpendicular to the ridge axis. It seems possible to limit areas for hydrothermal activity based on bathymetric and magnetic datasets acquired at the sea surface and thus with a reasonable amount of ship time required.

6) Conclusions

To sum up, along mid-ocean ridges hydrothermal vent systems occur in many shapes from low- to high-temperature and as basalt- or ultramafic-hosted vent fields. For the development of hydrothermal vent fields a combination of magmatic and tectonic activities is necessary whereby a higher amount is represented by tectonic activities. Hydrothermal vent fields are possibly of great future importance for industries because of their high metal content. In the past many hydrothermal vent fields have been found with luck or by plume detection with methane anomaly measurements. All these findings rely on the expensive and time-consuming use of deep-towed equipment. The goal of this work was the identification of hydrothermal systems or areas looking promising in terms of hydrothermal activities along two mid-ocean ridge systems in the western Indian Ocean based on sea surface acquired bathymetric and magnetic data.

Detailed structural maps including the seamount distribution and fault behavior have shown that differences exist between the slow spreading CIR and the intermediate SEIR. These are in terms of magmatic activities the lack of neovolcanic ridges along the SEIR and instead a higher amount of seamounts probably due to a shallower magma chamber. Both ridges have in common that the seamount distribution is more pronounced on the southwestern ridge flanks. Hence, in some working areas such as EXFX, JX, Section 1, and Section 4, the magma chamber underneath could be characterized by a slight asymmetry with a shift to the southwestern ridge side. Analyses of both ridge systems have shown that they are defined more by tectonically active areas than magmatic ones. Oceanic core complexes for example occur at both ridge systems and seem to be independent from the different spreading rates. Results from magnetic analyses have shown that the northeastern ridge flanks at the CIR and SEIR spread faster. To get an idea of the main features which are characteristic for hydrothermal activities, the three already known hydrothermal vent fields Sonne (inactive), Edmond (active), and Kairei (active) were analyzed and a table compiled which summarizes the main points. The main features are divided into magmatic causes, tectonic causes, and those which are a mixture of both. For all three hydrothermal vent fields a lack of seamounts in their vicinity is characteristic as well as a large distance of the fields to the spreading axis. The active hydrothermal vent fields Edmond and Kairei are both located on the steeper, stronger uplifted northeastern ridge shoulders, close to a discontinuity, and at the segment

ends. Faults, especially cross-cutting faults, are the pathways for the fluids to reach the seafloor and have been observed at Edmond. A very prominent behavior was observed during a detailed magnetic survey where a decrease of the magnetic susceptibility of the basalts was measured right above Edmond with expansion to the south. This behavior was modeled to get an idea of the dimensions of the hydrothermally altered rock body caused by a replacement of the magnetic minerals of the basalts by non-magnetic sulfide minerals. Afterwards a schematic sketch shows a possible situation for the Edmond hydrothermal vent field with its two inactive outflows Gauss and Score, the dimensions of the hydrothermally influenced body, and at least two fault zones which are responsible for the hydrothermal activity. Further investigations in that area should include seismic measurements to get precise information about the dimensions of that altered body. Additionally, further studies must be done at the three known hydrothermal vent fields with video-systems such as ROV to find out which dimensions the sulfide mound has and whether there are additional chimney complexes or not. It is important to understand the complex structure and functional principles of these fields.

To find further areas of potential hydrothermal activities the results of bathymetric and magnetic measurements are taken and 13 promising locations for the CIR and 18 locations for the SEIR are defined. In the future areas with a large distance to the spreading axis, uplifted inner corners, detachment faults, cross-cutting faults, decreased magnetic values, close proximity to a discontinuity at the segment ends, and oceanic core complexes should be investigated in terms of hydrothermal activities. As a result of this work it seems possible as a first step to limit areas along mid-ocean ridges for hydrothermal activities based on bathymetric and magnetic data acquired at the sea surface which saves research and ship time. Following investigations must be done with deep-towed video-systems in the areas defined in this work to confirm whether or not hydrothermal activity takes place there. Furthermore, seismic measurements over areas with hydrothermal activity can be of great importance to complete the picture in the depth and to get an overview of the dimensions because video-systems always have a limited view at the seafloor. An additional useful tool could be the sidescan sonar. It is also a deep-towed measurement tool which produces high resolution bathymetry maps and could acquire magnetic data close to the seafloor. For the expensive and time consuming deployment of all deep-towed measurement tools it is necessary to define smaller areas of interest from a larger dataset.

7) References

- ABELSON, M. & AGNON, A. (1997): Mechanics of oblique spreading and ridge segmentation. *Earth and Planetary Science Letters*. Vol. 148. 405-421.
- BAKER, E.T.; CORMIER, M.-H.; LANGMUIR, C.H. & ZAVALA, K. (2001): Hydrothermal plumes along segments of contrasting magmatic influence, 15°20'-18°30'N, East Pacific Rise: Influence of axial faulting. *Geochemistry Geophysics Geosystems G³*. Vol. 2. American Geophysical Union.
- BALLARD, R.D. & VAN ANDEL, T.H. (1977): Morphology and tectonics of the inner rift valley at 36°50'N on the Mid-Atlantic Ridge. *Geological Society of American Bulletin*. Vol. 88. 507-530.
- BARAN, J.M.; CARBOTTE, S.M. & COCHRAN, J.R. (2005): Variations in upper crustal structure due to variable mantle temperature along the Southeast Indian Ridge. *Geochemistry Geophysics Geosystems G³*. Vol. 6. Q11002.
- BARCKHAUSEN, U. & BARGELOH, H.-O. (2012): Magnetic Data Acquisition and Processing. pp. 68-71. In: SCHWARZ-SCHAMPERA, U. & Shipboard Scientific Party (2012): INDEX2011-Indian Ocean Exploration For Seafloor Massive Sulfides 2011. Cruise Report. BGR. Hannover.
- BARTELS, J. (1957): The geomagnetic measures for the time-variations of solar corpuscular radiation, described for use in correlation studies in other geophysical fields. *Ann. Intern. Geophys.* Vol. 4. 227-236.
- BASAVAIAH, N. (2011): *Geomagnetism – Solid Earth and Upper Atmosphere Perspectives*. Capital Publishing Company. India.
- BEHN, M.D. & ITO, G. (2008): Magmatic and tectonic extension at mid-ocean ridges: 1. Controls on fault characteristics. *Geochemistry Geophysics Geosystems G³*. An electronic Journal of the Earth Sciences. Vol. 9. Nr. 8. American Geophysical Union.
- BOSCHI, CH.; FRÜH-GREEN, G.L.; DELACOUR, A.; KARSON, J.A. & KELLY, D.S. (2006): Mass transfer and fluid flow during detachment faulting and development of an oceanic core complex, Atlantis Massif (MAR30°N). *Geochemistry Geophysics Geosystems G³*. Vol. 7. No. 1. 1-39. American Geophysical Union.
- BRIAIS, A. (1995): Structural Analysis of the Sementation of the Central Indian Ridge between 20°30'S and 25°30'S (Rodriguez Triple Junction). *Marine Geophysical Researches*. Vol. 17. 431-467. Netherlands.
- BUCK, W.R.; LAVIER, L.L. & POLIAKOV, A.N.B. (2005): Modes of faulting at mid-ocean ridges. *Nature*. Vol. 434. 719-723.

- CANDE, S.C. & KENT, D.V. (1995): Revised calibration of the geomagnetic polarity timescale for the Late Cretaceous and Cenozoic. *Journal of Geophysical Research*. Vol. 100. No. B4. 6093-6095. American Geophysical Union.
- CARESS, D.W. & CHAYES, D.N. (1996): Improved processing of Hydrosweep DS Multibeam Data on the R/V Maurice Ewing. *Marine Geophysical Research*. Vol. 18. 631-650.
- CLAGUE, D.A.; MOORE, J.G. & REYNOLDS, J.R. (2000): Formation of submarine flat-topped volcanic cones in Hawai'i. *Bulletin of Volcanology*. Vol. 62. No. 3. 214-233.
- CONDER, J.A. & FORSYTH, D.W. (2001): Seafloor spreading on the Southeast Indian Ridge over the last one million years: a test of the Capricorn plate hypothesis. *Earth and Planetary Science Letters*. Vol. 188. 91-105.
- ENGELS, M.; BARCKHAUSEN, U. & GEE, J.S. (2008): A new towed marine vector magnetometer: methods and results from a Central Pacific cruise. *Geophysical Journal Int.* Vol. 172. 115-129.
- EHRHARDT, A. & Shipboard Scientific Party (2011): GeoNORM-Geophysical Studies in the Northern Red Sea. Maria S. Merian Cruise No. MSM14/2. Cruise Report.
- FONTAINE, F.J.; CANNAT, M. & ESCARTIN, J. (2008): Hydrothermal circulation at slow-spreading mid-ocean ridges: The role of along-axis variations in axial lithospheric thickness. *The Geological Society of America. Geology*. Vol. 36. No. 10. 759-762.
- FOUQUET, Y.; CHERKASHOV, G.; CHARLOU, J.L.; ONDRÉAS, H.; BIROT, D.; CANNAT, M.; BORTNIKOV, N.; SILANTYEV, S.; SUDARIKOV, S.; CAMBON-BONAVITA, M.A.; DESBRUYÉRES, D.; FABRI, M.C.; QUERELLOU, J.; HOURDEZ, S.; GEBRUK, A.; SOKOLOVA, T.; HOISE, E.; MERCIER, E. et al. (2008): Serpentine cruise-ultramafic hosted hydrothermal deposits on the Mid-Atlantic Ridge: First submersible studies on Ashadze 1 and 2, Logatchev 2 and Krasnov vent fields. *InterRidge News*. Vol. 17. 16-21.
- FRANKE, D.; ADAM, J. & Shipboard Scientific Party (2008): Cruise report SO-197 (RISE Rift Processes in The South China Sea). *Bundesanstalt für Geowissenschaften und Rohstoffe*. p. 179.
- FRISCH, W. & MESCHÉDE, M. (2007): *Plattentektonik-Kontinentverschiebung und Gebirgsbildung*. 2. Aufl.

- GALLANT, R.M. & VON DAMM, K.L. (2006): Geochemical controls on hydrothermal fluids from the Kairei and Edmond Vent Fields, 23°-25°S, Central Indian Ridge. *Geochemistry Geophysics Geosystems* *G³*. Vol. 7. No. 6. 1-24. American Geophysical Union.
- GAMO, T.; NAKAYAMA, E.; SHITASHIMA, K.; ISSHIKI, K.; OBATA, H.; OKAMURA, K.; KANAYAMA, S.; OOMORI, T.; KOIZUMI, T.; MATSUMOTO, S. & HASUMOTO, H. (1996): Hydrothermal plumes at the Rodriguez triple junction, Indian ridge. *Earth and Planetary Science Letters*. Vol. 142. 261-270.
- GAMO, T.; CHIBA, H.; YAMANAKA, T.; OKUDAIRA, T.; HASHIMOTO, J.; TSUCHIDA, S.; ISHIBASHI, J.; KATAOKA, S.; TSUNOGAI, U.; OKAMURA, K.; SANO, Y. & SHINJO, R. (2001): Chemical characteristics of newly discovered black smoker fluids and associated hydrothermal plume at the Rodriguez Triple Junction, Central Indian Ridge. *Earth and Planetary Science Letters*. Vol. 193. 371-379.
- GERMAN, C.R.; KLINKHAMMER, G.P. & RUDNICKI, M.D. (1996): The Rainbow hydrothermal plume, 36°15'N, MAR. *Geophysical Research Letters*. Vol. 23. No. 21. 2979-2982.
- GERMAN, C.R. & PARSON, L.M. (1998): Distribution of hydrothermal activity along Mid-Atlantic Ridge: interplay of magmatic and tectonic controls. *Earth and Planetary Science Letters*. Vol. 160. 327-341.
- GERMAN, C.R.; BAKER, E.T.; MEVEL, C.; TAMAKI, K. & the FUJI Science Team (1998): Hydrothermal activity along the Southwest Indian Ridge. *Nature*. Vol. 395. 490-493.
- GERMAN, C.R. & LIN, J. (2004): The thermal structure of the oceanic crust, ridge spreading and hydrothermal circulation: how well do we understand their inter-connections? IN: GERMAN, C.R.; LIN, J. & PARSON, L.M. (Eds): *Mid Ocean-Ridges: Hydrothermal Interactions Between the Lithosphere and Oceans*. *Geophysical Monograph Series*. Vol. 148. 1-18.
- GERMAN, C.; TURNHERR, A.; KNOERY, J. et al. (2010): Heat, volume and chemical fluxes from submarine venting: a synthesis of results from the Rainbow hydrothermal field, 36°N MAR. *Deep-Sea Research Part 1-Oceanographic Research Papers*. Vol. 57. No. 4. 518-527.
- GIERLOFF-EMDEN, H.G. (1999): Radar-Altmetrie von Satelliten zur Erforschung des Reliefs des Meeresbodens. *Münchener Geographische Abhandlungen Reihe A*. p. 130.
- GRÁCIA, E.; CHARLOU, J.L.; RADFORD-KNOERY, J. & PARSON, L.M. (2000): Non-transform offsets along the Mid-Atlantic Ridge south of the Azores (38°N-34°N): Ultramafic exposures and hosting of hydrothermal vents. *Earth and Planetary Science Letters*. Vol. 177. 89-103.

- GRINDLAY, N.R.; FOX, P.J. & MACDONALD, K.C. (1991): Second order ridge axis discontinuities in the South Atlantic: morphology , structure and evolution. *Marine Geophysical Research*. Vol. 13. 21-49.
- HALBACH, P. (1997): FS Sonne Fahrt SO92-HYDROTRUNC-Die Entwicklung des Hydrothermalismus und seine strukturgeologische Kontrolle im Gebiet der Rodriguez Triple Junction, Zentraler Indischer Ozean. Wissenschaftlicher Abschlußbericht. FU Berlin.
- HALBACH, P.; BLUM, N.; MÜNCH, U.; PLÜGER, W.; GARBE-SCHÖNBERG, D. & ZIMMER, M. (1998): Formation and decay of modern massive sulfide deposit in the Indian Ocean. *Mineralium Deposita* (1998) Vol. 33. 302-309.
- HASHIMOTO, J.; OHTA, S.; GAMO, T.; CHIBA, H.; YAMAGUCHI, T.; TSUCHIDA, S.; OKUDAIRA, T.; WATABE, H.; YAMANAKA, T. & KITEIZAWA, M. (2001): First hydrothermal vent communities from the Indian Ocean discovered. *Zool. Sci.* Vol. 18. 717-721.
- HEINE, CH.; MÜLLER, R.D. & GAINA, C. (2004): Reconstructing the Lost Eastern Tethys Ocean Basin: Convergence History of the SE Asian Margin and Marine Gateways. *Geophysical Monograph Series*. Vol. 149. 37-54.
- HEINRICH, H. (1968): Die physikalischen Grundlagen des Protonen-Magnetometers. *Astania-Warte*. Hauszeitschrift. Heft 72. 25. Jahrgang.
- HERZIG, P.M. & PLÜGER, W.L. (1988): Exploration for hydrothermal activity near the Rodriguez Triple Junction, Indian Ocean. *Canadian Mineralogist*. Vol. 26. 721-736.
- HERZIG, P.M. & HANNINGTON, M.D. (1995): Polymetallic massive sulfides at the modern seafloor. A review. *Ore geology Reviews*. Vol. 10. 95-115.
- HERZIG, P.M.; PETERSEN, S. & HANNINGTON, M.D. (2000): Polymetallic Massive Sulphide Deposits at the Modern Seafloor and their Resource Potential. In: *Polymetallic Massive Sulphide and Cobalt-Rich Ferromanganese Crusts: Status and Prospects*. ISA Technical Study No. 2. (2000). Jamaica.
- HEYDE, I.; BARGELOH, H.-O.; ENGELS, M. & DEPPE, J. (2014): Magnetic data acquisition and processing. In: *SCHWARZ-SCHAMPERA, U. & Shipboard Scientific Party (2014): INDEX2013-Indian Ocean Exploration For Seafloor Massive Sulfides*. Cruise Report. BGR. Hannover. Unpublished.
- HOCUTT, C.H. (1987): Evolution of the Indian Ocean and the drift of India: A vicariant event. *Hydrobiologica*. Vol. 150. 203-223. Netherlands.
- HONSHO, CH.; TAMAKI, K. & FUJIMOTO, H. (1996): Three-dimensional magnetic and gravity studies of the Rodriguez Triple Junction in the Indian Ocean. *Journal of Geophysical Research*. Vol. 101. No. B7. 15,837-15,848. American Geophysical Union.

- HUMLER, E. & WHITECHURCH, H. (1988): Petrology of basalts from the Central Indian Ridge (lat. 25°23'S, long. 70°04'E): estimates of frequencies and fractional volumes of magma injections in a two-layered reservoir. *Earth and Planetary Science Letters*. Vol. 88. 169-181.
- ITO, G. & BEHN, M.D. (2008): Magmatic and tectonic extension at mid-ocean ridges: 2. Origin of axial morphology. *Geochemistry Geophysics Geosystems G³*. Vol. 9. No. 9. American Geophysical Union.
- JOCHUM, B.; ARIC, K. & SEIBERL, W. (1997): Marinemagnetik am Ostpazifischen Rücken. *Mitt. Österr. Geol. Ges.* Vol. 90. 127-136.
- JOHNSON, H.P. & TIVEY, M.A. (1995): Magnetic-properties of zero-age oceanic-crust-a new submarine lava flow on the Juan-De-Fuca Ridge. *Geophysical Research Letters*. Vol. 22. No. 2. 175-178.
- JONES, E.J.W. (1999): *Marine Geophysics*. University College London. John Wiley & Sons. Ltd. England.
- KAMESH RAJU, K.A. & RAMPRASAD, T. (1989): Magnetic lineations in the Central Indian Basin for the period A24-A21: a study in relation to the Indian Ocean Triple Junction Trace. *Earth and Planetary Science Letters*. Vol. 95. 395-402.
- KARSON, J.A. & BROWN, J.R. (1988): Geologic Setting of the Snake Pit Hydrothermal Site: An Active Vent Field on the Mid-Atlantic Ridge. *Marine Geophysical Researches*. Vol. 10. 91-107.
- KARSON, J.A. (1990): Seafloor spreading on the Mid-Atlantic Ridge; implications for the structure of ophiolites and oceanic lithosphere produced in slow-spreading environments. In: *Proceedings of the Symposium on Ophiolites and Oceanic Lithosphere-TROODOS87*. Ed. MALPAS, J.; MOORES, E.M.; PANAYIOTOU, A. & XENOPHONTOS, C. Cyprus: Geological Survey Department. Ministry of Agriculture and Natural Resources. 547-555.
- KENT, D.V.; HONNOREZ, B.M.; OPDYKE, N.D. & FOX, P.J. (1978): Magnetic properties of dredged oceanic gabbros and the source of marine magnetic anomalies. *Geophysical Journal. R. astr. Soc.* Vol. 55. 513-537.
- KLEINROCK, M.C. & HUMPHRIS, S.E. (1996): Structural control on sea-floor hydrothermal activity at the TAG active mound. *Nature*. Vol. 382. 149-153.
- KONGSBERG, S. (2006): EM120/122 Multibeam echo sounder, production description. Kongsberg Maritime AS. <http://www.km.kongsberg.com>
- KUMAGAI, H.; NAKAMURA, K.; TOKI, T.; MORISHITA, T.; OKINO, K.; ISHIBASHI, J.-I.; TSUNOGAI, U.; KAWAGUCCI, S.; GAMO, T.; SHIBUYA, T.; SAWAGUCHI, T.; NEO, N.; JOSHIMA, M.; SATO, T. & TAKAI, K. (2008): Geological background of the Kairei and

- Edmond hydrothermal fields along the Central Indian Ridge: Implications of their vent fluids distinct chemistry. *Geofluids*. Vol. 8. 239-251. Blackwell Publishing Ltd.
- LANGMUIR, C.; HUMPHRIS, S.; FORNARI, D.; VAN DOVER, C.; VON DAMM, K.; TIVEY, M.K.; COLODNER, D.; CHARLOU, J.-L.; DESONIE, D.; WILSON, C.; FOUQUET, Y.; KLINKHAMMER, G. & BOUGAULT, H. (1997): Hydrothermal vents near a mantle hot spot: the Lucky Strike vent field at 37°N on the Mid-Atlantic Ridge. *Earth and Planetary Science Letters*. Vol. 148. 69-91.
- LOWRIE, W. & ALVAREZ, W. (1981): One hundred Million Years of Geomagnetic Polarity History. *Geology*. Vol. 9. 392-397.
- LOWRIE, W. (2007): *Fundamentals of Geophysics*.
- MACDONALD, K.C. & FOX, P.J. (1983): Overlapping spreading centers: new accretion geometry on the East Pacific Rise. *Nature*. Vol. 302. 55-57.
- MAUS, S. (2010): An ellipsoidal harmonic representation of Earth's lithospheric magnetic field to degree and order 720. *Geochemistry Geophysics Geosystems G³*. Vol. 11. No.6.
- MELCHERT, B.; DEVEY, C.W.; GERMAN, C.R.; LACKSCHEWITZ, K.S.; SEIFERT, R.; WALTER, M.; MERTENS, C.; YOERGER, D.R.; BAKER, E.T.; PAULICK, H. & NAKAMURA, K. (2008): First evidence for high-temperature off-axis venting of deep crustal/mantle heat: The Nibelungen hydrothermal field, southern Mid-Atlantic Ridge. *Earth and Planetary Science Letters*. Vol. 275. 61-69.
- MEYER, U.F. (1999): Untersuchung struktureller Elemente des südöstlichen Weddellmeeres/Antarktis auf der Basis mariner Potentialfelddaten. *Ber. Polarforsch.* Vol. 323. Bremerhaven.
- MITCHELL, N.C. (1991): An evolving ridge system around the Indian Ocean Triple Junction. *Marine Geophysical Researches*. Vol. 13. 173-201.
- MITCHELL, N.C. & PARSON, L.M. (1993): The Tectonic Evolution of the Ocean Triple Junction, Anomaly 6 to present. *Journal of Geophysical Research*. Vol. 98. No.B2. 1793-1812. American Geophysical Union.
- MÜNCH, U. (1995): Tektonik und Magmatismus im Umfeld der RTJ. Forschungsfahrt SO92 'HYDROTRUNC'. Diplomkartierung.
- MUNSCHY, M. & SCHLICH, R. (1989): The Rodriguez Triple Junction (Indian Ocean): Structure and Evolution for the Past One Million Years. *Marine Geophysical Researches*. Vol. 11. 1-14.
- MUNSCHY, M. & SCHLICH, R. (1990): Etude géophysique des dorsales de l'Océan Indien dans la région du point triple de Rodrigues. *Oceanol. Acta*. 10. 119-128.

- MUTTER, J.C. & KARSON, J.A. (1992): Structural processes at slow-spreading ridges. *Science*. Vol. 257. 627-634.
- NOAA 2009 GEODAS DATABASE
<http://www.ngdc.noaa.gov/mgg/geodas/geodas.html>
- NORTON, I.O. & SCLATER, J.G. (1979): A model for the evolution of the Indian Ocean and the breakup of Gondwanaland. *Journal of Geophysical Research*. Vol. 84. No. B12. 6803-6830.
- PARSON, L.M.; PATRIAT, P.; SEARLE, R.C. & BRIAIS, A.R. (1993): Segmentation of the Central Indian Ridge between 12°12'S and the Indian Ocean Triple Junction. *Marine Geophysical Researches*. Vol. 15. 265-282.
- PARSON, L.M.; GRÁCIA, E.; COLLIER, C.; GERMAN, C. & NEEDHAM, D. (2000): Second-order segmentation: the relationship between volcanism and tectonism at the MAR, 38°N-35°40'N. *Earth Planetary Science Letters*. Vol. 178. 231-251.
- PATRIAT, P. & COURTILLET, V. (1984): On the stability of triple junctions and its relation to episodicity in spreading. *Tectonics*. Vol. 3. 317-332.
- PATRIAT, PH. & SEGOUFIN, J. (1988): Reconstruction of the Central Indian Ocean. *Tectonophysics*. Vol. 155. 211-234.
- PETERSEN, S.; KUHN, K.; KUHN, T.; AUGUSTIN, N.; HÉKINIAN, R.; FRANZ, L. & BOROWSKI, C. (2009): The geological setting of the ultramafic-hosted Logatchev hydrothermal field (14°45'N, Mid-Atlantic Ridge) and its influence on massive sulfide formation. *Lithos*. Vol 112. 40-56.
- PHIPPS MORGAN, J. & CHEN, Y.J. (1993): The Genesis of Oceanic Crust: Magma Injections, Hydrothermal Circulation, and Crustal Flow. *Journal of Geophysical Research*. Vol. 98. No. B4. 6283-6297.
- PLÜGER, W.L (1988): Geothermal Metallogenesis Indian Ocean (GEMINO-2). *Abschlußbericht SO-43. RWTH Aachen*. p. 301.
- POULIQUEN, G.; GALLET, Y.; PATRIAT, PH.; DYMENT, J. & TAMURA, CH. (2001): A geomagnetic record over the last 3.5 million years from deep-tow magnetic anomaly profiles across the Central Indian Ridge. *Journal of Geophysical Research*. Vol. 106. No. B6. 10,941-10,960.
- RESTON, T.J. & RANERO, C. R. (2011): The 3-D geometry of detachment faulting at mid-ocean ridges. *Geochemistry Geophysics Geosystems G³*. An electronic Journal of the Earth Sciences. Vol. 12. No. 7. American Geophysical Union.
- ROESER, H.A. (1986): The calculation of magnetic sea-floor anomalies in the complex plane, without FFT. *Internal report BGR Hannover*. No. 11032/86.

- RONA, P.A. (1980): TAG Hydrothermal Field: Mid-Atlantic Ridge crest at latitude 26°N. *Journal of the Geological Society*. Vol. 137. 385-402.
- ROYER, J.-Y. & SCHLICH, R. (1988): Southeast Indian Ridge between the Rodriguez Triple Junction and the Amsterdam and Saint-Paul Islands: Detailed Kinematics for the Last 20 m.y. *Journal of Geophysical Research*. Vol. 93. 13,524-13,550. American Geophysical Union.
- SANDWELL, D.T. & SMITH, W.H.F. (1997): Marine gravity anomaly from Geosat and ERS-1 satellite altimetry. *Journal of Geophysical Research*. Vol. 102. No. B5. 10,039-10,054.
- SATO, T.; OKINO, K. & KUMAGAI, H. (2009): Magnetic structure of an oceanic core complex at the southernmost CIR: Analysis of shipboard and deep-sea three-component magnetometer data. *An electronic Journal of the Earth Sciences*. Vol. 10. No. 6. 1-21. American Geophysical Union.
- SAUTER, D.; WHITECHURCH, H.; MUNSCHY, M. & HUMLER, E. (1991): Periodicity in the accretion process on the Southeast Indian Ridge at 27°40'S. *Tectonophysics*. Vol 195. 47-64.
- SAUTER, D.; NAFZIGER, J.-M.; WHITECHURCH, H. & MUNSCHY, M. (1996): Segmentation and morphotectonic variations of the Central Indian Ridge (21°10'S-22°25'S). *Journal of Geophysical Research*. Vol. 101. No.B9. 20,233-20,256.
- SCHMIDT, S. & GÖTZE, H.-J. (2012): IGMAS+ Interactive Geophysical Modelling Assistant. User Manual.
- SCHULZ, N.J.; DETRICK, R.S. & MILLER, S.P. (1988): Two- and Three-Dimensional Inversions of Magnetic Anomalies in the MARK Area (Mid-Atlantic Ridge 23°N). *Marine Geophysical Research*. Vol. 10. 41-57.
- SCHWARZ-SCHAMPERA, U. & Shipboard Scientific Party (2012): INDEX2011-Indian Ocean Exploration For Seafloor Massive Sulfides 2011. Cruise Report. BGR. Hannover.
- SCHWARZ-SCHAMPERA, U. & Shipboard Scientific Party (2014): INDEX2013-Indian Ocean Exploration For Seafloor Massive Sulfides 2013. Cruise Report. BGR. Hannover. unpublished.
- SCOTT, R.B.; RONA, P.A.; MCGREGOR, B.A. & SCOTT, M.R. (1974): TAG hydrothermal field. *Nature*. Vol. 251. 301-302.
- SEARLE, R. (2013): *Mid-Ocean Ridges*. Cambridge University Press.
- SENGÖR, A.M.C.; ALTINER, D.; CIN, A.; USTAÖMER, T. & HSÜ, K.J. (1988): Origin and assembly of the Tethyside orogenic collage at the expense of Gondwana Land. 119-81. In: AUDLEY-CHARLES, M.G. & HALLAM, A. (1988): *Gondwana and Tethys*. The Geological Society. Oxford University Press. Special Publications No. 37.

- SEVERINGHAUS, J.P. & MACDONALD, K.C. (1988): High inside corners at ridge-transform intersections. *Marine Geophysical Research*. Vol. 9. 353-367.
- SFLAS (1989): User Manual, Version 3.
- SMALL, CH.; COCHRAN, J.R.; SEMPÉRÉ, J-CH. & CHRISTIE, D. (1999): The structure and segmentation of the Southeast Indian Ridge. *Marine Geology*. Vol. 161. 1-12.
- SMITH, W.H.F. & SANDWELL, D.T. (1994): Bathymetric prediction from dense satellite altimetry and sparse shipboard bathymetry. *Journal of Geophysical Research*. Vol. 99. No. 311. 21,803-21,824.
- SMITH, W.H.F. & SANDWELL, D.T. (1997): Global Sea Floor Topography from Satellite Altimetry and Ship Depth Soundings. *Science*. Vol. 277. 1956-1962.
- SPENCER, J.E. (1999): Geologic continuous casting below continental and deep-sea detachment faults and at the striated extrusion of Sacsayhuaman, Peru. *Geology*. Vol. 27. No. 4. 327-330.
- TAMSETT, D. & SEARLE, R.C. (1988): Structure and Development of the Midocean Ridge Plate Boundary in the Gulf of Aden: Evidence from GLORIA Side-Scan Sonar. *Journal of Geophysical Research*. Vol. 93. 3157-3178.
- TAO, CH.; LIN, J.; GUO, S.; CHEN, Y.-J.; WU, G.; HAN, X.; GERMAN, CH.R.; YOERGER, D.R.; ZHOU, N.; LI, H.; SU, X.; ZHU, J. & the DY115-19 (Legs 1-2) and DY115-20 (Legs 4-7) Science Partys (2012): First active hydrothermal vents on an ultraslow-spreading center: Southwest Indian Ridge. *Geology*. Vol. 40. 47-50.
- TAPSCOTT, CH.R.; PATRIAT, PH.; FISHER, R.L.; SCLATER, J.G.; HOSKINS, H. & PARSONS, B. (1980): The Indian Ocean Triple Junction. *Journal of Geophysical Research*. Vol. 85. No. B9. 4723-4739. American Geophysical Union.
- TIVEY, M.A. & JOHNSON, H.P. (1987): The central anomaly magnetic high: Implications for ocean crust construction and evolution. *Journal of Geophysical Research*. Vol. 92. 12,685-12,694.
- TIVEY, M.A.; SCHOUTEN, H. & KLEINROCK, M.C. (2003): A near-bottom magnetic survey of the Mid-Atlantic Ridge axis at 26 N: implications for the tectonic evolution of the TAG segment. *Journal of Geophysical Research*. Vol. 108.
- TIVEY, M.A. & DYMENT, J. (2010): The magnetic signature of hydrothermal systems in slow spreading environments. In: RONA, P.A.; DEVEY, G.W.; DYMANT, J. & MURTON, B.J. (2010): Diversity of Hydrothermal Systems on Slow Spreading Ocean Ridges. *Geophysical Monograph Series*. Vol. 188. 43-61. American Geophysical Union.

- TUCHOLKE, B.E. & LIN, J. (1994): A geological model for the structure of ridge segments in slow spreading ocean crust. *Journal of Geophysical Research*. Vol. 99. No. B6. 11,937-11,958. American Geophysical Union.
- TUCHOLKE, B.E.; BEHN, M.D.; BUCK, W.R. & LIN, J. (2008): Role of melt supply in oceanic detachment faulting and formation of megamullions. *Geology*. Vol. 36. 455-458.
- VAN DOVER, C.L.; HUMPHRIS, S.E.; FORNARI, D.; CAVANAUGH, C.M.; COLLIER, R.; GOFFREDI, S.K.; HASHIMOTO, J.; LILLEY, M.D.; REYSENBACH, A.L.; SHANK, T.M.; VON DAMM, K.L.; BANTA, A.; GALLANT, R.M.; GÖTZ, D.; GREEN, D.; HALL, J.; HARMER, T.L.; HURTADO, L.A. et al. (2001): Biogeography and ecological setting of Indian Ocean hydrothermal vent sites. *Science*. Vol. 294. 818-823.
- VAN WIJK, J.W. & BLACKMAN, D.K. (2005): Deformation of oceanic lithosphere near slow-spreading ridge discontinuities. *Tectonophysics*. Vol. 407. 211-225.
- VINE, F.J. & MATTHEWS, D.H. (1963): Magnetic Anomalies Over Ocean Ridges. *Nature* No. 4897. Vol. 199. 947-949.
- WESSEL, P. & SMITH, W.H.F. (1995): New Version of the Generic Mapping Tools Released. *EOS Trans. AGU*. Vol. 76. p. 329.
- WHITMARSH, R.B. & LAUGHTON, A.S. (1976): A Long Range Sonar Study of the Mid-Atlantic Ridge Crest near 37°N (FAMOUS area) and its Tectonic Implications. *Deep-Sea Research*. Vol. 23. 1005-1023.
- WILCOCK, W.S.D. & DELANEY, J.R. (1996): Mid-ocean ridge sulfide deposits: Evidence for heat extraction from magma chambers or cracking fronts?. *Earth and Planetary Science Letters*. Vol. 145. 49-64.

8) Acknowledgments

Without the help that I received from many people this dissertation would not have been possible.

My special thanks go to my two supervisors Prof. Andrea Hampel and PD Dr. Udo Barckhausen for all their support and constant feedback they gave to me. Especially Udo accompanies me since my bachelor thesis and always supported me with advice whether on land or at sea. Thank you for this time.

Furthermore, I would like to thank the Federal Institute for Geosciences and Natural Resources Hannover (BGR) and the team of the INDEX project for three years doing research in the western Indian Ocean and the possibility to write my dissertation.

Professor Martin Meschede from the University of Greifswald laid the foundation for my interest in marine geology during one of his lectures as he quoted Isaac Newton “What we know is a drop and what we do not know is an ocean.”. This sentence has accompanied me through my whole study. It is thanks to him that I have had an excellent education, a research cruise and the personal contact to Udo.

Lastly, I would like to thank my parents, my boyfriend and my friends for their constant support and encouragement. My parents supported me my whole study and teach me never to give up and maintain my happiness. They send me lots of packets with chocolate and have had an ear for hours of telephone calls. Furthermore, they waited patiently for my return from several research cruises far away. Without my parents all of this would not have been possible. I thank you so much for everything you have done for me!

9) Curriculum Vitae

PERSONAL INFORMATION: Carolin Bartsch, born on 05.April 1987 in Rathenow

EDUCATION:

08/2011	PhD student at Federal Institute for Geosciences and Natural Resources Hannover
07/2011	Master of Science Masterthesis: "Mud volcanoes from the central Mediterranean Ridge south of Crete: sediment dynamics and evolution" (Supervisors: Prof. Dr. Martin Meschede and Prof. Dr. Achim Kopf)
10/2010 – 03/2011	WS 2010/2011 Master Marine Geoscience at the University of Bremen
10/2009 – 07/2011	Study Master of Science
09/2009	Bachelor of Science Bachelorthesis: „Die strukturelle Untersuchung des Investigatorrückens und der Christmas Island Seamount Provinz im nordöstlichen Indischen Ozean anhand von Bathymetrie und Parasound“ (Supervisors: Prof. Dr. Martin Meschede and Dr. Udo Barckhausen)
10/2006 - 09/2009	Study Bachelor of Science at the Ernst-Moritz-Arndt University Greifswald
06/2006	A level
08/1999 – 06/2006	Anne-Frank academic high school, Berlin

GEOLOGICAL EXPERIENCE:

10/2013 – 11/2013	Research cruise with FS SONNE (INDEX2013) BGR detection of polymetallic massive sulfides at the spreading system in the Indian Ocean
11/2012 – 12/2012	Research cruise with FUGRO GAUSS (INDEX2012) BGR

	detection of polymetallic massive sulfides at the spreading system in the Indian Ocean
07/2012 – 07/2012	Research cruise with FUGRO GAUSS (training cruise INDEX2012) BGR
09/2011 – 11/2011	Research cruise with FS SONNE (INDEX 2011) BGR detection of polymetallic massive sulfides at the spreading system in the Indian Ocean
03/2011 – 04/2011	Research cruise with FS POSEIDON (P410) first drill of an accretionary wedge at the mediterranean ridge in front of Crete, with its characteristically „backstop“
03/2010 – 04/2010	Research cruise with FS METEOR (M81/2 A+B CLIP) IFM-GEOMAR to find the source of the Caribbean Large Igneous Province
08/2008 – 09/2008	Research cruise with FS SONNE (SO199 CHRISP) IFM-GEOMAR clarification of the intra plate volcanism and geodynamical evolution of the southeast Indian Ocean
04/ 2008	Inter-university coal class, Berlin
02/2008	Research cruise with FS ALKOR, Kiel
02/2008	Inter-university class „Klastische Sedimentation“, München

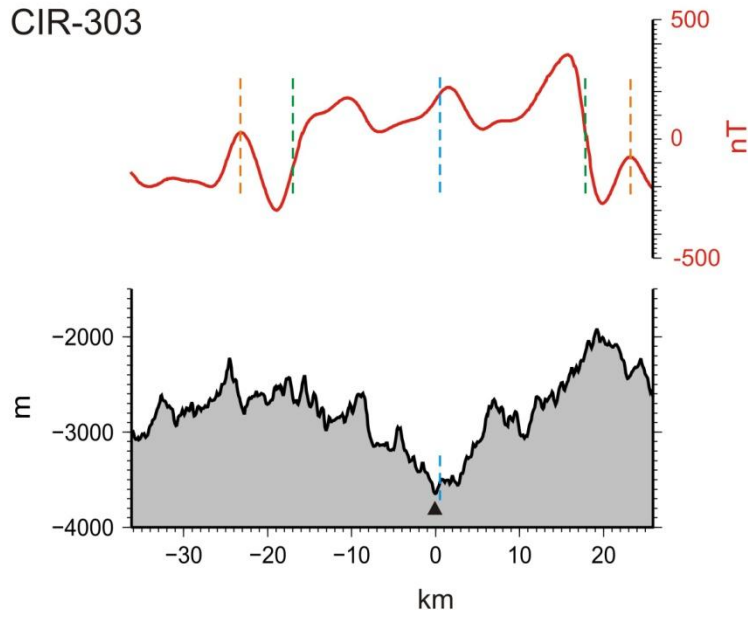
SCIENTIFIC EXPERIENCE:

03/2014	74. Annual conference of Deutsche Geophysikalische Gesellschaft, Karlsruhe Talk: „Hydrothermale Aktivitäten entlang des Zentralindischen Rückens-magnetische und struktureologische Charakteristika“
12/2013	American Geophysical Union Fall Meeting, San Francisco Poster: “Two Hydrothermal Fields at the Southern Central Indian Ridge (CIR) – Structural and Magnetic Investigations”
09/2013	ArcGIS 10.1 Grundkurs
06/2013	UKW – Sprechfunkzeugnis für den Binnenschiffahrtfunk (IBU)

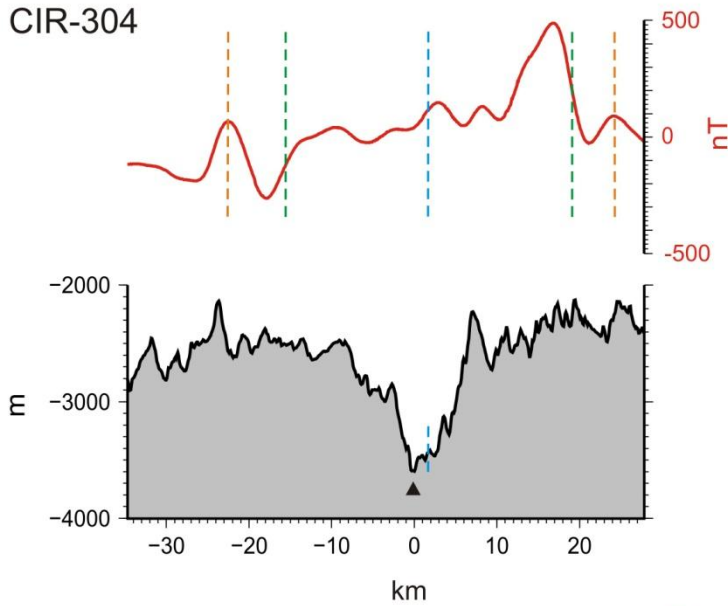
- 03/2013 Workshop Seafloor Mineral Resources – Scientific, Environmental, and Societal Issues. Kiel
- 03/2013 – 03/2013 73. Annual conference of Deutsche Geophysikalische Gesellschaft, Leipzig
- Poster: „Structural and magnetic investigations of the spreading systems north and south of the Rodriguez Triple Junction (Indian Ocean)”
- 10/2012 – 10/2012 GeoHannover 2012-Georesources for the 21st Century, Hannover
- Poster: „The spreading system north of the Rodriguez Triple Junction (Indian Ocean)-structural investigations with respect to hydrothermal systems and the associated seafloor massive sulfides (SMS)”
- 03/2012 – 03/2012 14th Symposium on Tectonics, Structural Geology and Geology of Crystalline Rocks, Kiel
- Poster: „Structural investigations of the spreading system north of the Rodriguez Triple Junction (Indian Ocean)”
- 03/2012 – 03/2012 Safety training for Offshore-Wind farm-Personal, Hamburg
- 12/2010 – 03/2011 HiWi at University Bremen, analysis of bathymetric data
- 10/2009 – 08/2010 WiHi in structural geology
- 08/2009 – 09/2009 Cooperation as student in scientific projects at the Institute for Social Medicine, Epidemiology and Health Economics, Charité – University Medical Center Berlin
- 09/2007 – 07/2009 HiWi for rock characterisation

10) Appendix A & B

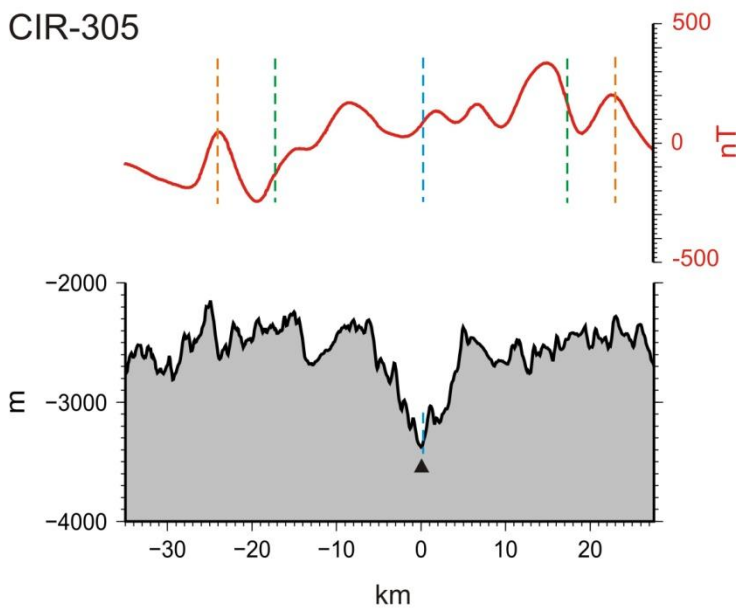
CIR-303



CIR-304

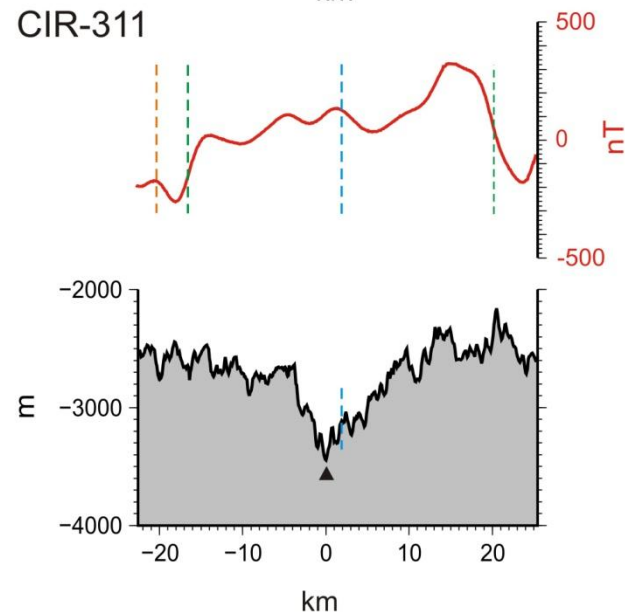
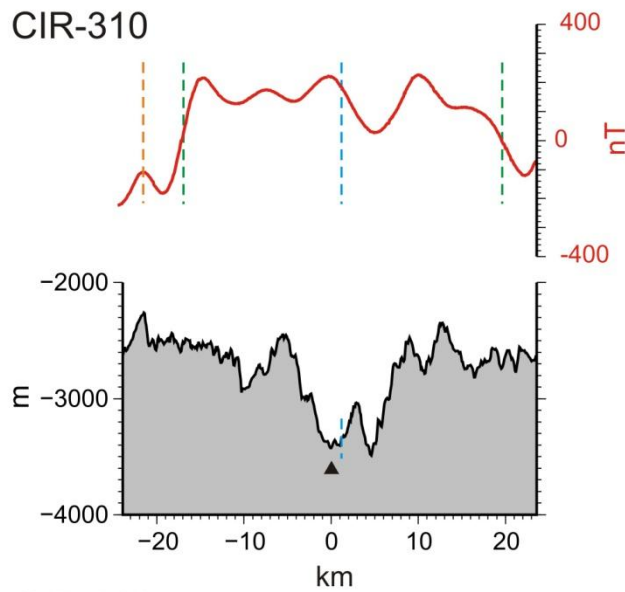
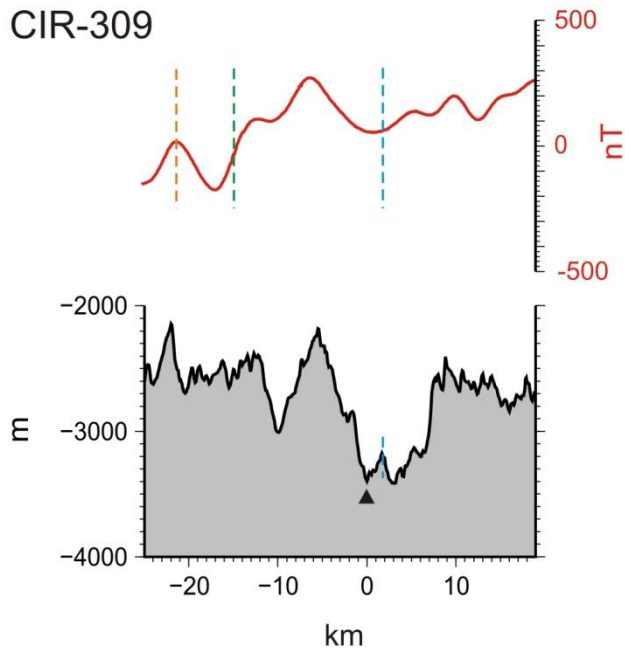


CIR-305



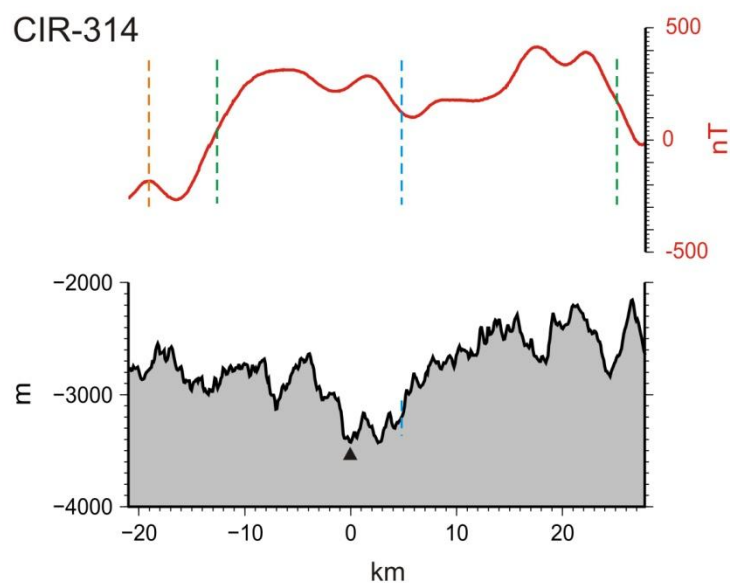
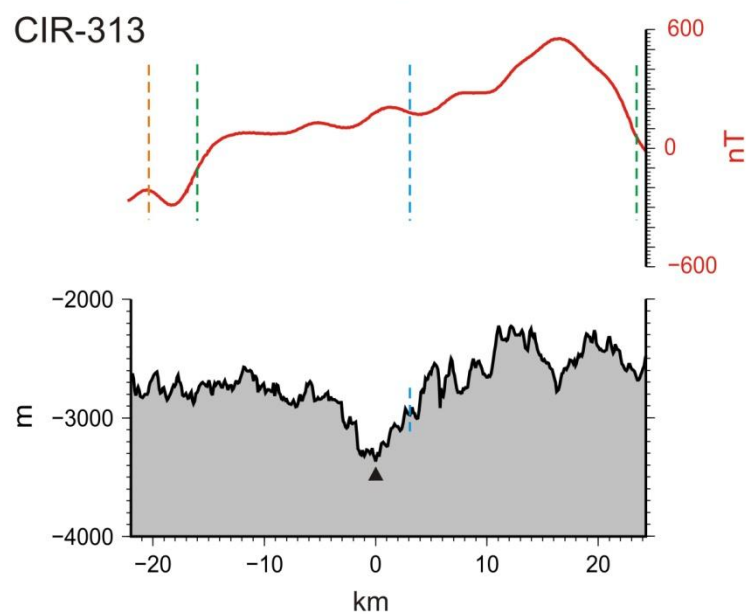
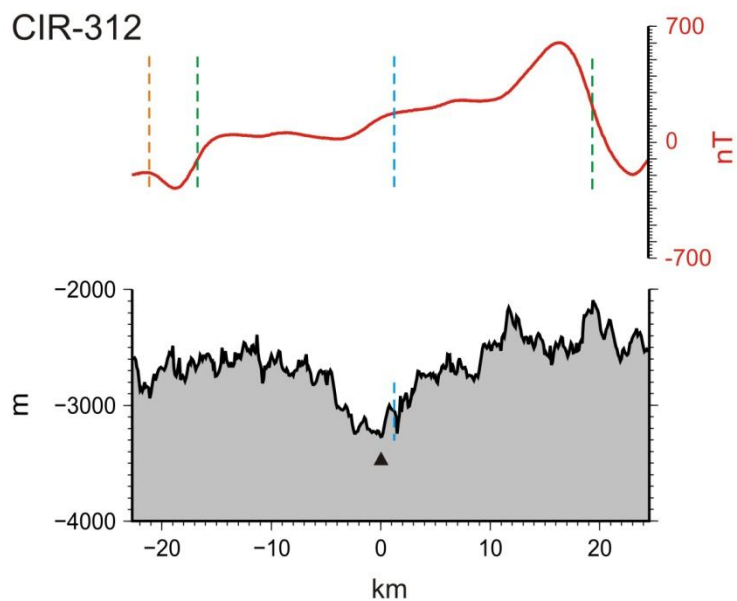
- 303-305 Profiles
- Jaramillo event
 - Anomaly 1 (0-0.78 Ma)
 - Center of magnetic Anomaly 1
 - Bathymetric profiles
 - Magnetic profiles
 - ▲ Recent active spreading center

Figure A1: Magnetic (top) and bathymetric (bottom) profiles CIR303-CIR305 across the CIR from northwest to southeast (working area EXFX). The boundaries of Anomaly 1 are labeled with green lines and the boundaries of the Jaramillo event with orange lines. The ridge axis, defined as the bathymetric minimum, is shown with a black triangle. The blue lines represent the center of magnetic Anomaly 1.



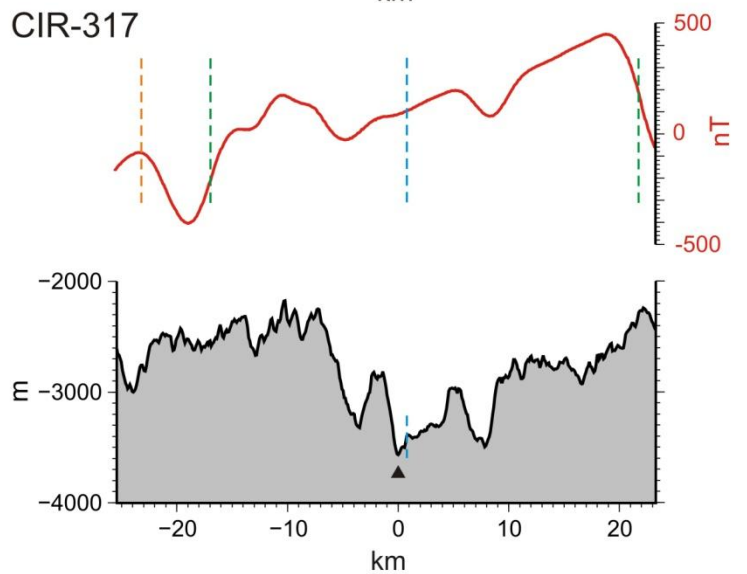
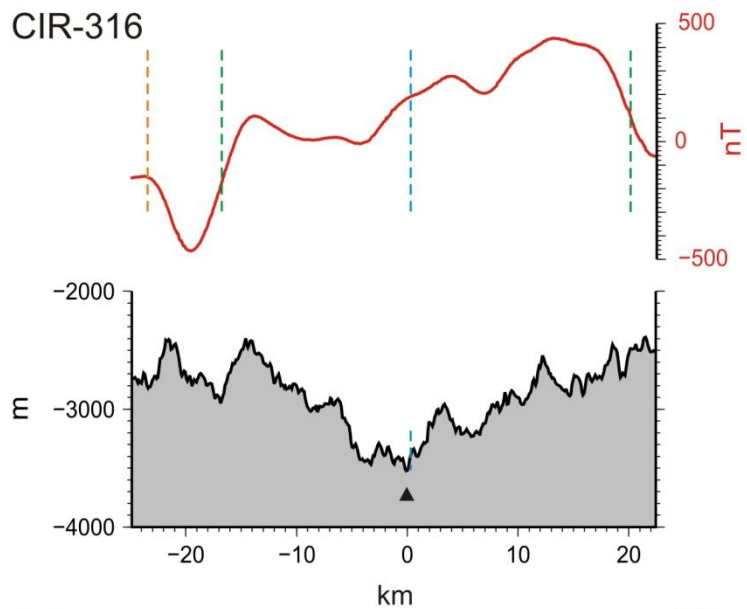
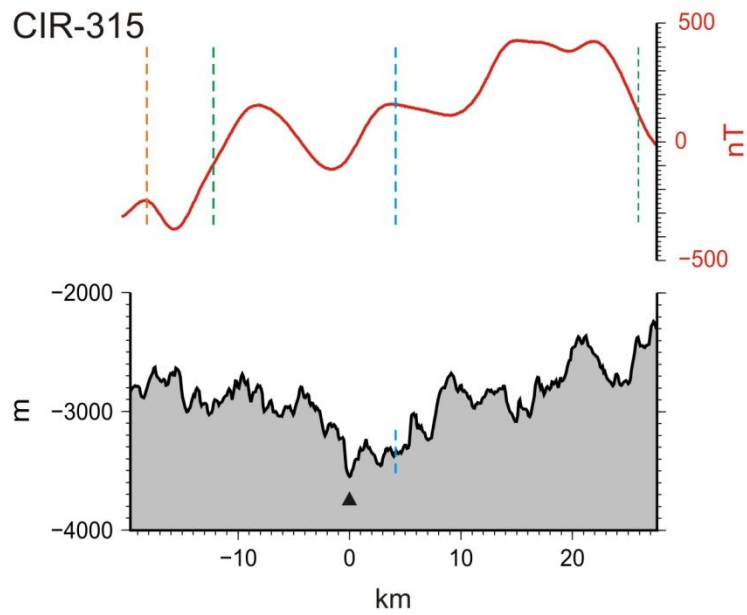
- 309-311 Profiles
- Jaramillo event
 - Anomaly 1 (0-0.78 Ma)
 - Center of magnetic Anomaly 1
 - Bathymetric profiles
 - Magnetic profiles
 - ▲ Recent active spreading center

Figure A2: Magnetic (top) and bathymetric (bottom) profiles CIR309-CIR311 across the CIR from northwest to southeast (working area EXFX). The boundaries of Anomaly 1 are labeled with green lines and the boundaries of the Jaramillo event with orange lines. The ridge axis, defined as the bathymetric minimum, is shown with a black triangle. The blue lines represent the center of magnetic Anomaly 1.



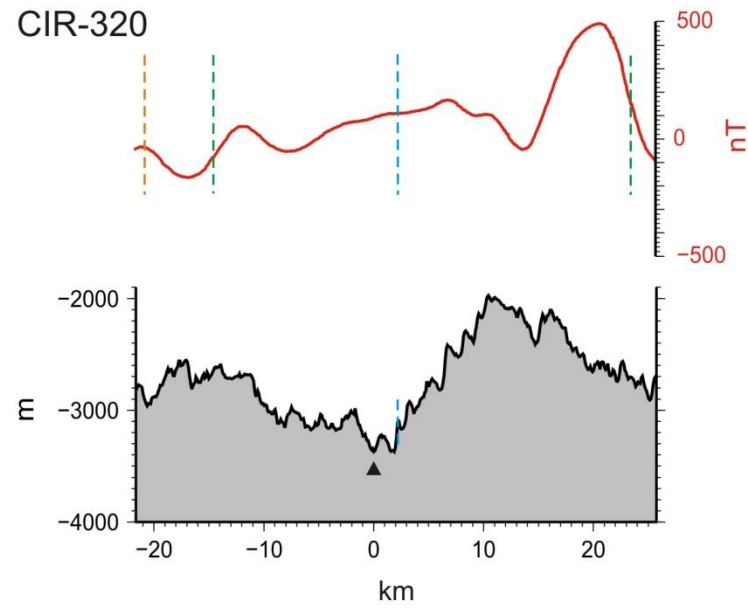
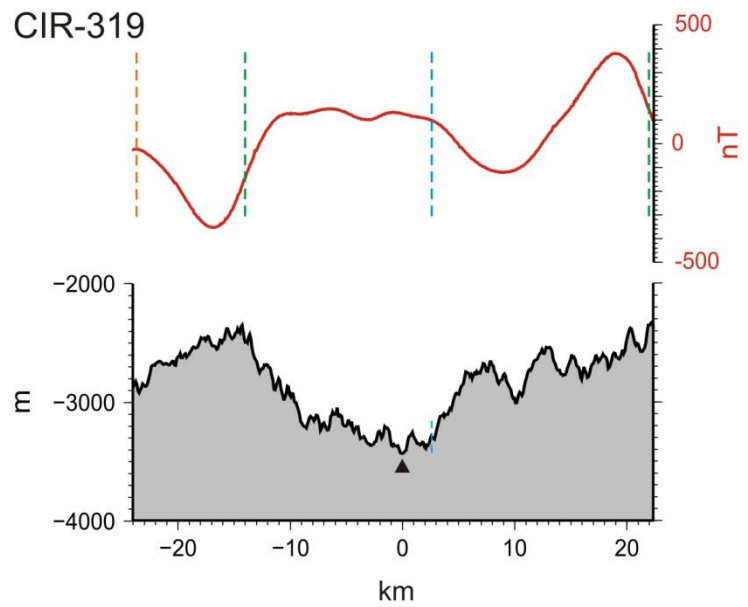
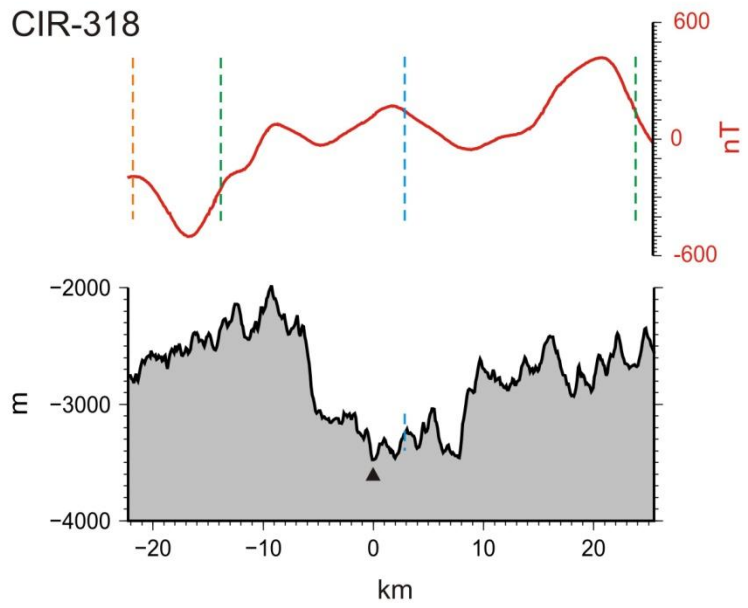
- 312-314 Profiles
- Jaramillo event
 - Anomaly 1 (0-0.78 Ma)
 - Center of magnetic Anomaly 1
 - Bathymetric profiles
 - Magnetic profiles
 - ▲ Recent active spreading center

Figure A3: Magnetic (top) and bathymetric (bottom) profiles CIR312-CIR314 across the CIR from northwest to southeast (working area EXFX). The boundaries of Anomaly 1 are labeled with green lines and the boundaries of the Jaramillo event with orange lines. The ridge axis, defined as the bathymetric minimum, is shown with a black triangle. The blue lines represent the center of magnetic Anomaly 1.



- 315-317 Profiles
- Jaramillo event
 - Anomaly 1 (0-0.78 Ma)
 - Center of magnetic Anomaly 1
 - Bathymetric profiles
 - Magnetic profiles
 - ▲ Recent active spreading center

Figure A4: Magnetic (top) and bathymetric (bottom) profiles CIR315-CIR317 across the CIR from northwest to southeast (working area EXFX). The boundaries of Anomaly 1 are labeled with green lines and the boundaries of the Jaramillo event with orange lines. The ridge axis, defined as the bathymetric minimum, is shown with a black triangle. The blue lines represent the center of magnetic Anomaly 1.



- 318-320 Profiles
- Jaramillo event
 - Anomaly 1 (0-0.78 Ma)
 - Center of magnetic Anomaly 1
 - Bathymetric profiles
 - Magnetic profiles
 - ▲ Recent active spreading center

Figure A5: Magnetic (top) and bathymetric (bottom) profiles CIR318-CIR320 across the CIR from northwest to southeast (working area EXFX). The boundaries of Anomaly 1 are labeled with green lines and the boundaries of the Jaramillo event with orange lines. The ridge axis, defined as the bathymetric minimum, is shown with a black triangle. The blue lines represent the center of magnetic Anomaly 1.

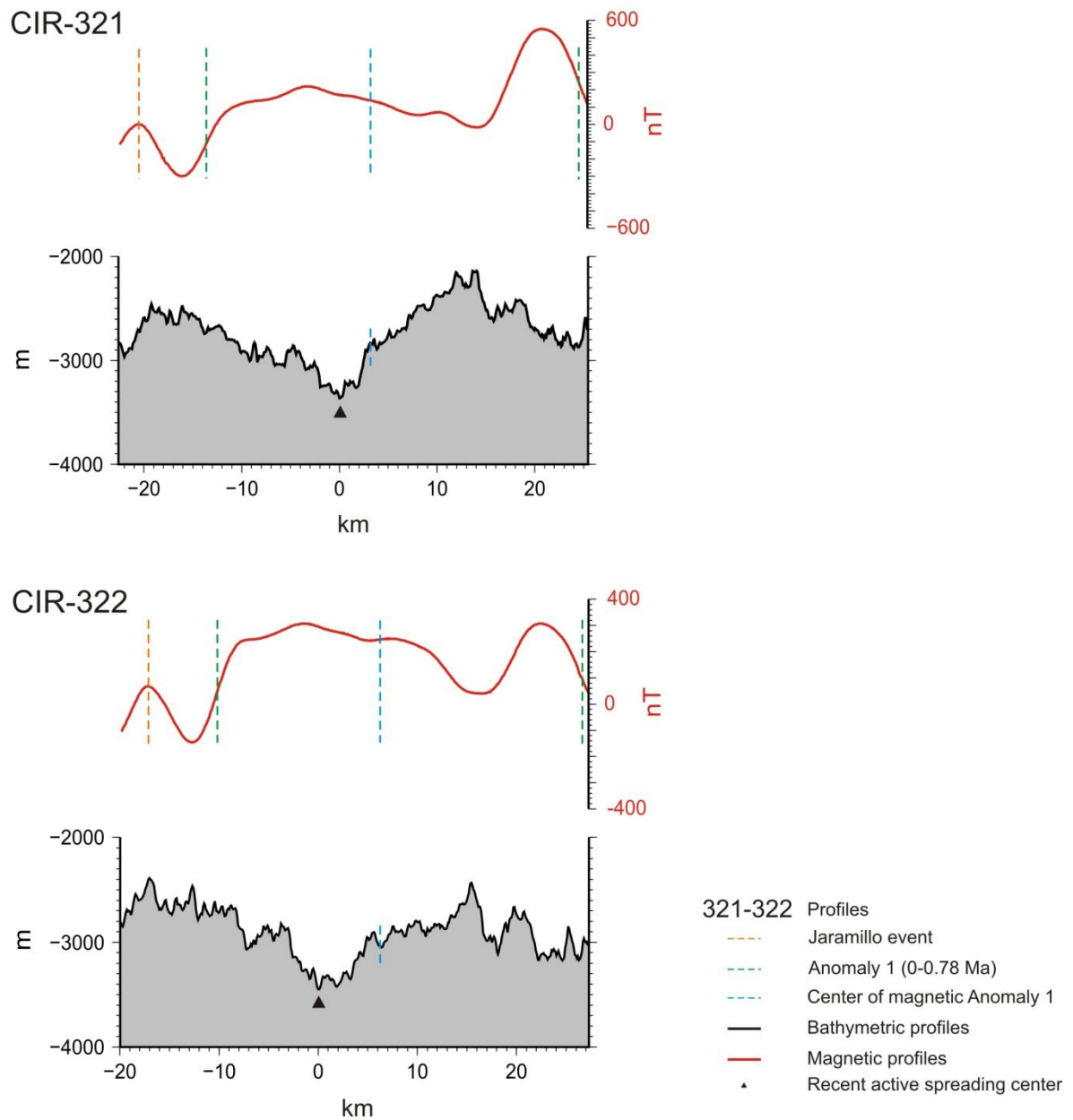


Figure A6: Magnetic (top) and bathymetric (bottom) profiles CIR321-CIR322 across the CIR from northwest to southeast (working area EXFX). The boundaries of Anomaly 1 are labeled with green lines and the boundaries of the Jaramillo event with orange lines. The ridge axis, defined as the bathymetric minimum, is shown with a black triangle. The blue lines represent the center of magnetic Anomaly 1.

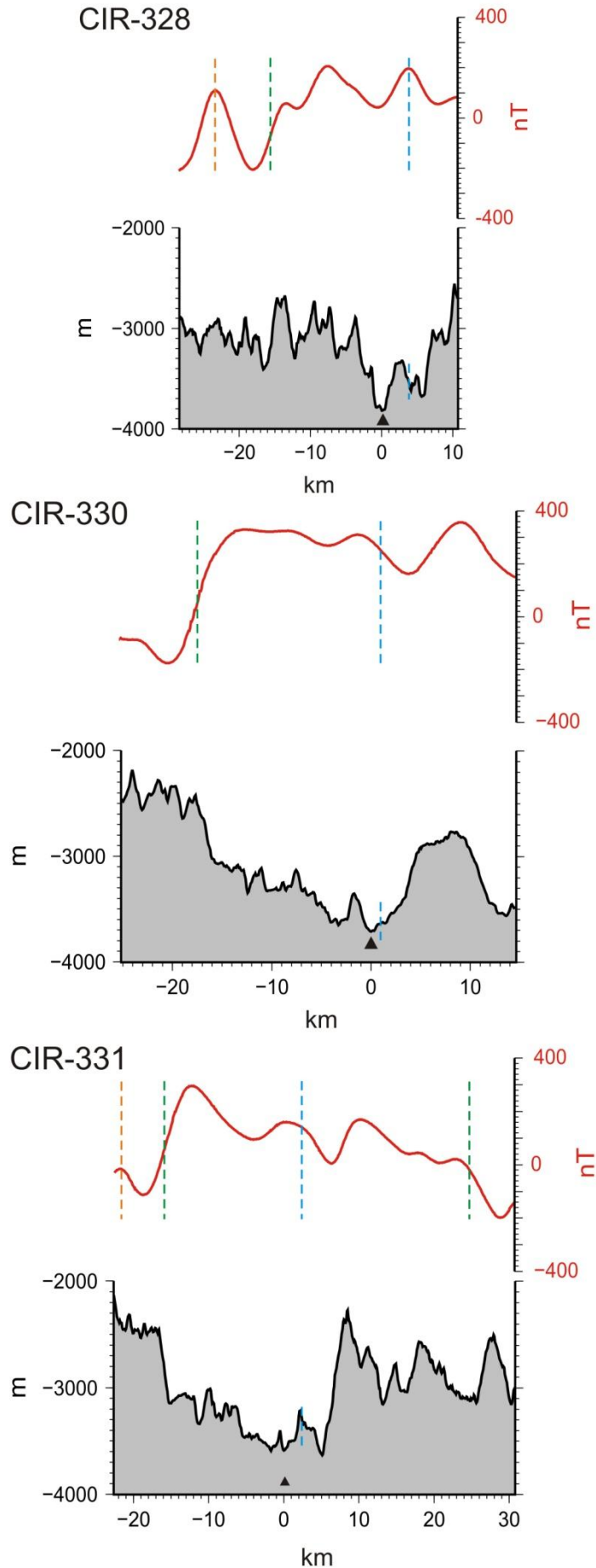


Figure A7: Magnetic (top) and bathymetric (bottom) profiles CIR328-CIR331 across the CIR from northwest to southeast (working area JX and Meso). The boundaries of Anomaly 1 are labeled with green lines and the boundaries of the Jaramillo event with orange lines. The ridge axis, defined as the bathymetric minimum, is shown with a black triangle. The blue lines represent the center of magnetic Anomaly 1.

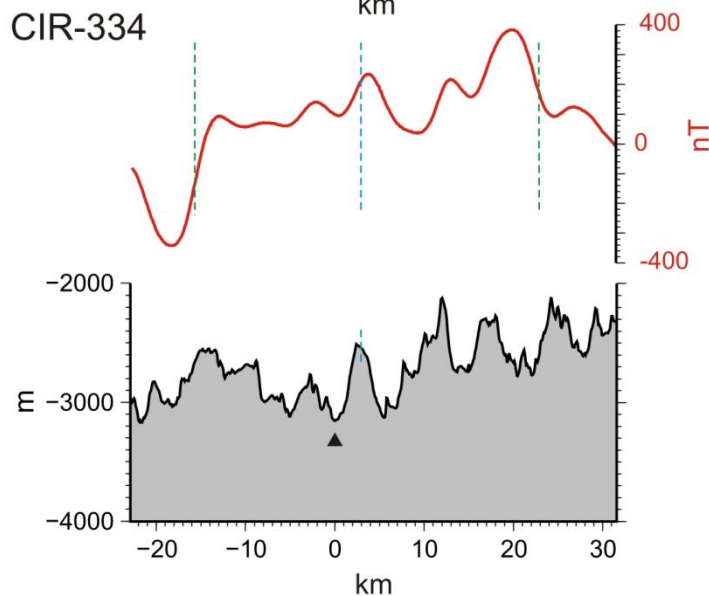
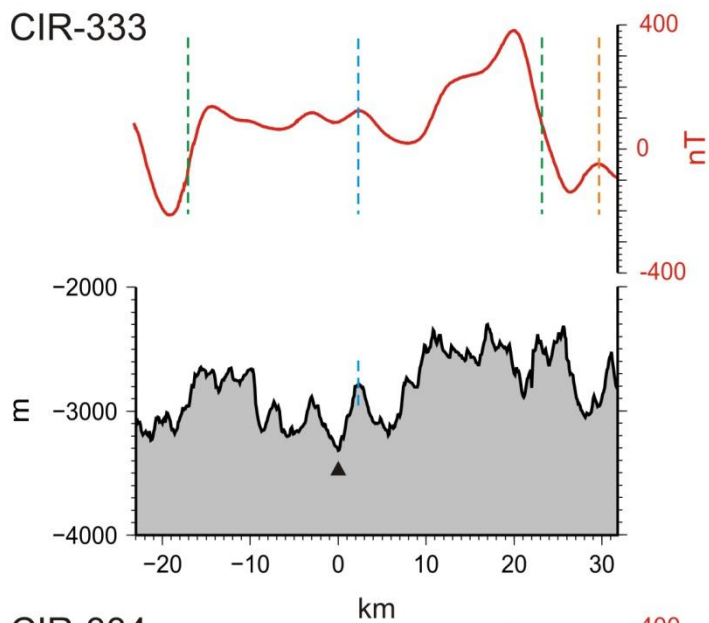
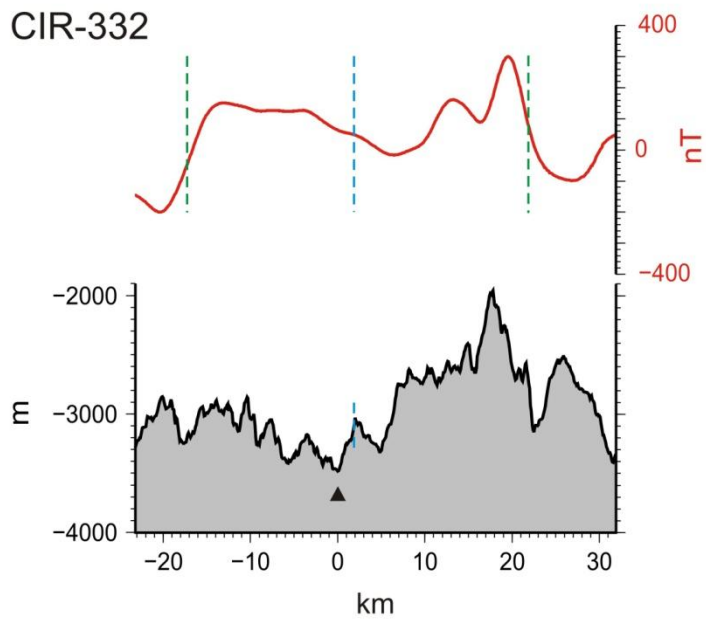


Figure A8: Magnetic (top) and bathymetric (bottom) profiles CIR332-CIR334 across the CIR from northwest to southeast (working area JX and Meso). The boundaries of Anomaly 1 are labeled with green lines and the boundaries of the Jaramillo event with orange lines. The ridge axis, defined as the bathymetric minimum, is shown with a black triangle. The blue lines represent the center of magnetic Anomaly 1.

- 332-334 Profiles
- Jaramillo event
 - Anomaly 1 (0-0.78 Ma)
 - Center of magnetic Anomaly 1
 - Bathymetric profiles
 - Magnetic profiles
 - ▲ Recent active spreading center

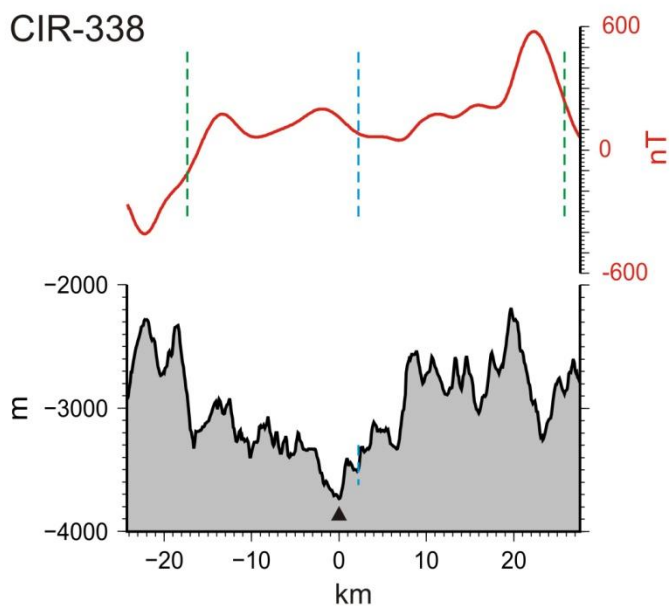
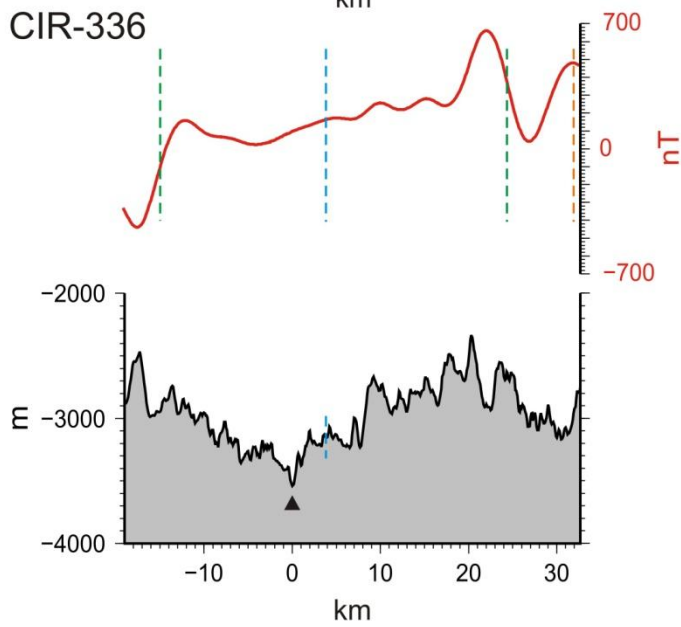
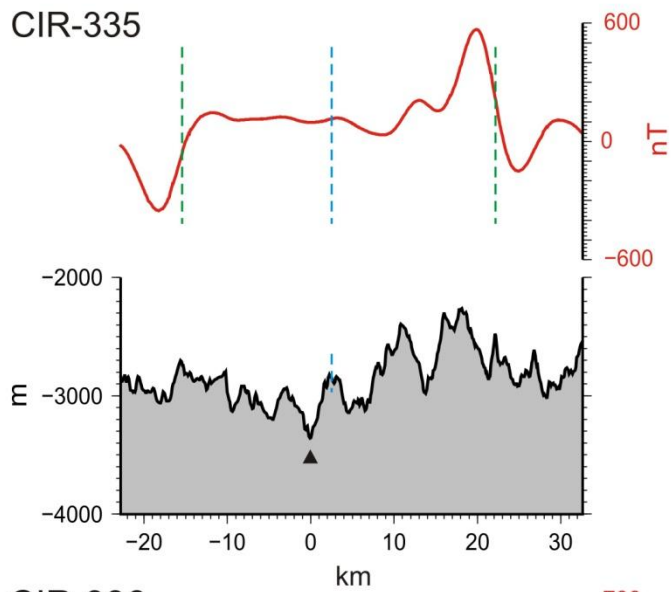


Figure A9: Magnetic (top) and bathymetric (bottom) profiles CIR335-CIR338 across the CIR from northwest to southeast (working area JX and Meso). The boundaries of Anomaly 1 are labeled with green lines and the boundaries of the Jaramillo event with orange lines. The ridge axis, defined as the bathymetric minimum, is shown with a black triangle. The blue lines represent the center of magnetic Anomaly 1.

- 335-338 Profiles
- Jaramillo event
 - Anomaly 1 (0-0.78 Ma)
 - Center of magnetic Anomaly 1
 - Bathymetric profiles
 - Magnetic profiles
 - ▲ Recent active spreading center

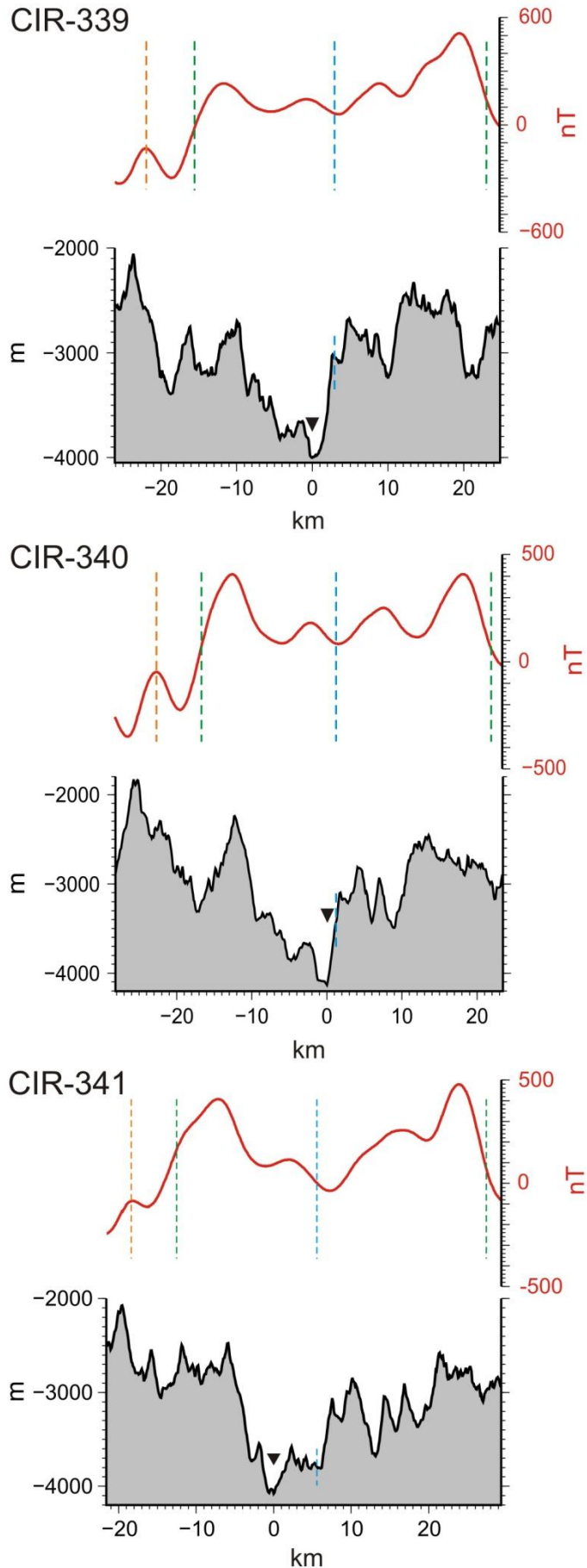


Figure A10: Magnetic (top) and bathymetric (bottom) profiles CIR339-CIR341 across the CIR from northwest to southeast (working area JX and Meso). The boundaries of Anomaly 1 are labeled with green lines and the boundaries of the Jaramillo event with orange lines. The ridge axis, defined as the bathymetric minimum, is shown with a black triangle. The blue lines represent the center of magnetic Anomaly 1.

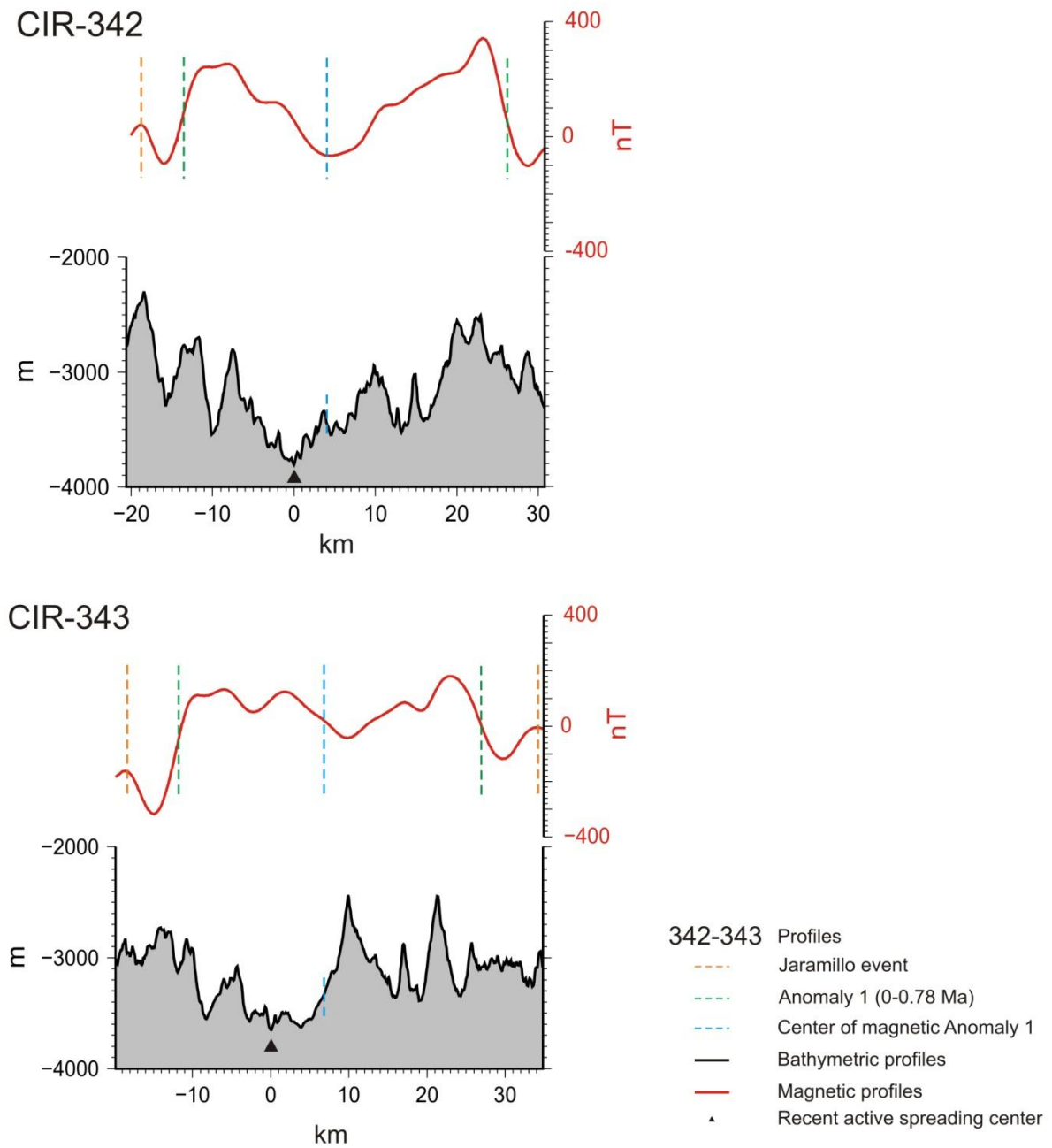


Figure A11: Magnetic (top) and bathymetric (bottom) profiles CIR342-CIR343 across the CIR from northwest to southeast (working area JX and Meso). The boundaries of Anomaly 1 are labeled with green lines and the boundaries of the Jaramillo event with orange lines. The ridge axis, defined as the bathymetric minimum, is shown with a black triangle. The blue lines represent the center of magnetic Anomaly 1.

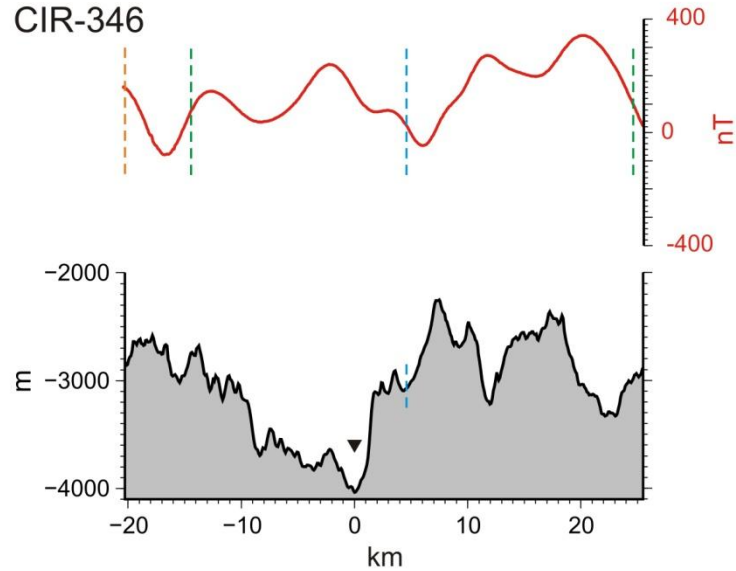
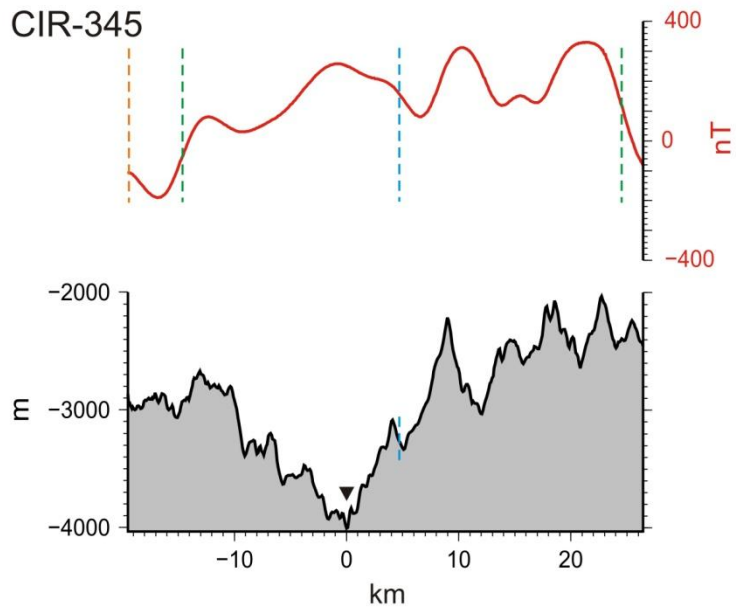
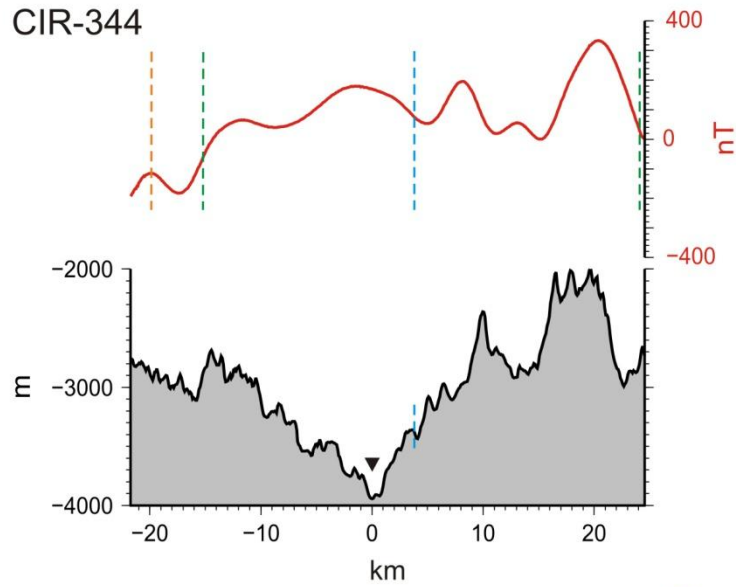


Figure A12: Magnetic (top) and bathymetric (bottom) profiles CIR344-CIR346 across the CIR from northwest to southeast (working area Edmond). The boundaries of Anomaly 1 are labeled with green lines and the boundaries of the Jaramillo event with orange lines. The ridge axis, defined as the bathymetric minimum, is shown with a black triangle. The blue lines represent the center of magnetic Anomaly 1.

- 344-346 Profiles
- Jaramillo event
 - Anomaly 1 (0-0.78 Ma)
 - Center of magnetic Anomaly 1
 - Bathymetric profiles
 - Magnetic profiles
 - ▲ Recent active spreading center

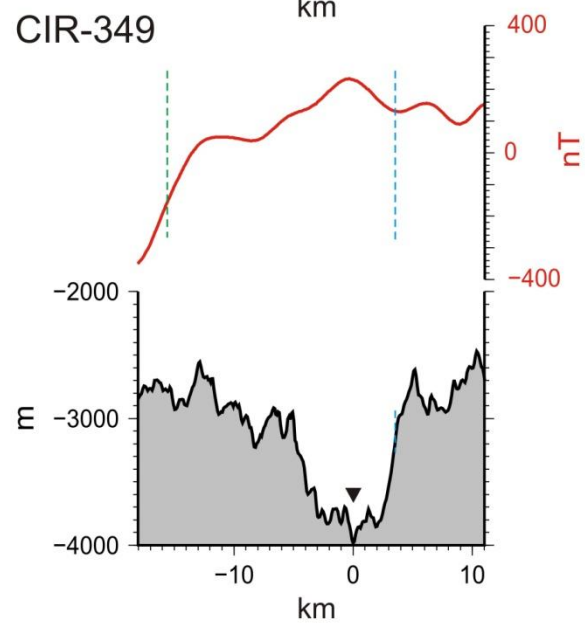
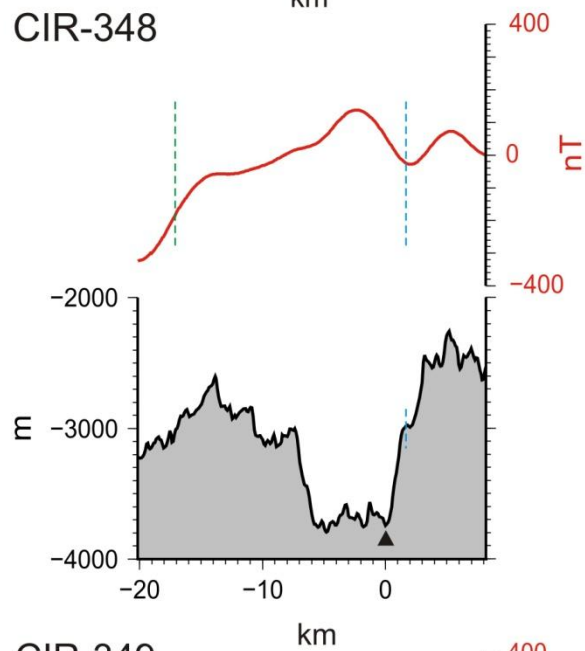
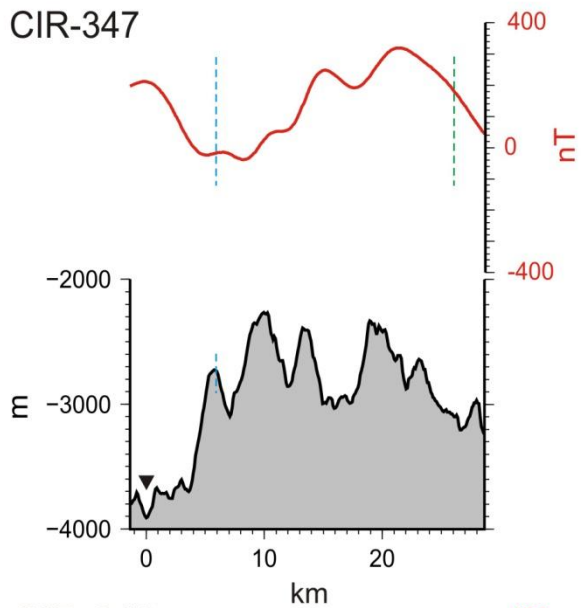
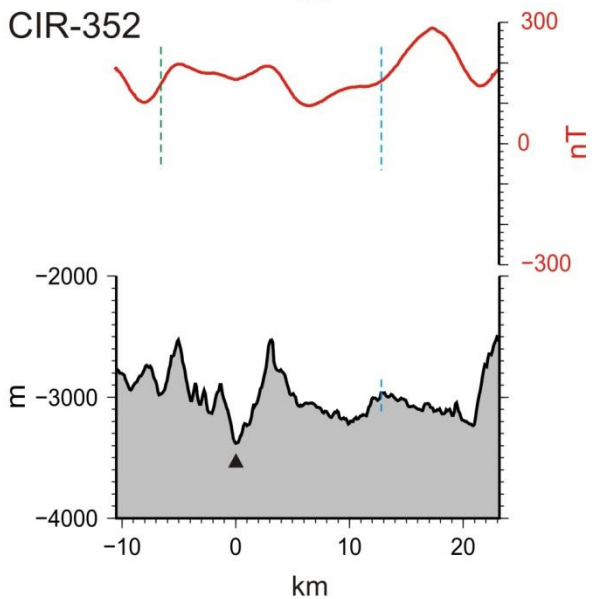
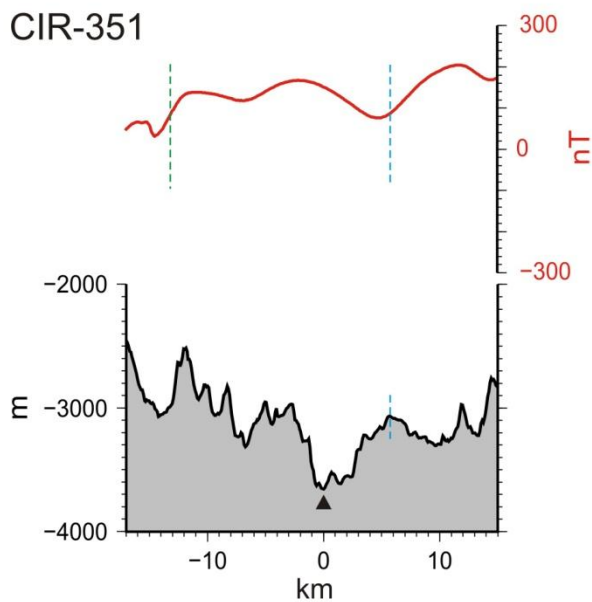
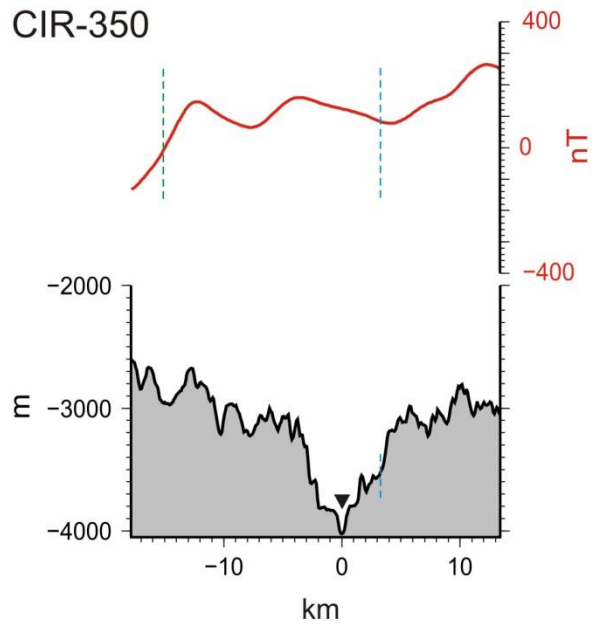


Figure A13: Magnetic (top) and bathymetric (bottom) profiles CIR347-CIR349 across the CIR from northwest to southeast (working area Edmond). The boundaries of Anomaly 1 are labeled with green lines. The ridge axis, defined as the bathymetric minimum, is shown with a black triangle. The blue lines represent the center of magnetic Anomaly 1.

- 347-349 Profiles
- Anomaly 1 (0-0.78 Ma)
 - Center of magnetic Anomaly 1
 - Bathymetric profiles
 - Magnetic profiles
 - ▲ Recent active spreading center



- 350-352 Profiles
- Anomaly 1 (0-0.78 Ma)
 - Center of magnetic Anomaly 1
 - Bathymetric profiles
 - Magnetic profiles
 - ▲ Recent active spreading center

Figure A14: Magnetic (top) and bathymetric (bottom) profiles CIR350-CIR352 across the CIR from northwest to southeast (working area Edmond). The boundaries of Anomaly 1 are labeled with green lines. The ridge axis, defined as the bathymetric minimum, is shown with a black triangle. The blue lines represent the center of magnetic Anomaly 1.

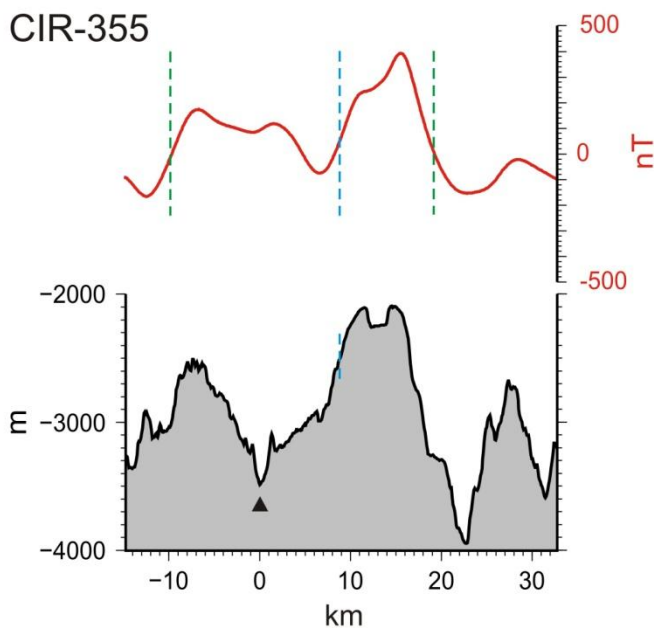
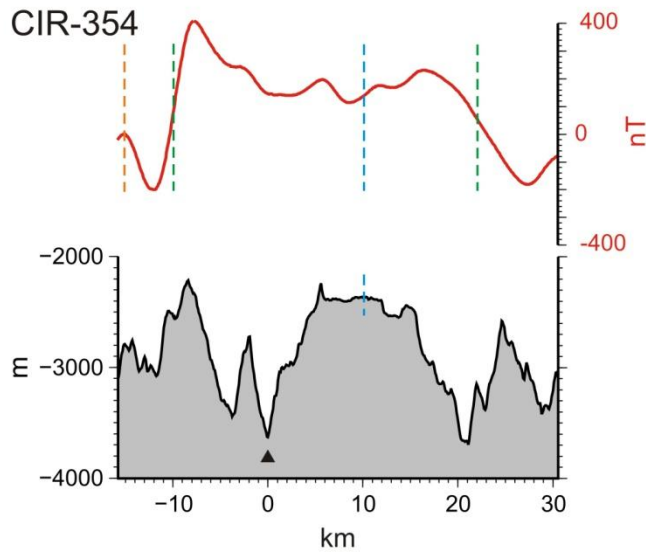
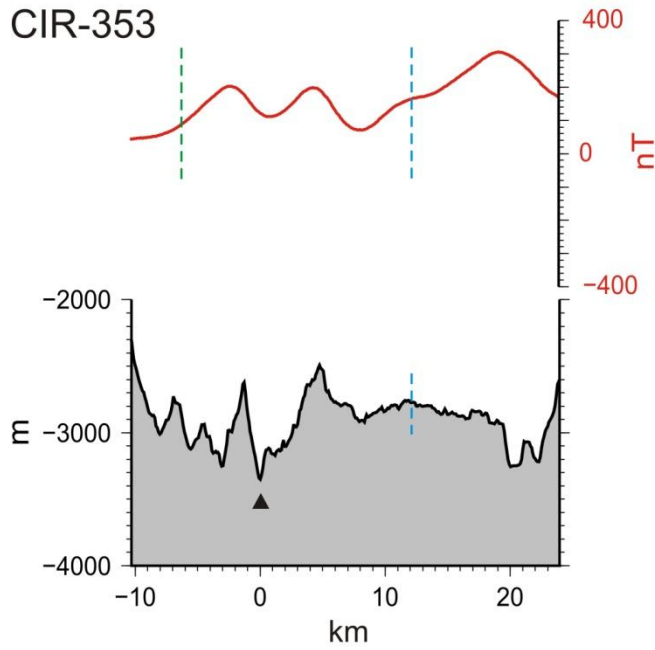


Figure A15: Magnetic (top) and bathymetric (bottom) profiles CIR353-CIR355 across the CIR from northwest to southeast (working area Edmond). The boundaries of Anomaly 1 are labeled with green lines and the boundaries of the Jaramillo event with orange lines. The ridge axis, defined as the bathymetric minimum, is shown with a black triangle. The blue lines represent the center of magnetic Anomaly 1.

- 353-355 Profiles
- Jaramillo event
 - Anomaly 1 (0-0.78 Ma)
 - Center of magnetic Anomaly 1
 - Bathymetric profiles
 - Magnetic profiles
 - ▲ Recent active spreading center

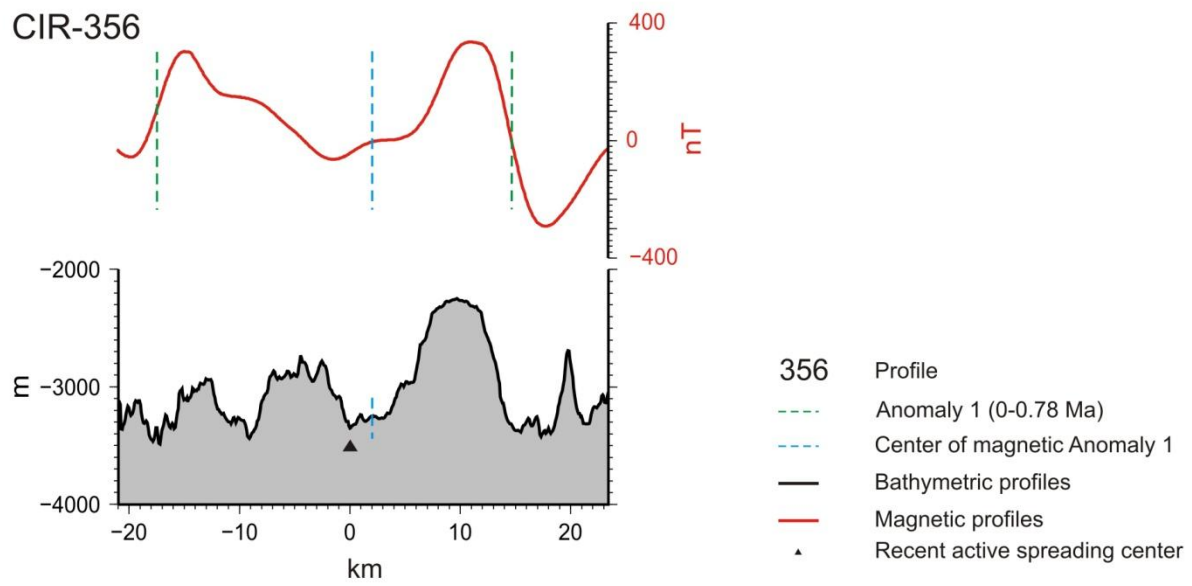


Figure A16: Magnetic (top) and bathymetric (bottom) profile CIR356 across the CIR from northwest to southeast (working area Edmond). The boundaries of Anomaly 1 are labeled with green lines. The ridge axis, defined as the bathymetric minimum, is shown with a black triangle. The blue lines represent the center of magnetic Anomaly 1.

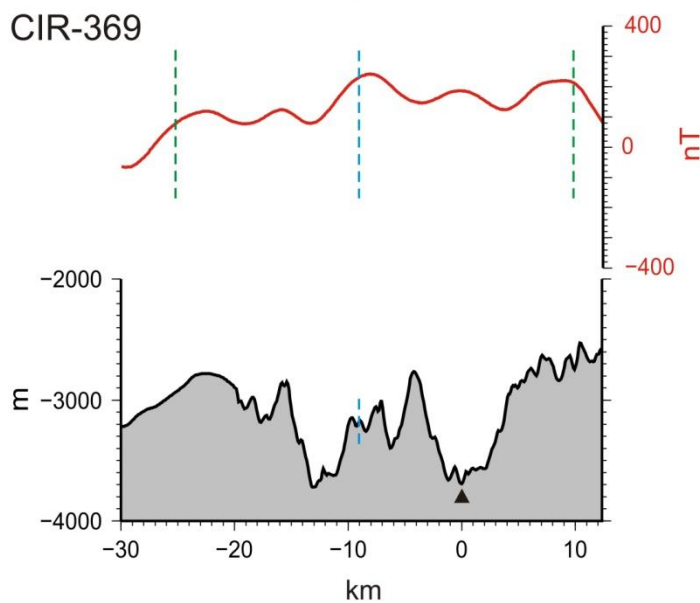
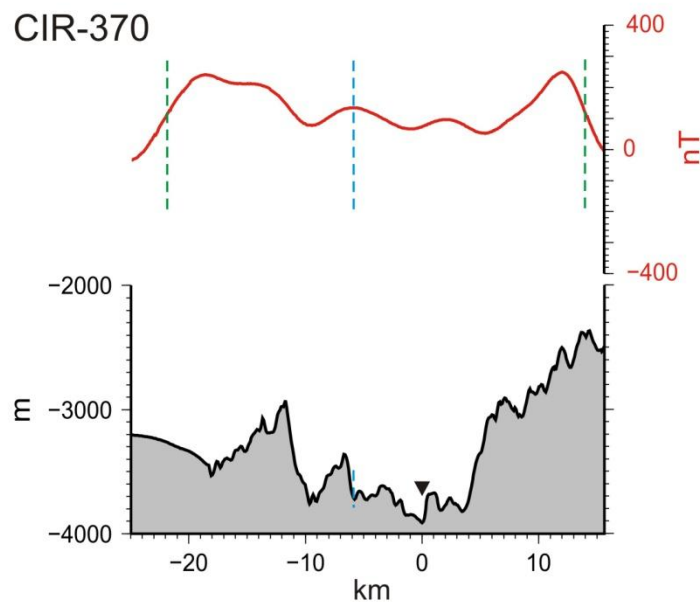
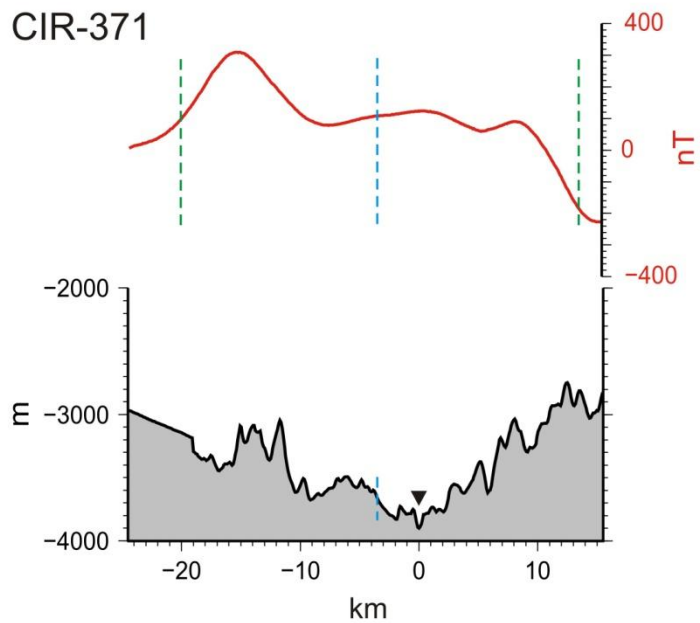


Figure A17: Magnetic (top) and bathymetric (bottom) profiles CIR371-CIR369 across the CIR from northwest to southeast (working area Kairei). The boundaries of Anomaly 1 are labeled with green lines. The ridge axis, defined as the bathymetric minimum, is shown with a black triangle. The blue lines represent the center of magnetic Anomaly 1.

- 371-369 Profiles
- Anomaly 1 (0-0.78 Ma)
 - - - Center of magnetic Anomaly 1
 - Bathymetric profiles
 - Magnetic profiles
 - ▲ Recent active spreading center

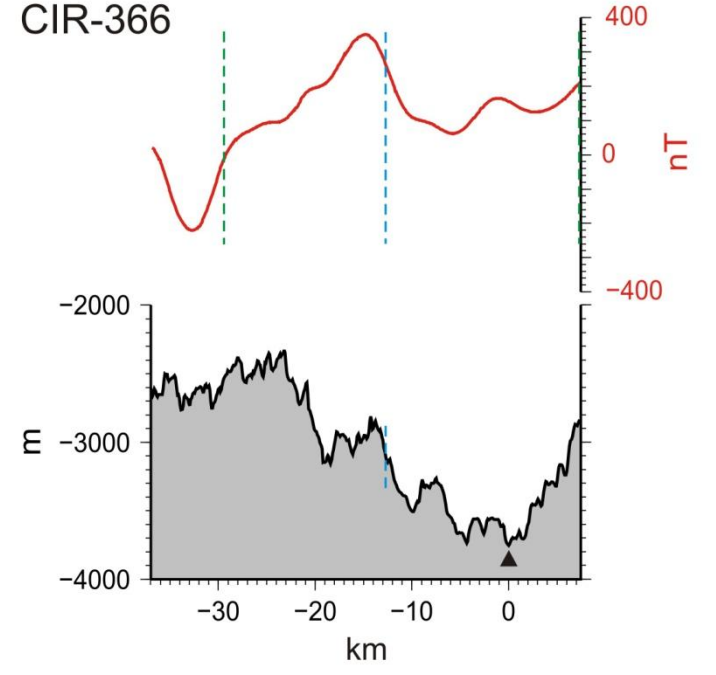
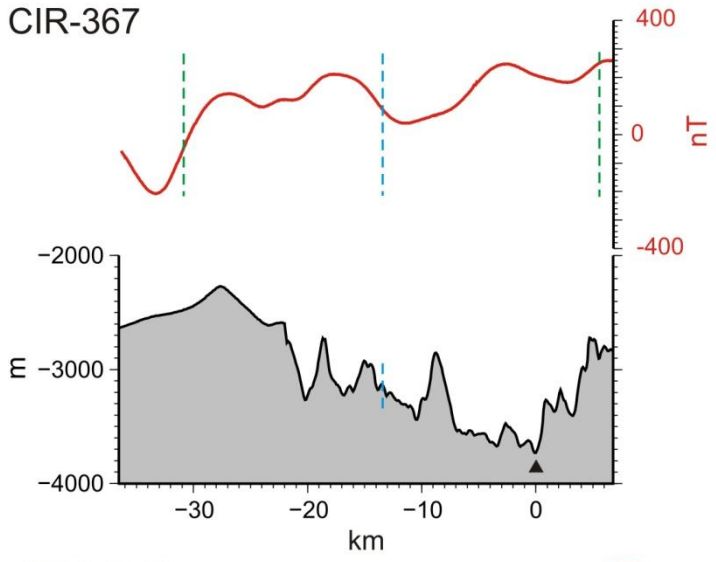
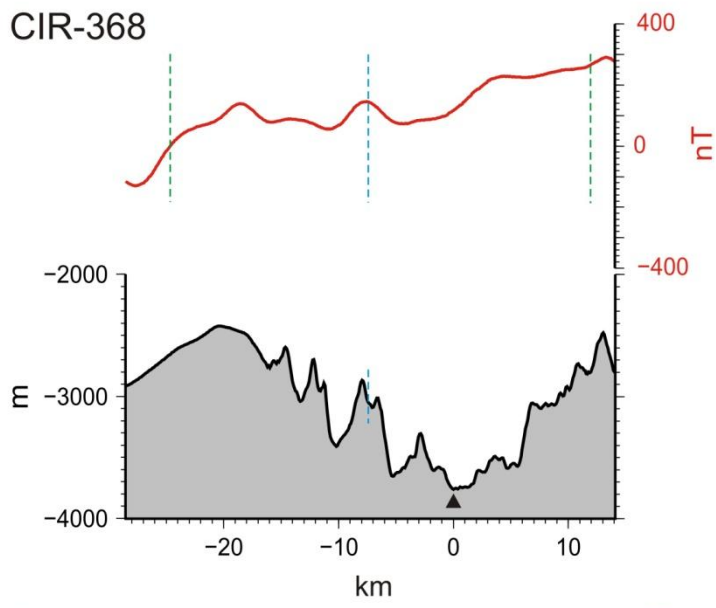


Figure A18: Magnetic (top) and bathymetric (bottom) profiles CIR368-CIR366 across the CIR from northwest to southeast (working area Kairei). The boundaries of Anomaly 1 are labeled with green lines. The ridge axis, defined as the bathymetric minimum, is shown with a black triangle. The blue lines represent the center of magnetic Anomaly 1.

368-366 Profiles

- Anomaly 1 (0-0.78 Ma)
- Center of magnetic Anomaly 1
- Bathymetric profiles
- Magnetic profiles
- ▲ Recent active spreading center

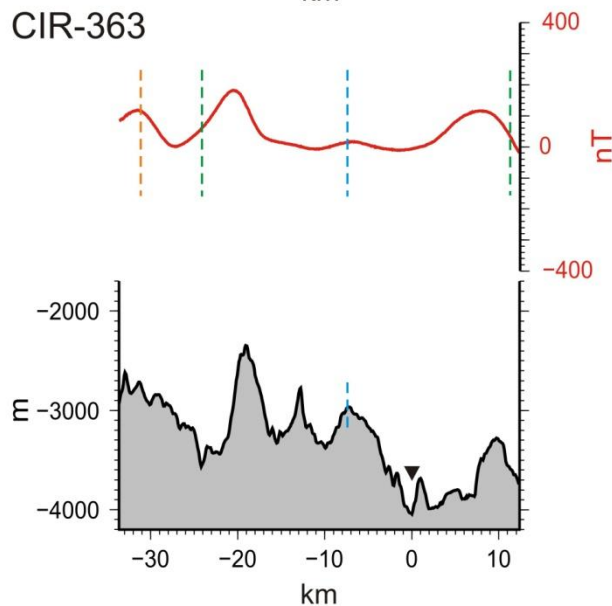
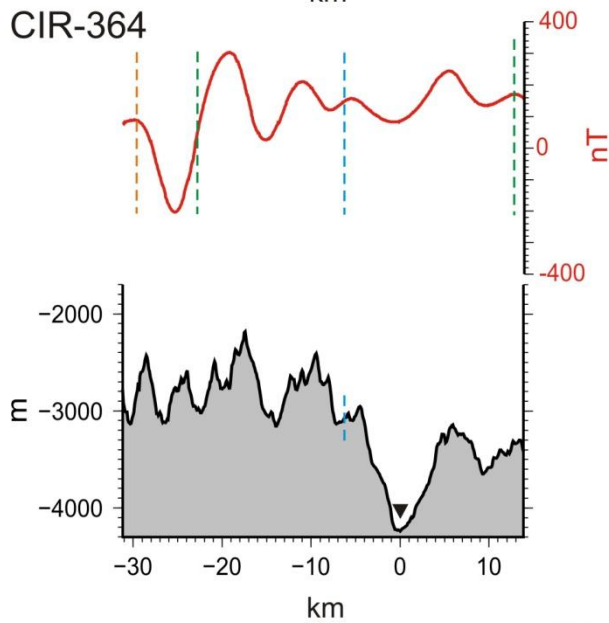
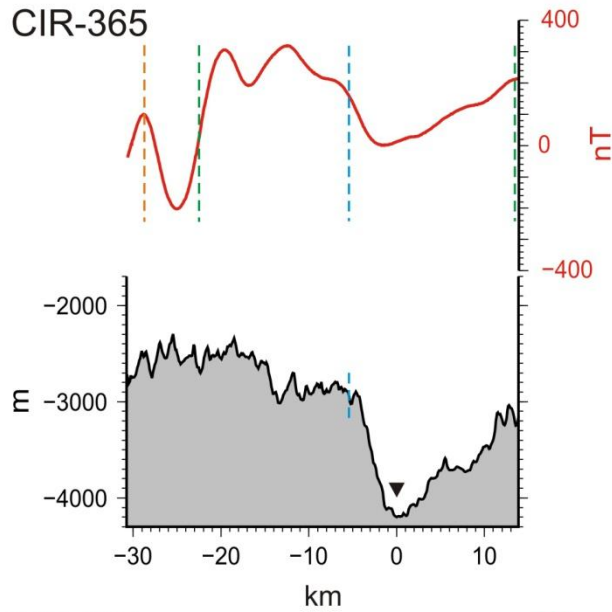


Figure A19: Magnetic (top) and bathymetric (bottom) profiles CIR365-CIR363 across the CIR from northwest to southeast (working area Kairei). The boundaries of Anomaly 1 are labeled with green lines and the boundaries of the Jaramillo event with orange lines. The ridge axis, defined as the bathymetric minimum, is shown with a black triangle. The blue lines represent the center of magnetic Anomaly 1.

- 365-363 Profiles
- Jaramillo event
 - Anomaly 1 (0-0.78 Ma)
 - Center of magnetic Anomaly 1
 - Bathymetric profiles
 - Magnetic profiles
 - ▲ Recent active spreading center

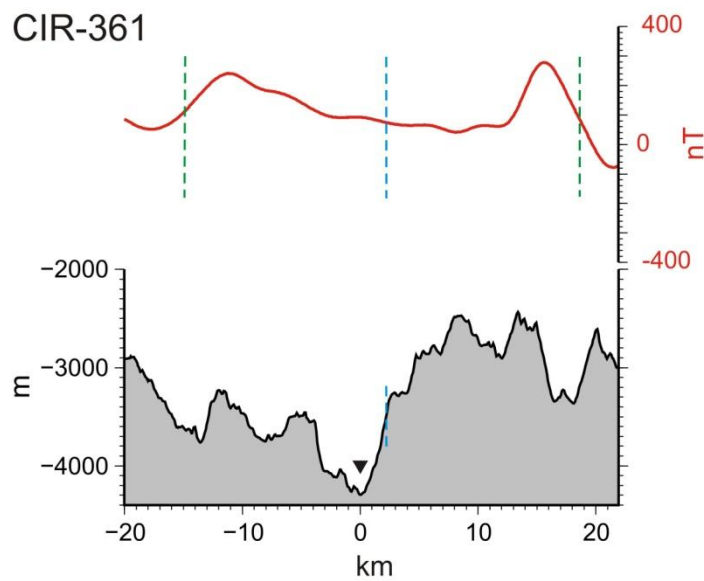
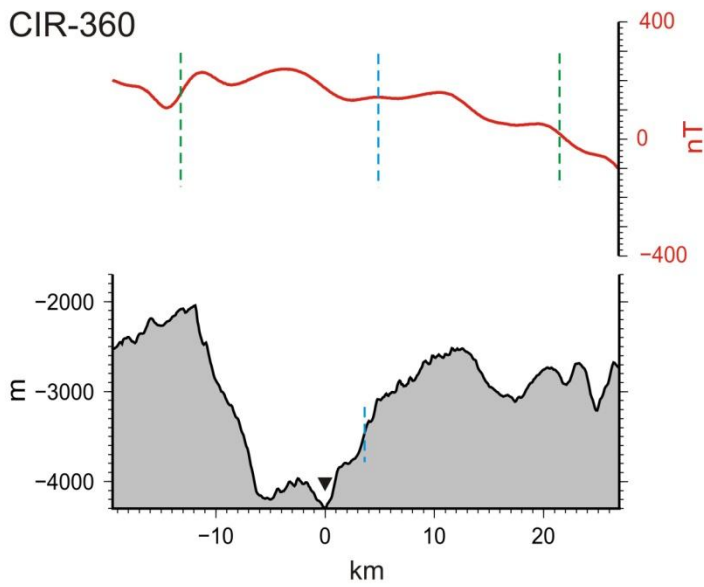
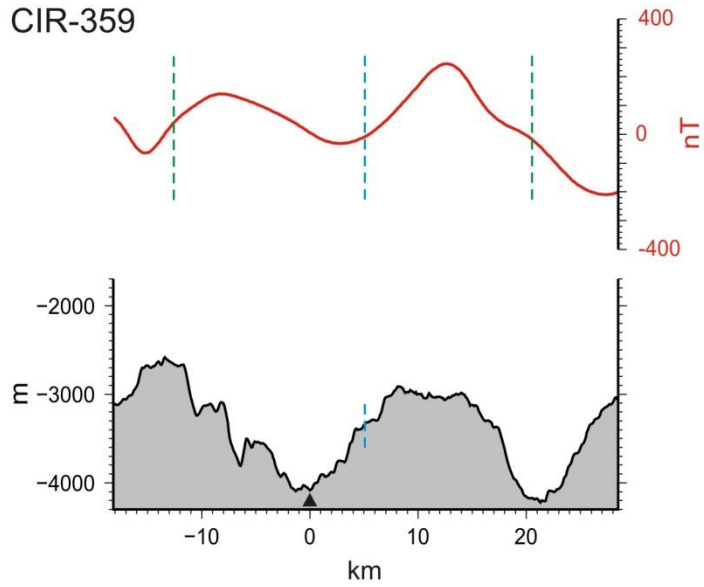


Figure A20: Magnetic (top) and bathymetric (bottom) profiles CIR359-CIR361 across the CIR from northwest to southeast (working area Kaiei). The boundaries of Anomaly 1 are labeled with green lines. The ridge axis, defined as the bathymetric minimum, is shown with a black triangle. The blue lines represent the center of magnetic Anomaly 1.

- 359-361 Profiles
- Anomaly 1 (0-0.78 Ma)
 - Center of magnetic Anomaly 1
 - Bathymetric profiles
 - Magnetic profiles
 - ▲ Recent active spreading center

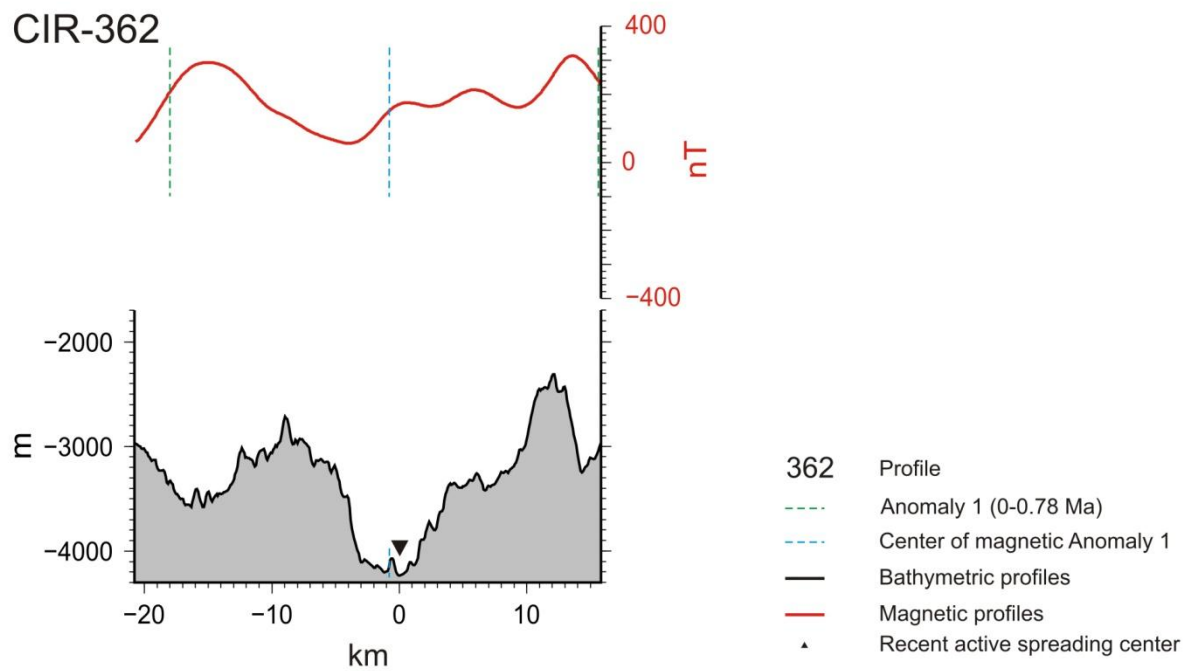


Figure A21: Magnetic (top) and bathymetric (bottom) profile CIR362 across the CIR from northwest to southeast (working area Kairei). The boundaries of Anomaly 1 are labeled with green lines. The ridge axis, defined as the bathymetric minimum, is shown with a black triangle. The blue lines represent the center of magnetic Anomaly 1.

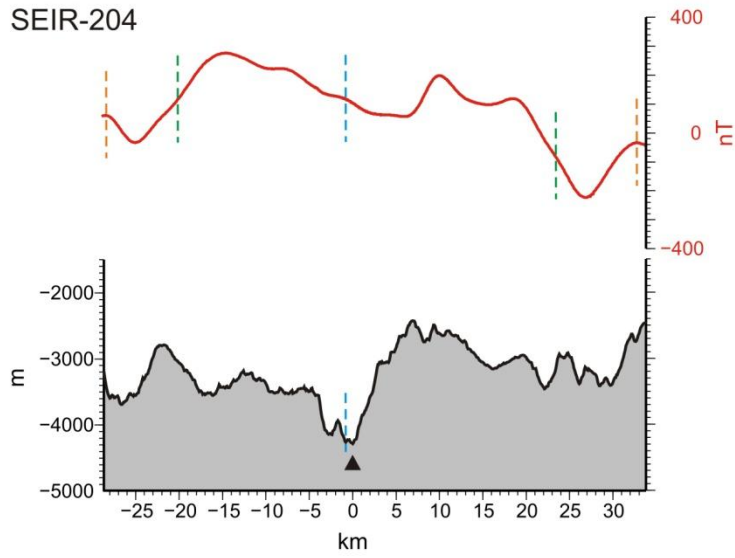
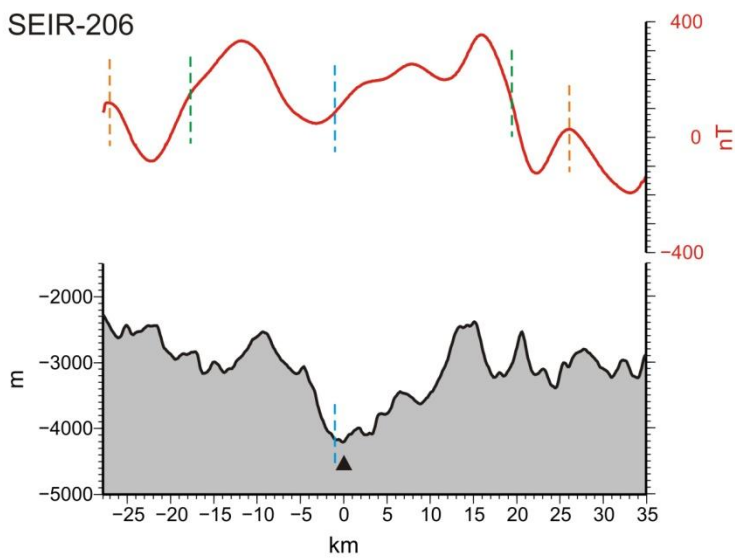
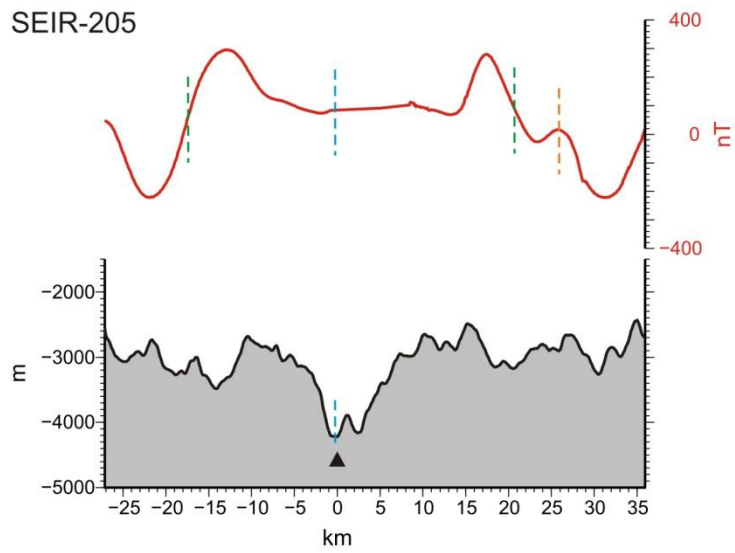


Figure A22: Magnetic (top) and bathymetric (bottom) profiles SEIR204-SEIR206 across the SEIR from northwest to southeast (working area Section1). The boundaries of Anomaly 1 are labeled with green lines and the boundaries of the Jaramillo event with orange lines. The ridge axis, defined as the bathymetric minimum, is shown with a black triangle. The blue lines represent the center of magnetic Anomaly 1.



- 204-206 Profiles
- Jaramillo event
 - Anomaly 1 (0-0.78 Ma)
 - Center of magnetic Anomaly 1
 - Bathymetric profiles
 - Magnetic profiles
 - ▲ Recent active spreading center

SEIR-207

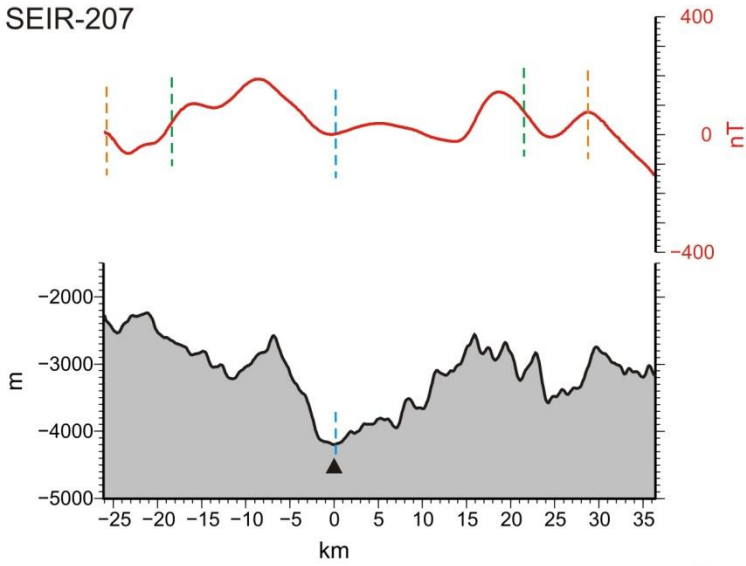
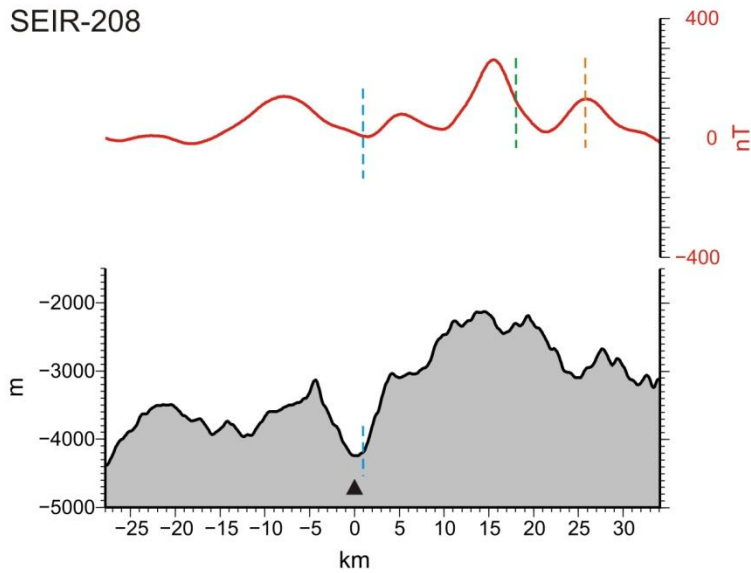
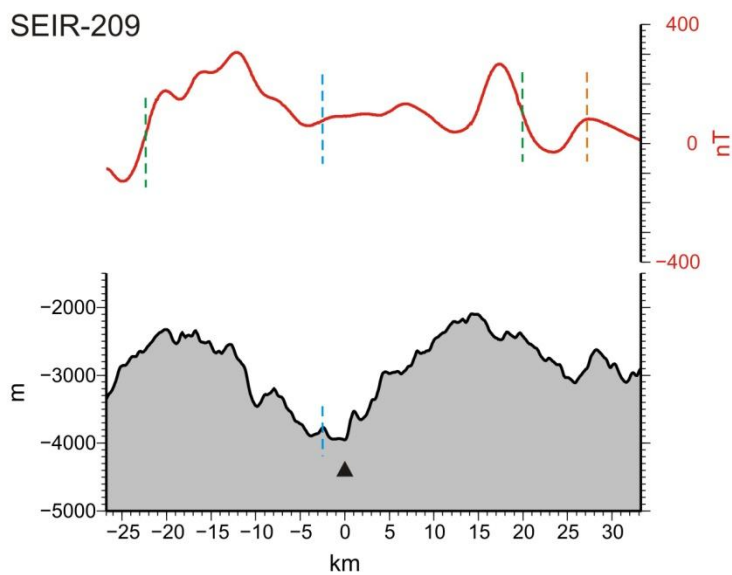


Figure A23: Magnetic (top) and bathymetric (bottom) profiles SEIR207-SEIR209 across the SEIR from northwest to southeast (working area Section1). The boundaries of Anomaly 1 are labeled with green lines and the boundaries of the Jaramillo event with orange lines. The ridge axis, defined as the bathymetric minimum, is shown with a black triangle. The blue lines represent the center of magnetic Anomaly 1.

SEIR-208



SEIR-209



- 207-209 Profiles
- Jaramillo event
 - Anomaly 1 (0-0.78 Ma)
 - Center of magnetic Anomaly 1
 - Bathymetric profiles
 - Magnetic profiles
 - ▲ Recent active spreading center

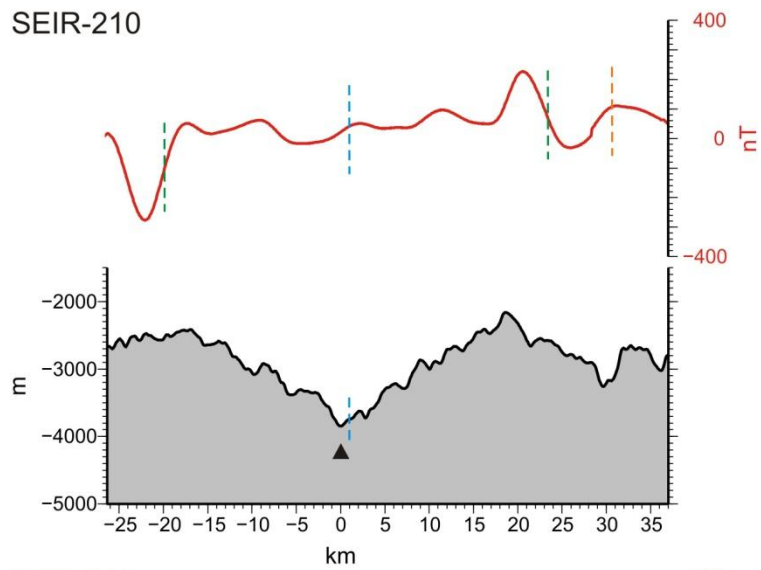
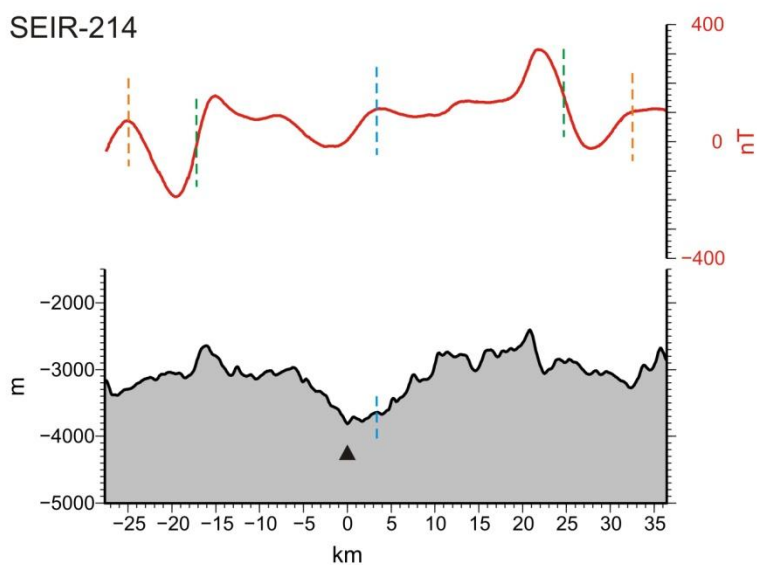
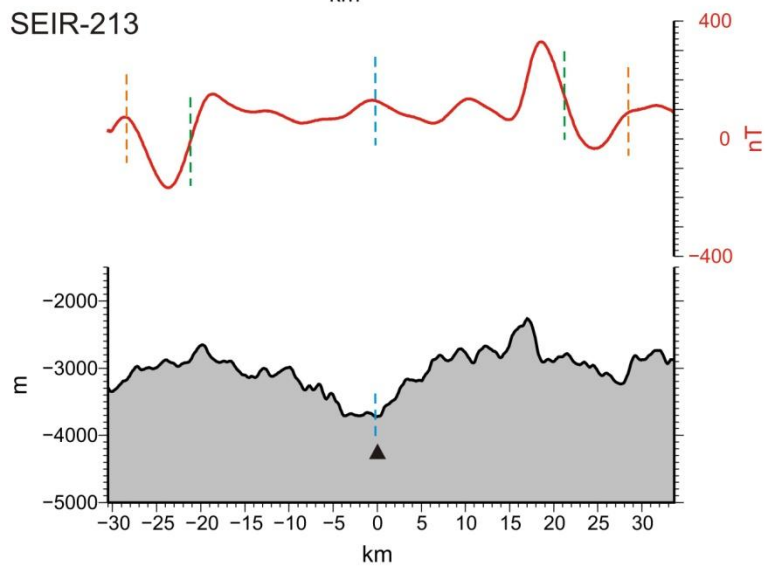


Figure A24: Magnetic (top) and bathymetric (bottom) profiles SEIR210-SEIR214 across the SEIR from northwest to southeast (working area Section1). The boundaries of Anomaly 1 are labeled with green lines and the boundaries of the Jaramillo event with orange lines. The ridge axis, defined as the bathymetric minimum, is shown with a black triangle. The blue lines represent the center of magnetic Anomaly 1.



- 210-214 Profiles
- Jaramillo event
 - Anomaly 1 (0-0.78 Ma)
 - Center of magnetic Anomaly 1
 - Bathymetric profiles
 - Magnetic profiles
 - ▲ Recent active spreading center

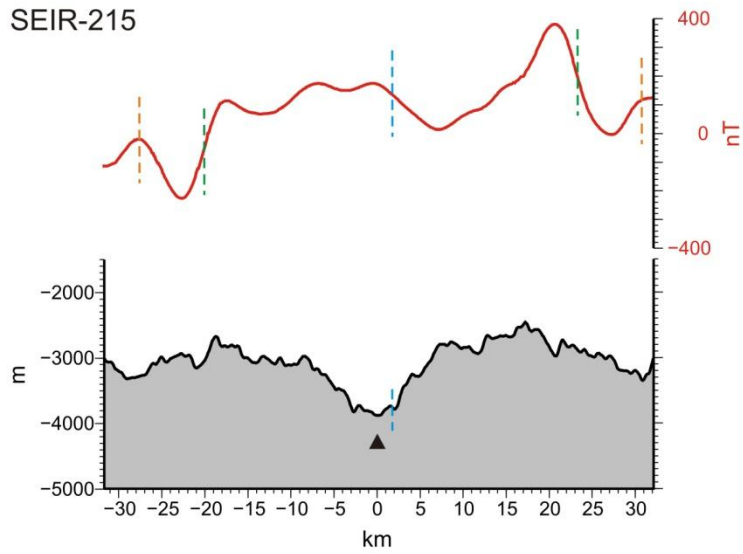
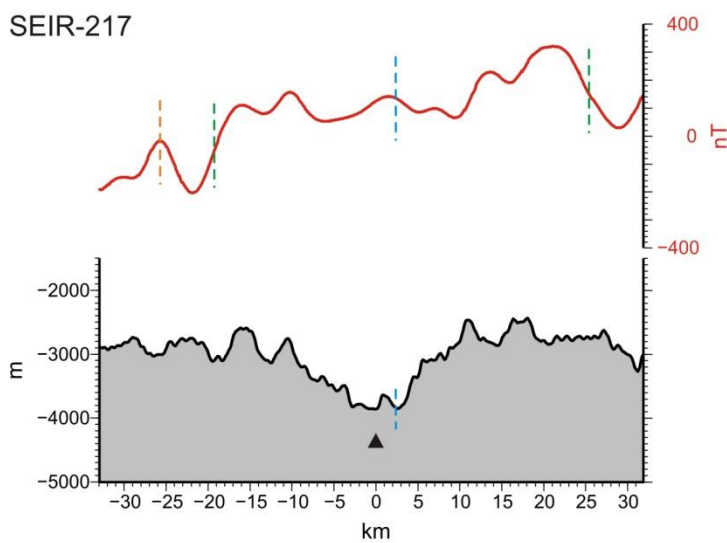
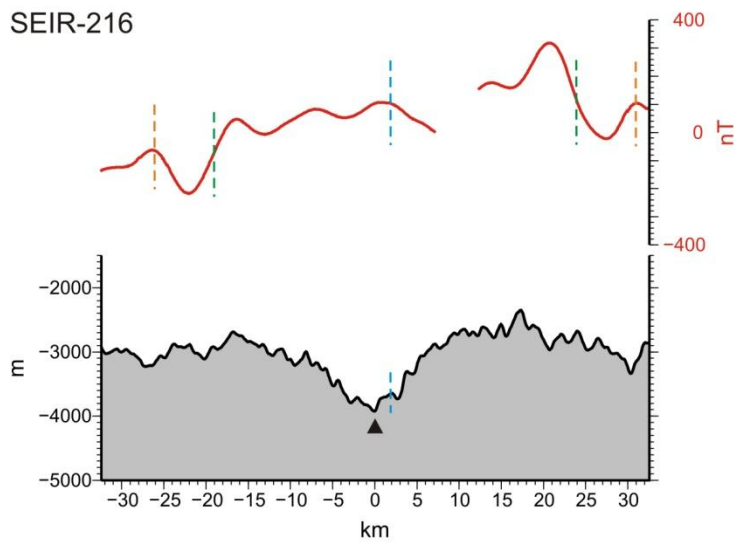


Figure A25: Magnetic (top) and bathymetric (bottom) profiles SEIR215-SEIR217 across the SEIR from northwest to southeast (working area Section1). The boundaries of Anomaly 1 are labeled with green lines and the boundaries of the Jaramillo event with orange lines. The ridge axis, defined as the bathymetric minimum, is shown with a black triangle. The blue lines represent the center of magnetic Anomaly 1.



- 215-217 Profiles
- Jaramillo event
 - Anomaly 1 (0-0.78 Ma)
 - Center of magnetic Anomaly 1
 - Bathymetric profiles
 - Magnetic profiles
 - ▲ Recent active spreading center

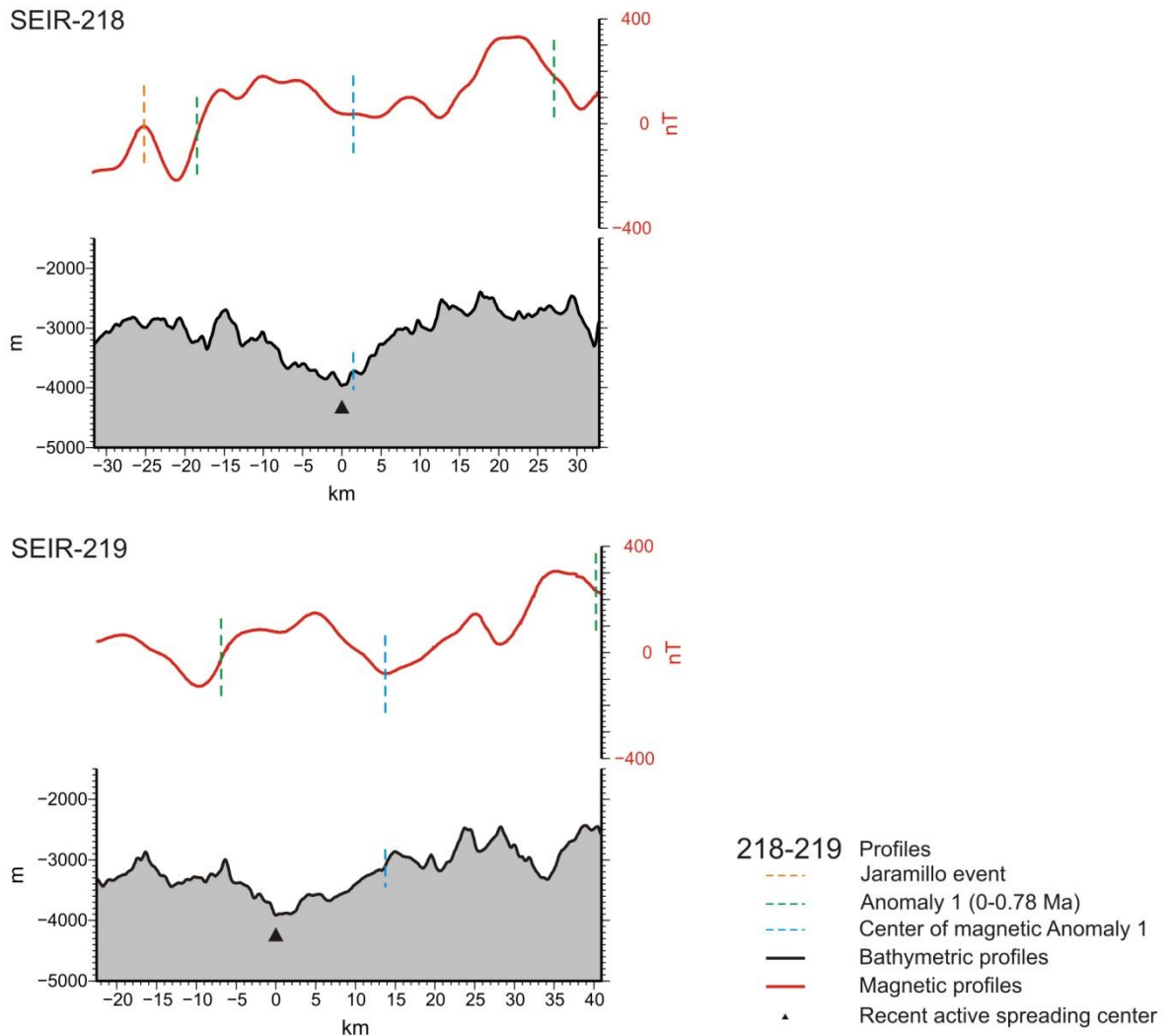
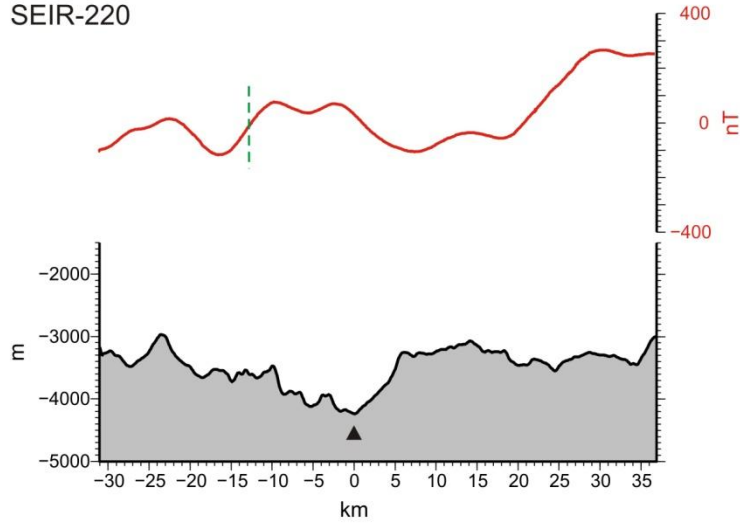
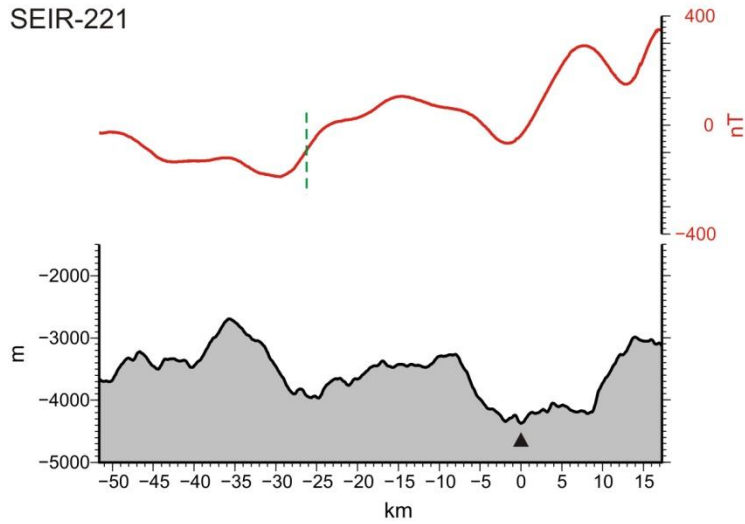


Figure A26: Magnetic (top) and bathymetric (bottom) profiles SEIR218-SEIR219 across the SEIR from northwest to southeast (working area Section1). The boundaries of Anomaly 1 are labeled with green lines and the boundaries of the Jaramillo event with orange lines. The ridge axis, defined as the bathymetric minimum, is shown with a black triangle. The blue lines represent the center of magnetic Anomaly 1.

SEIR-220



SEIR-221



SEIR-222

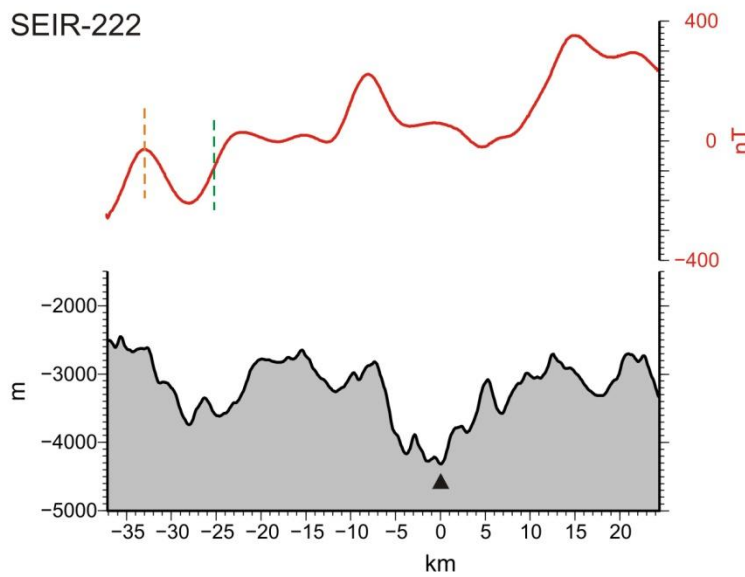
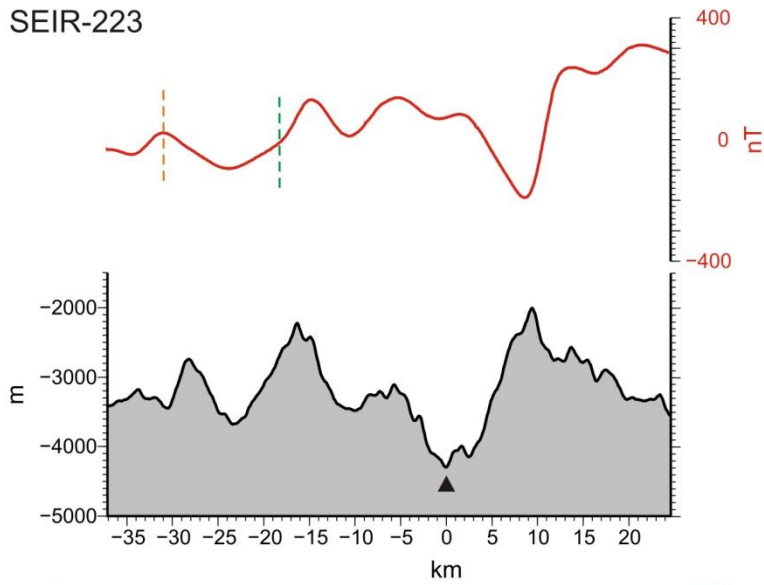


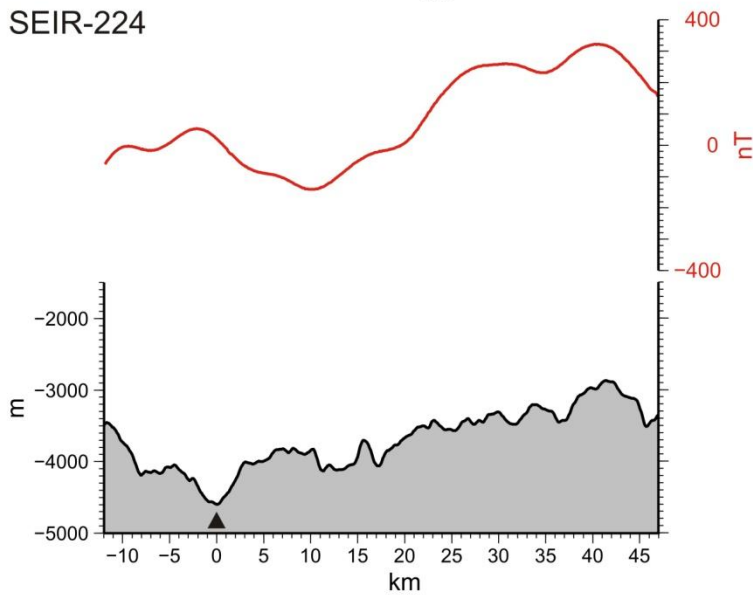
Figure A27: Magnetic (top) and bathymetric (bottom) profiles SEIR220-SEIR222 across the SEIR from northwest to southeast (working area Section2). The boundaries of Anomaly 1 are labeled with green lines and the boundaries of the Jaramillo event with orange lines. The ridge axis, defined as the bathymetric minimum, is shown with a black triangle.

- 220-222 Profiles
- Jaramillo event
 - Anomaly 1 (0-0.78 Ma)
 - Center of magnetic Anomaly 1
 - Bathymetric profiles
 - Magnetic profiles
 - ▲ Recent active spreading center

SEIR-223



SEIR-224



SEIR-225

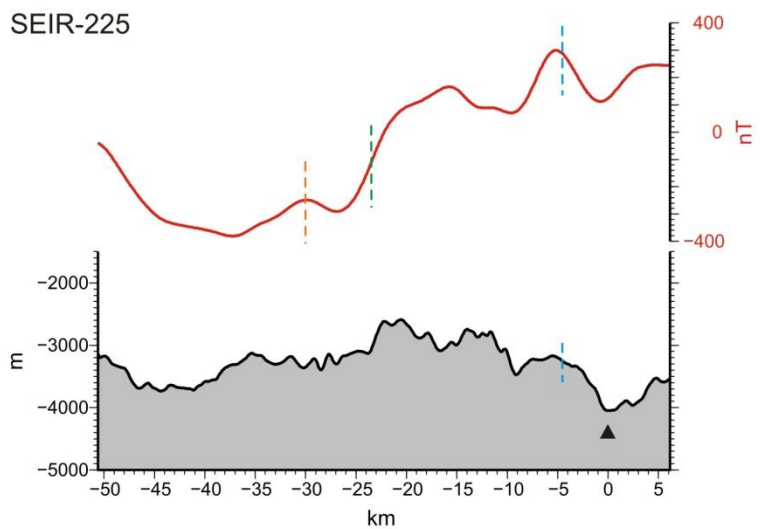


Figure A28: Magnetic (top) and bathymetric (bottom) profiles SEIR223-SEIR225 across the SEIR from northwest to southeast (working area Section2). The boundaries of Anomaly 1 are labeled with green lines and the boundaries of the Jaramillo event with orange lines. The ridge axis, defined as the bathymetric minimum, is shown with a black triangle. The blue lines represent the center of magnetic Anomaly 1.

- 223-225 Profiles
- Jaramillo event
 - Anomaly 1 (0-0.78 Ma)
 - Center of magnetic Anomaly 1
 - Bathymetric profiles
 - Magnetic profiles
 - ▲ Recent active spreading center

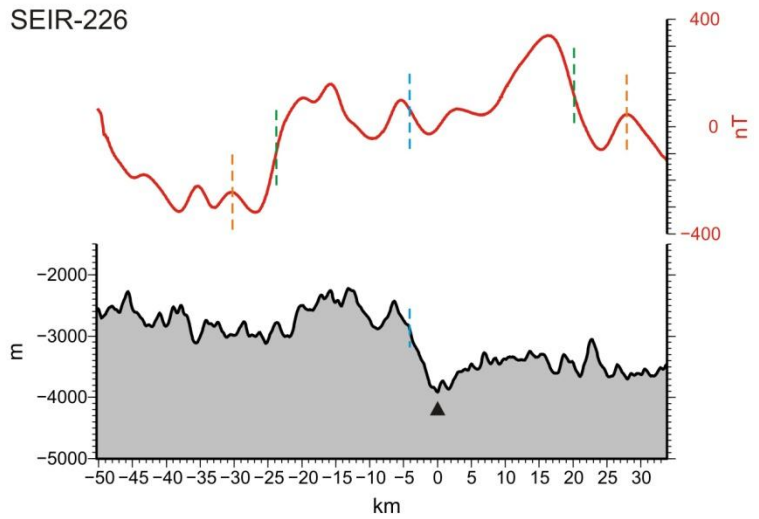
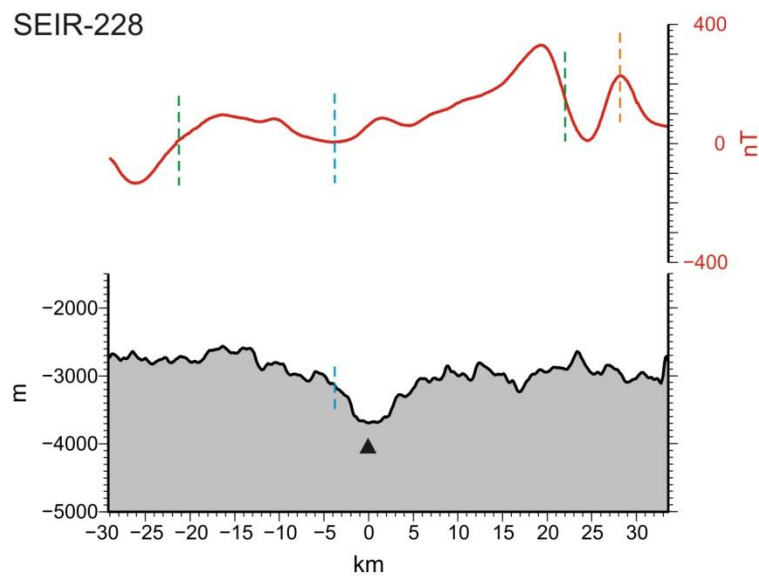
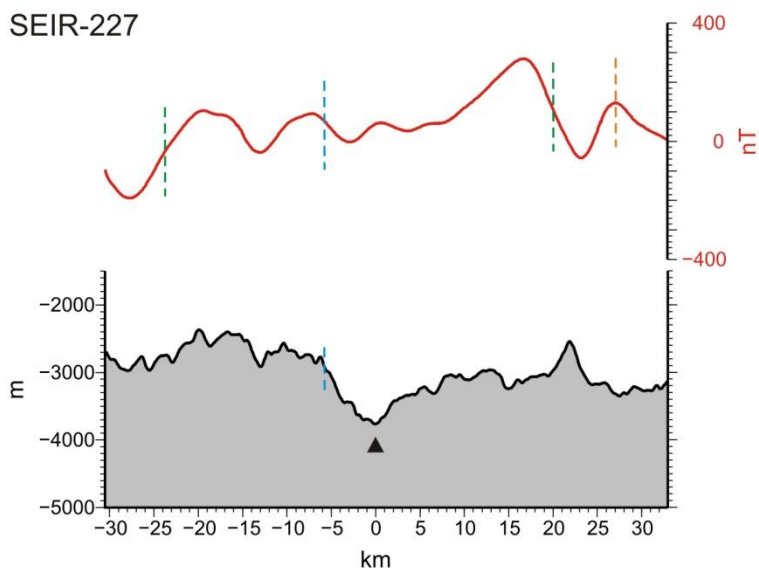
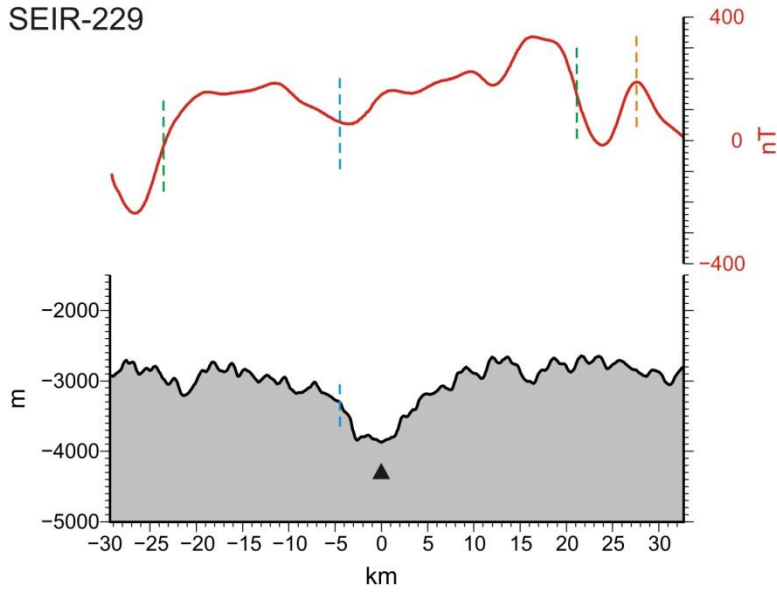


Figure A29: Magnetic (top) and bathymetric (bottom) profiles SEIR226-SEIR228 across the SEIR from northwest to southeast (working area Section3). The boundaries of Anomaly 1 are labeled with green lines and the boundaries of the Jaramillo event with orange lines. The ridge axis, defined as the bathymetric minimum, is shown with a black triangle. The blue lines represent the center of magnetic Anomaly 1.

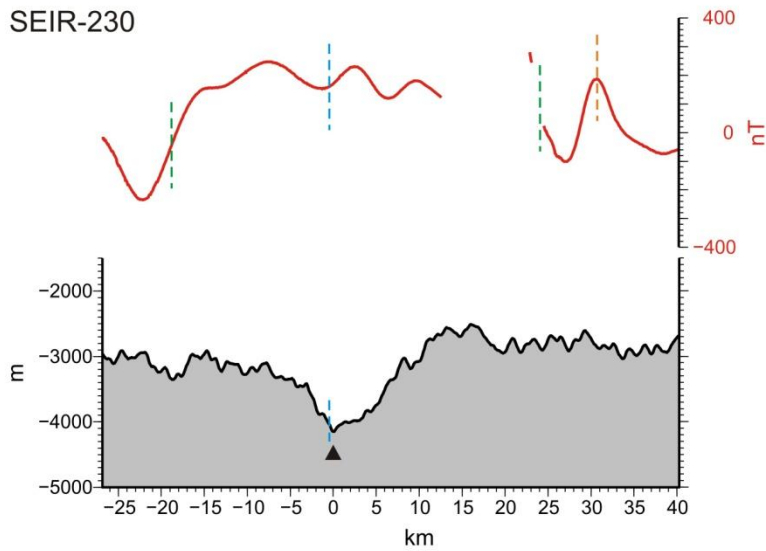


- 226-228 Profiles
- Jaramillo event
 - Anomaly 1 (0-0.78 Ma)
 - Center of magnetic Anomaly 1
 - Bathymetric profiles
 - Magnetic profiles
 - ▲ Recent active spreading center

SEIR-229



SEIR-230



SEIR-231

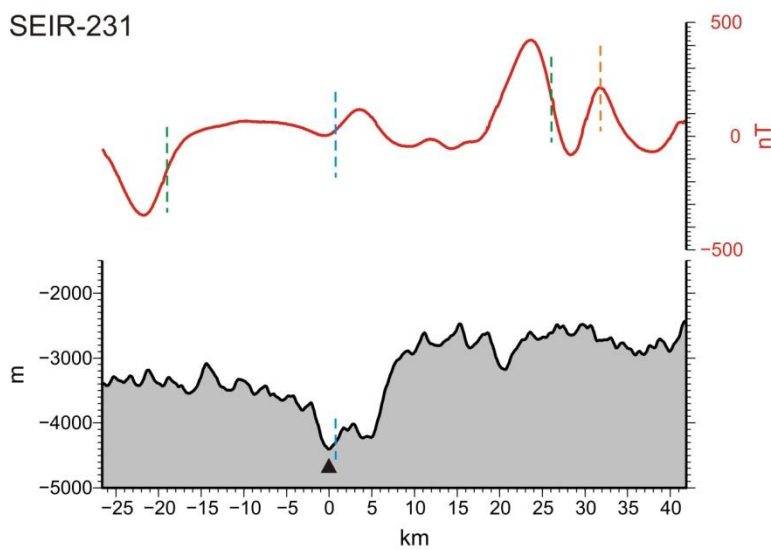


Figure A30: Magnetic (top) and bathymetric (bottom) profiles SEIR229-SEIR231 across the SEIR from northwest to southeast (working area Section3). The boundaries of Anomaly 1 are labeled with green lines and the boundaries of the Jaramillo event with orange lines. The ridge axis, defined as the bathymetric minimum, is shown with a black triangle. The blue lines represent the center of magnetic Anomaly 1.

- 229-231 Profiles
- Jaramillo event
 - Anomaly 1 (0-0.78 Ma)
 - Center of magnetic Anomaly 1
 - Bathymetric profiles
 - Magnetic profiles
 - ▲ Recent active spreading center

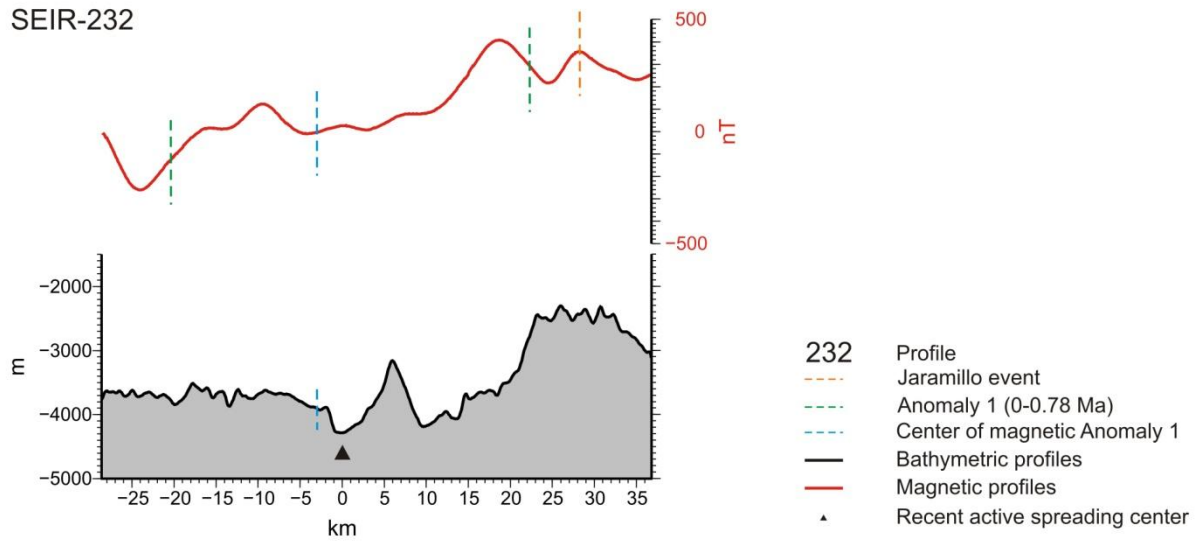
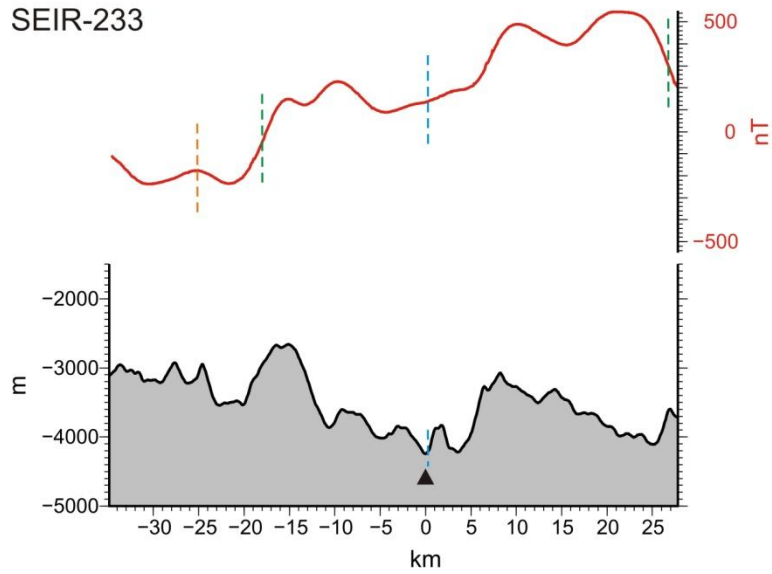
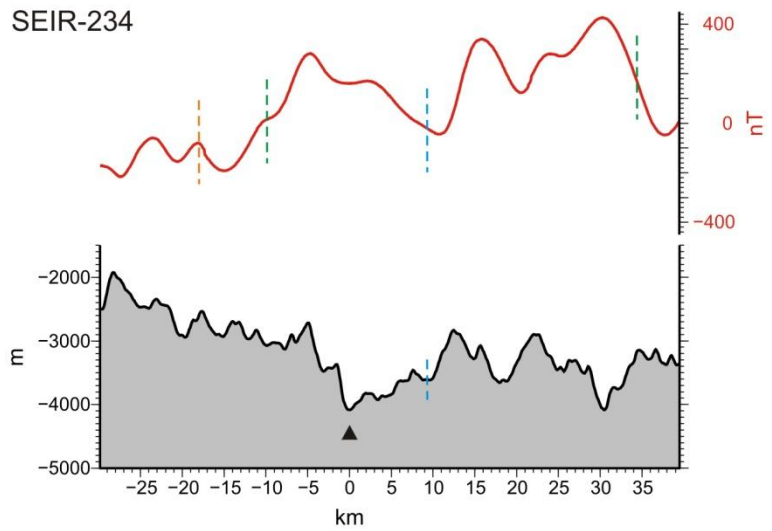


Figure A31: Magnetic (top) and bathymetric (bottom) profile SEIR232 across the SEIR from northwest to southeast (working area Section3). The boundaries of Anomaly 1 are labeled with green lines and the boundaries of the Jaramillo event with orange lines. The ridge axis, defined as the bathymetric minimum, is shown with a black triangle. The blue lines represent the center of magnetic Anomaly 1.

SEIR-233



SEIR-234



SEIR-235

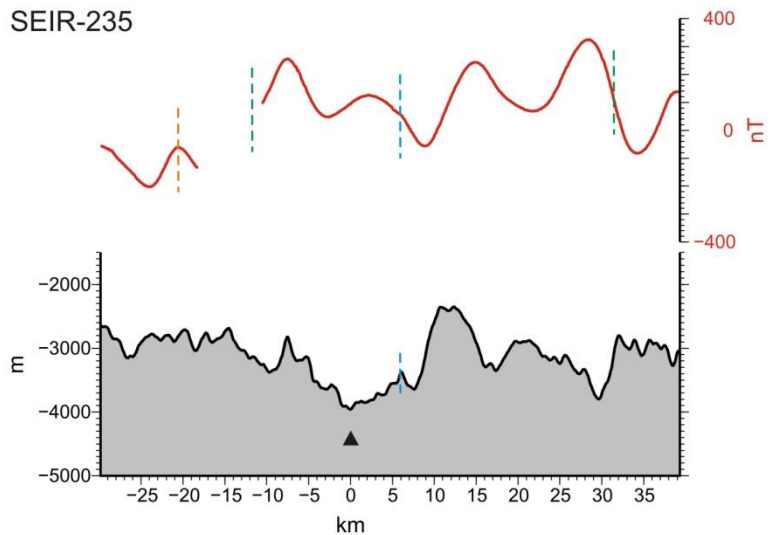
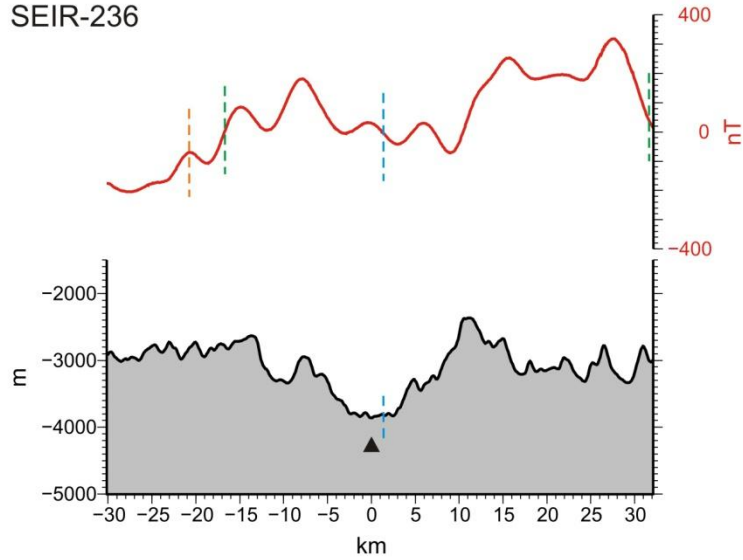


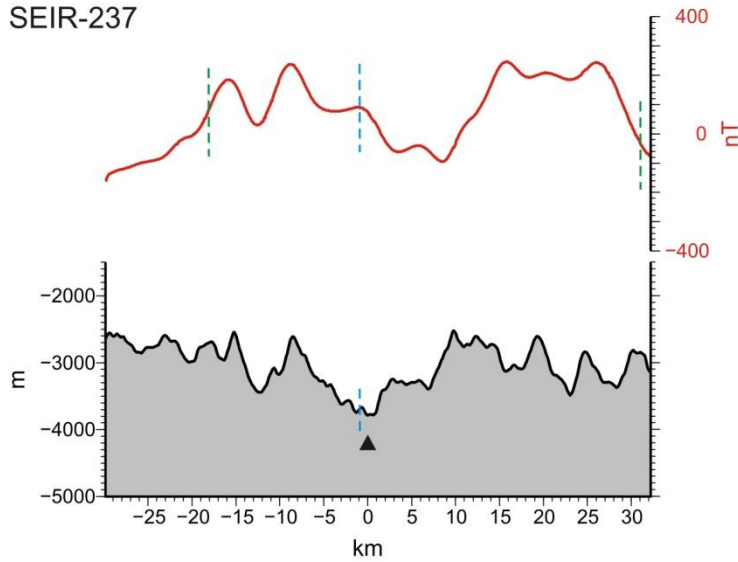
Figure A32: Magnetic (top) and bathymetric (bottom) profiles SEIR233-SEIR235 across the SEIR from northwest to southeast (working area Section4). The boundaries of Anomaly 1 are labeled with green lines and the boundaries of the Jaramillo event with orange lines. The ridge axis, defined as the bathymetric minimum, is shown with a black triangle. The blue lines represent the center of magnetic Anomaly 1.

- 233-235 Profiles
- Jaramillo event
 - Anomaly 1 (0-0.78 Ma)
 - Center of magnetic Anomaly 1
 - Bathymetric profiles
 - Magnetic profiles
 - ▲ Recent active spreading center

SEIR-236



SEIR-237



SEIR-238

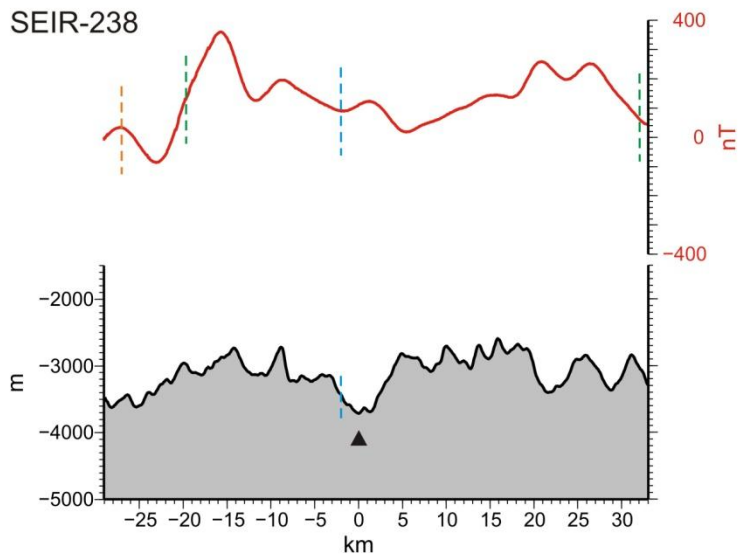


Figure A33: Magnetic (top) and bathymetric (bottom) profiles SEIR236-SEIR238 across the SEIR from northwest to southeast (working area Section4). The boundaries of Anomaly 1 are labeled with green lines and the boundaries of the Jaramillo event with orange lines. The ridge axis, defined as the bathymetric minimum, is shown with a black triangle. The blue lines represent the center of magnetic Anomaly 1.

- 236-238 Profiles
- Jaramillo event
 - Anomaly 1 (0-0.78 Ma)
 - Center of magnetic Anomaly 1
 - Bathymetric profiles
 - Magnetic profiles
 - ▲ Recent active spreading center

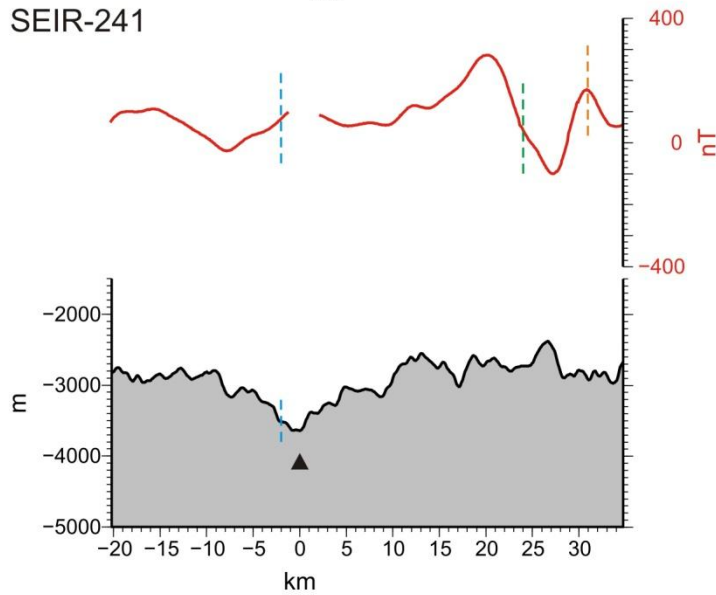
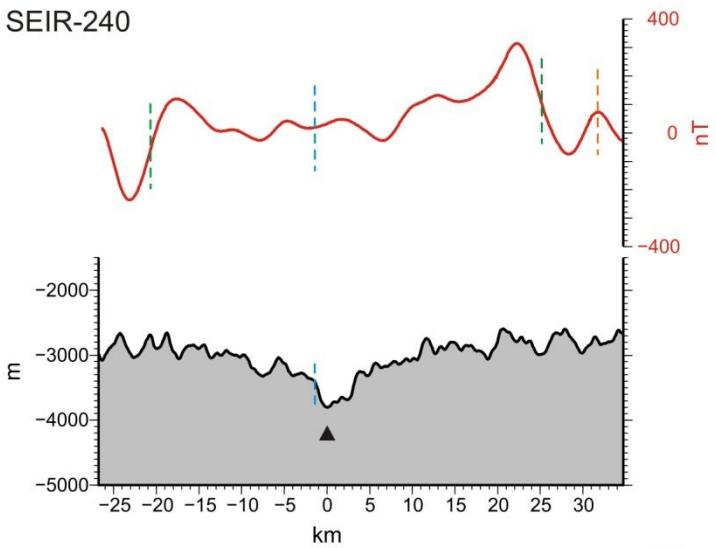
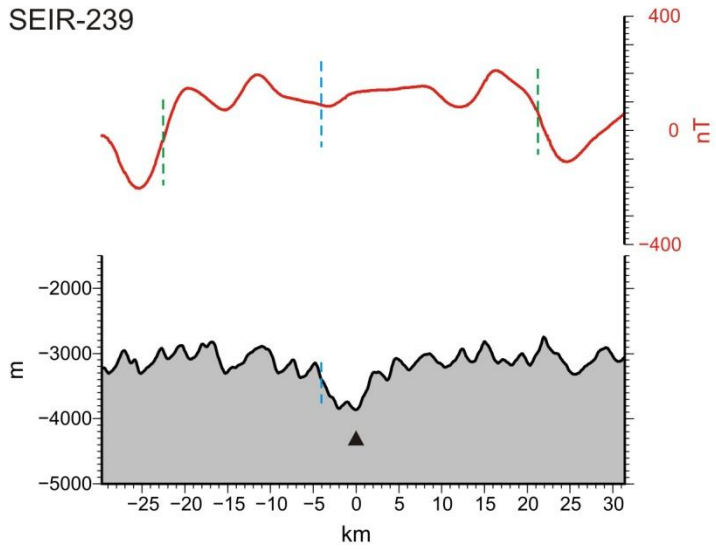


Figure A34: Magnetic (top) and bathymetric (bottom) profiles SEIR239-SEIR241 across the SEIR from northwest to southeast (working area Section4). The boundaries of Anomaly 1 are labeled with green lines and the boundaries of the Jaramillo event with orange lines. The ridge axis, defined as the bathymetric minimum, is shown with a black triangle. The blue lines represent the center of magnetic Anomaly 1.

- 239-241 Profiles
- Jaramillo event
 - Anomaly 1 (0-0.78 Ma)
 - Center of magnetic Anomaly 1
 - Bathymetric profiles
 - Magnetic profiles
 - ▲ Recent active spreading center

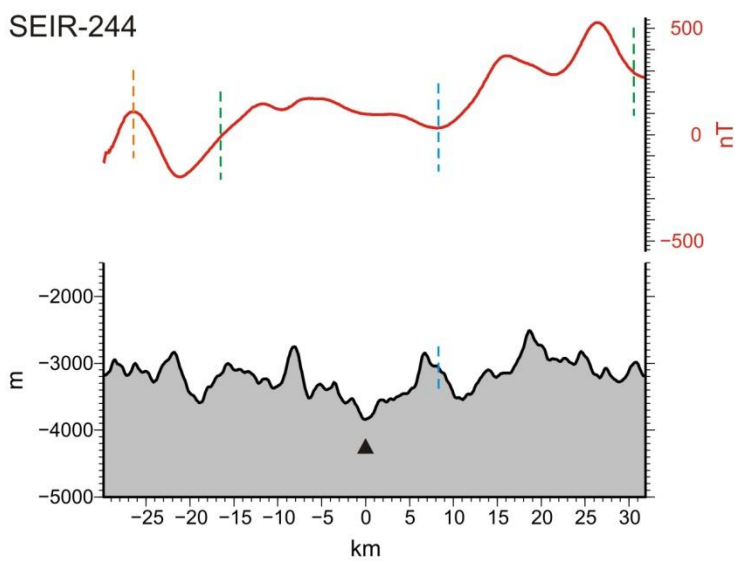
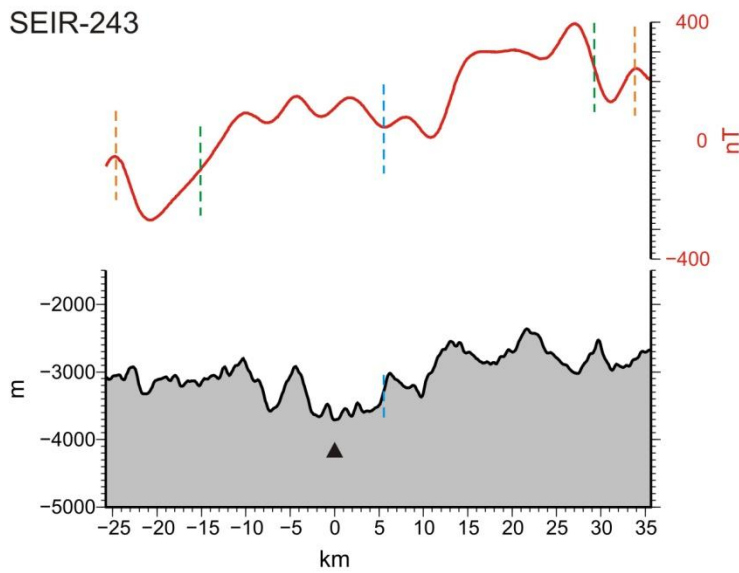
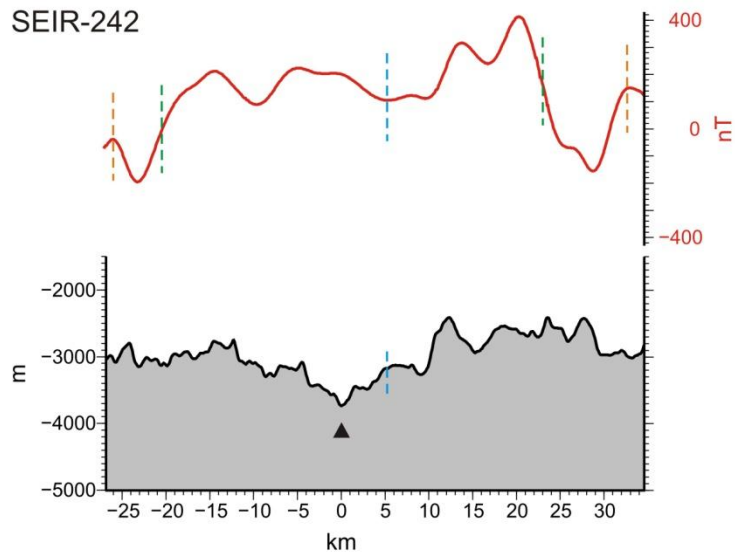


Figure A35: Magnetic (top) and bathymetric (bottom) profiles SEIR242-SEIR244 across the SEIR from northwest to southeast (working area Section4). The boundaries of Anomaly 1 are labeled with green lines and the boundaries of the Jaramillo event with orange lines. The ridge axis, defined as the bathymetric minimum, is shown with a black triangle. The blue lines represent the center of magnetic Anomaly 1.

- 242-244 Profiles
- Jaramillo event
 - Anomaly 1 (0-0.78 Ma)
 - Center of magnetic Anomaly 1
 - Bathymetric profiles
 - Magnetic profiles
 - ▲ Recent active spreading center

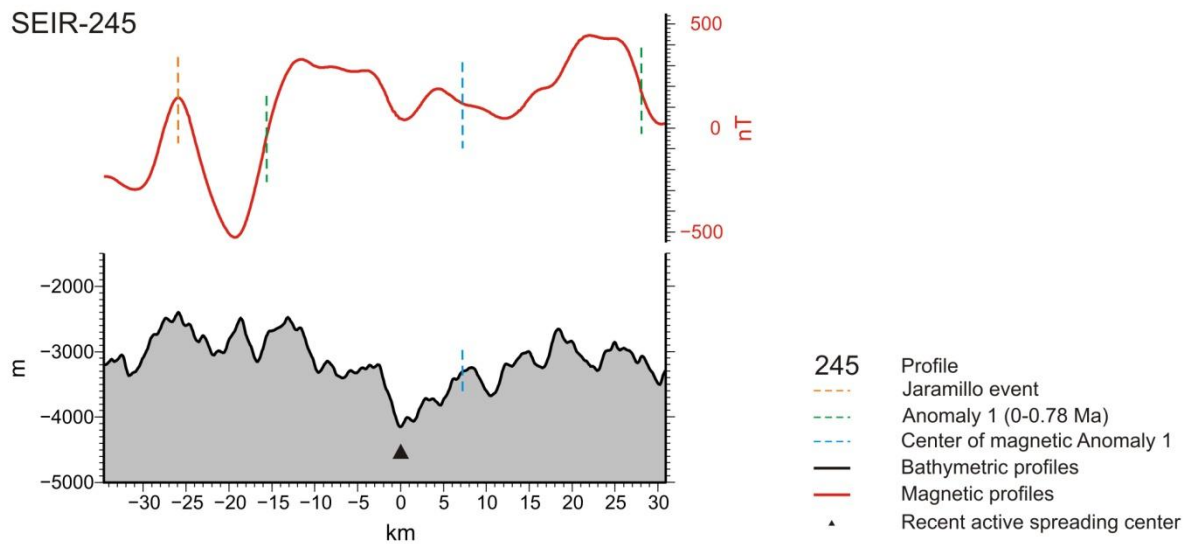
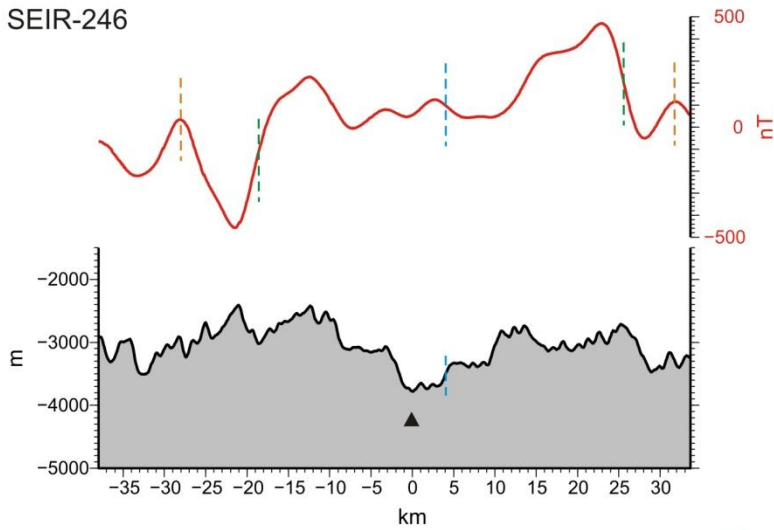
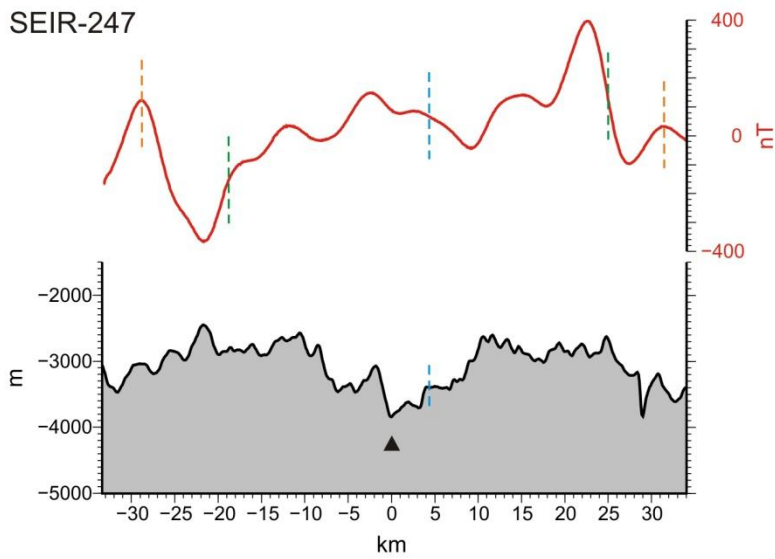


Figure A36: Magnetic (top) and bathymetric (bottom) profile SEIR245 across the SEIR from northwest to southeast (working area Section4). The boundaries of Anomaly 1 are labeled with green lines and the boundaries of the Jaramillo event with orange lines. The ridge axis, defined as the bathymetric minimum, is shown with a black triangle. The blue lines represent the center of magnetic Anomaly 1.

SEIR-246



SEIR-247



SEIR-248

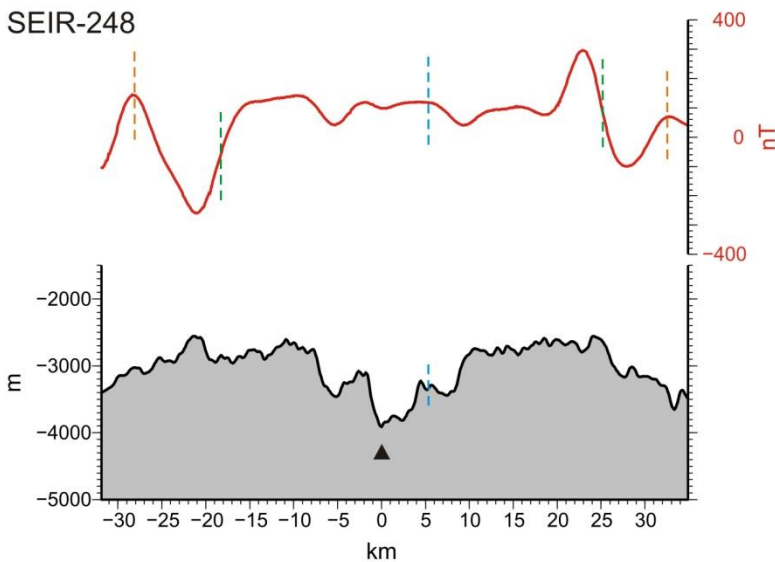


Figure A37: Magnetic (top) and bathymetric (bottom) profiles SEIR246-SEIR248 across the SEIR from northwest to southeast (working area Section4). The boundaries of Anomaly 1 are labeled with green lines and the boundaries of the Jaramillo event with orange lines. The ridge axis, defined as the bathymetric minimum, is shown with a black triangle. The blue lines represent the center of magnetic Anomaly 1.

- 246-248 Profiles
- Jaramillo event
 - Anomaly 1 (0-0.78 Ma)
 - Center of magnetic Anomaly 1
 - Bathymetric profiles
 - Magnetic profiles
 - ▲ Recent active spreading center

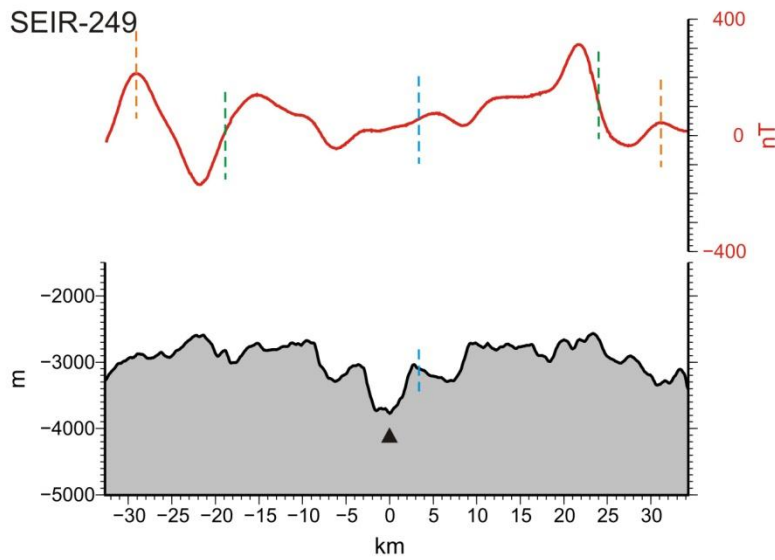
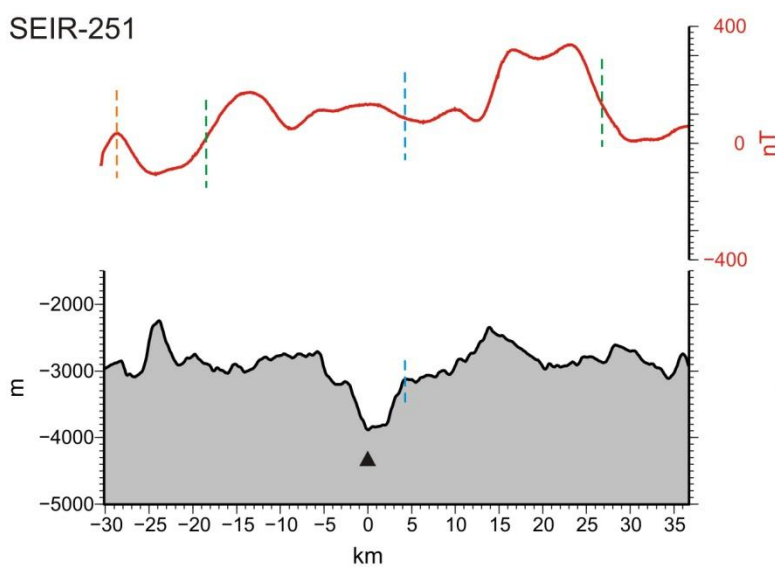
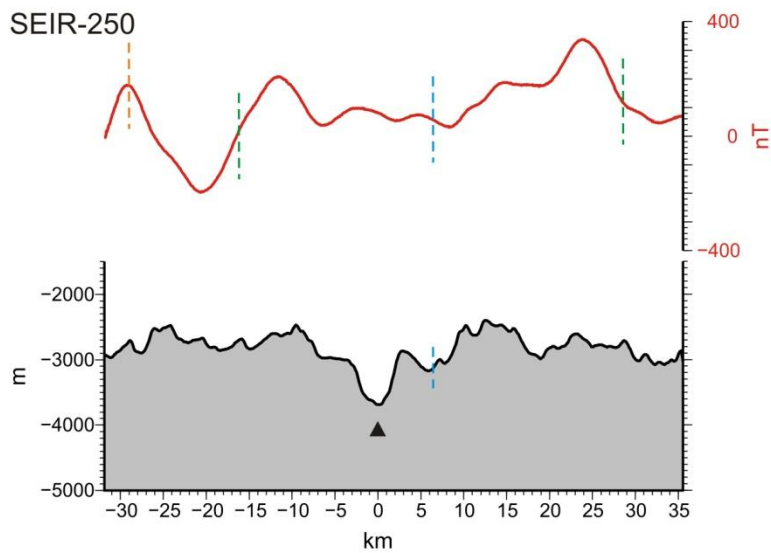


Figure A38: Magnetic (top) and bathymetric (bottom) profiles SEIR249-SEIR251 across the SEIR from northwest to southeast (working area Section4). The boundaries of Anomaly 1 are labeled with green lines and the boundaries of the Jaramillo event with orange lines. The ridge axis, defined as the bathymetric minimum, is shown with a black triangle. The blue lines represent the center of magnetic Anomaly 1.



- 249-251 Profiles
- Jaramillo event
- Anomaly 1 (0-0.78 Ma)
- Center of magnetic Anomaly 1
- Bathymetric profiles
- Magnetic profiles
- ▲ Recent active spreading center

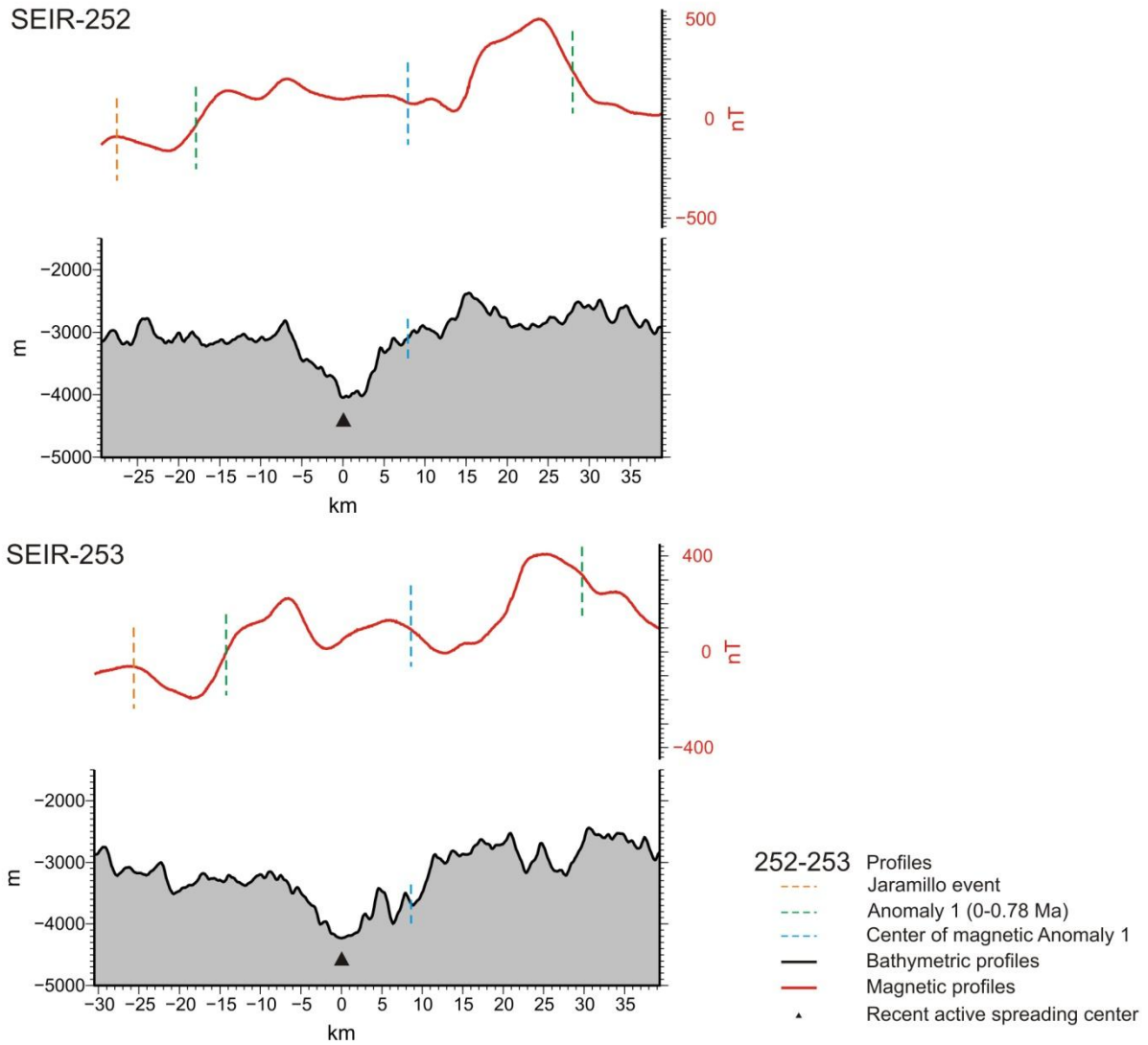


Figure A39: Magnetic (top) and bathymetric (bottom) profiles SEIR252-SEIR253 across the SEIR from northwest to southeast (working area Section4). The boundaries of Anomaly 1 are labeled with green lines and the boundaries of the Jaramillo event with orange lines. The ridge axis, defined as the bathymetric minimum, is shown with a black triangle. The blue lines represent the center of magnetic Anomaly 1.

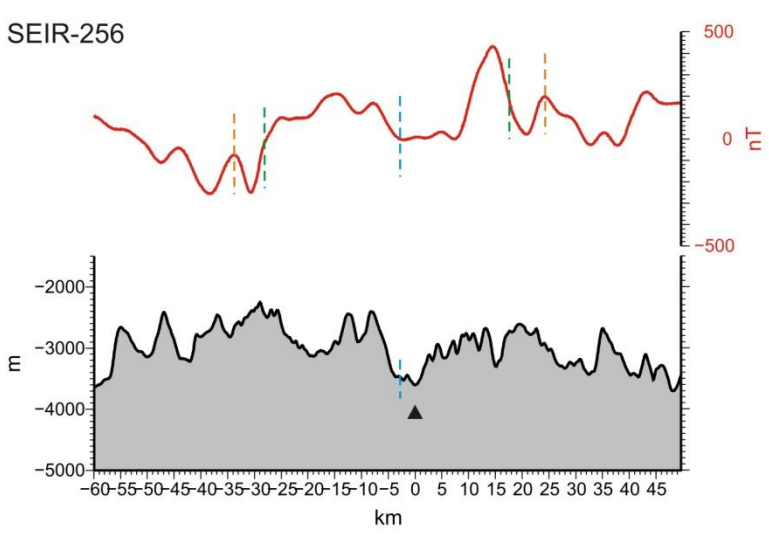
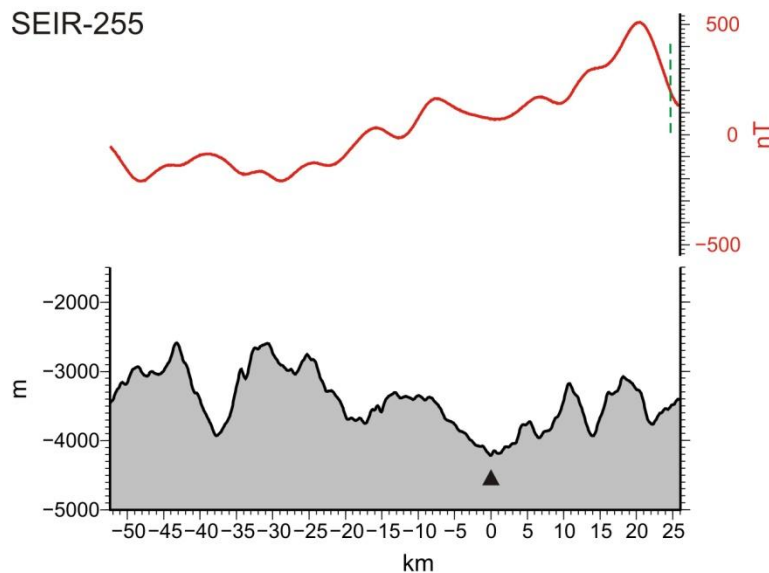
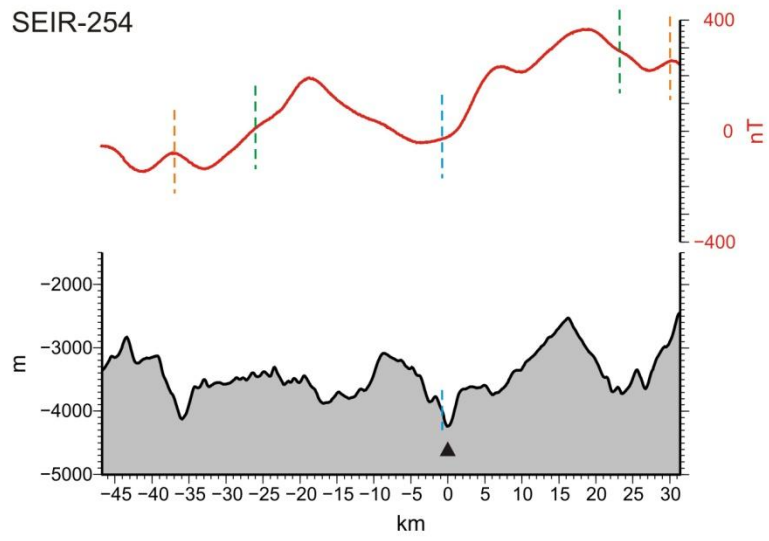


Figure A40: Magnetic (top) and bathymetric (bottom) profiles SEIR254-SEIR256 across the SEIR from northwest to southeast (working area Section5). The boundaries of Anomaly 1 are labeled with green lines and the boundaries of the Jaramillo event with orange lines. The ridge axis, defined as the bathymetric minimum, is shown with a black triangle. The blue lines represent the center of magnetic Anomaly 1.

- 254-256 Profiles
- Jaramillo event
- Anomaly 1 (0-0.78 Ma)
- Center of magnetic Anomaly 1
- Bathymetric profiles
- Magnetic profiles
- ▲ Recent active spreading center

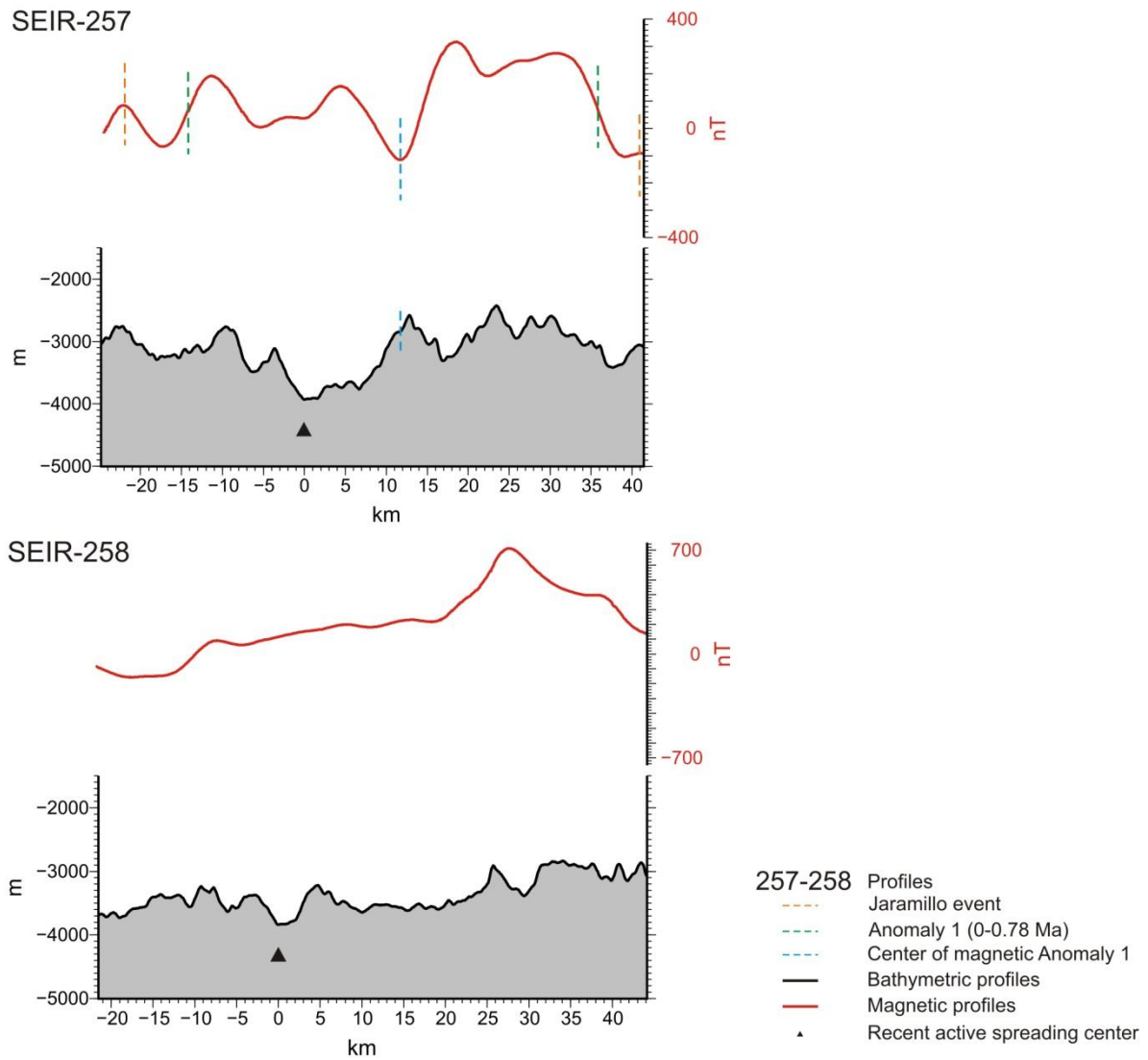
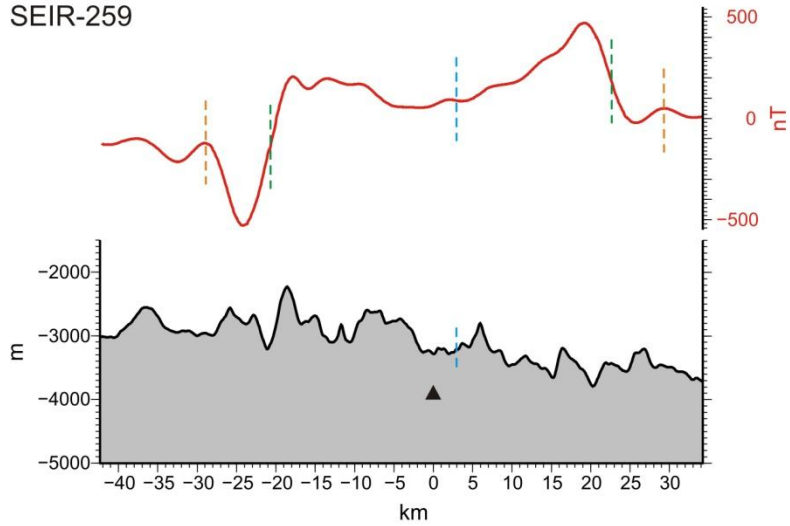
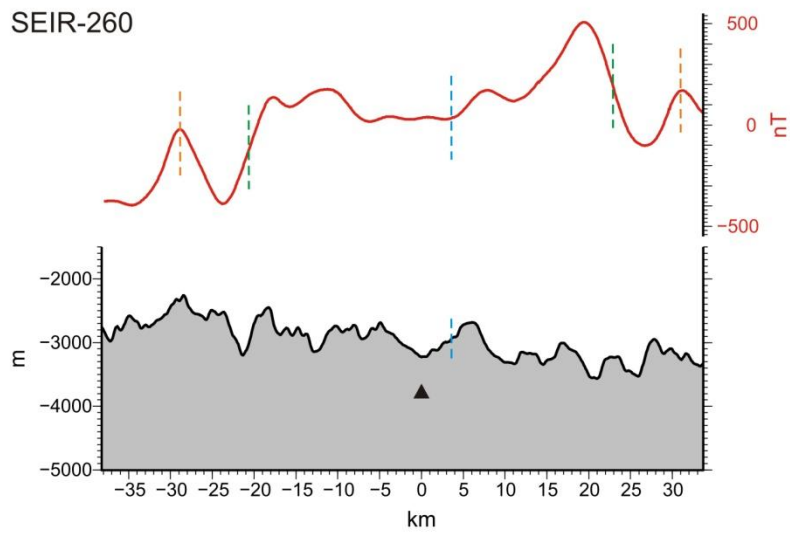


Figure A41: Magnetic (top) and bathymetric (bottom) profiles SEIR257-SEIR258 across the SEIR from northwest to southeast (working area Section5). The boundaries of Anomaly 1 are labeled with green lines and the boundaries of the Jaramillo event with orange lines. The ridge axis, defined as the bathymetric minimum, is shown with a black triangle. The blue lines represent the center of magnetic Anomaly 1.

SEIR-259



SEIR-260



SEIR-261

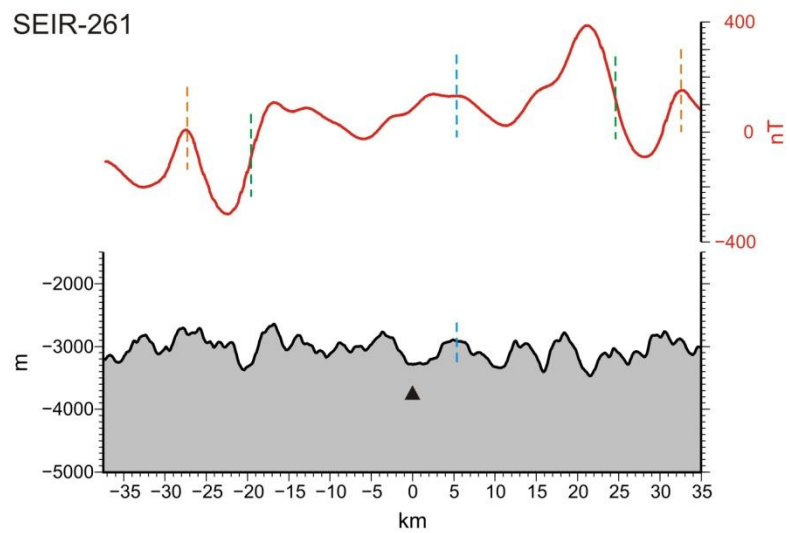


Figure A42: Magnetic (top) and bathymetric (bottom) profiles SEIR259-SEIR261 across the SEIR from northwest to southeast (working area Section6). The boundaries of Anomaly 1 are labeled with green lines and the boundaries of the Jaramillo event with orange lines. The ridge axis, defined as the bathymetric minimum, is shown with a black triangle. The blue lines represent the center of magnetic Anomaly 1.

- 259-261 Profiles
- Jaramillo event
 - Anomaly 1 (0-0.78 Ma)
 - Center of magnetic Anomaly 1
 - Bathymetric profiles
 - Magnetic profiles
 - ▲ Recent active spreading center

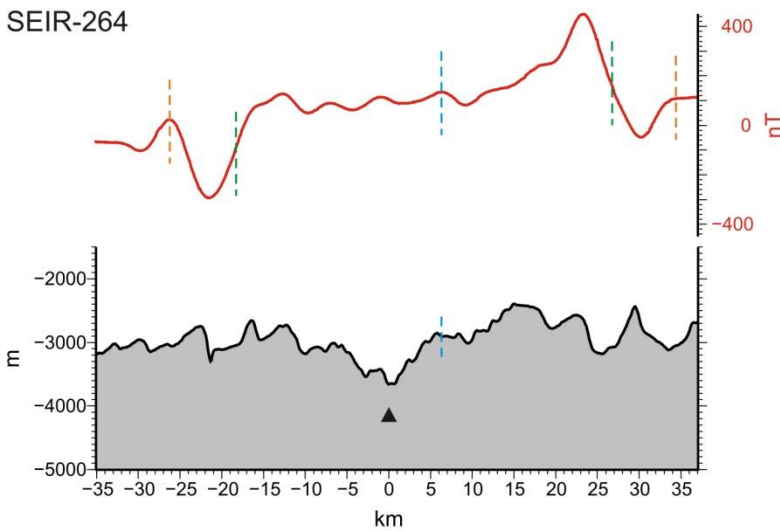
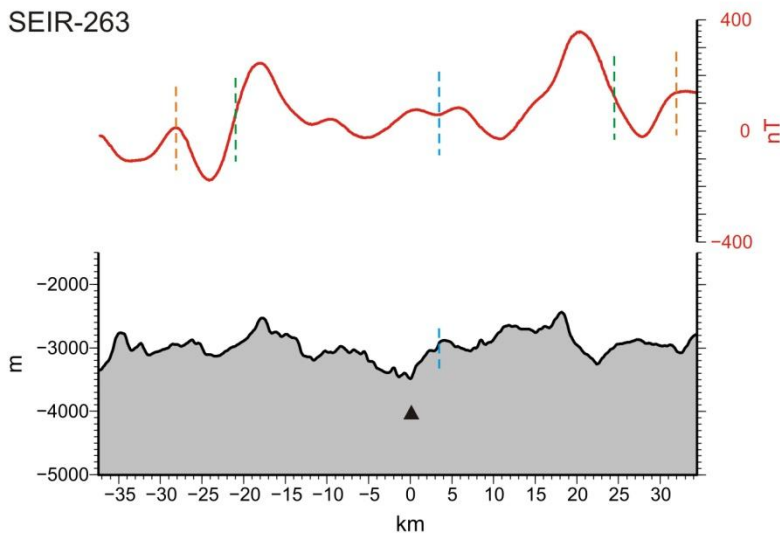
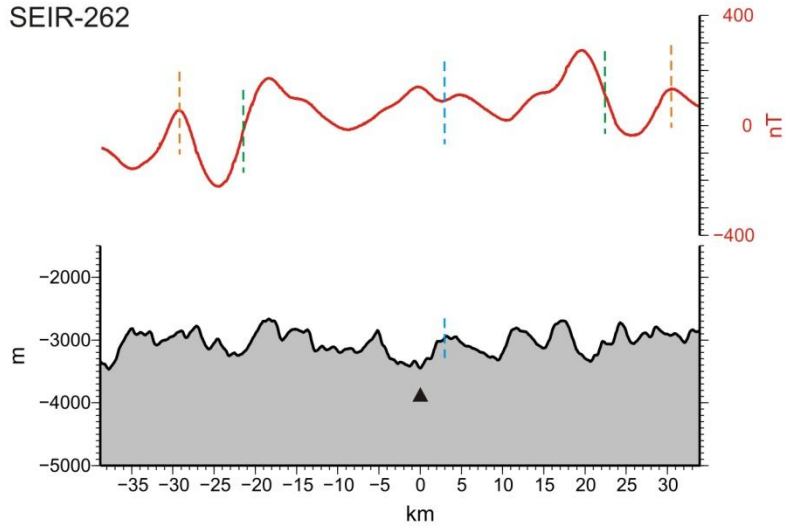


Figure A43: Magnetic (top) and bathymetric (bottom) profiles SEIR262-SEIR264 across the SEIR from northwest to southeast (working area Section6). The boundaries of Anomaly 1 are labeled with green lines and the boundaries of the Jaramillo event with orange lines. The ridge axis, defined as the bathymetric minimum, is shown with a black triangle. The blue lines represent the center of magnetic Anomaly 1.

- 262-264 Profiles
- Jaramillo event
 - Anomaly 1 (0-0.78 Ma)
 - Center of magnetic Anomaly 1
 - Bathymetric profiles
 - Magnetic profiles
 - ▲ Recent active spreading center

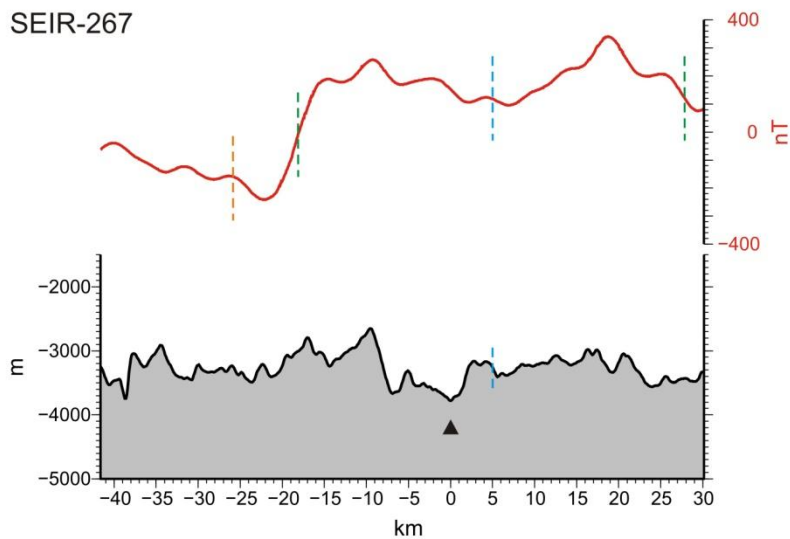
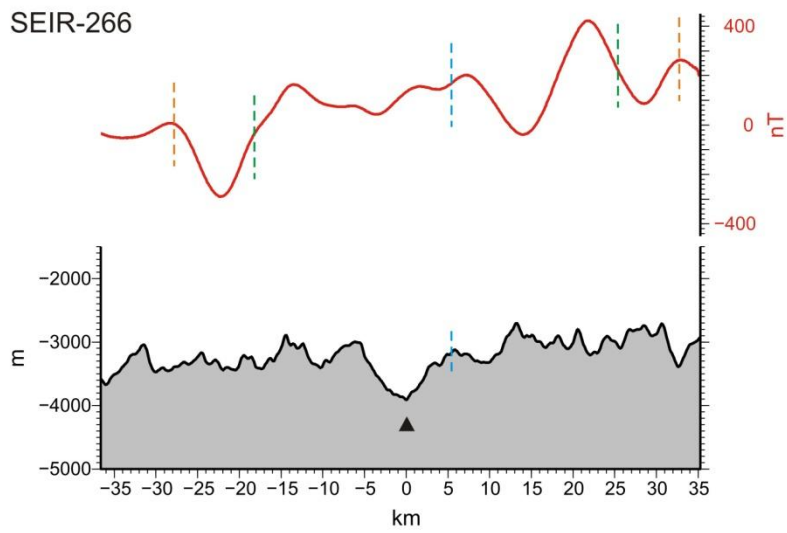
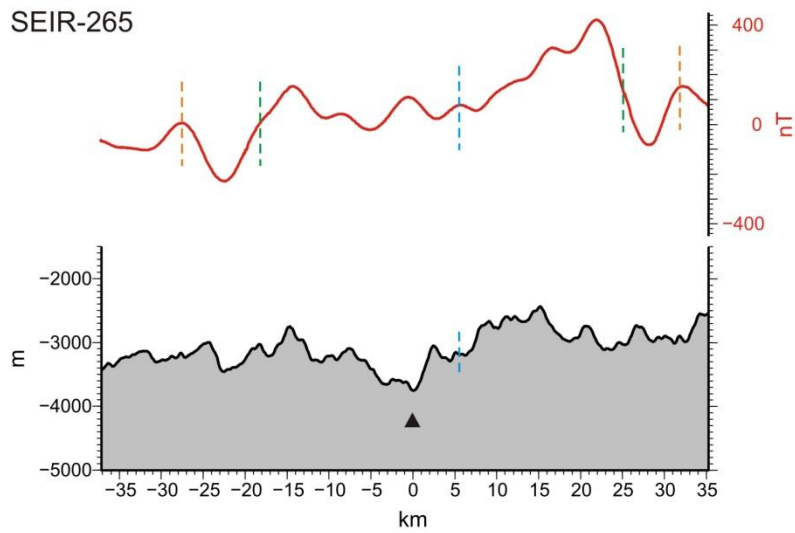


Figure A44: Magnetic (top) and bathymetric (bottom) profiles SEIR265-SEIR267 across the SEIR from northwest to southeast (working area Section6). The boundaries of Anomaly 1 are labeled with green lines and the boundaries of the Jaramillo event with orange lines. The ridge axis, defined as the bathymetric minimum, is shown with a black triangle. The blue lines represent the center of magnetic Anomaly 1.

- 265-267 Profiles
- Jaramillo event
 - Anomaly 1 (0-0.78 Ma)
 - Center of magnetic Anomaly 1
 - Bathymetric profiles
 - Magnetic profiles
 - ▲ Recent active spreading center

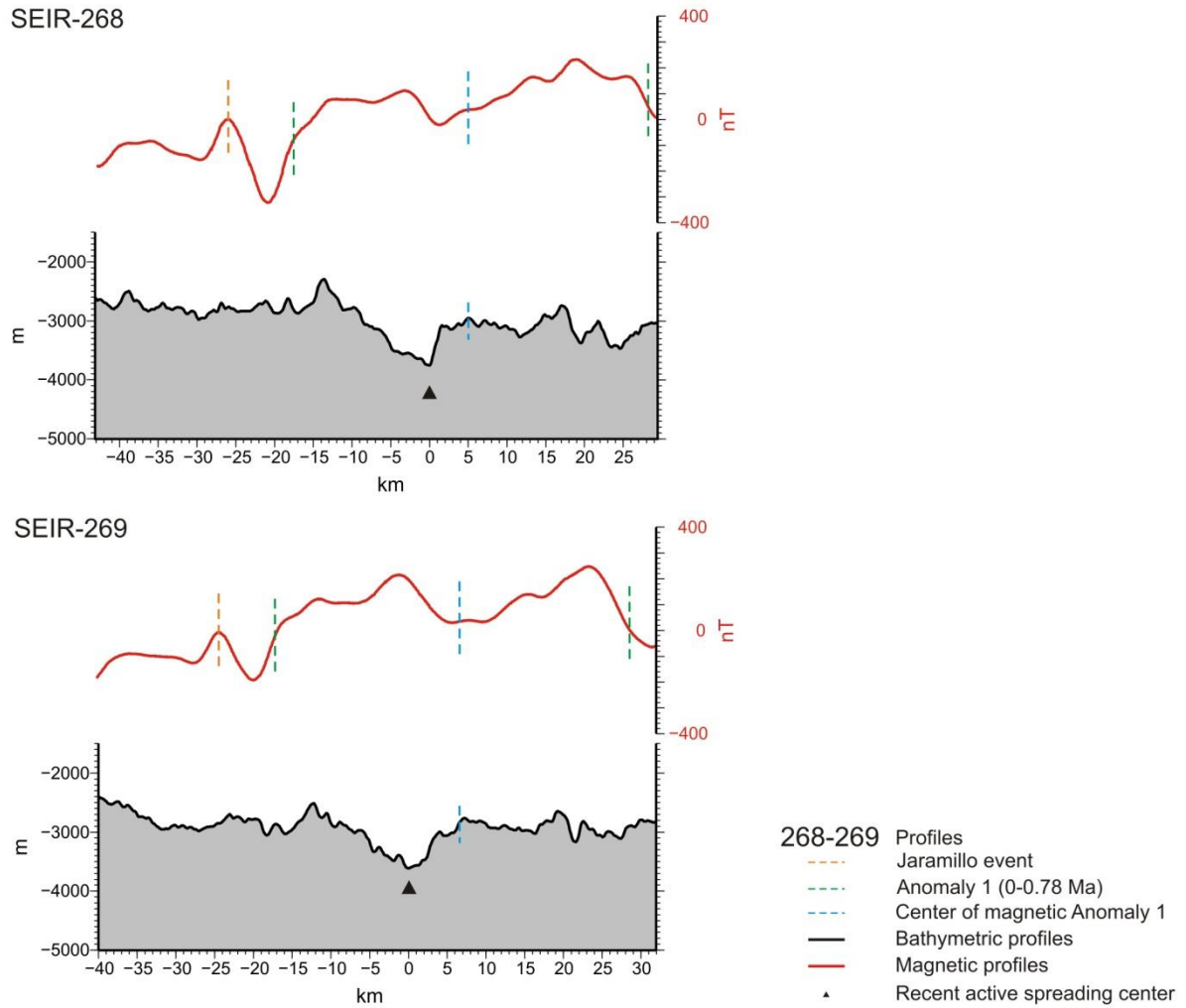


Figure A45: Magnetic (top) and bathymetric (bottom) profiles SEIR268-SEIR269 across the SEIR from northwest to southeast (working area Section6). The boundaries of Anomaly 1 are labeled with green lines and the boundaries of the Jaramillo event with orange lines. The ridge axis, defined as the bathymetric minimum, is shown with a black triangle. The blue lines represent the center of magnetic Anomaly 1.

Profile number	Position of bathymetric low from the center of magnetic Anomaly 1	Distance between each other [km]	Spreading rates [cm/a]	Distance Anomaly 1 from each other [km]
303	W	0.5	4.49	35
304	W	1.5	4.42	34.5
305	W	+/-0	4.49	35
309	W	1.5	2.18 (4.36)	17
310	W	1	4.61	36
311	W	2	4.7	37
312	W	1	4.61	36
313	W	3	5.0	39
314	W	4.5	4.87	38
315	W	4	4.87	38
316	W	+/-0	4.61	36
317	W	0.5	4.87	38
318	W	3	4.7	37
319	W	2.5	4.61	36
320	W	2	4.87	38
321	W	3	4.87	38
322	W	6	4.7	37

328	W	4	2.43 (4.87)	19
330	W	1	2.37 (4.74)	18.5
331	W	2	5.12	40
332	W	2	5.0	39
333	W	2	5.13	40
334	W	3	4.87	38
335	W	2.5	4.81	37.5
336	W	4	5.0	39
338	W	2	5.51	43
339	W	3	4.94	38.5
340	W	1	4.94	38.5
341	W	5.5	5.13	40
342	W	4	5.0	39
343	W	7	5.0	39

344	W	4	5.0	39
345	W	4.5	5.0	39
346	W	4.5	5.0	39
347	W	6	2.56 (5.13)	20
348	W	2	2.37 (4.74)	18.5
349	W	3.5	2.44 (4.87)	19
350	W	3	2.37 (4.74)	18.5
351	W	6	2.44 (4.87)	19
352	W	13	2.44 (4.87)	19
353	W	12	2.37 (4.74)	18.5

Profile number	Position of bathymetric low from the center of magnetic Anomaly 1	Distance between each other [km]	Spreading rates [cm/a]	Distance Anomaly 1 from each other [km]
354	W	10	4.10	32
355	W	9	3.72	29
356	W	2	4.10	32

371	E	3.5	4.36	34
370	E	6	4.62	36
369	E	9	4.49	35
368	E	7.5	4.7	37
367	E	13	4.62	36
366	E	13	4.7	37
365	E	5.5	4.62	36
364	E	6	4.62	36
363	E	7.5	4.49	35
359	W	5	4.23	33
360	W	5	4.36	34
361	W	2	4.23	33
362	E	1	4.36	34

204	E	1	5.58	43.5
205	E – same	+/-0	4.81	37.5
206	E	1	4.74	37
207	same - W	+/-0	5.0	39
208	W	1	2.18 (4.36)	17
209	E	2.8	5.51	43
210	W	1	5.51	43
213	E – same	+/-0	5.39	42
214	W	3	5.39	42
215	W	2	5.51	43
216	W	2	5.51	43
217	W	2	5.64	44
218	W	1.5	5.77	45
219	W	13 (mag. 0 OCC)	6.03	47
226	E	4	5.64	44
227	E	6	5.64	44
228	E	4	5.51	43
229	E	4.5	5.64	44
230	E	+/-0	5.51	43
231	W	1	5.77	45
232	E	3	5.39	42

233	W - same	+/-0	5.77	45
234	W	9	5.64	44
235	W	6	5.51	43
236	W	1	6.15	48

Profile number	Position of bathymetric low from the center of magnetic Anomaly 1	Distance between each other [km]	Spreading rates [cm/a]	Distance Anomaly 1 from each other [km]
237	E	1	6.28	49
238	E	2	6.54	51
239	E	4	5.51	43
240	E	2	5.90	46
241	E	2		
242	W	5	5.64	44
243	W	5.5	5.64	44
244	W	8	6.03	47
245	W	7	5.51	43
246	W	4	5.64	44
247	W	4	5.64	44
248	W	5	5.51	43
249	W	3	5.51	43
250	W	6	5.77	45
251	W	4	5.77	45
252	W	7.5	5.90	46
253	W	8.5	5.64	44
254	E	1	6.28	49
255				
256	E	3	5.77	45
257	W	11.5	6.28	49
258				
259	W	3	5.51	43
260	W	3.5	5.51	43
261	W	5	5.64	44
262	W	3	5.64	44
263	W	3.5	5.77	45
264	W	6	5.77	45
265	W	5	5.51	43
266	W	5	5.64	44
267	W	5	5.90	46
268	W	5	5.77	45
269	W	6.5	5.77	45

Table A1: Each profile of the Central- and Southeast Indian Ridge with individual magnetic results such as spreading rates and anomaly distances.

Appendix B

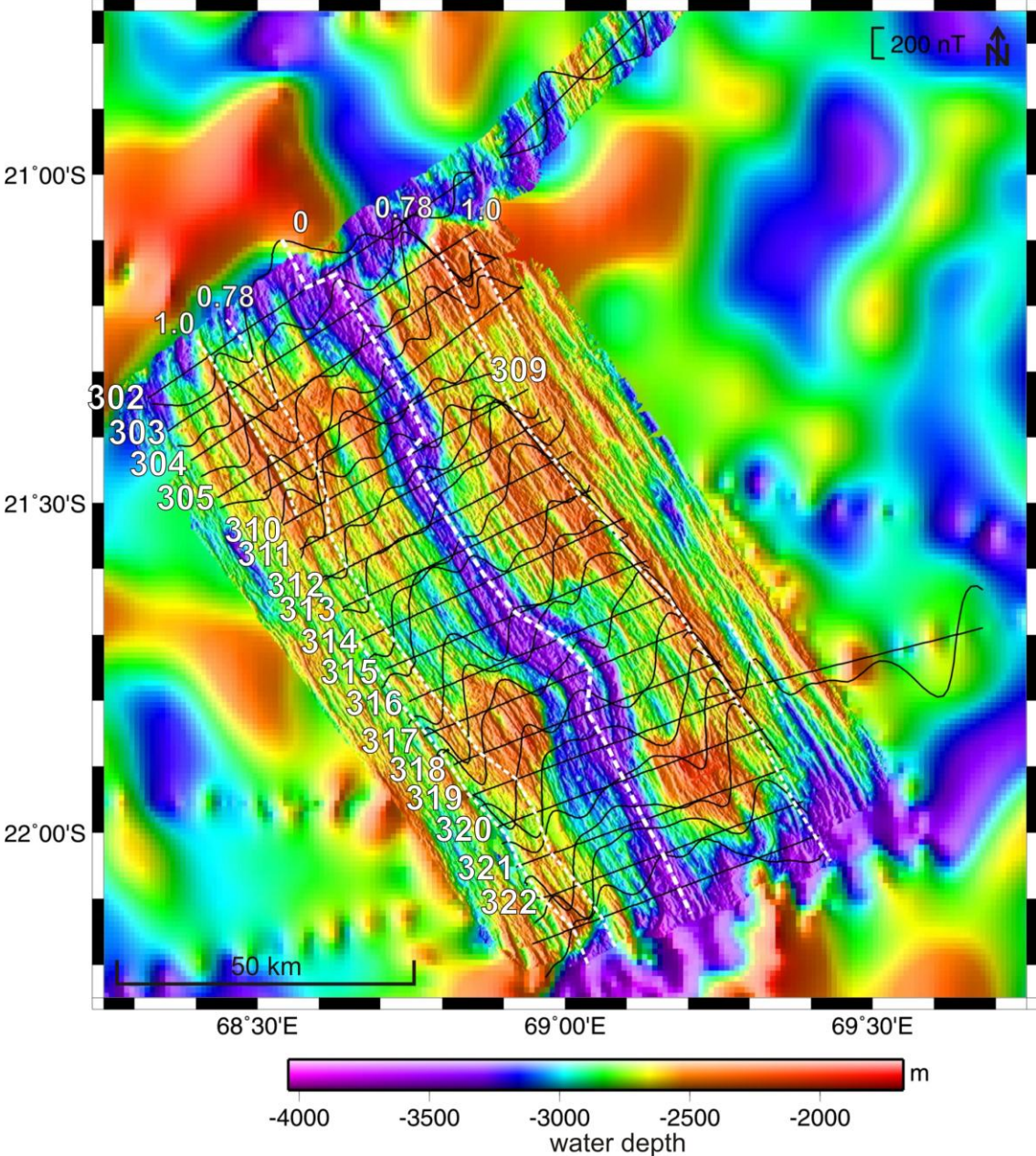


Figure B1: Bathymetric map of the working area EXFX (Central Indian Ridge) with superimposed magnetic profiles. The white numbers on the left side label the profiles and the white dotted lines represent the center of magnetic Anomaly 1 (0), the boundaries of Anomaly 1 (0.78) and the boundaries of the Jaramillo event (1.0).

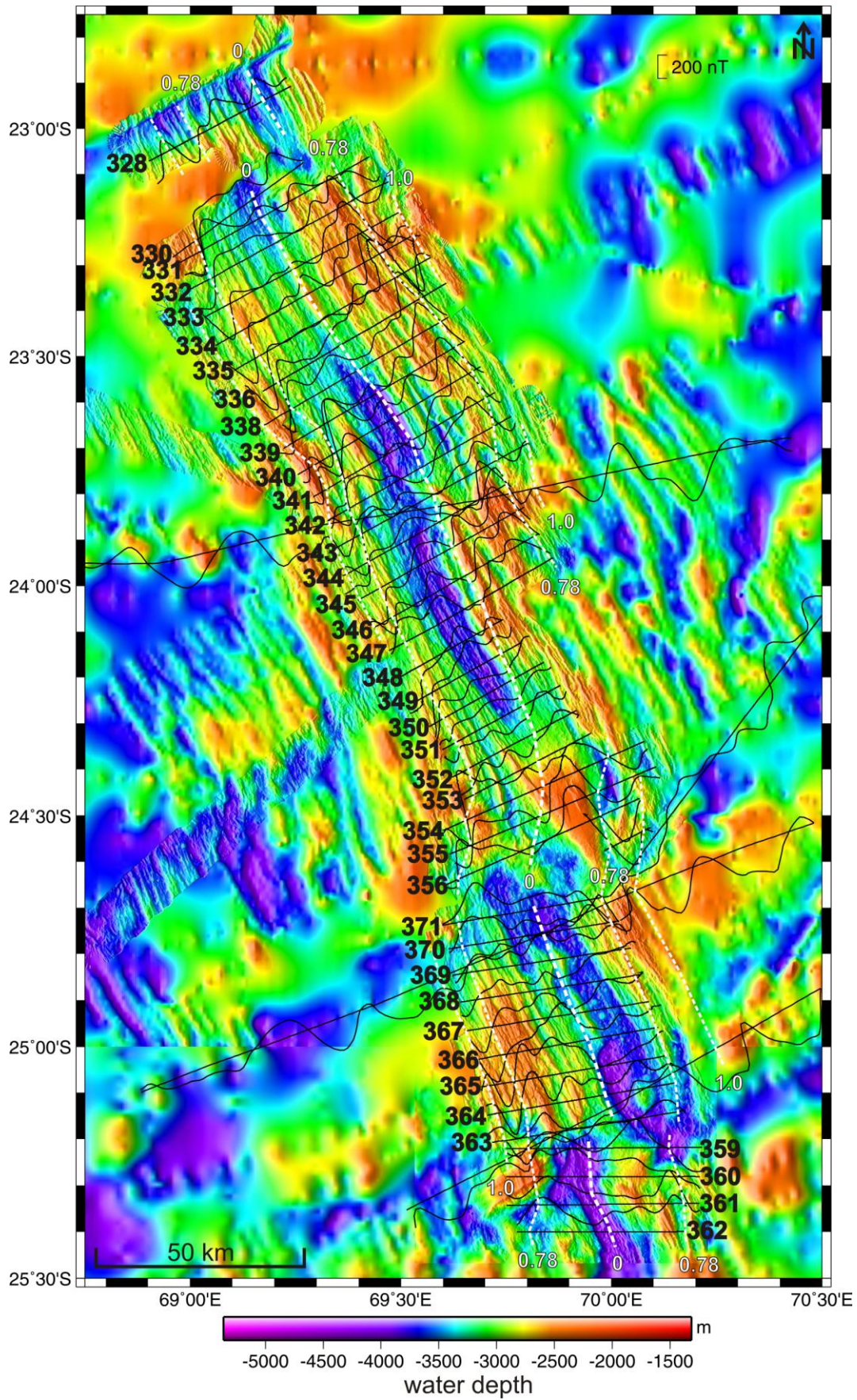


Figure B2: Bathymetric map of the working areas JX, Meso, Edmond, and Kairei (Central Indian Ridge) with superimposed magnetic profiles. The black numbers on the left side label the profiles and the white dotted lines represent the center of magnetic Anomaly 1 (0), the boundaries of Anomaly 1 (0.78) and the boundaries of the Jaramillo event (1.0).

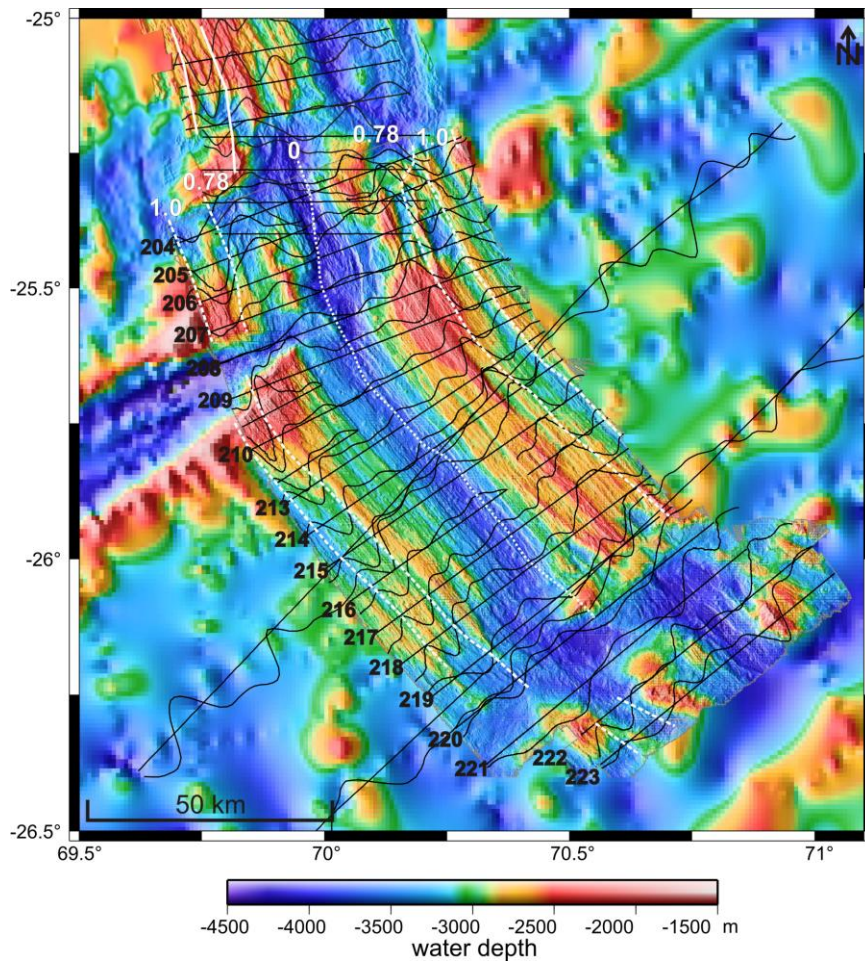


Figure B3: Bathymetric map of the working areas Section 1 and 2 (Southeast Indian Ridge) with superimposed magnetic profiles. The black numbers on the left side label the profiles and the white dotted lines represent the center of magnetic Anomaly 1 (0), the boundaries of Anomaly 1 (0.78) and the boundaries of the Jaramillo event (1.0).

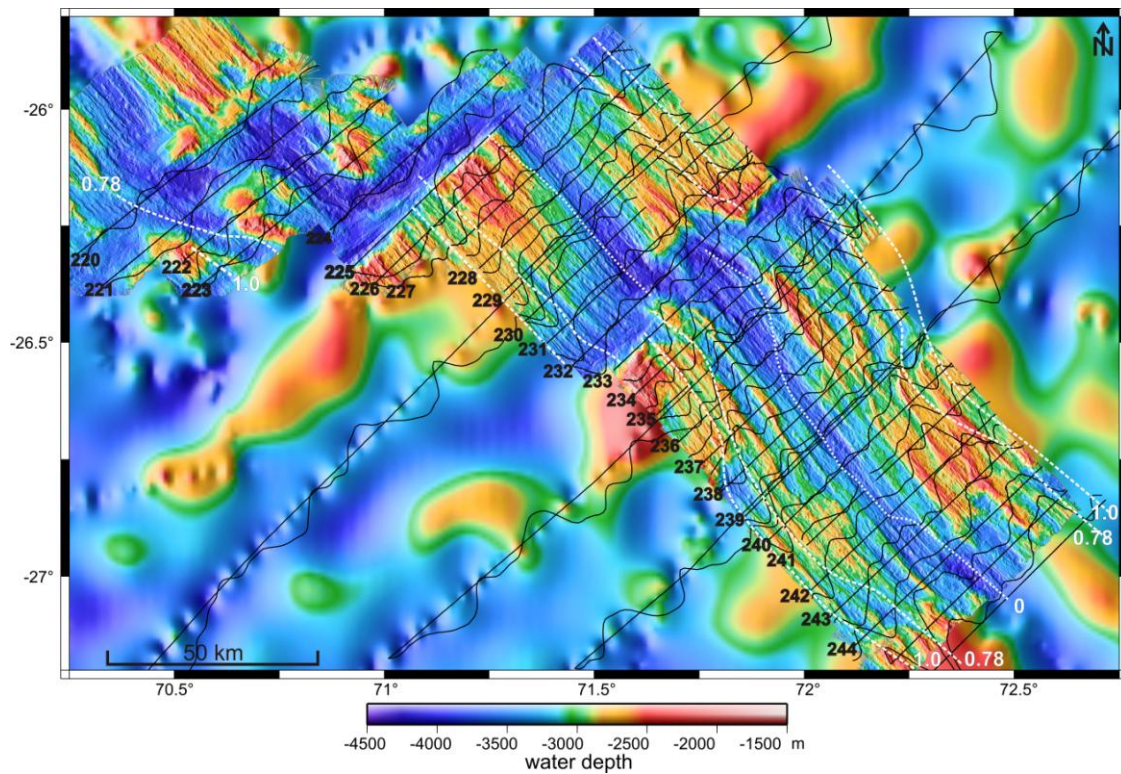


Figure B4: Bathymetric map of the working areas Section 2, 3, and 4 (Southeast Indian Ridge) with superimposed magnetic profiles. The black numbers on the left side label the profiles and the white dotted lines represent the center of magnetic Anomaly 1 (0), the boundaries of Anomaly 1 (0.78) and the boundaries of the Jaramillo event (1.0).

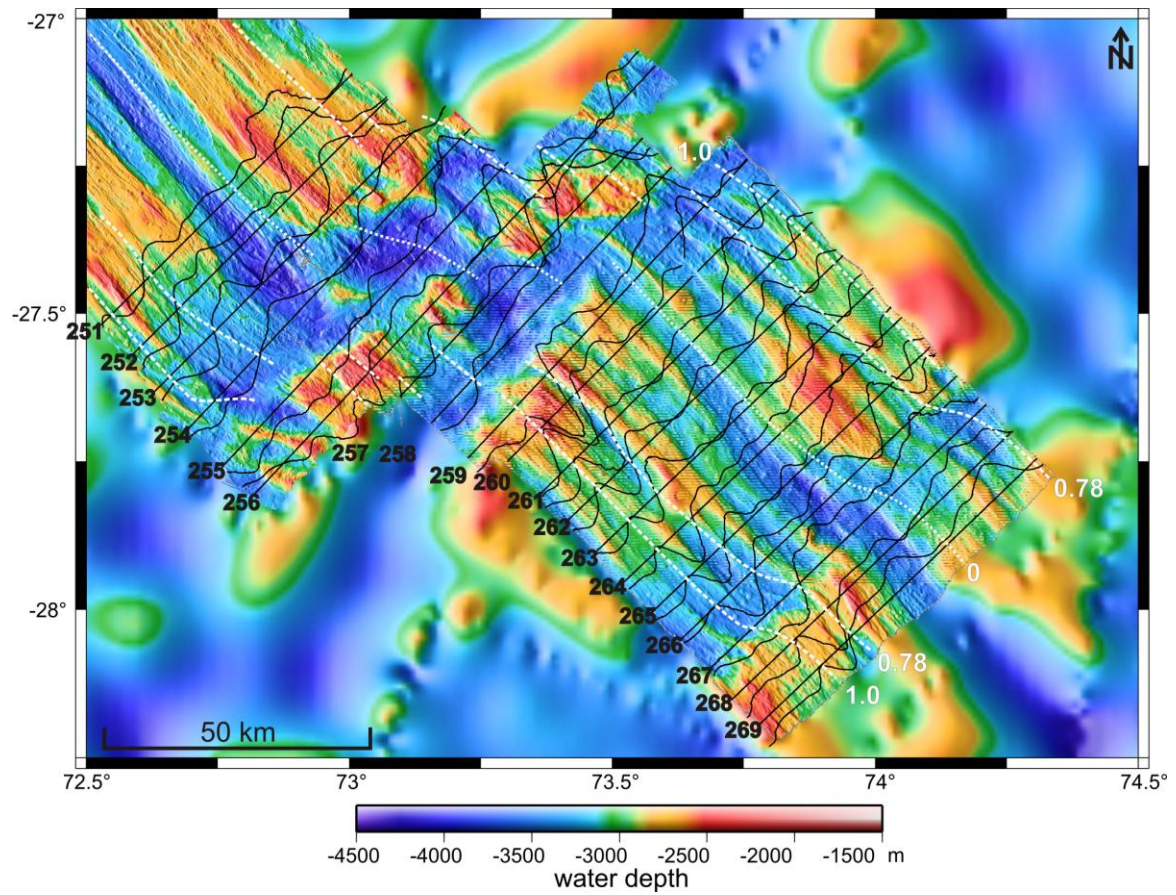


Figure B5: Bathymetric map of the working areas Section 5 and 6 (Southeast Indian Ridge) with superimposed magnetic profiles. The black numbers on the left side label the profiles and the white dotted lines represent the center of magnetic Anomaly 1 (0), the boundaries of Anomaly 1 (0.78) and the boundaries of the Jaramillo event (1.0).

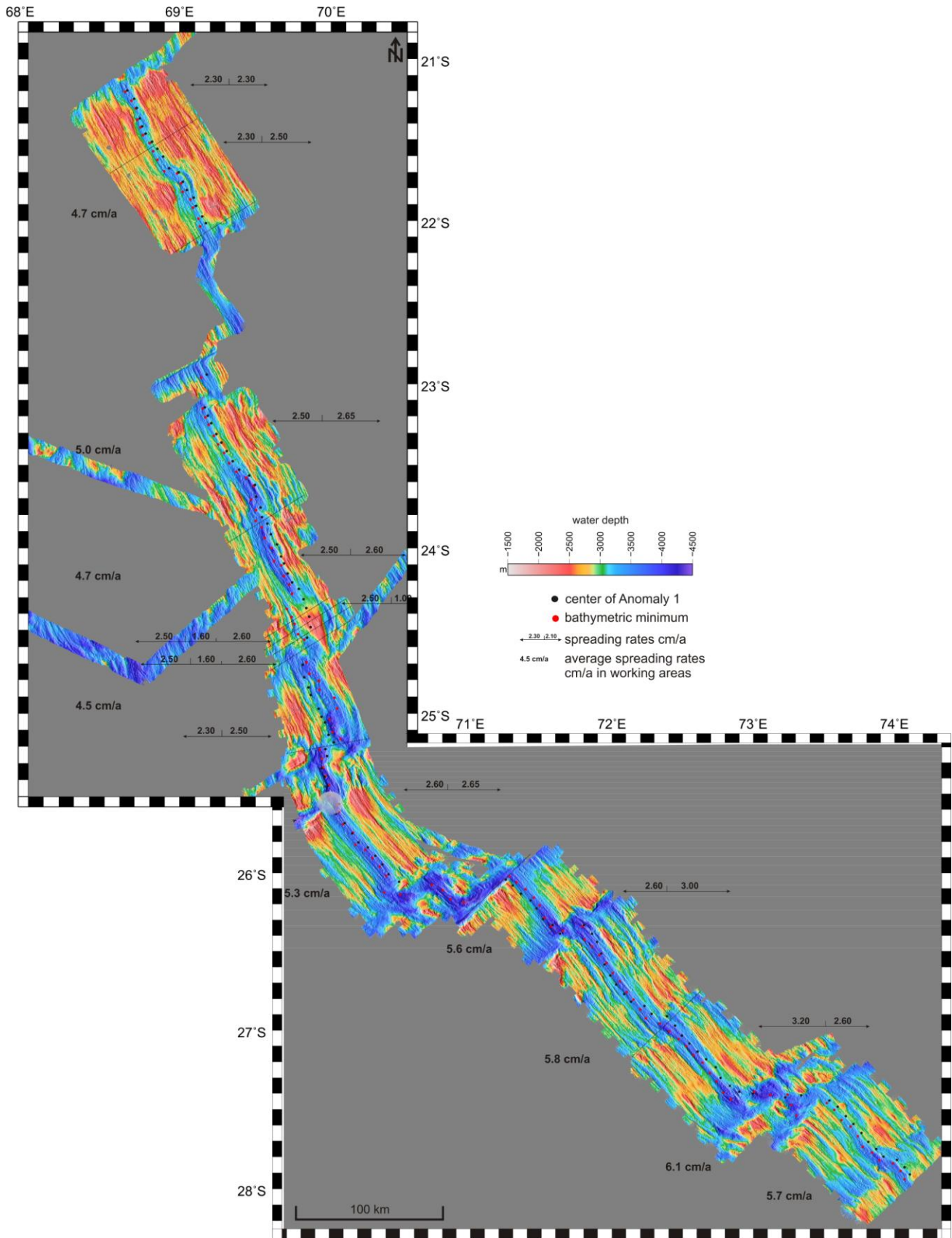


Figure B6: Bathymetric map of the Central and Southeast Indian Ridge labeled with the main magnetic results like average full spreading rates on the left side and the symmetric or asymmetric spreading behavior of the ridge flanks (arrows with numbers in cm/a). The red dots mark the spreading center defined as bathymetric minimum and the black dots label the center of magnetic Anomaly 1.

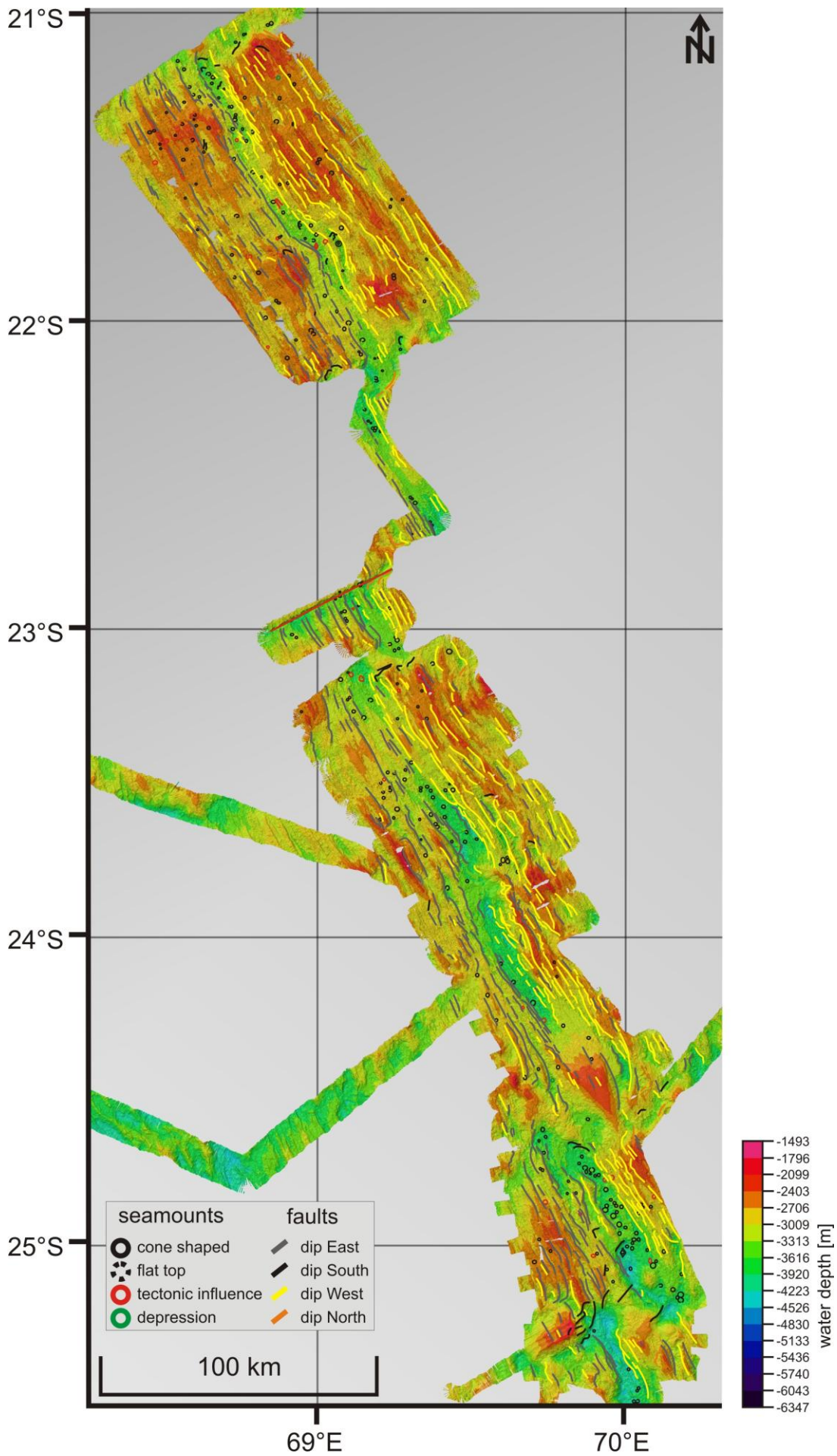


Figure B7: Bathymetric and structural map of the Central Indian Ridge. The seamounts are labeled with circles and the faults with lines.

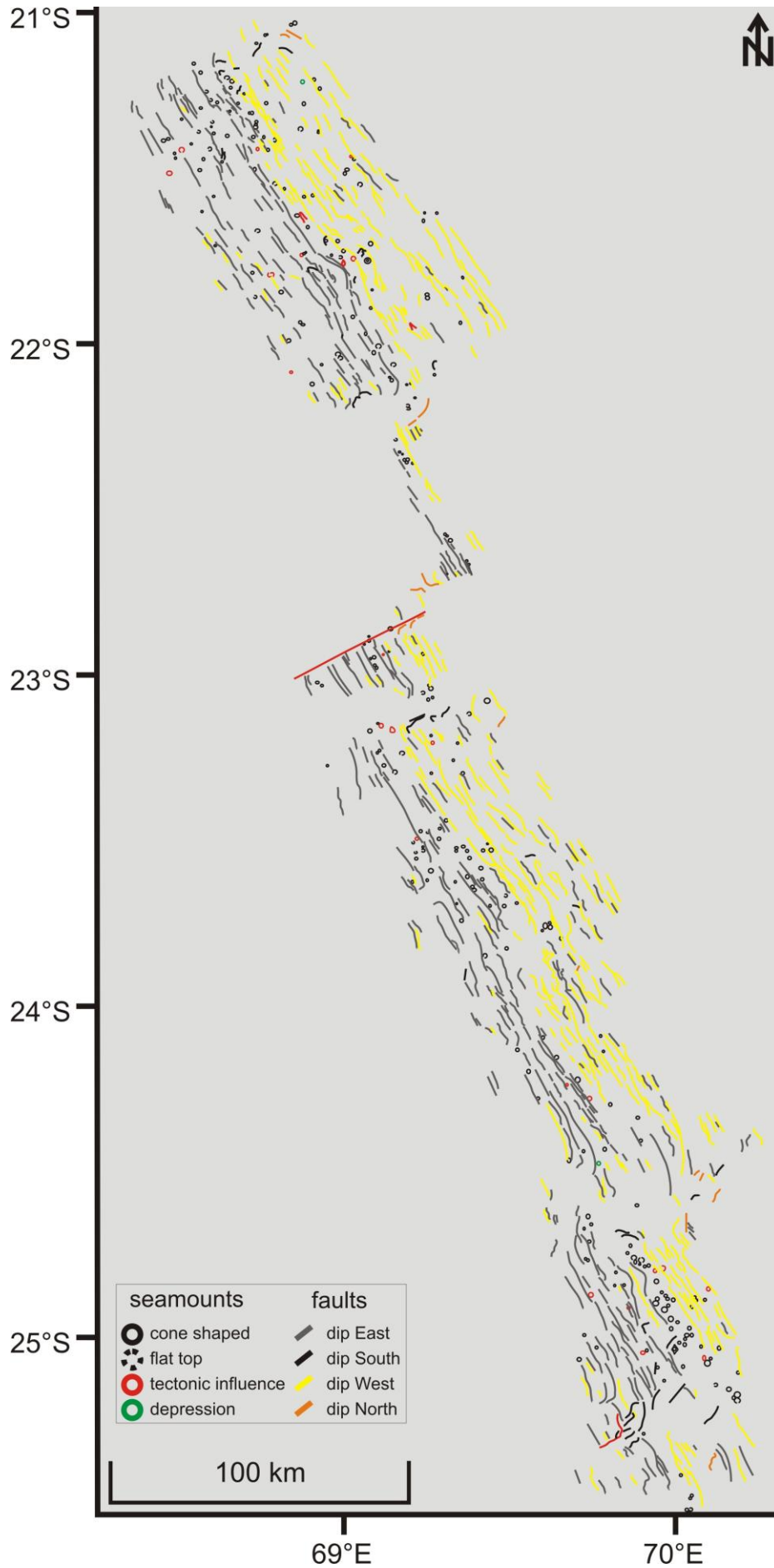


Figure B8: Structural map of the Central Indian Ridge labeled with circles for the seamounts and with lines for the faults dipping in different directions.

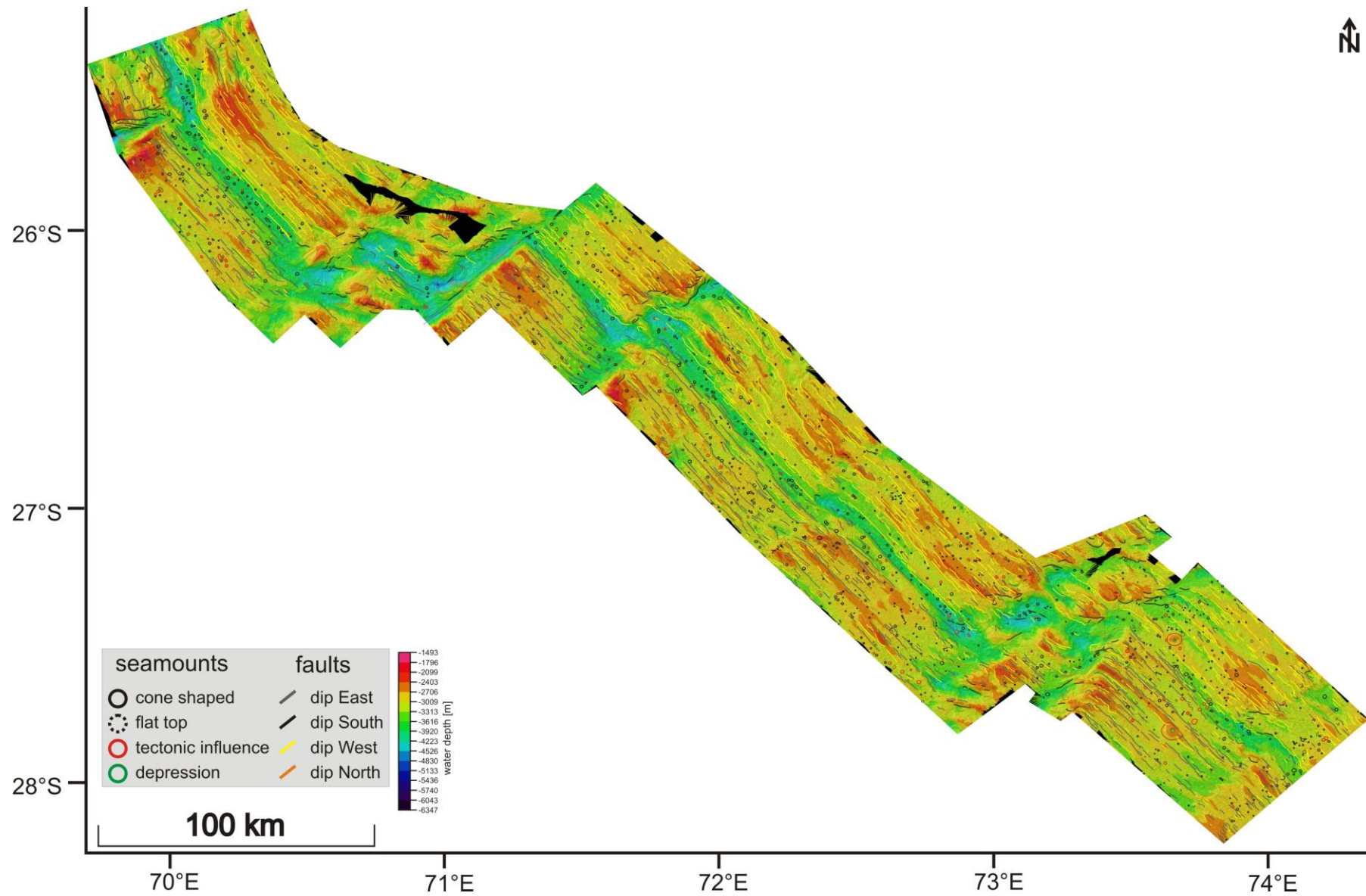


Figure B9: Bathymetric and structural map of the Southeast Indian Ridge. The seamounts are marked with different circles depending on their shape and the faults are labeled with lines.

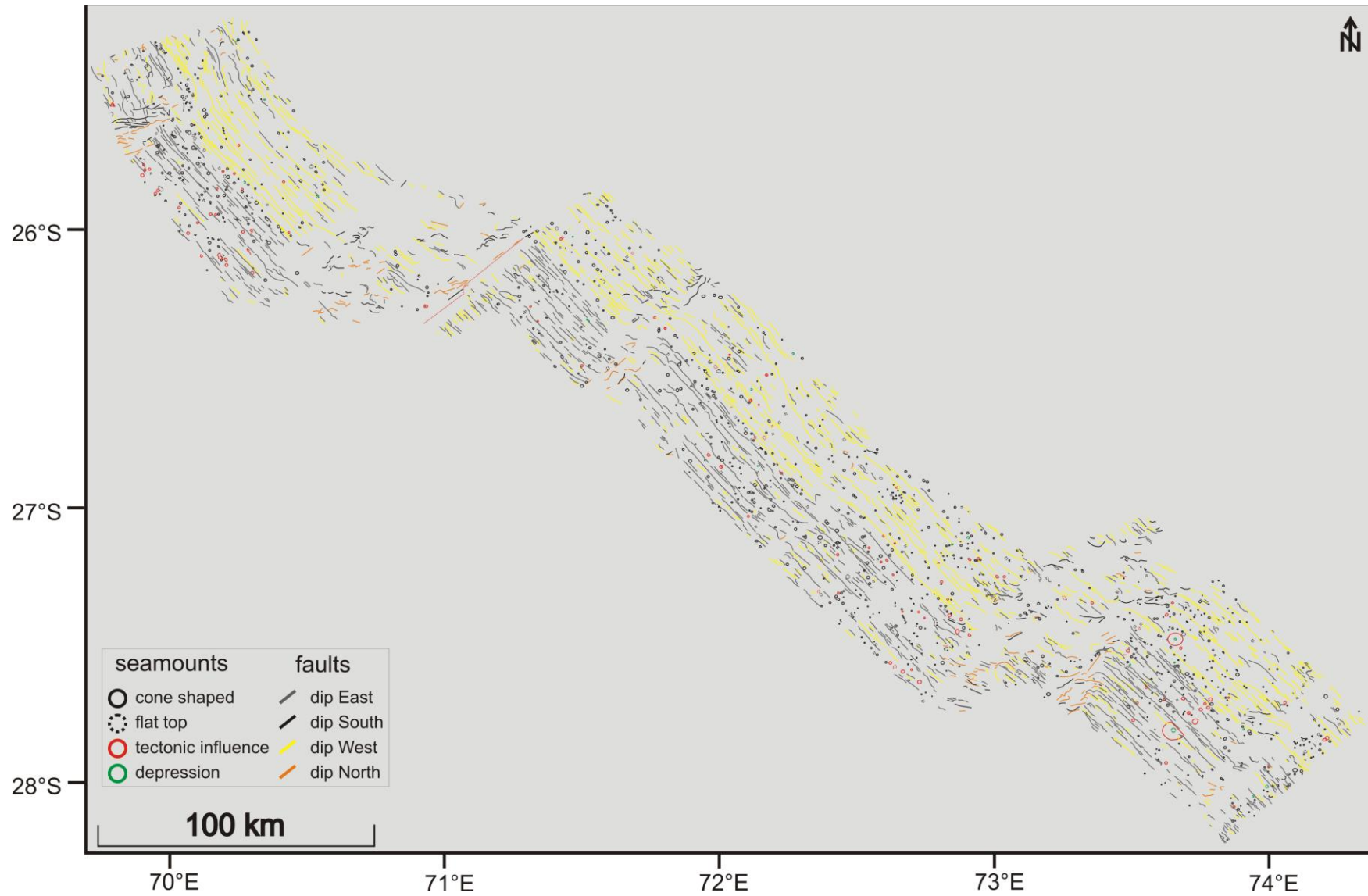


Figure B10: Structural map of the Southeast Indian Ridge labeled with circles for the seamounts and with lines for the faults dipping in different directions.